UNIVERSITY OF SOUTHAMPTON

Faculty of Engineering and Physical Sciences
Institute of Sound and Vibration Research

Fan proximity acoustic treatments for improved noise suppression in turbofan engines

by

Sergi Pallejà Cabré

BSc, MSc

ORCiD: 0000-0002-5414-7716

A thesis for the degree of
Doctor of Philosophy

January 2021

University of Southampton

Abstract

Faculty of Engineering and Physical Sciences
Institute of Sound and Vibration Research

Doctor of Philosophy

Fan proximity acoustic treatments for improved noise suppression in turbofan engines

by Sergi Pallejà Cabré

Fan noise is one of the dominant sources of aircraft engine noise, both at approach and at take-off. Improved attenuation of fan noise with acoustic liners and the reduction of fan noise at source remain key technology challenges for the foreseeable future. Over-Tip-Rotor (OTR) acoustic treatments have been investigated experimentally during the last decade and significant fan noise reductions have been measured, most recently at NASA by using a rotor-alone rig and multiple lined circumferential grooves. This thesis aims at improving our understanding of the noise reduction mechanisms of OTR liners through the development of an analytical prediction model. The fan noise is modelled with point or distributed monopole and dipole sources based on Green's functions for infinite hard or lined cylindrical ducts containing uniform mean flow; these are combined with an anechoic or unflanged inlet termination and an embedded lined section of finite length representing the 'rotor-alone' source with its OTR liner. Key aspects of the propagation/attenuation and liner impedance modelling are cross verified with reference FEM solutions. OTR predictions of liner insertion loss are obtained for comparison with the NASA experimental data, which entailed coupling of the propagation model with that of a partially non-locally reacting impedance model, and these yielded peak broadband in-duct noise reductions of up to 4 dB, in line with the measurements. To complement the analytical work, wind tunnel experiments have been conducted at ECL on a simplified over-tip liner configuration. The rotor and OTR liner were represented by a static aerofoil with its tip located over a flat plate containing a flush-mounted liner insert and separated from the airfoil tip by a small gap. The measured sound spectra exhibit peak broadband gap noise reductions of 5-10 dB due to the OTR liner and noise reduction in trailing edge noise of up to 5 dB in the absence of a gap.

Contents

List of Figures

List of Tables

Declaration of Authorship

I, Sergi Pallejà Cabré, declare that this thesis titled, 'Fan proximity acoustic treatments for improved noise suppression in turbofan engines' and the work presented in it are my own and have been generated by me as the result of my own original research.

I confirm that:

1. This work was done wholly or mainly while in candidature for a research degree at this University;
2. Where any part of this thesis has previously been submitted for a degree or any other qualification at this University or any other institution, this has been clearly stated;
3. Where I have consulted the published work of others, this is always clearly attributed;
4. Where I have quoted from the work of others, the source is always given. With the exception of such quotations, this thesis is entirely my own work;
5. I have acknowledged all main sources of help;
6. Where the thesis is based on work done by myself jointly with others, I have made clear exactly what was done by others and what I have contributed myself;
7. Parts of this work have been published as indicated in Section 1.6 of the thesis.

Signed:..... Date:.....

Acknowledgements

I would like to acknowledge the funding form the European Union's Horizon 2020 research and innovation programme under a Marie Sklodowska-Curie Innovative Training Network (ITN) grant (Agreement No 722401) within the SmartAnswer consortium.

This thesis culminates three years of intense learning and research in the fields of duct acoustics and fan noise, which completion would not have been possible without the support of many individuals.

First and foremost, I would like to express my sincere gratitude to my supervisors Brian Tester and Jeremy Astley for their continuous invaluable mentoring, guidance and support. Thank you for always asking the right questions, encouraging stimulating discussions and for your patient constructive feedback.

I would like to express my appreciation to Rick Bozak and his colleagues at NASA for sharing their data of the OTR W-8 tests and the SDT RAN test, used in the validation of our model. I am also grateful to Alan McAlpine and Paul Murray for their valuable feedback and advice during my progression reviews and afterwards, and to Phil Joseph and Chaitanya Paruchuri for interesting suggestions and discussions on particular aspects of the thesis.

Thanks to the SmartAnswer network I have had the chance to meet many passionate researchers spread around the world, both established and early stage like me. Thank you all for sharing this experience and for the discussions in our meetings, both in the lecture room and in the restaurant. I would like to give my special thanks to those who have helped me providing insight and support during my secondments: Hadrien Bériot, Michel Roger, Georgios Bampanis and Néstor González Díez.

I am also thankful to Sue Bridle for helping me in all administrative issues, and to all my colleagues at the ISVR and those back in Catalonia and spread around the world for making my time here so enjoyable and for sharing the ups and downs of the PhD road.

Finally, my deepest gratitude to my family for always supporting and believing in me, I would not be the person I am without them. And thank you Irene, my friend and my love, for taking this journey together and being there in the difficult times.

"Nothing in life is to be feared, it is only to be understood. Now is the time to understand more, so that we may fear less."

Marie Skłodowska Curie

List of Abbreviations

AAPL	Aero-Acoustic Propulsion Laboratory
ADP	Advanced Ducted Propulsor
ANCF	Advanced Noise Control Fan
AOA	Angle Of Attack
BL	Boundary Layer / Baseline
BPF	Blade Passing Frequency
BPR	By-Pass Ratio
CAA	Computational Aero-Acoustics
CFD	Computational Fluid Dynamics
COR	Cut-Off Ratio
DDOF	Double Degree Of Freedom
ECL	École Centrale de Lyon
FEM	Finite Element Method
FEMAO	Finite Element Method Adaptive Order
FML	Foam Metal Liner
FPL	Fan Proximity Liners
FWH	Ffowcs-Williams & Hawkings
GRC	Glenn Research Center
IL	Insertion Loss
LE	Leading Edge
LEN	Leading Edge Noise
LES	Large Eddie Simulation
MDOF	Multiple Degree Of Freedom
NACA	National Advisory Committee for Aeronautics
NASA	National Aeronautics and Space Administration
NIT	Normal Incidence Tube
OAPWL	Overall Power Level
OASPL	Overall Sound Pressure Level
ODE	Ordinary Differential Equation
OGV	Outlet Guide Vane
OTR	Over-Tip-Rotor
POA	Percentage Open Area
PS	Pressure Side
PSD	Power Spectral Density
PWL	Sound Power Level
RAN	Rotor Alone Nacelle
RANS	Reynolds-Averaged Navier-Stokes

SDOF	Single Degree Of Freedom
SDT	Source Diagnostic Test
SPL	Sound Pressure Level
SS	Suction Side
TE	Trailing Edge
TEF	Trailing Edge Feathers
TEN	Trailing Edge Noise
TL	Transmission Loss
TLV	Tip Leakage Vortex
TRL	Technology Readiness Level
UAV	Unmanned Aerial Vehicles

List of Symbols

Latin lower case

a	duct radius
c	speed of sound / airfoil chord
d	groove depth
d_h	facing sheet hole diameter
e	tip gap size
f	frequency / external force
g	Green's function in the time domain
h	liner cavity depth
j	imaginary unit
k	acoustic wavenumber
k_n	axial wavenumber in Cartesian groove
k_z	azimuthal wavenumber in Cartesian groove
l	length
m	azimuthal mode order / mass injection
m_r	facing sheet mass reactance
n	radial mode order
p	acoustic pressure
q	generic acoustic source
r	radial coordinate
s	standard deviation
t	time / facing sheet thickness
u	acoustic particle velocity
(x, y, z)	Cartesian coordinates
z	acoustic impedance

Latin upper case

A	specific acoustic admittance / complex modal amplitude
B	number of fan rotor blades
C	reflection coefficient matrix
D	fan diameter
E	expectation
G	Green's function in the frequency domain
He	Helmholtz number
I	acoustic intensity
J_m	Bessel function of the first kind
M	Mach number

N	number of elements
P	acoustic power
R	specific acoustic resistance
S	surface
S_{ff}	source cross-spectrum
S_{pp}	pressure cross-spectrum
U	flow velocity
U_c	convection velocity
V	number of stator vanes
$\bar{W}$	weighting function
X	specific acoustic reactance
Y_m	Bessel function of the second kind
Z	specific acoustic impedance

Greek lower case

α	normal incidence absorption coefficient / radial wavenumber
β	radial wavenumber in Cartesian groove
γ	heat capacity ratio / dipole alignment angle
δ	delta function / boundary layer thickness
ϵ	facing sheet end correction
θ	azimuthal angle
κ	axial wavenumber
λ	acoustic wavelength
ξ	acoustic particle displacement
ρ	air density
σ	porosity
τ	emission time
ϕ	polar angle
ϕ_{ff}	wall pressure spectrum
ω	angular frequency

Greek upper case

Γ	duct contour
Θ	stagger angle
Ψ	observation angle: azimuthal angle corrected with the angle of incidence
$\bar{\Omega}$	fan rotor angular frequency

Chapter 1

Introduction

Contents

Aircraft noise is a concern for population due to its annoyance and the potential health effects it may cause on the communities near airports, including cardiovascular problems, sleep disturbance and children's cognition problems among others [11, 12]. The continuous growth in air traffic experienced prior to the COVID-19 pandemic increases the levels of community noise exposure, rising the pressure on policymakers and resulting in increasingly stringent noise regulations [13]. Despite the drastic impact of the pandemic in the civil aviation industry [14], lighter environmental regulations post-COVID are unlikely [15]. Aircraft noise generated during take-off and landing is key for the certification of aircraft, influencing airframe and aero-engine manufacturers to treat acoustic pollution as one of the driving factors in the design of their products alongside the operational costs [16].

In aircraft with modern turbofan engines, the engine noise is dominant at take-off and the airframe noise when landing. The main airframe noise sources are the wing trailing edge, slats, flaps and undercarriage [16]. The main noise sources in turbofan engines are the fan, the jet, the compressor, the combustion chamber and the turbine [17]. A combined reduction of airframe and engine noise and all their different components is required to achieve any improvement in the overall aircraft noise reduction [17, 18].

The turbofan engine, used in most commercial aircraft, represent a large noise contributor to the overall aircraft noise. The relative strength of each noise source in the engine has changed over the years as the different components have been optimised and the bypass ratio (BPR) has increased, as shown in Figure 1.1. The progressive increase in BPR, the ratio of mass bypassed to mass through the core, has reduced the speed of the jet, and hence its noise, and has improved the engine fuel efficiency. In modern high-bypass-ratio designs, fan noise is one of the dominant engine sources both at approach and at take-off, resulting in a critical noise-reduction target for the next generation of turbofan engines [18].

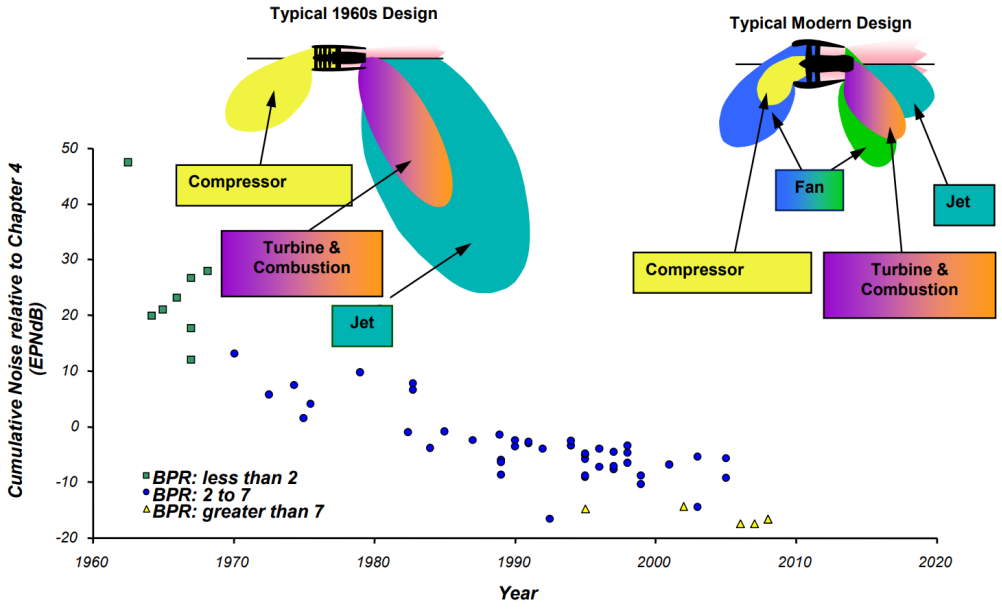

Figure 1.1: Progress made in reducing aircraft noise noting the increase of the BPR and diagram of the main noise sources in the engine [1].

Acoustic liners have been traditionally used for fan noise reduction, installed in the intake and bypass ducts, as indicated in Figure 1.2. Typical designs are manufactured with a perforated or porous face sheet supported by a honeycomb structure. These so-called single-degree-of-freedom (SDOF) and multiple-degree-of-freedom (MDOF) liners are generally designed to attenuate tonal and broadband noise over certain frequencies to minimize the certification noise levels [19]. The design of innovative liner configurations, the modelling of the physics involved in the noise reduction and the measurement of their acoustic behaviour have been subject of research for many years [20–22].

The expected increase of the bypass ratio in the next generation of turbofan engines can lead to a significant increase in fan diameter (D) but without an increase in liner length (L) to minimize nacelle weight and drag [2, 23]. Consequently, as the performance of the liners is proportional to L/D, the relatively shorter nacelles can reduce the overall noise reduction performance of intake liners [24, 25]. As mentioned before, passive acoustic

treatments or liners are a well-known and efficient ways to attenuate fan noise and maximising the treated area is always a key parameter in liner performance. An area that has not been fully evaluated or exploited in the past is the duct casing in the immediate proximity of the fan rotor. The so-called Fan Proximity Liners (FPL) consist of the fan case, the Over-Tip-Rotor (OTR) region and the interstage, depicted in blue, green and red respectively in Figure 1.2.

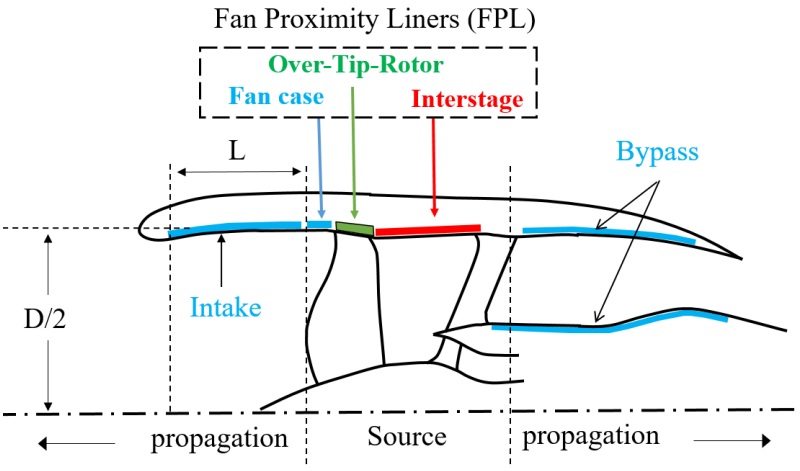

Figure 1.2: Conventional liners (Intake and Bypass) and Fan Proximity Liners.

Over-Tip-Rotor acoustic treatments have been investigated during the last decade as a technology with the potential to further attenuate the fan noise in turbofan engines, mainly at NASA GRC, where significant noise reductions have been measured. The tests showed a range of noise reductions and associated loss in aerodynamic performance (measured as loss in adiabatic efficiency), which depend upon the liner design used, the test rig and the operating conditions. Details of the experimental set-up and discussion of the results is given in Section 1.1, but a summary of the results obtained is shown in Table 1.1.

Table 1.1: Summary of OTR published experimental results.

Publication	**Noise Reduction**	**Loss in Adiabatic Efficiency**
Sutliff et. al. [26]	4 dB PWL (inlet & aft)	-
Elliot et. al. [27]	1 dB OAPWL	-
Sutliff et. al. [28][19]	5 dB inlet PWL / 2.5 dB OAPWL	1-2 %
Hughes and Gazzaniga [29]	-	6.5 - 9.3 %
Bozak et. al. [30]	-	0.75 %
Gazella et. al. [31]	1 dB / 3 dB (inlet/aft) PWL	-
Bozak and Dougherty [5]	2.5-3.5 dB (inlet) PWL	-
Bozak and Podboy [32]	-	< 0.5 %

1.1 Over-Tip-Rotor Liners: a literature review

The types of Fan Proximity Liners that have been in the spotlight in terms of experimental evaluation and maturation of its Technology Readiness Level (TRL) are the OTR acoustic treatments. They have been investigated during the last decade as a technology with the potential to further attenuate the fan noise in turbofan engines. These studies have been led by NASA GRC in collaboration with other research centres, companies and universities. They include any liner design which is embedded in the fan duct wall at or near the location of the fan rotor plane. The OTR region presents a harsh aeroacoustic environment which limits the materials and technologies that can be used for the design of the liners. These conditions define a series of characteristics that would be required for the materials, including high acoustic absorption, high-temperature resistance, containment properties/high impact resistance, low flammability and minimal fluid retention [19, 33, 34].

The main body of this literature survey aims to summarize the findings published on OTR liners and group these within the following three categories: the physical mechanism of noise reduction, the experimental data on noise reduction and on aerodynamic performance. Additional literature review has been required in the project in topics such as noise generation, source modelling, sound propagation, mode-matching methods and acoustic impedance modelling, which are described in the respective chapters of this manuscript.

Interstage liners, located in the region between the fan and the Outlet Guide Vanes (OGVs), have also been object of interest due to the additional acoustically treated area and the importance of fan-OGV interaction noise but are outside the scope of this thesis. The main difficulty in the modelling and design of liners in the interstage region is the swirling mean flow induced by the rotation of the fan blades. The swirling flow can reduce the effectiveness of the acoustic treatments by preventing the disturbances from reaching the duct walls [35]. Recent work in this topic include an analytical Green's function for homentropic [36] or variable entropy [23] swirling flow in a lined duct, which could potentially be used to extend the current work to interstage liners.

1.1.1 Physical Mechanism

The idea of placing the liners over-the-rotor is aimed at reducing the noise generated in the region of the fan tip by modifying the interaction between the unsteady fan tip flow and the fan case. Primarily it is understood that the liner is placed in the fan case over the fan blade tip to absorb the pressure fluctuations by different mechanisms explained below.

Experimental tests have indicated that OTR liners mitigate the acoustic near-field, showing that noise reduction of this acoustic treatment is caused by a combination of acoustic attenuation and source modification [26]. To confirm this conclusion, a series of tests were conducted with different liner concepts installed in OTR configuration and in the inlet location to assess the relative importance of the physical noise reduction mechanisms. When placed in the OTR location, the liners produced a higher noise reduction and thereby indicated that the physical mechanism is also attributed to source modification [19]. These last experiments also tested the liner designs in two hardware configurations: with and without static vanes, to investigate the impact of this concept in reducing the rotor-stator interaction noise. The results indicated that the noise reduction mechanism is not only attributed to source modification but also to a reduction in the propagating noise from the rotor-stator interaction. A recent study [32] linked the reduction in rotor-stator interaction noise to a reduction of the turbulence intensity in the fan wake cause by the OTR liners, potentially reducing broadband fan-OGVs interaction noise by 1-2 dB.

In summary, the noise reduction mechanism caused by the OTR liners is attributed to a combination of three factors: modification of the source itself, conventional absorption of acoustic waves propagating over the liner and a reduction in the rotor-stator interaction noise. However, a consensus on the physical mechanism for the noise reduction using OTR acoustic treatments has not been reached. Further investigation into understanding of the physical mechanisms and predicting the noise suppression caused by the OTR liners is required [19][34].

1.1.2 Noise Reduction Performance

Prototypes of foam metal liners for OTR acoustic treatment were tested in the Advanced Noise Control Fan (ANCF) test bed [26], which is a low-speed fan used for validation of noise reduction concepts at the Aero-Acoustic Propulsion Laboratory (AAPL) at NASA John H. Glenn Research Center (GRC). The foam metal liners were tested at different axial positions, including the OTR. The best acoustic performance was measured when placed in the OTR position, resulting in up to 4 dB of broadband noise reduction in both inlet and aft far fields.

To evaluate the effect of the OTR acoustic treatments in a higher bypass ratio (BPR) turbofan, two liner concepts were tested in the Pratt & Whitney Advanced Ducted Propulsor (ADP) as it is representative of an ultra-high bypass ratio, low tip speed turbofan engine [27]. One foam metal liner had the metal foam exposed on the flow surface and the other had a perforated rigid plastic resin rub surface; both were compared with a conventional rigid hard wall baseline. It was found that the OTR with a cover sheet showed an Overall Sound Pressure Level (OASPL) reduction of around 1 to 2 dB for this high bypass ratio

hardware, which is lower than found in the previous experiments. However, the treatment with the exposed metal foam produced more noise than the hard wall baseline case, around 1 dB higher.

A Williams International FJ44-3A was used as a test bed at NASA GRC to assess the effect on the performance of foam metal OTR liners in a high-speed turbofan engine and its noise reduction benefits were compared against a hard wall baseline and to typical SDOF liners designed using standard methodologies [19, 28]. The noise reductions obtained with the SDOF liners located at a conventional inlet position (12-inch long) were of similar magnitude to those obtained with the much shorter (2-4 inch) foam metal liner installed over-the-rotor, suggesting potential source modification effects. Up to 5 dB noise reduction in *inlet* Power Level (PWL) was achieved below fan tip sonic speed, with a total OAPWL reduction of 2.5 dB. The use of circumferential grooves in the OTR liners showed a smaller performance penalty, which is explained in the following pages. However, it was found that grooves generate additional broadband noise that is not fully attenuated by the OTR liner [34].

The reduction in aerodynamic performance penalty observed in previous publications [30] was attributed to the circumferential grooves in the casing installed over the fan tip and its effect on reducing the dynamic pressure on the acoustic treatment, as detailed in the next subsection. This lead to testing of liner designs consisting of a casing of circumferential grooves integrated with various acoustic treatments [5]. These tests were developed aiming to improve understanding of the physical mechanisms of noise reduction using OTR acoustic treatments to improve the Technology Readiness Level (TRL) of various OTR liner designs in the ANCF [31] and in the W-8 Single Stage Axial Compressor Facility [5], both installations at NASA GRC.

In the ANCF tests, the liner designs were (1) compared against a hard-wall baseline, (2) installed in OTR configuration and in the inlet to assess the relative importance of the physical noise suppression mechanisms and (3) tested with and without static vanes to investigate the impact of this concept in reducing the rotor-stator interaction noise. The best liner concept achieved the noise reductions of up to 3dB. The thin face sheet was a common factor in the designs with higher noise reduction. Some treatments showed an increase in noise when comparing the results of rotor-alone vs rotor-stator, which was attributed to an increase in strength of the rotor tip vortex impinging on the stator vanes.

The results from the W-8 Single Stage Axial Compressor showed a net benefit of the OTR liner designs of 2.5-3.5 dB of reduction in the PWL of the forward propagating modes. A noise penalty of 2.5-6 dB from the circumferential grooves was present between 4-8 kHz at low fan speeds. The impact of the grooves at high fan speeds was found to be minimal [5]. Recent Grazing Flow Impedance Tube tests at NASA showed that the additional groove noise is likely to be cavity tones/resonances that are clipped by the fan [37].

1.1.3 Aerodynamic Performance

The aim of reducing the noise generated by the engine needs to be traded off against any loss of aerodynamic performance. A number of investigations have been developed to assess the effect of the OTR liner concepts on the aerodynamic performance of the engine and to optimize the design for a minimal aerodynamic penalty while presenting the desired noise reduction [19, 29, 30].

In one of the investigations [29] two OTR metal foam liners where tested, one that had the metal foam exposed on the flow surface and the other with a perforated rigid plastic resin rub. Both were compared to a conventional rigid hard wall baseline. The OTR perforated rub strip showed a drop in performance with respect to the baseline case with a loss in adiabatic efficiency from 2.7% to 4.0% as the speed increases. The exposed metal foam OTR showed even worse performance, with a loss in adiabatic efficiency from 6.8% at 55% speed to 9.3% at 100% speed. Better results were obtained in the tests of FML OTR on the Williams International FJ44-3A [19], which showed a reduction of 1-2% in the engine performance, a significant improvement over previous tests.

Further work was undertaken to quantify the impact of OTR liners with circumferential grooves with respect to a baseline hard wall rub-strip in the aerodynamic performance of a turbofan rotor [30]. The variation in pressure ratio, fan temperature ratio and fan adiabatic efficiency were used to quantify the performance loss. The fan pressure ratio was not affected by the OTR treatment. However, the fan temperature ratio near the blade tips increased, with a rapid rise near sonic tip speeds. The adiabatic efficiency loss was 0.75%, indicating a benefit from using the circumferential grooves in the OTR liner designs to minimize the loss of aerodynamic performance. Further tests evaluating the acoustically treated circumferential grooves [32] found the loss in adiabatic efficiency to fall within the measurements repeatability margin.

1.2 Fan noise sources

Fan noise in turbofan engines can be broadly divided into *tonal* and *broadband* depending on the nature of the noise source physical mechanisms. Tonal noise is related to the periodic rotational motion of the fan blades whilst broadband noise is attributed to the pressure fluctuations created by unsteady turbulent flow. A brief overview of the main turbofan tonal and broadband sources is given below based on the work presented in [3, 16, 35, 38, 39] and following the categorization given by Peake and Parry [35]. A sketch of the main fan noise sources covered in this section is shown in Fig. 1.3. Tonal and broadband noise source mechanisms are depicted in green and blue respectively.

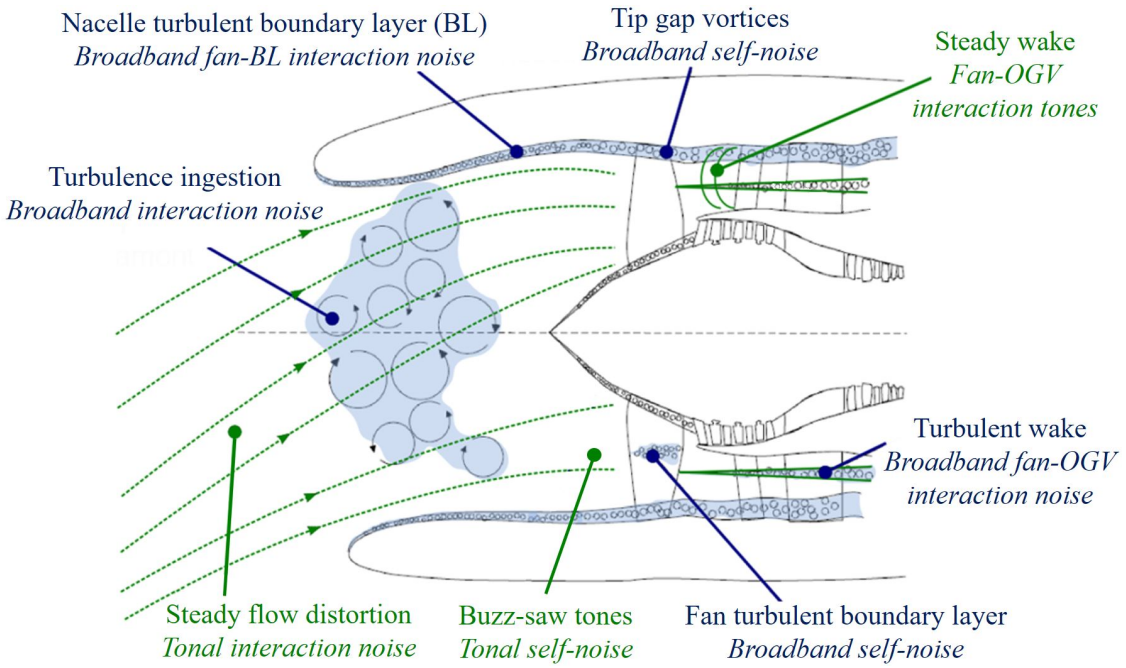

Figure 1.3: Main flow features and fan noise source mechanisms, adapted from [2].

Broadband noise sources located in the vicinity of the fan proximity liners are of special interest for this work since they can be subjected to source modification effects caused by a porous boundary condition in the near field of the source. Candidate rotor blade-based sources are the trailing edge noise and fan-boundary layer interaction noise radiated from the blade tip region and tip gap noise. As mentioned previously, a recent study [32] suggests that OTR liners can also affect the fan-OGV interaction noise by reducing the turbulence intensity in the fan wake.

1.2.1 Tonal noise

Fan self-noise

Tonal self-noise is produced by the steady periodic forces that the rotating fan blades exert on the fluid as a reaction of the steady blade loading. This steady forces in the rotating frame of reference generate a disturbance at the blade passing frequency (BPF) $B\Omega$, where B is the number of identical, equally-spaced blades and Ω the rotation frequency of the shaft. The time-harmonic modal pressure field generated contains modes of azimuthal orders that are multiples of the number of blades, $m = nB$, at harmonics of the BPF, $\omega = nB\Omega$. A direct consequence of this result is that, for an isolated rotor, the relative tip Mach number must be supersonic for any mode to propagate and therefore to efficiently radiate sound.

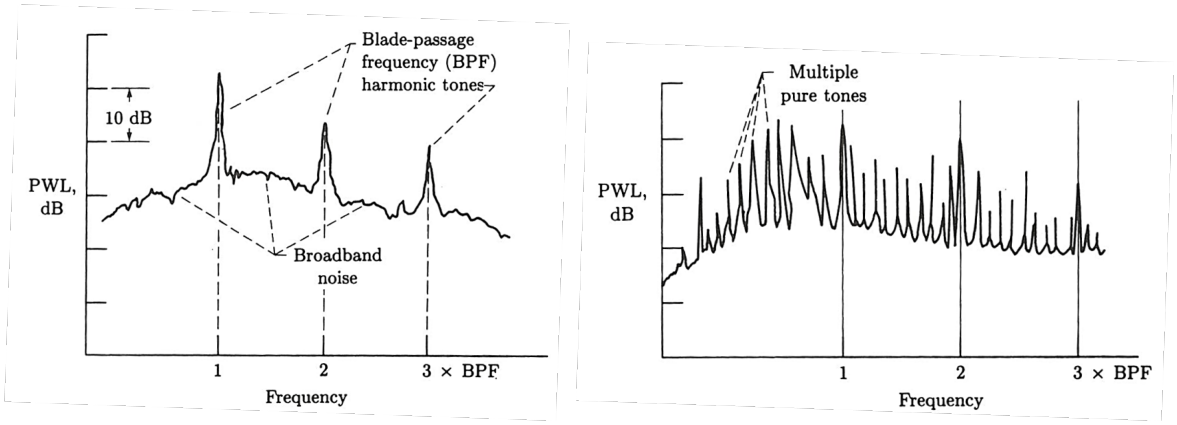

(a) Subsonic tip speed

(b) Supersonic tip speed

Figure 1.4: Typical turbomachinery sound power spectra [3]

However, if the fan tip speed is supersonic non-uniformities in the blades such as profile, spacing or stagger angles can induce variations in the strength of the shock waves developing upstream around the blades. Then, noise will be radiated not only at multiples of the BPF, as it would in an ideal (supersonic) uniform fan in a uniform flow, but also at all multiples of the shaft rotation frequency (buzz-saw tones). This can be observed in Fig. 1.4b, where a typical sound power spectrum is depicted for supersonic tip speed.

Fan-OGVs interaction

The wakes generated by the fan present steady mean components and unsteady fluctuating components. The identical mean blade wakes shed from each blade are steady in the rotating frame of reference and produce a periodic rotating field in the stationary OGVs frame of reference with azimuthal orders multiple of the number of fan blades, $m = nB$. The unsteady components are caused by the turbulence within the wakes and produce broadband noise when interacting with the OGVs, as outlined in 1.2.2.

The tonal noise produced by the interaction of the fan wakes with the OGVs was modelled by Tyler and Sofrin [40]. The source frequency is again at multiples of the BPF, $\omega = nB\Omega$, due to the fan wakes impinging on the stator blades, but now the azimuthal modes orders are $m = nB + lV$, where V is the number of OGVs and l is an integer. Note that the azimuthal interaction modes are not steady in the rotating frame of reference and they can propagate even at subsonic fan tip speeds, resulting in the dominant tonal source at this regime. These tones are depicted in Fig. 1.4a for a typical turbomachinery sound power spectra with subsonic tip speed. With an appropriate choice of fan blades (B) and OGVs (V) such that $V > 1.1(1 + M_t)nB$, a target n^{th} BPF harmonic and the lower harmonics are cut-off over the entire subsonic fan tip speed range.

Steady flow distortion

The turbofan engine nacelle is often scarfed or drooped to accommodate a non-zero angle of incidence in flight [41]. These nacelle design features, including non-circular intakes in some large engines to meet ground clearance requirements, lead to non-axisymmetric mean flow upstream of the fan. Therefore, the flow that the fan encounters is non-uniform in the circumferential direction, with azimuthal components unsteady in the rotating frame of reference that induce loads variations on the fan blades and generate tonal noise. Depending on the azimuthal periodicity of the flow distortion the tones are analogous to those predicted by Tyler and Sofrin for rotor-stator interaction [40]. This is also the case for the scattering of fan tonal noise by liner splices, which break the azimuthal symmetry of intake liners [42–44].

1.2.2 Broadband noise

Fan self-noise

The dominant source of fan self-noise is the trailing edge noise, caused by the local interaction of the eddies within the turbulent boundary layer generated on the suction surface of the fan blades with the trailing edge. This noise mechanism was described by Ffowcs Williams & Hall [45] and showed the aerodynamic noise amplification of turbulent flows in the presence of surface edges.

Tip clearance noise can also be considered as fan self-noise, although it is not clear how significant it is among other noise sources [46]. The pressure difference in the suction side and the pressure side of the fan blades creates a jet-like flow through the tip gap that rolls up into a tip leakage vortex (TLV). The source mechanism is attributed to the interaction of the jet-like flow with the blade tip edge and to the scattering by the tip edge and/or the trailing edge of the unsteady perturbations induced by the tip vortex. Recent computational work has shown that TLV noise can also generate noise at certain engine operation conditions by impinging on the adjacent blade leading edge [47].

Fan broadband interaction noise

The common noise generation mechanism of fan broadband interaction sources is the unsteady load fluctuations caused by the interaction of incoming turbulence with the fan blade or the OGVs. These can be categorised as follows:

- **Fan-boundary layer interaction:** Due to the very small fan tip clearance of typical turbofan engines, the fan blade tips are immersed into the turbulent boundary layer.

The eddies within the boundary layer interact with the blade surface and generate sound by inducing unsteady load fluctuations.

- **Fan-OGVs interaction:** As mentioned above, the wakes generated by the fan present fluctuating components caused by the turbulence within the wakes. These fluctuating components produce broadband noise when interacting with the OGVs and constitute the dominant source of broadband noise.

- **Turbulence ingestion:** The interaction of turbulence structures in the free stream upstream of the fan with the leading edge of the fan blades induce random unsteady loads on the blades that generate broadband noise. The atmospheric free stream turbulence levels are generally much lower than those in a static test rig. This motivated the use of inlet turbulent flow control screens to be able to replicate the in-flight atmospheric environment in static tests.

1.3 Modelling of noise sources

The analytical models for fan noise are often based on some form of acoustic analogy in which the sound field is governed by a non-homogeneous wave equation and the complex aerodynamic sound generation mechanisms are represented as equivalent acoustic sources. The first aero-acoustic analogy was introduced by Lighthill [48] and was later generalised by Ffowcs Williams and Hawkings [49] (FWH) to include moving solid boundaries that can represent the fan blades. Goldstein [50] extended the FWH analogy by replacing the free-field Green's function with that of an infinite hard wall duct with uniform axial mean flow. Further extensions have been proposed using the Green's function for a hollow or annular lined duct with uniform mean flow [51] and swirling flow [23, 36, 52].

A large amount of work has been done in modelling the tonal and broadband fan noise sources. The equivalent acoustic sources in the acoustic analogies can be described by distributions of static or rotating sources, like monopoles and dipoles, with specified spatial and frequency correlations distributed over the blades. Moreau [2] gives a review of the state-of-the-art analytical and numerical methods for turbomachinery noise prediction categorised by tonal and broadband noise. However, this section will only review the fundamental formulation of the wave equation and of simple point sources in free-field and their physical meaning. Although this formulation can be found in the open literature it is a useful introduction for Chapter 4, which describes the Green's function formulation adopted in this work and the related literature review regarding the modelling of the source strength and correlations.

1.3.1 The wave equation

The starting point for most acoustic propagation problems is the homogeneous wave equation. By assuming a homogeneous, adiabatic (no heat exchange) and frictionless (no viscosity) fluid with uniform entropy, i.e. homentropic, the Euler equations governing the fluid dynamics of the medium can be written in the form:

- Conservation of mass:
$$\frac{\mathrm{D}\rho}{\mathrm{D}t} + \rho\boldsymbol{\nabla}\cdot\boldsymbol{u} = 0 \quad , \tag{1.1}$$
- Conservation of momentum:
$$\rho\frac{\mathrm{D}\boldsymbol{u}}{\mathrm{D}t} + \boldsymbol{\nabla}p = \mathbf{0} \quad , \tag{1.2}$$
- Conservation of energy:
$$\frac{\mathrm{D}p}{\mathrm{D}t} + \gamma p\boldsymbol{\nabla}\cdot\boldsymbol{u} = 0 \quad , \tag{1.3}$$

where Eq. 1.3 is derived from combining the conservation of mass (Eq. 1.1) with the equation of state
$$\frac{\mathrm{D}p}{\mathrm{D}t} = c^2\frac{\mathrm{D}\rho}{\mathrm{D}t} \quad , \tag{1.4}$$

and assuming a perfect gas governed by
$$\rho c^2 = \gamma p \quad , \tag{1.5}$$

where ρ, p, $\boldsymbol{u}$ and γ are the density, pressure, velocity and specific heat ratio of the fluid respectively, c is the speed of sound and $\frac{\mathrm{D}}{\mathrm{D}t}$ denotes the material derivative (time derivative moving with the flow): $\frac{\mathrm{D}}{\mathrm{D}t} = \frac{\partial}{\partial t} + \boldsymbol{u}\cdot\boldsymbol{\nabla}$.

The pressure and density fluctuations around a steady state caused by sound waves are generally very small. In such cases, the Euler equations can be simplified by linearisation. This assumption would not hold in cases where the amplitude of the fluctuations is very high, such in the shock systems that cause the buzz-saw tones in turbofan engines. For the linearisation it is also assumed that the flow can be decomposed into a steady base flow, $p_0, \rho_0, \boldsymbol{u}_0$, plus unsteady small amplitude perturbations, $p', \rho', \boldsymbol{u}'$:

$$p(\boldsymbol{x},t) = p_0(\boldsymbol{x}) + p'(\boldsymbol{x},t) \qquad \rho(\boldsymbol{x},t) = \rho_0(\boldsymbol{x}) + \rho'(\boldsymbol{x},t) \qquad \boldsymbol{u}(\boldsymbol{x},t) = \boldsymbol{u}_0(\boldsymbol{x}) + \boldsymbol{u}'(\boldsymbol{x},t) \quad . \tag{1.6}$$

By introducing the flow decomposition into Eq. 1.1-1.3 and discarding the non-linear terms, the following set of linearised Euler equations is obtained:

- Conservation of mass:

$$\frac{\mathrm{D}_0\rho'}{\partial t} + \boldsymbol{\nabla}\cdot\left(\rho_0\boldsymbol{u'} + \rho'\boldsymbol{u}_0\right) = 0 \quad , \tag{1.7}$$

- Conservation of momentum:

$$\rho_0\frac{\mathrm{D}_0\boldsymbol{u'}}{\mathrm{D}t} + \rho'\frac{\mathrm{D}_0\boldsymbol{u}_0}{\mathrm{D}t} + \rho_0\left(\boldsymbol{u'}\cdot\boldsymbol{\nabla}\right)\boldsymbol{u}_0 + \boldsymbol{\nabla}p' = \mathbf{0} \quad , \tag{1.8}$$

- Conservation of energy:

$$\frac{\mathrm{D}_0 p'}{\mathrm{D}t} + \left(\boldsymbol{u'}\cdot\boldsymbol{\nabla}\right)p_0 + \gamma p_0\boldsymbol{\nabla}\cdot\boldsymbol{u'} + \gamma p'\boldsymbol{\nabla}\cdot\boldsymbol{u}_0 = 0 \quad , \tag{1.9}$$

where the material derivative $\frac{\mathrm{D}_0}{\mathrm{D}t}$ is defined as $\frac{\mathrm{D}_0}{\mathrm{D}t} = \frac{\partial}{\partial t} + \boldsymbol{u_0}\cdot\boldsymbol{\nabla}$.

Assuming that the perturbations do not affect the base flow, one could use the base flow as an input to Eq. 1.7-1.9 and then solve the acoustic problem. The base flow can be obtained from simplified models (stagnant fluid, uniform flow, etc.), numerically using CFD (RANS, LES, etc) or from measurements. Only the simple model of uniform flow is descried here since it forms the basis for work in subsequent chapters.

Considering that the base flow is uniform, i.e. $\rho_0, p_0, \boldsymbol{u}_0, c_0$ are constant, the linearised Euler equations (Eq. 1.7-1.9) can be further simplified to:

- Conservation of mass:

$$\frac{D\rho'}{Dt} + \rho_0\boldsymbol{\nabla}\cdot\boldsymbol{u'} = 0 \quad , \tag{1.10}$$

- Conservation of momentum:

$$\rho_0\frac{\mathrm{D}_0\boldsymbol{u'}}{\mathrm{D}t} + \boldsymbol{\nabla}p' = \mathbf{0} \quad , \tag{1.11}$$

- Conservation of energy:

$$\frac{\mathrm{D}_0 p'}{\mathrm{D}t} + \gamma p_0\boldsymbol{\nabla}\cdot\boldsymbol{u'} = 0 \quad . \tag{1.12}$$

The homogeneous convective wave equation (Eq. 1.13) can be obtained by manipulating Eq. 1.10-1.12 to yield

$$\frac{\mathrm{D}_0^2 p'}{\mathrm{D}t^2} - c_0^2\boldsymbol{\nabla}^2 p' = 0 \quad , \tag{1.13}$$

where c_0 is the speed of sound in the fluid defined in Eq. 1.5. Details of the complete derivation of the generalised linearised wave equations can be found in [50, 53].

It is common in acoustics to consider a time-harmonic sound field of the form $p'(\boldsymbol{x}, t) = p'(\boldsymbol{x}, \omega)e^{j\omega t}$. Then, the wave equation in Eq. 1.13 is simplified into the convective Helmholtz

equation:

$$\nabla^2 p' - (jk + \boldsymbol{M} \cdot \boldsymbol{\nabla})^2 \, p' = 0 \quad , \tag{1.14}$$

where $k = \omega / c_0$ is the wave number and $\boldsymbol{M} = \frac{\boldsymbol{u}_0}{c_0}$ the base flow Mach number.

1.3.2 Simple sources

The solutions of the homogeneous wave equations give mathematical forms of sound waves that can exist in the fluid in the absence of boundaries. These can be used to determine how the sound propagates within the fluid, but they do not provide any information of how the perturbations are generated.

The acoustic field can be physically excited by different kinds of sources including injection of an unsteady mass, external forces (momentum), external stresses or an external unsteady heat source. These noise generation mechanisms represent the right-hand-side of the acoustic analogies. This section is limited to the injection of mass (or volume displacement) and momentum since these are the dominant mechanisms in fan noise: the so-called thickness noise and the unsteady loads normal to the rotor blade surface respectively.

If the assumptions made to obtain the homogeneous wave equations are now modified such that a mass injection (or displacement of volume) and an external force can be applied to the fluid, the equations of conservation of mass and momentum are now [53]:

- Conservation of mass:

$$\frac{\mathrm{D}\rho}{\mathrm{D}t} + \rho \boldsymbol{\nabla} \cdot \boldsymbol{u} = m \quad , \tag{1.15}$$

- Conservation of momentum:

$$\rho \frac{\mathrm{D}\boldsymbol{u}}{\mathrm{D}t} + \boldsymbol{\nabla} p = \boldsymbol{f} \quad , \tag{1.16}$$

where $\boldsymbol{f}$ is an external force per unit volume and m is the rate at which mass is injected per unit volume.

Following an analogous linearisation process the following form of the inhomogeneous convective wave equation can be obtained:

$$\frac{1}{c_0^2} \frac{D^2 p'}{Dt^2} - \boldsymbol{\nabla}^2 p' = \frac{Dm}{Dt} - \boldsymbol{\nabla} \cdot \boldsymbol{f} \quad . \tag{1.17}$$

The terms on the right-hand side are the source terms that excite the acoustic field. The solution of Eq. 1.17 and the mathematical representation of these sources in a hard wall or lined duct play a key role in the modelling of Over-Tip-Rotor liners, which is described and analysed in detail in Chapter 4.

1.4 Research objectives and original contributions

The lack of full understanding and consensus on the physical mechanism of noise reduction using OTR acoustic treatments and the need for a prediction method to estimate the optimum surface impedance for OTR liners has been identified in the literature [19, 28, 33, 34].

The modelling of Over-Tip-Rotor liners is a challenge due to the high complexity of the physics involved. The sound generation, propagation and attenuation in the vicinity of the fan are each a complex problem on their right. The sources of sound are a combination of tones of the blade passing frequency and aerodynamic broadband sources that can be divided into self-noise (trailing edge noise and tip clearance noise) and interaction noise (fan-OGV interaction and tip-BL interaction). The suggested modification of the sources by the liner and the expected high-pressure fluctuations acting on the liner surface make the modelling of the propagation and attenuation non-trivial, involving non-locally reacting cavities and non-linear effects. If the tip relative Mach number is supersonic, shock waves would be present adjacent to the liner increasing the difficulties of impedance prediction. In addition, the swirling flow component of the mean flow transitions as it flows through the fan stage, from a practically axial mean flow upstream of the fan to a combination of axial and a significant swirling flow component downstream in the interstage region.

This thesis aims at improving understanding of the noise reduction of OTR liners trough a simplification of the problem described above such that analytical prediction methods can be developed to guide the choice of low-TRL fan proximity liner designs for optimal noise reduction. The objectives can be divided into three groups:

1. **Analytical modelling**: Development of an analytical prediction model for the noise reduction performance of OTR liners. The model should include the modelling of the fan sources and the coupling with the OTR liner, the matching of the solution in sections of the duct with different impedance boundary conditions and the convective effects of mean flow.

2. **Numerical verification**: Development of numerical simulations to verify the analytical tools required for building the OTR prediction model including the modelling of source proximity effects, unconventional impedance models and mode-matching in the proximity of a point source.

3. **Experimental validation**: Comparison of the analytical noise reduction estimates with published OTR experimental data to validate the analytical OTR prediction model. Performing fundamental experiments to complement and support the findings obtained with the numerically verified analytical prediction model.

The work presented here rely on well-established methods that have been extended or modified to provide a better understanding of OTR liners and a prediction model for their noise suppression performance. The approach taken in the project has been mainly analytical, aimed at developing models that simplify the complex physics, yet being representative of the acoustic problem. Uniform axial mean flow has been assumed throughout the formulation, limiting the prediction tools to fan case liners and OTR liners, the latter representing a bolder assumption. A linear propagation model is assumed and hence OTR liner effects on supersonic fan noise is also outside the scope of this work. The main assumptions of the proposed model are summarised in Table 1.2.

Table 1.2: Main assumptions of the analytical OTR liner prediction model.

Geometry	Axially segmented hollow circular duct
Propagation	Linear
Mean flow	Uniform or 'plug' flow
Impedance	Ingard-Myers boundary condition and locally or 'semi-locally' reacting liners
Source	Point/distributed stationary/rotating monopoles and dipoles

The analytical models presented here are cross-verified with selected numerical high fidelity FEM simulation results obtained with the software Simcenter 3D acoustics and are compared to experimental NASA OTR data. To complement the analytical work, wind tunnel experiments have been conducted during a secondment at ECL where the rotor and OTR liner were represented by a static aerofoil with its tip located over a flat plate containing a flush-mounted lined insert and separated from the airfoil tip by a small gap. The key achievements and original contributions are listed below:

1. Experimental investigation of the performance of Over-Tip liners in reducing the noise of an airfoil over a flat surface, including the study of the effects of source proximity to the liner.

2. Modelling and numerical FEM cross-verification of acoustically treated circumferential grooves with a semi-locally reacting analytical impedance model, that is locally reacting in the axial direction and non-locally reacting in the azimuthal direction.

3. Study of the impact of the source proximity to a hard/lined wall on the power output of ducted sources, including the effect of the liner impedance, radial source position and excitation frequency.

4. Development and numerical FEM cross-verification of an extended mode-matching analytical method to include noise sources close to and within the lined section and reflections from an inlet termination applicable to OTR and fan case liners,

including the assessment of 'back-reaction' effects on the source due to its proximity to the matching interface.

5. Development of an analytic acoustic model to predict the performance of OTR liner designs also applicable to fan case liners. An attempt to validate the analytical model is presented by comparing the predictions with experimental data from the NASA W-8 test rig. The prediction model is then used in a simple design study to illustrate the potential benefits of OTR liners in the next generation of turbofan engines.

1.5 Outline of contents

This report consists of seven chapters, structured in a way that aims to answer the objectives of this thesis and reflect the different areas of acoustics necessary to build a prediction model for Over-Tip-Rotor liners. In particular, the contents of each chapter can be summarised as follows:

- In Chapter 1, a literature review about OTR liners and the basics of fan noise sources and their modelling is presented. It also includes the motivation, objectives and original contributions of this research.
- An experimental study of a simplified configuration for Over-Tip Liners is presented in Chapter 2, focused on improving understanding of the noise reduction performance of OTR liners and showing the impact of the proximity of the noise sources to the acoustic treatment.
- Chapter 3 is focused on impedance modelling. It starts with a review of the basic impedance boundary conditions for duct acoustics and the modelling of SDOF/DDOF locally reacting liners. The core of the chapter is the development of an analytical model to predict the effective impedance of acoustically treated circumferential grooves and the cross-verification of the analytical models with FEM numerical simulations.
- An introduction to analytical duct acoustics and Green's functions for circular lined ducts with uniform mean flow is given in Chapter 4. The chapter includes the formulation of static and rotating distributions of point sources and is then focused on the impact that the source model, the impedance boundary condition and the source radial location have on the source power output.
- The mode-matching method is introduced in Chapter 5 for a cylindrical finite lined duct section matched to infinite hard wall duct extensions. The analytical model

is then extended to include sources close to and within the lined duct section and reflections from an inlet termination, which are verified with FEM solutions.

- In Chapter 6, all the modelling work described in the previous chapters comes together to obtain a simplified prediction model for OTR and fan case liners. The liner performance estimates are compared with experimental data from the NASA W-8 test rig to validate the analytical prediction model, which is then applied to a 'design' engine to show the potential benefits of OTR liners in the next generation of turbofan engines.
- The main conclusions and future work are summarised in Chapter 7.

1.6 Publications

- S. Palleja-Cabre, B. J. Tester, J. Astley, and G. Bampanis, "Aeroacoustic assessment of the performance of Over-Tip liners in reducing airfoil noise," in *AIAAJ* (under review).
- S. Palleja-Cabre, B. J. Tester, R. J. Astley, and H. Beriot, "Impedance modelling of acoustically treated circumferential grooves for over-tip-rotor fan noise suppression," *International Journal of Aeroacoustics*, vol. 0, no. 0, pp. 1–17, 2020, doi: 10.1177/1475472X20954427.
- S. Palleja-Cabre, B. J. Tester, J. Astley, and G. Bampanis, "Aeroacoustic assessment of the performance of Over-Tip liners in reducing noise of an aerofoil over a flat surface," in *AIAA AVIATION 2020 FORUM*, 2020, doi: 10.2514/6.2020-2608.
- S. Palleja-Cabre, B. J. Tester, R. J. Astley, and R. Bozak, "Modelling of Over-The-Rotor Acoustic Treatments for Improved Noise Suppression in Turbofan Engines," in *25th AIAA/CEAS Aeroacoustics Conference*, 2019, doi: 10.2514/6.2019-2580.

Chapter 2

Experimental study of a simplified configuration for Over-Tip Liners

Contents

Published experimental work (Section 1.1.1) suggest that the distinct feature of OTR liners with respect to conventional intake or bypass liners is the noise reduction through *source modification*. That is, modifying the way the source generates sound due to its proximity to a lined or porous surface. The aerodynamics of the flow in the tip gap region of a turbofan engine and the potential modifications that the flow structure may suffer as a result of the lined surface is a complex problem out of the scope of this thesis. Instead, the approach taken here is to make use of an acoustic analogy, with the implicit assumption that the base flow is known and is not influenced by the acoustic sound filed. Therefore, references to source modification effects do not mean changes in the base flow but purely acoustic back-reaction effects on the source.

It is well known that the field generated by an acoustic source depends on the boundary conditions. The presence of rigid or porous surfaces, the distance from the source to the surface and the source excitation frequency affect the power output and the directivity pattern of the noise source. These effects are studied here for simplified configurations and analysed for ducted sources in Chapter 4.

The rotor-blade broadband self-noise sources of special interest for the modelling of fan proximity liners are trailing edge noise and tip leakage noised due to its proximity to the acoustic treatment. Trailing edge noise is caused by the local interaction of the eddies within the turbulent boundary layer on the suction surface of the fan blades with the trailing edge. Tip clearance noise is associated with the jet-like flow through the tip gap driven by the pressure difference between the suction side and the pressure side of the rotor blades that rolls up into a tip leakage vortex (TLV). The main source mechanism of tip gap noise is attributed to the interaction of the turbulent structures in the jet-like cross-flow with the blade tip suction side edge and the scattering by the tip edge and/or the trailing edge of the unsteady perturbations induced by the tip vortex [46, 54, 55]. Recent LES simulations of the experimental set-up tested in [46, 54] have shown agreement with the experiments and identified the former noise mechanism as dominant employing an acoustic decomposition [56].

The aim of this chapter is to improve understanding of the noise reduction performance of OTR liners through a fundamental experimental evaluation. The fan rotor and OTR liner are represented here by a *static* airfoil with its tip located over a flat plate containing a flush-mounted lined insert and separated from the airfoil tip by a small gap. With this configuration, the noise reduction mechanisms related to gap noise can be studied separately from other noise source mechanisms in the engine. It also means that the measurements can be performed in an open jet, permitting the use of far-field and noise localisation measurements. Previous work on the aeroacoustic assessment of tip leakage noise sources in a similar set-up was performed by Jacob *et al.* [46] and Grilliat *et al.* [54], who showed that the incoming flow combined with the camber of the airfoil and its angle of attack, creates a jet-type cross-flow through the tip gap that resembles the noise generation mechanism of a tip vortex. This idea is used here to assess the performance of acoustic liners in reducing such noise source mechanisms, either by modifying the source and/or attenuating the noise as it propagates over the liner, and to relate the findings to OTR acoustic treatments. The performance of Over-Tip liners in suppressing airfoil noise sources in the absence of a tip gap, such as trailing edge noise, is also explored. The analysis is based on differences in measured far-field sound spectra combined with spiral microphone array localisation techniques to quantify the contribution of each source region to the measured noise spectra. This experimental approach has been recently applied to characterise the noise sources in a swept airfoil with a free tip in [57].

A second experimental evaluation was also conducted to further simplify the problem and confirm the findings related to the source proximity effects on the power output and directivity pattern of point sources. The test consists of a single-frequency artificial monopole-like source located over a finite hard/lined insert and the results are compared with analytical predictions for a point source over an infinite flat lined plane in Section 2.5. A third experiment in which the airfoil tip was modified by drilling two holes at the tip of the airfoil was explored (Appendix A). The holes are acoustically excited by the

grazing flow and produce a near tonal noise that dominates the acoustic spectrum. The tests were unsuitable for the purposes of this study due to the sensitivity of the cavity excitation to the problem variables and hence are not covered here.

The structure of this chapter is as follows. In Section 2.1 the experimental set-up of the two experimental tests and the Over-Tip liners are described. The airfoil gap noise generation and the liner noise suppression for a fixed test case are analysed in Section 2.2 and Section 2.3 using differences in far-field sound spectra and in radiated source power respectively. A parametric study is described in Section 2.4, which includes the scaling of gap noise with the free-stream velocity, the effect of gap size and airfoil loading, the use of different liner configurations and of trailing edge feathers. A comparison of the experimental results of both experiments with an analytical point source model is described in Section 2.5.

2.1 Experimental set-up

2.1.1 Wind-tunnel set-up

The acoustic measurements presented in this chapter were performed in the low-speed open-jet anechoic wind tunnel of Ecole Centrale de Lyon (ECL), which has been described in detail elsewhere [58, 59]. A rectangular nozzle with a vertical exit cross-section of 15 cm x 30 cm delivers a uniform flow, at velocities ranging between 19 m/s to 32 m/s, into an anechoic chamber of 4 m x 5 m x 6 m. The contraction ratio of the nozzle is 2:1 from an initial section of 30 cm x 30 cm. The set-up for the two experimental evaluations are described below.

A. Static airfoil

A cambered airfoil NACA 6512-10 with a chord of $c = 13$ cm is held vertically between two horizontal plates. The upper end of the airfoil is placed in a slit disc inserted in the upper plate such that the angle of attack can be varied by rotating the disc and the gap adjusted by simply slipping and locking the airfoil in the upper disc. A hard wall or a liner insert was flush mounted in the lower support, in direct contact with the cross-flow within the gap. The set-up with and without the airfoil is shown in Fig. 2.1a-2.1b.

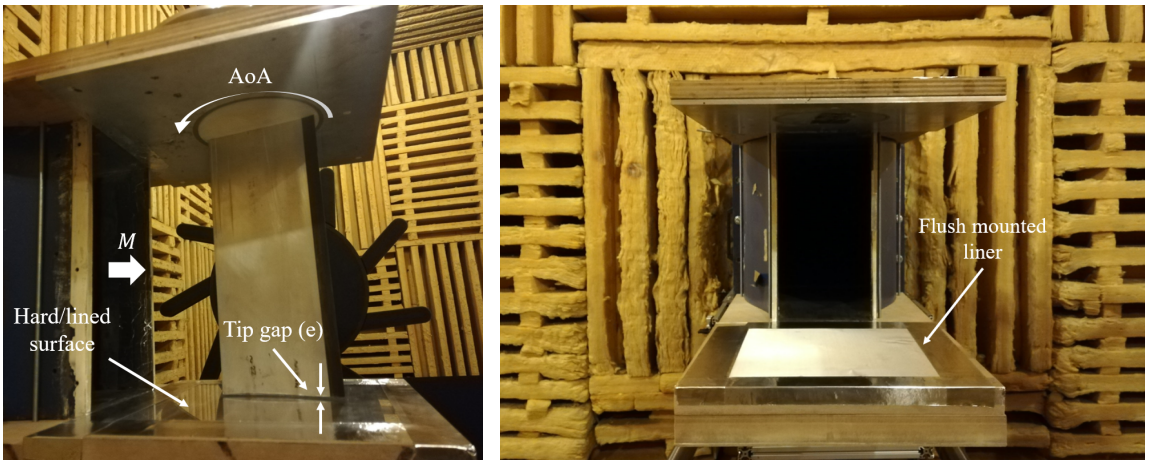

(a) (b)

Figure 2.1: Over-tip liner test set-up: (a) Full set-up with the airfoil and (b) Support plates with a flush mounted liner.

B. No-flow artificial point source

This experiment consists of an artificial single frequency point source located over a (finite) hard/lined insert, as shown in Figure 2.2. An external speaker isolated inside an acoustically treated box generates a sinusoidal signal of a prescribed frequency that propagates through a tube connected to a straight probe. The plane wave propagating through the tube generates a monopole-like source at the end of the probe, which can be displaced vertically to adjust the distance between the point source and the hard/lined surface. The wind tunnel is not in operation for this test.

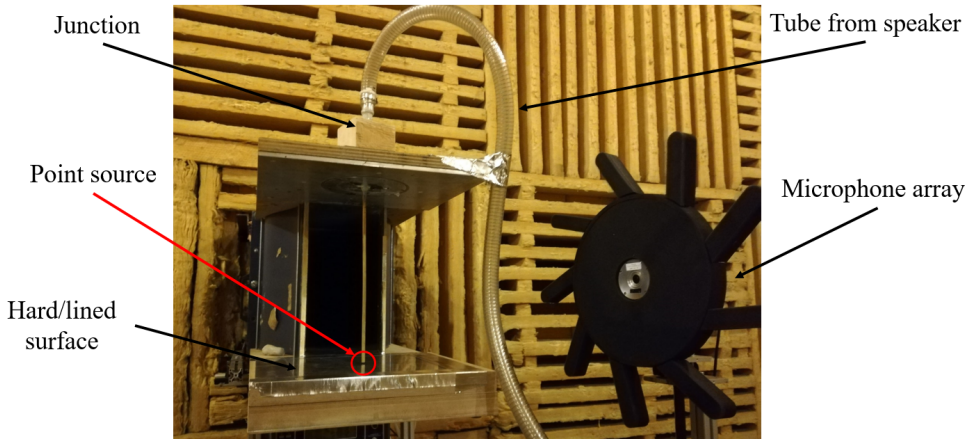

Figure 2.2: Experimental set-up of the no-flow point source test.

2.1.2 Over-Tip liners

Simple SDOF cavity liners were used in both tests so that well-established models could be used to predict the liner acoustic impedance. Non-linear effects were not expected due to the low sound pressure levels incident on the liner inserts. Three wire meshes of different acoustic resistance were bonded directly to a honeycomb structure with a cavity depth of h=2 cm using spray adhesive to minimise blockage. Impedance tube tests of liner samples were performed using a Bruel & Kjaer two-microphone impedance measurement tube type 4206. The specific resistance (R) and mass reactance (m_r) of the liners, shown in Table 2.1, are obtained by curve fitting of the impedance tube results to Eq. 2.1 [60], where k is the wavenumber. The measured acoustic impedance and normal incidence absorption coefficient (Eq. 2.2) and the corresponding fitted curves are shown in Fig. 2.3. The notation $e^{j\omega t}$ is used here.

$$Z = R + j\left[m_r k - cot(kh)\right] \quad . \tag{2.1}$$

$$\alpha = \frac{4R}{(R+1)^2 + \left[m_r k - cot(kh)\right]^2} \quad . \tag{2.2}$$

Table 2.1: Specific acoustic resistance and mass reactance of each liner configuration.

Liner ID	4	5	7
$\boldsymbol{R}$	1.11	0.36	1.47
$\boldsymbol{m_r}$	0.47 cm	0.30 cm	1.83 cm

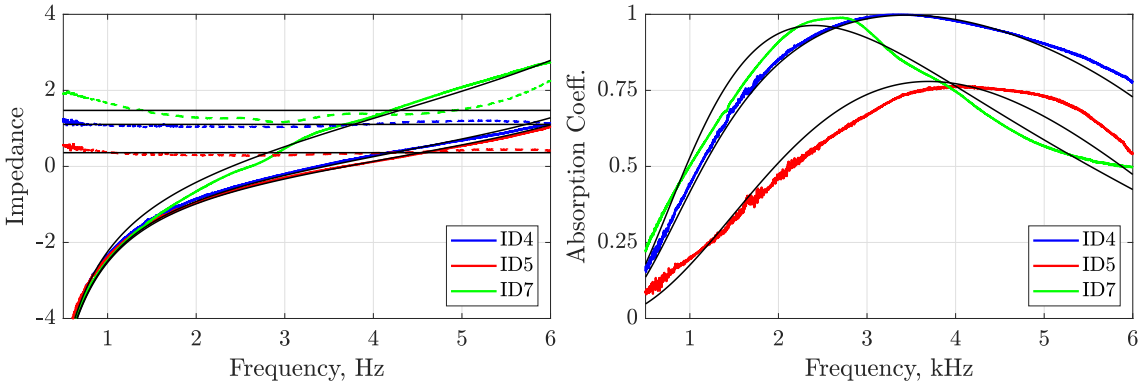

(a) Resistance and reactance

(b) Absorption coefficient

Figure 2.3: Characterisation of over-tip liner impedance. In (a) dashed lines are the specific acoustic resistance and solid colour lines the specific acoustic reactance. In both figures the black lines are the curve-fitted values.

2.1.3 Far-field and spiral microphone array

The acoustic far-field was measured on a portion of a sphere with coordinates (R,θ,ϕ) employing a rotating vertical arc of six microphones B&K 1/2" type 4189, equally spaced along the arc from ϕ = 0 deg. (mid-span plane) to ϕ = 75 deg., as shown in Fig. 2.4a. The array, of a radius of R = 1.25 m, was aligned with the airfoil LE and is fixed to a remote-controlled rotating table to modify the azimuthal angle θ of the meridian plane. Appropriate values of ϕ and θ were used to minimise the noise scattered from the support plates and the hydrodynamic pressure of the wind-tunnel jet respectively. Spurious reflections or scattering measured on the microphones due to the components of the arc array itself are addressed by the spectral difference procedure described in Section 2.2. All far-field acquisitions were made with an external unit PXI-036, averaging over 30 samples of 1 second, with a sampling frequency of 51.2 kHz and a bandwidth of 1 Hz over the frequency range 0-25.6 kHz.

The spiral microphone array shown in Fig. 2.4b, consisted of 81 sensors and was located 0.55 m away from the airfoil and parallel to the flow direction. The mean polar-azimuthal array aperture is about 48 deg. relative to the mid-span and leading edge position of the airfoil. The post-processing technique to localize the noise sources and provide relevant power level spectra for each source is based on a deconvolution algorithm called CIRA, implemented in LMS software under a MicrodB license; a description of the CIRA method can be found in [61]. The practical aspects concerning the low-frequency spatial resolution limits and the correction for the apparent flow displacement caused by the flow convection have been addressed in [59].

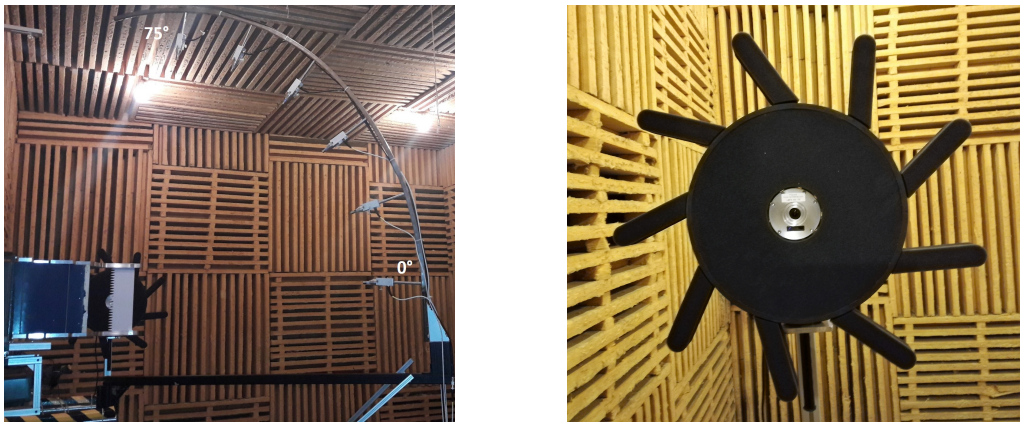

(a) Far-field microphone arc array [59]

(b) Spiral microphone array as viewed from the airfoil

Figure 2.4: Far-field and spiral microphone arrays used in the experiments.

2.2 Differences of Far-Field Sound Spectra

The quantification of the noise reduction of a particular airfoil-noise source mechanism in the presence of other background noise and additional sources has to be treated carefully to avoid misleading noise reduction spectra, as noted in [57–59]. The background noise sources include noise radiating from the wind tunnel upstream of the contraction, the noise generated by the flow at the edges of the nozzle, noise diffraction at the edges of the support plates and jet mixing noise. Therefore, to isolate airfoil-noise sources, the background noise contribution is assumed to be uncorrelated with the airfoil noise and is removed by subtracting the dimensional noise spectral density measured *without* airfoil from the total sound spectral density *with* the airfoil.

To measure the reduction of gap noise using an over-tip liner, it is necessary to separate the contributions of gap noise from that of trailing edge noise (TEN) in the total measured spectra. To measure the contribution of TEN, a zero-gap hard/lined baseline case is used (i.e. where gap noise is absent). The gap noise contribution ($S^{\mathrm{H/L}}_{pp,\mathrm{gap}}$) is obtained by subtracting the dimensional noise spectra of the baseline case ($S^{\mathrm{H/L}}_{pp,\mathrm{no\ gap}}$) from the total measured spectra ($S^{\mathrm{H/L}}_{pp,\mathrm{total}}$), as shown in Eq. 2.3. The subtraction is performed *both* for the hard (H) and lined (L) configurations and the procedure already removes background noise sources. The analysis bandwidth of the far-field measured auto spectral densities (S_{pp}) has been set to 32/64 Hz to avoid the large high-frequency scatter due to statistical errors. The reduction of gap noise ($\mathrm{PSD}_{\mathrm{gap}}$ IL) and total noise ($\mathrm{PSD}_{\mathrm{total}}$ IL) is obtained following Eq.2.4-2.5.

$$\mathrm{PSD}^{\mathrm{H/L}}_{\mathrm{gap}} = 10\log_{10}\left(S^{\mathrm{H/L}}_{pp,\mathrm{gap}}\right) = 10\log_{10}\left(S^{\mathrm{H/L}}_{pp,\mathrm{total}} - S^{\mathrm{H/L}}_{pp,\mathrm{no\ gap}}\right) \quad . \tag{2.3}$$

This experiment presents a multi-variable problem: (1) the gap size, (2) the geometrical angle of attack (AoA), (3) the flow speed (M) and (4) the impedance of the hard/lined insert. The results presented in this section and Section 2.3 are limited to a fixed gap size of $e = 5$ mm, AoA $= 18$ deg. and $U = 27$ m/s for a hard wall reference case and two liner configurations (ID4-5). The baseline case required to isolate the gap noise in each configuration is performed for $e = 0$ mm, AoA $= 18$ deg. and $U = 27$ m/s. All references to AoA refer to the geometrical angle between the nozzle exit and the airfoil chord line and does not account for the jet deflection due to the airfoil. The far-field results presented in this section have been obtained from the mid-span microphone of the arc array and on the pressure side of the airfoil, that is $(\phi, \theta) = (0, -90)$ deg.. Note that the spiral array used for the source localization and extraction procedure of Section 2.3 is located on the suction side of the airfoil.

The total PSD measured for a selection of cases is shown in Fig. 2.5a. Small variations between the baseline (hard + no gap) and reference (hard + gap) cases can be observed up to 5 kHz. That is, below this frequency the spectra is dominated by TEN, whereas above 5 kHz gap noise becomes significant. A discussion on the physical mechanisms of gap noise, which also includes TEN, is given in Section 2.4. The resulting PSD gap noise spectra for the hard wall and lined cases after the subtraction of the TEN and background noise are shown in Fig. 2.5b. At those frequencies where TEN dominates over gap noise the difference of S_{pp} with and without gap can be very small, resulting in zero or negative values after the subtraction and hence does not permit an accurate assessment of the gap sources at those frequencies. This is less of a problem for frequencies higher than 5 kHz, where the gap noise spectra for the hard and lined cases can be isolated. However, high variability in the isolated gap noise spectra for the lined configurations is observed over 12-15 kHz and 18-20 kHz due to, effectively, measuring the background noise with and without the gap. That is, the PSD levels of the baseline (hard + no gap) and lined (with gap) configurations are of similar magnitude than the background noise over those frequency ranges, as shown in Fig. 2.5a.

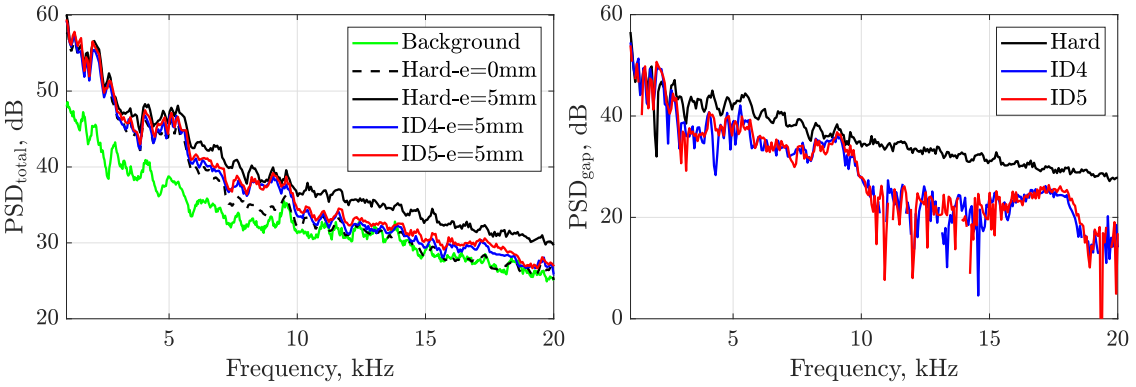

(a) Total measured PSD spectra

(b) Gap noise reduction spectra

Figure 2.5: Measured total PSD and isolated gap noise PSD spectra

The noise reduction due to the over-tip liners, the PSD Insertion Loss (PSD IL), can now derived by taking the difference, in dB terms, of the PSD levels in Fig. 2.5a and 2.5b, as indicated in Eq. 2.4-2.5.

$$\text{PSD}_{\text{gap}}\text{IL(dB)} = \text{PSD}^{\text{H}}_{\text{gap}} - \text{PSD}^{\text{L}}_{\text{gap}} = 10\log_{10}\left(S^{\text{H}}_{pp,\text{gap}}\right) - 10\log_{10}\left(S^{\text{L}}_{pp,\text{gap}}\right) \quad . \tag{2.4}$$

$$\text{PSD}_{\text{total}}\text{IL(dB)} = \text{PSD}^{\text{H}}_{\text{total}} - \text{PSD}^{\text{L}}_{\text{total}} = 10\log_{10}\left(S^{\text{H}}_{pp,\text{total}}\right) - 10\log_{10}\left(S^{\text{L}}_{pp,\text{total}}\right) \quad . \tag{2.5}$$

The resulting gap noise reduction spectra and the normal incidence absorption coefficient for each liner are shown in Fig. 2.6a and Fig. 2.7 respectively. Three humps can be observed in the noise reduction spectra that can be broadly related to the resonances and anti-resonances of the liners. The normal incident absorption curves show two anti-resonances at 8.5 kHz and 17 kHz, with peak noise reduction around 11 kHz and 19 kHz. Although the PSD_{total} IL achieved with liner ID4 is generally around 1 dB higher than with liner ID5 (Fig. 2.6b), as expected from the magnitude of the absorption coefficient curves, the subtraction procedure forces the two PSD_{gap} IL spectra to collapse. The results of this section show that over-tip liners can provide broadband PSD gap noise reduction of 5-10 dB (Fig. 2.6a), corresponding to 2-3 dB of PSD total reduction (Fig. 2.6b).

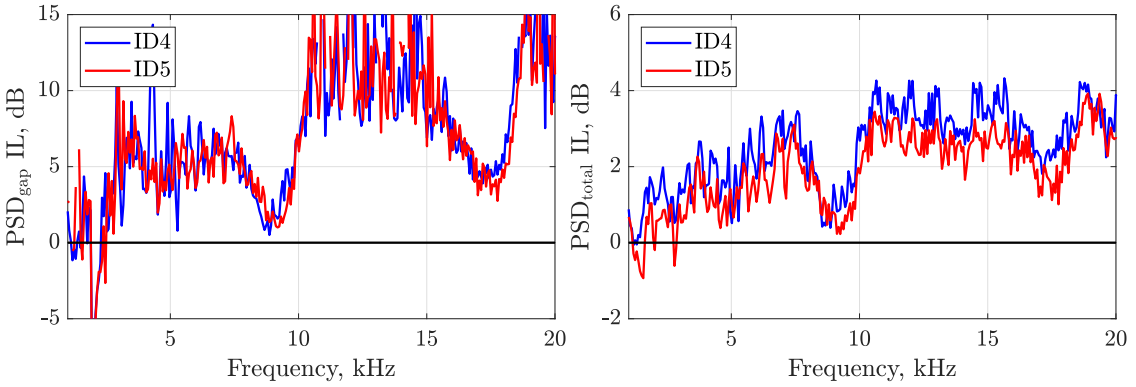

(a) Gap noise reduction spectra

(b) Total PSD noise reduction spectra

Figure 2.6: Over-tip liner noise reduction performance.

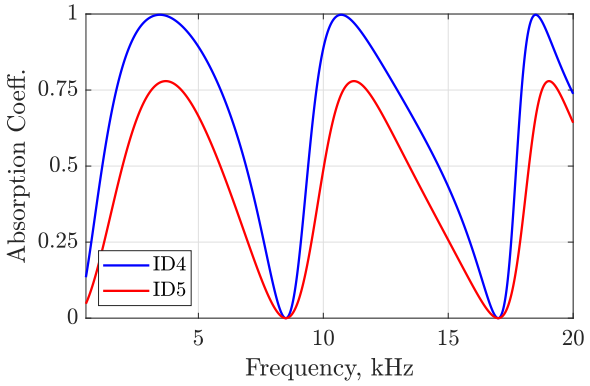

Figure 2.7: Normal incidence absorption coefficients.

2.3 Noise localisation and extraction

Corresponding sound power maps can be obtained for each test case and prescribed frequency range by using the data acquired with the spiral array and the CIRA post-processing technique, which assumes that the sources are uncorrelated monopoles. However, the power here is defined as the monopoles source powers integrated over the source region that is then radiated into the aperture of the spiral array and not the total power radiated over the sphere surrounding the airfoil. The sources of acoustic power can be defined as selected spatial areas or regions of interest, such as the trailing and leading edge of the airfoil or the gap region, to obtain the spectrum of the power radiated by the sources within that region, subject to the usual resolution limits of the spiral array. That is, it provides a means of quantifying the contribution of each noise source region.

The results in this section are limited to the zero-gap baseline (hard and lined with ID4) and the hard wall reference and liner ID4 configurations with a tip gap as described in Section 2.2. The equivalent sound power maps for these cases are shown in Fig. 2.8 for three ranges of frequencies of interest based on the analysis of the far-field data: f=[4-6] kHz, which is expected to be dominated by TEN; f=[6-9] kHz, where both noise sources may have a prominent role and should capture the first hump of the over-tip liner noise reduction; and f=[9-12] kHz, which is expected to be dominated by gap noise and capture the second hump of liner noise reduction. Note that in all the PWL maps the nozzle is located on the right hand side of the image and the flow goes from right to left.

Starting with Fig. 2.8a, it can be observed that with no gap the dominant source is TEN centred around the mid-span of the airfoil. A TE contribution towards the tip of the airfoil can be observed when a tip gap is introduced (Fig. 2.8b), which is attenuated locally in the vicinity of the liner (Fig. 2.8c). A similar trend can be observed for the range of f=[6-9] kHz, although the dominant sources when the gap is present are now shifted towards the tip of the airfoil around the TE (Fig. 2.8e). The over-tip liner mitigates the noise sources in the gap region but does not affect the TEN radiated from span sections located further away, as shown in Fig. 2.8f. In the third frequency range, the no gap baseline only shows weak sources generated at the nozzle exit (Fig. 2.8g). However, with a tip clearance, the noise sources are much better defined and localized within the gap (Fig. 2.8h) and are strongly reduced in the presence of the over-tip liner (Fig. 2.8i). It is clear that at this frequency range the sources located in the gap region are dominant.

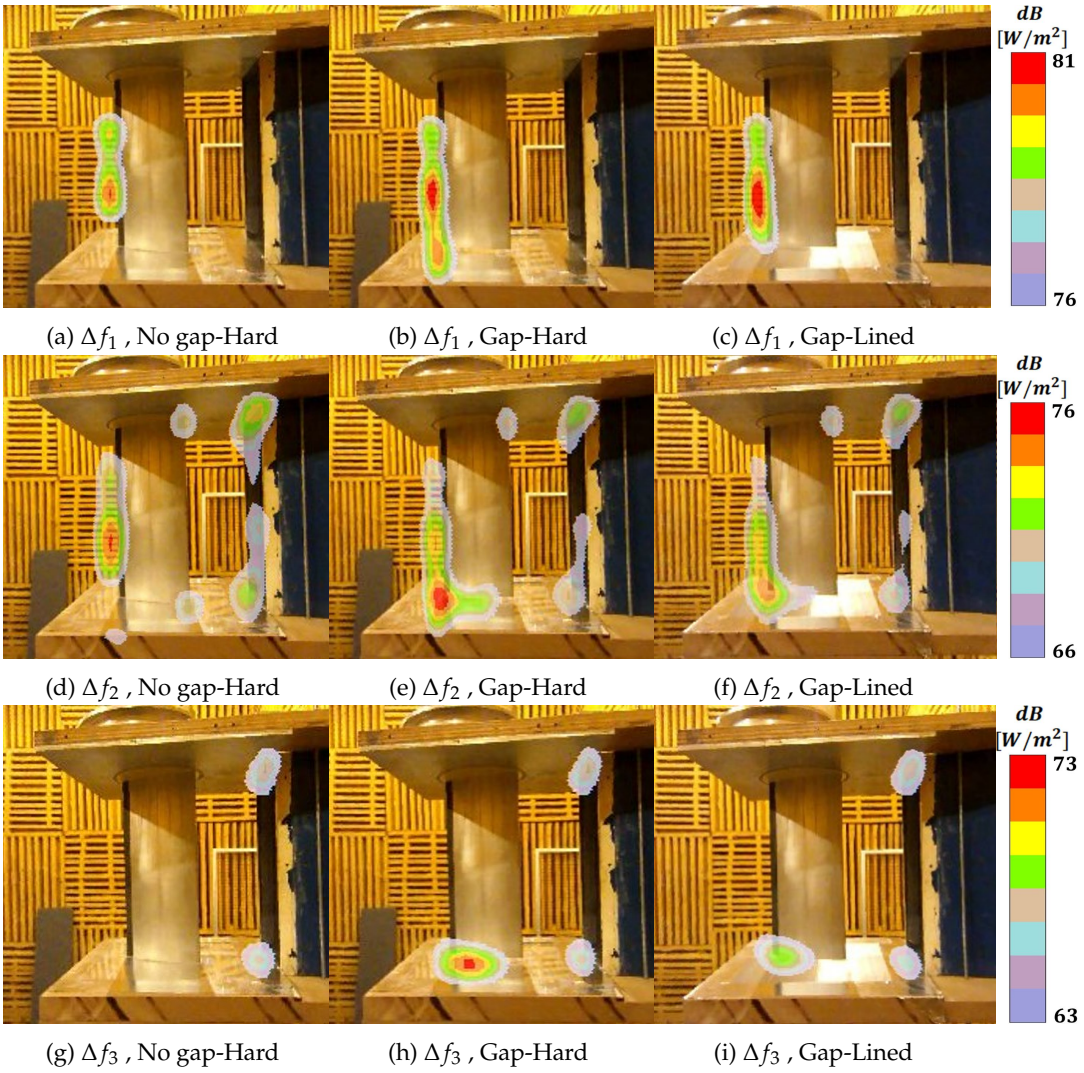

(a) Δf_1 , No gap-Hard (b) Δf_1 , Gap-Hard (c) Δf_1 , Gap-Lined

(d) Δf_2 , No gap-Hard (e) Δf_2 , Gap-Hard (f) Δf_2 , Gap-Lined

(g) Δf_3 , No gap-Hard (h) Δf_3 , Gap-Hard (i) Δf_3 , Gap-Lined

Figure 2.8: PWL maps for the baseline, reference and lined cases for the frequency ranges of (a)-(c) Δf_1=[4-6] kHz, (d)-(f) Δf_2=[6-9] kHz and (g)-(i) Δf_3=[9-12] kHz.

The definition of the domains for source power extraction is not obvious due to the close proximity of gap noise and TEN, especially relevant at those frequencies around the threshold where TEN or gap noise are the dominant sources. A compromise is made by selecting the gap region and a small part of the TE, here called 'GAPB' for GAP-box, and *the rest* of the TE, called 'TENB'. In should be noted that TEN is the acronym for Trailing Edge Noise, and TENB is the name for the integration area or box containing most of the trailing edge. The two areas are defined in red and green respectively in Fig. 2.9a. The power from the full domain and the equivalent integrated power in each area is shown in Fig. 2.9b-2.9d. The variation in the PWL from TENB between the different configurations is insignificant (Fig. 2.9d), showing that the noise sources in most of the TE are independent of the gap flow or the liner and confirms the choice of integration areas. As expected, the PWL spectra in the GAPB are significantly affected by the problem variables (Fig. 2.9c). An anomalous behaviour on the power extraction results from GAPB is observed around 2-3 kHz for the lined configurations. The analysis of the results

at those frequencies will be drawn from the full domain power spectra of Fig. 2.9b, which show the same trends as in GAPB but to a lesser extent due to the additional contribution of TEN.

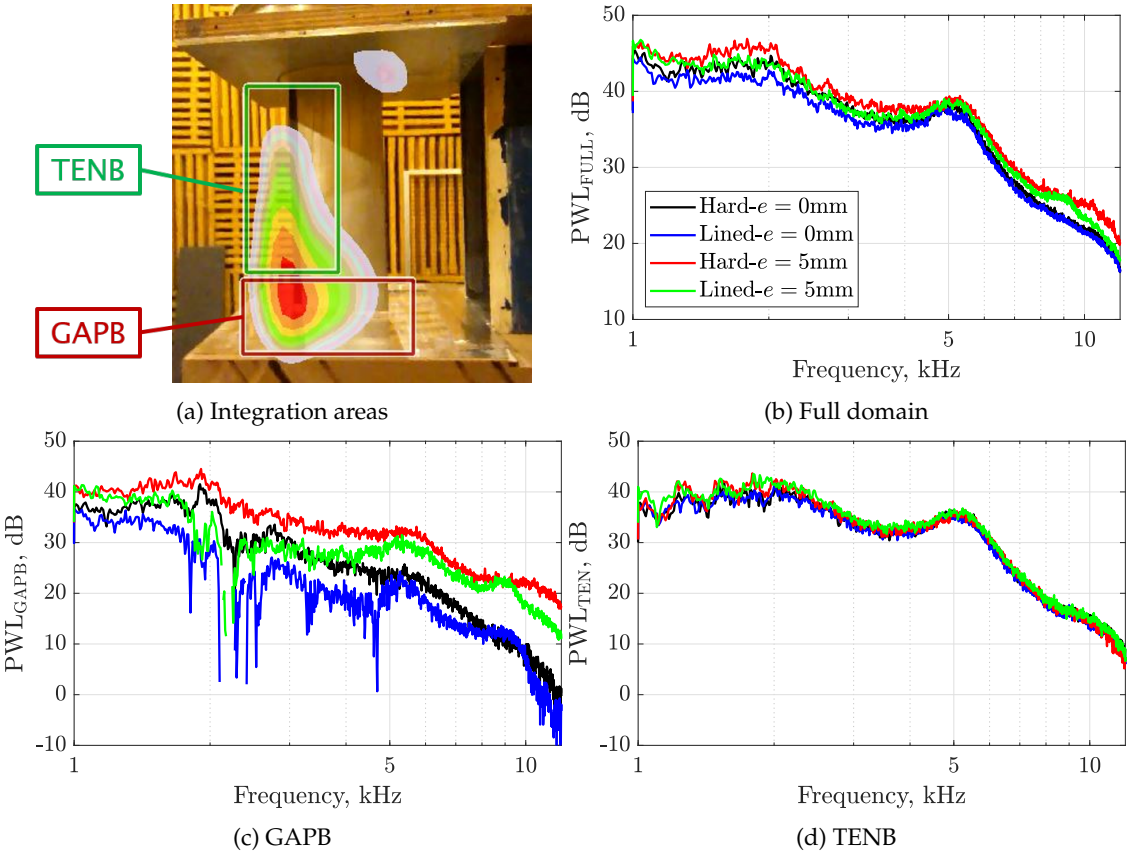

(a) Integration areas

(b) Full domain

(c) GAPB

(d) TENB

Figure 2.9: (a) Definition of the integration areas and (b)-(d) power extracted in different areas.

An estimation of how much additional noise is generated due to the tip leakage flow can be obtained by using the power extraction technique, i.e. by subtracting the PWL from GAPB and from the full domain with and without the gap, as shown in Eq. 2.6. This operation can be performed both for the hard and lined configuration to assess whether the presence of the liner affects the noise generation mechanisms. The results shown in Fig. 2.10 and 2.11 have been filtered with a Savitzky–Golay filter to smooth the data while maintaining the general trends.

$$\Delta\mathrm{PWL}^{\mathrm{H/L}}(\mathrm{dB}) = \mathrm{PWL}^{\mathrm{H/L}}_{\mathrm{gap}} - \mathrm{PWL}^{\mathrm{H/L}}_{\mathrm{no\text{-}gap}} \quad . \tag{2.6}$$

Ignoring the peaks in the lined results from GAPB, it can be observed in Fig. 2.10 that the noise generated due to the tip leakage flow affects the whole range of frequencies but is particularly pronounced in the gap region in the range of 6-12 kHz. In this frequency range, it provides an additional 8-18 dB (Fig. 2.10a) that accounts for 2-3.5 dB over the

full domain (Fig. 2.10b). However, it does not vary significantly between the hard wall and the lined configurations and indicates that the noise generation mechanisms are not modified by the presence of the over-tip liner, at least up to 9 kHz. The full domain PWL in Fig. 2.10b suggest that the noise generation above 9 kHz is significantly lower in the lined configuration, which may not have been captured in the GAPB due to the low signal levels. Note that this procedure and analysis are based on differences of PWLs: although the trends are the same with a hard or lined insert, the absolute values are smaller in the lined configuration as shown in Fig. 2.9b-2.9c.

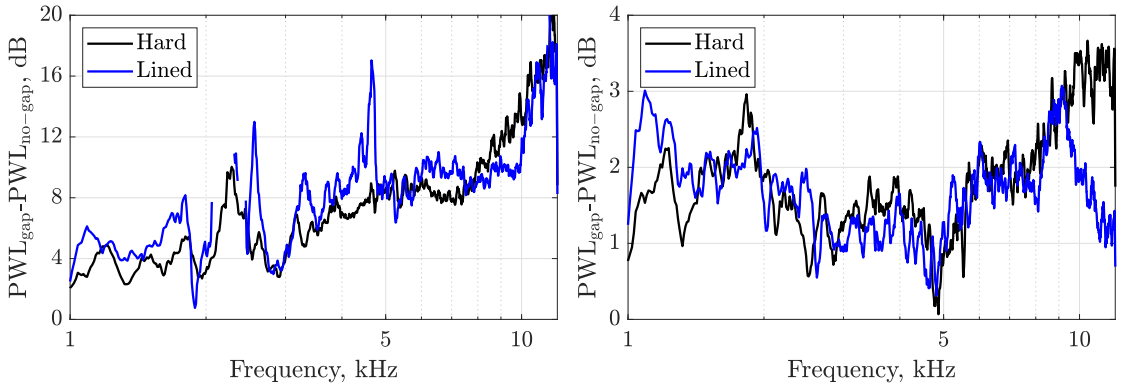

(a) GAPB (b) Full domain

Figure 2.10: Quantification of the gap noise generated by the tip leakage flow with the hard wall and the liner insert.

In the same way, the difference between the PWL for a given gap size (zero or 5mm in this section) and hard or lined insert quantifies the noise reduced by the over-tip liner (Eq. 2.7), as shown in Fig. 2.11a and Fig. 2.11b for the GAPB and the full domain respectively. Similar trends to those obtained by differences of the far-field sound spectra are observed here for frequencies above 5 kHz: the anti-resonance at 8.5 kHz with null noise reduction and a peak PWL IL around 11 kHz. This approach also gives insight in the frequency range of 3-5 kHz, where both TEN and gap noise are of similar strength and far-field differences not reliable, showing that the liner can provide broadband peak PWL IL in the gap area of up to 5 dB, accounting for 1-2 dB in the full domain. The performance of the over-tip liner is not significantly modified by the tip-leakage flow, i.e. small variation with or without a gap, which suggests that the liner suppresses the noise sources located in its vicinity whether they are TE or gap noise sources. The noise reduction in the absence of tip gap shows the potential of over-tip liners in turbo-machinery applications even if the role of gap noise is not fully quantified.

$$\text{PWL IL(dB)} = \text{PWL}_e^{\text{H}} - \text{PWL}_e^{\text{L}} \quad . \tag{2.7}$$

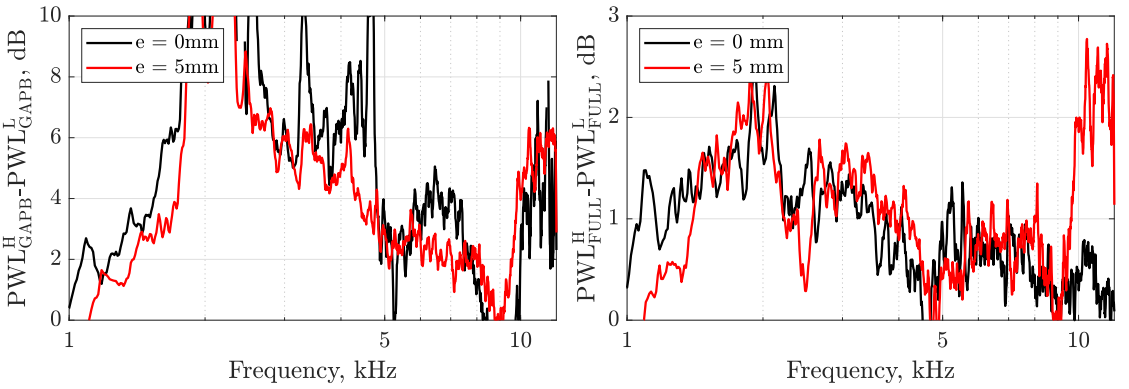

(a) GAPB (b) Full domain

Figure 2.11: Measured Over-tip liner PWL noise reduction with and without tip gap.

2.4 Parametric studies

2.4.1 Scaling laws

The baseline ($e = 0$ mm, AoA=18 deg., hard/liner ID4), reference ($e = 5$ mm, AoA=18 deg., hard) and lined ($e = 5$ mm, AoA=18 deg., liner ID4) configurations have been tested at three different speeds, namely [S1,S2,S3]=[17,27,32] m/s. Previous work on the aeroacoustics of tip leakage flow [46, 54] suggests two physical mechanisms of noise generation of similar magnitude: (1) the interaction of turbulent eddies in the cross-flow and TLV with the suction side edge and the trailing edge, which varies according to the 5^{th} power of the free-stream velocity and (2) secondary eddies in the jet-like cross-flow that radiate with a power of the free-stream velocity of 7 to 8.

The isolated gap noise (PSD_{gap}) for S=[S1,S2,S3] has been plotted against the Strouhal Number based on the free-stream velocity and the airfoil chord in Fig. 2.12. The data in Fig. 2.12 was acquired with the mid-span microphone of the arc array and in the pressure side of the airfoil ($(\phi, \theta) = (0, -90)$ deg.). As noted previously, gap noise cannot be accurately isolated at low frequencies and therefore the spectra in terms of Strouhal number is less reliable for lower flow velocities. However, at the frequencies where gap noise is dominant, the curves collapse when scaling with the 5^{th} power of the free-stream velocity (Fig. 2.12a). This is not the case with the power of 7 or 8, the later shown in Fig. 2.12b. These results suggest that the interaction of turbulence with the tip edges is the dominant source of gap noise for the whole frequency spectrum in the current tests. The low Mach number of the experiments reported here (M=[0.05-0.1]) in comparison to the M=0.2 used in [46, 54] may cause the masking of any jet-like noise radiation.

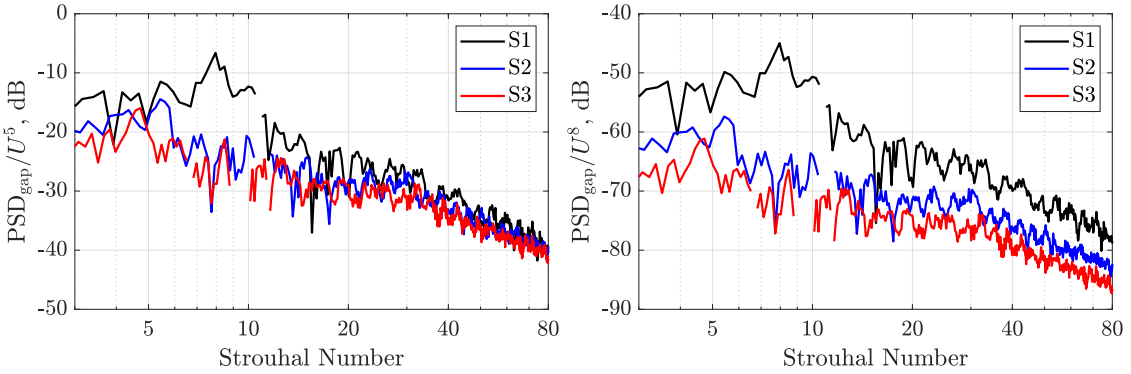

(a) Scaling with U^5

(b) Scaling with U^8

Figure 2.12: Scaling of gap noise with the free-stream velocity U.

Far-field measurements have been performed for a range of meridian positions of the microphone arc array to assess the directivity pattern of gap noise and the noise reduction performance of the over-tip liner. The isolated gap noise spectrum for $U = 32$ m/s measured at the various meridian positions is shown in Fig. 2.13a with respect to the Strouhal number. The observation angle ($\psi = \theta + \text{AoA}$) is the azimuthal angle (θ) corrected with the angle of incidence of the airfoil (AoA), i.e. the angle relative to the chord. This plot can be compared like to like with Fig. 11 of [46] by scaling the latter using the Strouhal number. In both tests, a dipole-like directivity attributed to TE noise can be observed for St=[1-6], which is stronger in the suction side possibly due to a thicker boundary layer. The symmetry between the pressure side and suction side is less clear at higher frequencies, showing a discrepancy with the results in [46] and stronger radiation of the gap sources towards the pressure side in this instance.

The PSD$_{\text{total}}$ noise reductions by the over-tip liner at each observation angle is shown in Fig. 2.13b. The same trends can be observed in the suction and pressure side of the airfoil, although the magnitude of the reduction is higher in the latter. The three humps of noise reduction discussed in the preceding sections are consistent for all measured angles. The bands of anti-resonance centred in 8.5 kHz and 17 kHz are noticeable for St$\sim$[40,80] respectively. The progressive increase of noise reduction with the observation angle can be linked to the amount of lined surface over which the waves travel from the source to the receiver. Given the geometry of the liner and the far-field array and assuming that the dominant sources are located close to the TE, for AoA=18 deg., higher observation angles correspond to longer distances travelled over the lined surface.

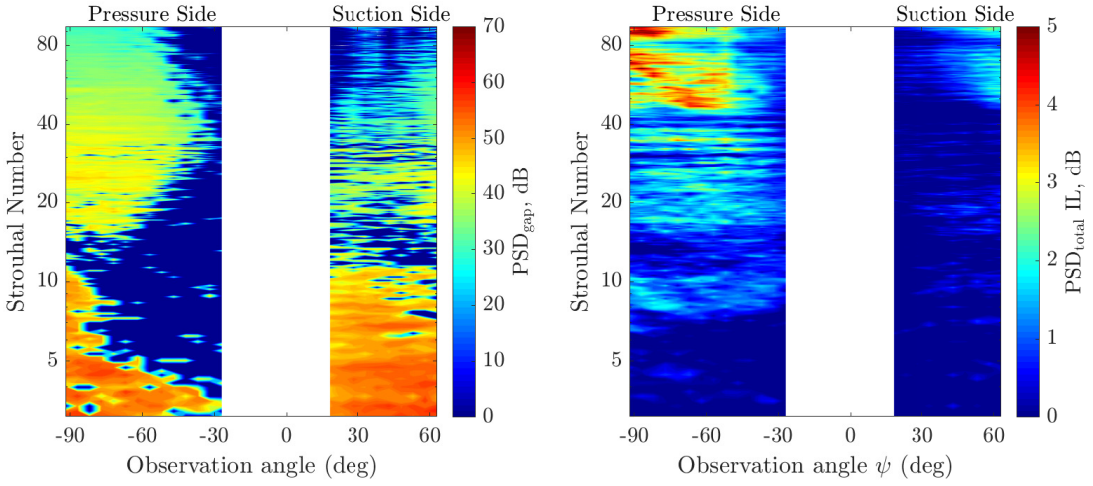

(a) Gap noise

(b) Total over-tip liner noise reduction

Figure 2.13: Directivity of (a) gap noise and (b) total over-tip liner noise reduction.

2.4.2 Effect of gap size

The effect of the gap size on the tip-leakage noise and in the over-tip liner noise reduction performance is discussed in this part of the section. The discussion is based on far-field measurements acquired at (ϕ,θ)=(0,−90) (pressure side) and (ϕ,θ)=(0,+45) (suction side) for S3, AoA=18 deg., hard/liner ID4 and a range of gap sizes $e = [4 : 3 : 25]$ mm. Measurements with the spiral array were taken simultaneously and the resulting extracted power is used to extend the discussion to the GAPB area, which has been shifted upwards in accordance with the gap size.

The spectrum of the additional noise due to the gap (ΔPSD_{total}=PSD^{gap}_{total}-$PSD^{no\text{-}gap}_{total}$) in the hard wall case is shown in Fig. 2.14a and 2.14b for the pressure side and the suction side respectively. The trends of the noise increase with the gap size vary across the spectrum but can be broadly divided into three groups: f=[2-6] kHz, f=[6-12] kHz and f=[12-20] kHz, which apply both in the pressure side and the suction side of the airfoil. The integrated spectrum for each frequency range and gap size is shown in Fig. 2.14c-2.14e. An increase of noise followed by saturation is observed in the first frequency range (f=[2-6] kHz). Arguably, this is what is expected: a higher velocity of the cross-flow and a consequent noise rise until the gap size is big enough such that it behaves as a free tip vortex. The noise localization maps for this frequency range and S3 in Fig. 2.15a-2.15d confirm that although TEN remains of a similar magnitude as gap noise for low gap sizes, the dominant sources are shifted towards the airfoil tip TE as the gap is increased and eventually saturate in accordance to Fig. 2.14c. The second frequency range (f=[6-12] kHz), for which gap noise is dominant, does not present any saturation at the higher gap sizes but a monotonic increase of additional noise. This trend is also observed in the PWL

maps of Fig. 2.15e-2.15h. In contrast, the noise sources at the higher frequencies (f=[12-20] kHz) are quite insensitive to the gap size. The trends outlined above agree with the quantification of additional noise from the GAPB shown in Fig. 2.17a. This parametric study suggests that not two but possibly three different tip-leakage noise generation mechanisms are present in the current tests. Measurements of the unsteady pressure fluctuations on the airfoil surface and of the flow in the vicinity of the tip could provide more insight into the noise generation mechanisms and complement the discussion presented here.

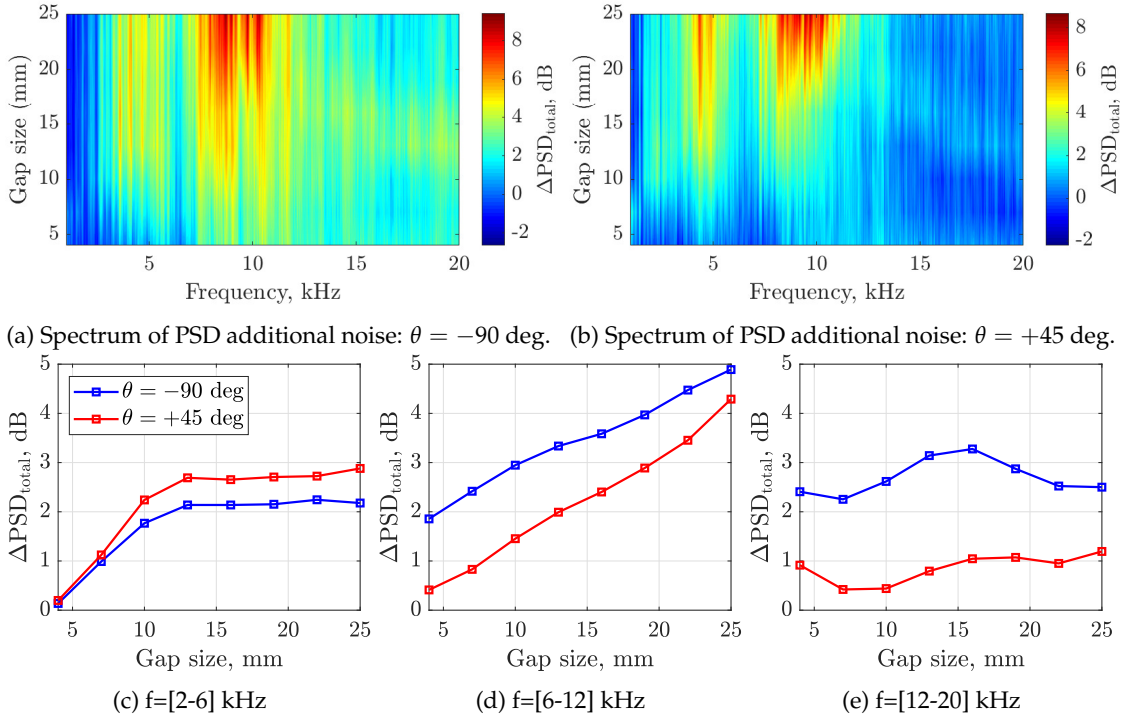

(a) Spectrum of PSD additional noise: $\theta = -90$ deg. (b) Spectrum of PSD additional noise: $\theta = +45$ deg.

(c) f=[2-6] kHz (d) f=[6-12] kHz (e) f=[12-20] kHz

Figure 2.14: Spectrum of PSD additional noise for different gap sizes and integration for discrete frequency ranges.

The noise reduction of the over-tip liner is presented in an analogous format in Fig. 2.16 and Fig. 2.17b, the former based on the far-field measurements and the latter on the PWL extraction from the GAPB. The resonances and anti-resonances of the over-tip liner can once again be observed for the full range of gap sizes and have been used to define the integration bands of Fig. 2.16c-2.16e. In the second and third frequency bands, the dominant noise sources were found to be located at the tip of the airfoil and consequently they move away from the lined surface as the gap size is increased. As a result, the PSD IL is reduced with gap size as observed in Fig. 2.16d-2.16e for $\theta = -90$ deg. and to a lesser extend for $\theta = +45$ deg.. This trend is clearer for the isolated gap noise from GAPB shown in Fig. 2.17b and has been predicted with an analytical model of a point source over an infinite lined surface described in Section 2.5 (Fig. 2.27). In the first frequency band, the same trend can be observed for gap sizes higher than e=10 mm, i.e. gap noise dominated, although the increase of PSD IL at lower gap sizes is less clear. It could be

linked to a predicted shift and increase of the peak of noise reduction towards lower frequencies with gap size (Fig. 2.27) affecting the frequencies between 1-3 kHz, 8.5-10 kHz and 17-18 kHz.

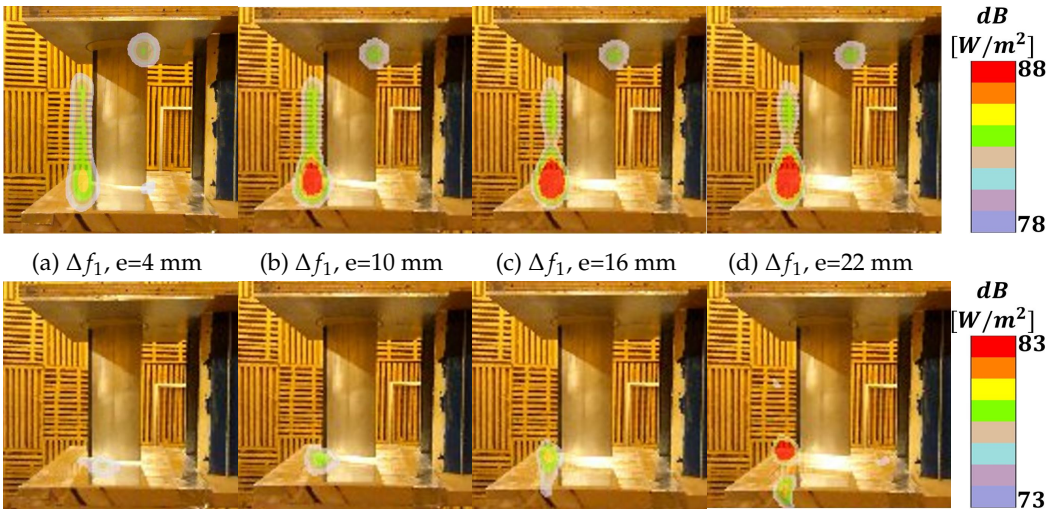

(a) Δf_1, e=4 mm (b) Δf_1, e=10 mm (c) Δf_1, e=16 mm (d) Δf_1, e=22 mm

(e) Δf_2, e=4 mm (f) Δf_2, e=10 mm (g) Δf_2, e=16 mm (h) Δf_2, e=22 mm

Figure 2.15: PWL maps for the hard wall case at different gap sizes for the frequency ranges of (a)-(d) Δf_1=[3-6] kHz and (e)-(h) Δf_2=[9-12] kHz.

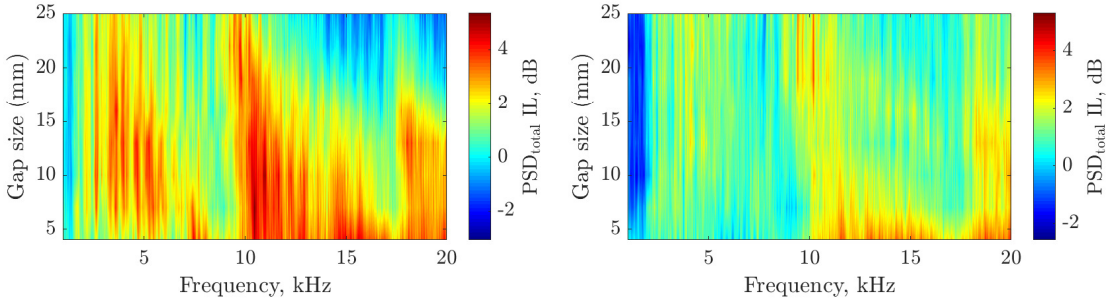

(a) Spectrum of PSD noise reduction: $\psi = -90$ deg. (b) Spectrum of PSD noise reduction: $\psi = +45$ deg.

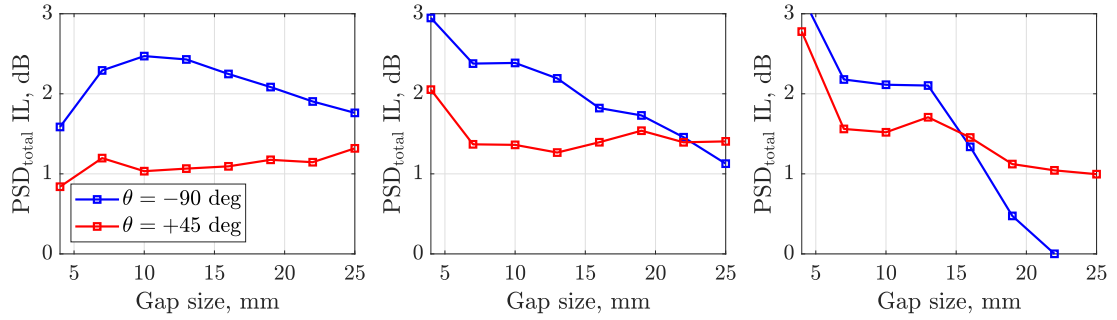

(c) f=[2-10] kHz (d) f=[10-18] kHz (e) f=[18-20] kHz

Figure 2.16: Spectrum of PSD noise reduction for different gap sizes and integration for discrete frequency ranges.

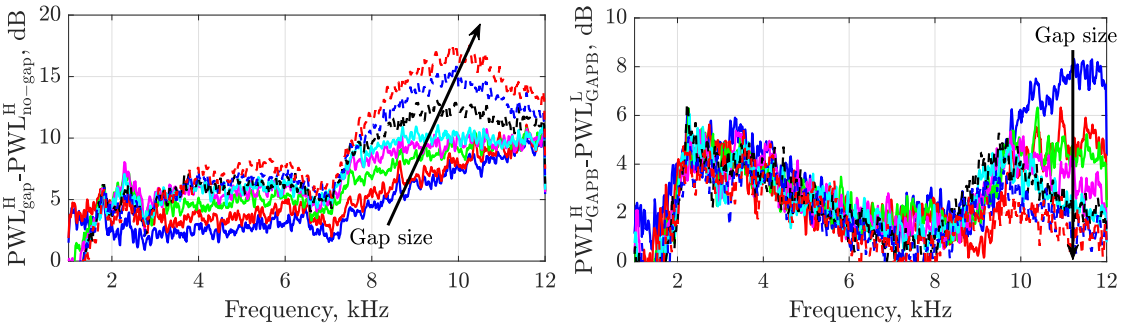

(a) Quantification of gap noise

(b) Over-tip liner noise reduction

Figure 2.17: Quantification of the gap noise generated by the tip leakage flow and PWL noise reduction by the over-tip liner in GAPB.

2.4.3 Effect of airfoil loading

This section investigates the effect of the airfoil loading, controlled by the geometrical AoA and fixed at 18 deg. in previous sections, on the generation of gap noise and the noise reduction performance of Over-Tip liners. The loading of the airfoil controls the pressure difference between the pressure and suction side and has a direct impact on the cross-flow through the tip gap and hence the noise radiation from the gap region.

The far-field measurements shown in this part of the section were acquired at two fixed positions of the arc array (ϕ,θ)=(0,$-$90) (pressure side) and (ϕ,θ)=(0,+45) (suction side) for gaps of e=[0,4] mm, U=32 m/s and hard wall and liner ID4 configurations. The sweep of geometrical angle of attack is performed for AoA=[0,5,10,15,20] deg. The spiral microphone array is also fixed at θ=90 deg. as in the rest of the experiments of this chapter. Neither the azimuthal location of the far-field arc array or the spiral array was corrected to account for the rotation of dipole directivity of the main noise sources. This effect is estimated with the analytical point source model of Section 2.5 assuming a dipole source at the TE normal to the chord. The predictions suggest that the change of relative angle between the airfoil and the microphone arc array modifies the predicted PSD by only 0.2 dB. For the range of AoA tested, the far-field arc array is located within the beamwidth of the TE dipole.

The measured PSD spectra are shown in Fig. 2.18 for the range of AoA with and without the gap for an analysis bandwidth of 16 Hz. The main feature that dominates the PSD spectra is the broadband hump over 2 to 3.5 kHz with discrete narrow peaks, which is repeated at twice those frequencies over 4 to 7 kHz. This behaviour is attributed to acoustic waves scattered by the trailing edge travelling upstream and creating a feedback loop but there is no consensus on the underlying physical mechanism activating the loop [62]. An exhaustive literature review is not intended here but some of the physical arguments include oscillations in the wake [63], laminar separation at the trailing edge [64], amplification of the laminar boundary layer Tollmien–Schlichting (T-S) instability waves [65]

and more recently of the Kelvin-Helmholtz instability [66]. This aeroacoustic/hydrodynamic feature is reduced when increasing the angle of attack and has a relatively small effect over the frequencies of interest in this study.

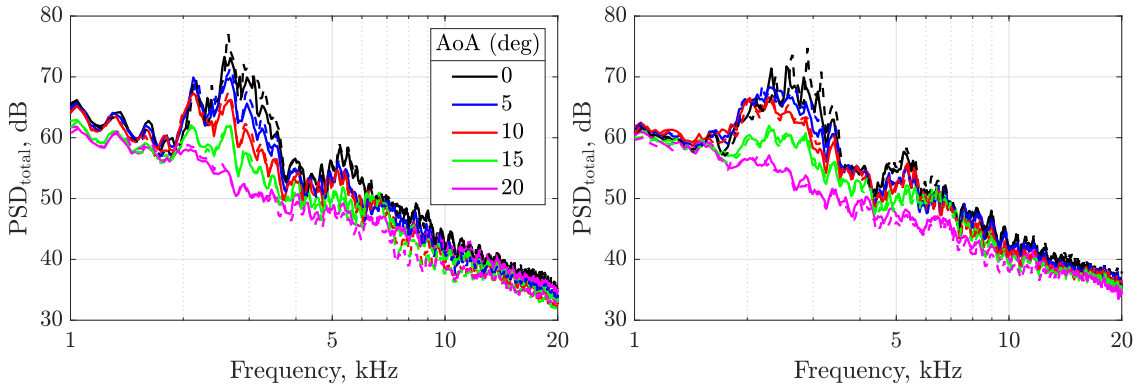

(a) (ϕ,θ)=(0,−90) deg. (b) (ϕ,θ)=(0,+45) deg.

Figure 2.18: Measured PSD for a range of AoA with e=0 mm (dashed lines) and e=5 mm (solid lines).

The spectrum of the additional noise due to the gap (ΔPSD_{total}=PSD^{gap}_{total}-$PSD^{no\text{-}gap}_{total}$) for each AoA is shown in Fig. 2.19 for an analysis bandwidth of 64 Hz. To support the analysis of the far-field data, PWL maps obtained from post-processing of the spiral array data for f=[9-12] kHz are presented in Fig. 2.20 for the hard wall case with/without gap and the lined configuration (ID4). It can be observed from the measurements at the pressure side (Fig. 2.19a) that an increase in the AoA results in additional gap noise radiation, especially for frequencies above 6 kHz. This does not mean that the magnitude of gap noise increases with AoA, Fig. 2.20e-2.20h show that the magnitude of the sources close to the gap is higher at AoA=10 deg., for instance, than at higher incidences. The increase in ΔPSD_{total} with AoA is linked to a reduction in the strength of the trailing edge noise sources radiating along the span, as observed in Fig. 2.20a-2.20d.

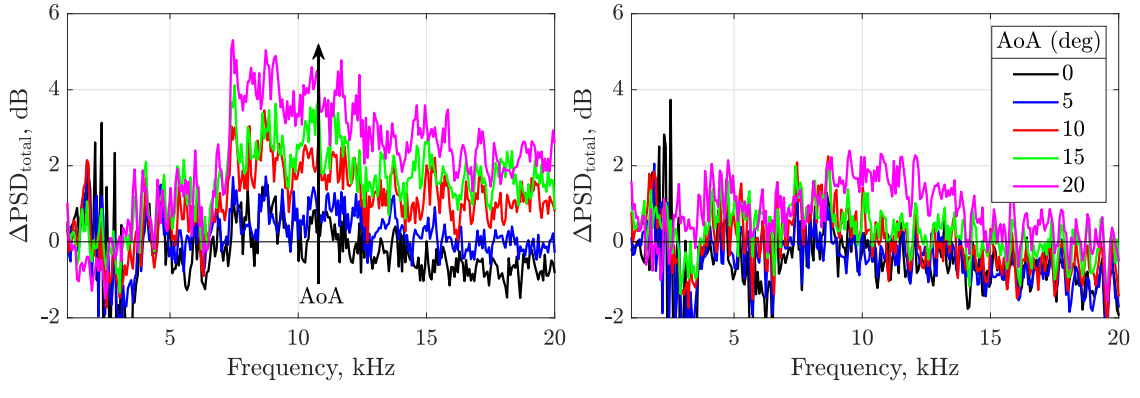

(a) (ϕ,θ)=(0,−90 deg.) (b) (ϕ,θ)=(0,+45) deg.

Figure 2.19: Spectrum of PSD additional noise for a range of AoA.

The trend observed for the measurements at the pressure side is not as clear for those at the suction side (Fig. 2.19b). The lower additional radiation in the suction side has been also observed in Section 2.4.2 but is not yet fully understood. These results also suggests that the configuration without gap can be noisier than with gap even for the intermediate values of AoA.

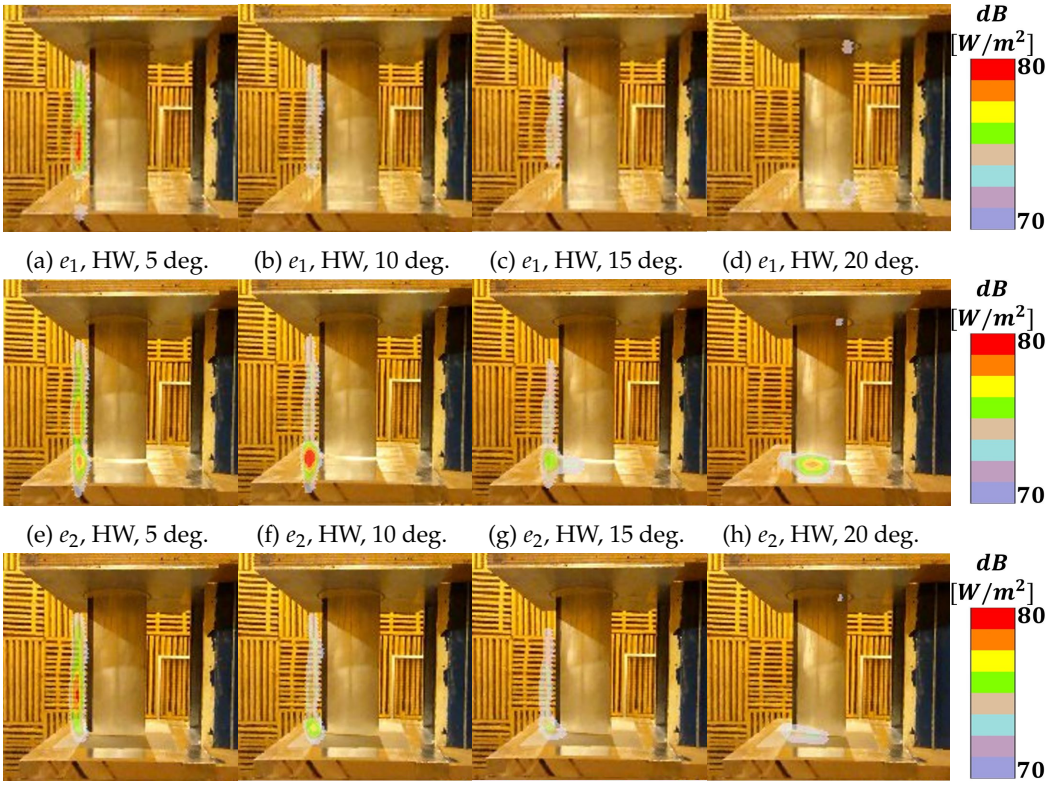

(a) e_1, HW, 5 deg. (b) e_1, HW, 10 deg. (c) e_1, HW, 15 deg. (d) e_1, HW, 20 deg.

(e) e_2, HW, 5 deg. (f) e_2, HW, 10 deg. (g) e_2, HW, 15 deg. (h) e_2, HW, 20 deg.

(i) e_2, ID4, 5 deg. (j) e_2, ID4, 10 deg. (k) e_2, ID4, 15 deg. (l) e_2, ID4, 20 deg.

Figure 2.20: PWL maps for the hard wall case and the lined configuration (ID5) at different AoA for the frequency range Δf=[9-12] kHz and [e_1,e_2]=[0,4] mm.

The effect of airfoil loading on the noise reduction of over-tip liners in shown in Fig. 2.21 in the form of PSD IL (Eq. 2.5). The noise reduction spectra present, as expected, the two anti-resonances and three humps of attenuation discussed previously and predicted from the impedance tube tests. The magnitude of the noise follows the same trends discussed in the previous paragraphs, both in the measurements at the pressure and suction sides. The over-tip liner continues to reduce the noise sources located in its vicinity, as observed again in Fig. 2.20i-2.20l. However, as the sources located further away from the liner (TEN) become weaker with increasing AoA, the noise reductions of gap noise become more apparent. Hence, the improved noise reduction benefit at higher AoA might not be related to gap noise itself but to the reduction of the TEN along the span of the airfoil.

An analytic exercise is depicted in Fig.2.22 to illustrate the noise reduction rationale outlined in the previous paragraph. The analytical model of a point source over an infinite lined plane described in Appendix B is used here for a distribution of incoherent dipoles

along the trailing edge of the airfoil and normal to the chord. The strength of the dipoles at each span position is shown in Fig.2.22a, which assumes an elliptical distribution for the TEN plus a Gaussian distribution for the gap noise at the airfoil tip. The strength of the tip sources is kept constant but the TEN noise is progressively reduced to represent the effect of increasing the AoA. This simple approach provides a predicted PSD IL that follows the trends observed in Fig. 2.21 over the frequencies where significant additional gap noise have been measured.

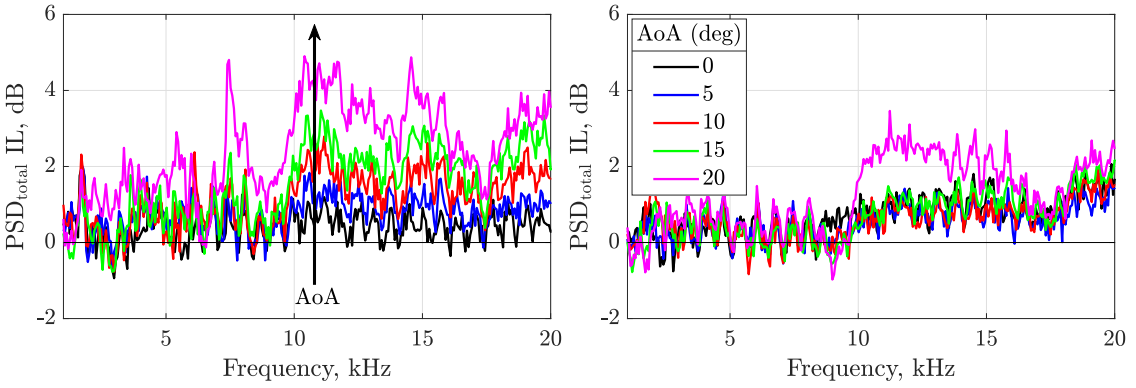

(a) (ϕ,θ)=(0,−90) deg. (b) (ϕ,θ)=(0,+45) deg.

Figure 2.21: Spectrum of PSD IL for a range of AoA.

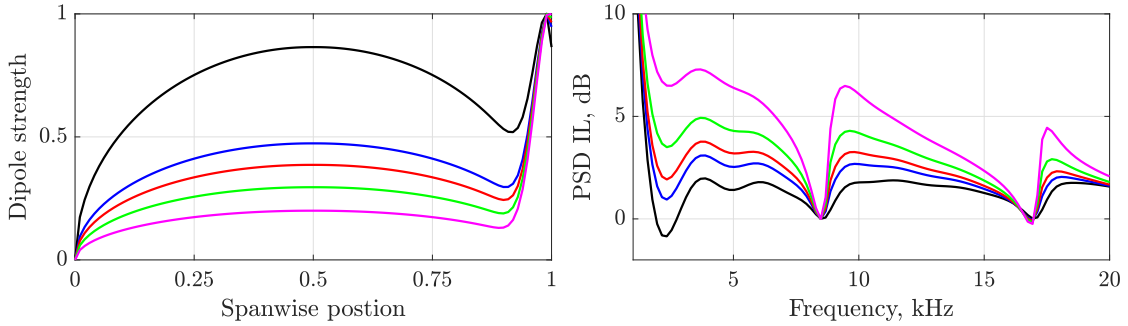

(a) Dipole strength distribution (b) Predicted PSD IL

Figure 2.22: Effect of the source strength distribution in the predicted liner PSD IL.

2.4.4 Source modification tests

The literature on OTR acoustic treatments [5, 19, 26–28, 31] suggests that the noise reduction mechanisms of OTR liners are a combination of source modification and conventional attenuation of acoustic waves propagating over the liner. The results presented here are aimed at providing a better understanding of the relative strength of these mechanisms for this particular experimental configuration. Five different liner configurations were tested using both the far-field and the spiral arrays. Although the results presented here are based on the far-field array data, the same conclusions can be drawn from results based on the spiral array data (with the sound power extraction technique). A plan

view of each liner insert with the location of the aerofoil is depicted in Fig. 2.23. The full liner ID4 was partially covered with a rigid hard wall surface, flush mounted to minimise noise attenuation over certain areas. The shaded and light areas of the liners in Fig. 2.23 represent the lined and hard wall areas respectively. The logic behind this selection is that the 'local' liner should only reduce sound in the near field of the source, whereas the 'remote' liner should attenuate the sound propagating over the liner between the source and the observer; the 'pressure side' (PS) and 'suction side' (SS) are a combination of both. Note that this is an engineering approach since the exact location of the source in the top view is not clear and shielding effects may be present.

The PSD reduction measured with the far-field array in the pressure side ($(\phi, \theta) = (0, -90)$ deg.) and in the suction side ($(\phi, \theta) = (0, +45)$ deg.) is shown in Fig. 2.24a and Fig. 2.24b respectively. As in previous figures, the results have been filtered with a Savitzky–Golay filter to smooth the data while maintaining the general trends. Only the data up to 12 kHz is shown because above that frequency the reduced noise levels approach those of the background noise and hence all liner configurations exhibit a similar performance.

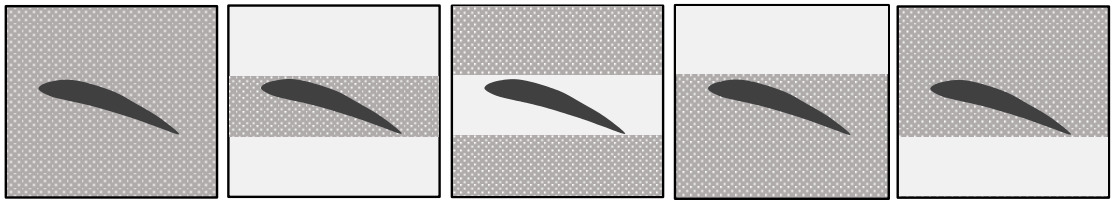

(a) Full Liner (b) Local Liner (c) Remote Liner (d) PS Liner (e) SS Liner

Figure 2.23: Liner configurations tested for the source modification tests.

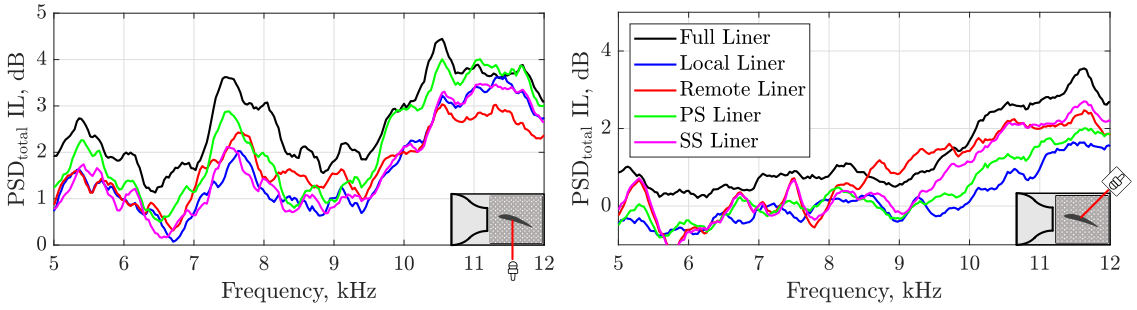

(a) Pressure Side: $(\phi, \theta) = (0, -90)$ deg. (b) Suction Side: $(\phi, \theta) = (0, +45)$ deg.

Figure 2.24: Measured noise PSD reductions for different over-tip liners.

The PSD reduction measured on the pressure side position (Fig. 2.24a) is similar for all configurations up to approximate 9.5 kHz. The following points can be drawn from the results in the gap noise dominated frequency range (9-12 kHz): (1) the PS liner has the closest performance to the full liner, as expected since the measurements are made from a PS position; (2) the SS liner and the local liner have also a similar performance, which also is expected for the same reason; (3) the remote liner has the lowest noise

reduction, which could suggest that a potential source modification effect present in the other configurations is missing in the remote liner configuration.

The same logic is now followed for the measurements on the suction side position (Fig. 2.24b) for the gap noise dominated frequency range (9-12 kHz): (1) the remote liner has the best performance at some frequencies and practically the same as the SS liner at the higher frequencies, suggesting no source modification effects; (2) the PS liner has similar but better performance than the local liner, which is not expected.

In summary, the measurements taken on the pressure side may suggest some weak source modification effects but the data from the suction side is inconclusive. Measurements averaged over a range of meridian positions could give a better picture of the problem and account for any changes in directivity induced by the different liner configurations. Additional measurements of the unsteady pressure fluctuations on the airfoil surface for a hard wall case and with the over-tip liner could give more insight on source modification effects that may occur due to the presence of the lined surface.

2.4.5 Use of TE feathers

The effects of trailing edge feathers is considered next. The motivation behind the use of TE feathers is to reduce the contribution of TEN such that the dominant noise sources are located nearer the tip of the airfoil, and hence more prone to over-tip liner noise reductions. Note that the feathers are not installed along the full span of the airfoil section, leaving the area near the tip with the baseline trailing edge. Besides, the liner configuration with wire mesh ID7 has been manufactured with a shallower cavity depth of 13 mm to move the first anti-resonance of the liner towards higher frequencies ($\sim$13 kHz) and to avoid a local minimum in the noise reduction spectra at frequencies of interest.

The power from the full domain and the equivalent power radiated from GAPB are shown in Fig. 2.25a and Fig. 2.25b respectively. The four curves correspond to: (1) the hard wall reference case with baseline or standard TE (BL), (2) the hard wall reference case but with feathered TE (TEF), (3) the lined configuration with BL and (4) the lined configuration with TEF. The corresponding PWL maps for the frequency range f=[6-9] kHz, for which TEF are most effective, are shown in Fig. 2.25c-2.25f. The effect of the TEF is most clearly seen in Fig. 2.25a for f=[6-9] kHz, with a drastic reduction of the TEN hump for both hard and lined configurations, which is also observed in the PWL maps. A smaller but still significant effect of the TEF is present in the gap region, as shown in Fig. 2.25b. The spectra is dominated by gap noise for frequencies over 9 kHz and the use of the baseline or feathered trailing edge does not make any difference, both configurations now collapsing to the hard/lined solution.

The gap noise generated by the tip leakage flow and the noise reduction by the over-tip liner can be quantified following an analogous procedure to that in Section 2.3. These are compared with the baseline and feathered trailing edges in Fig. 2.26. Tip gap noise is not affected by the use of TE feathers (Fig. 2.26a). That is unlikely to occur if the treatment were extended to the tip of the airfoil since one of the main noise generation mechanisms would be modified. The liner noise reduction is also found to be little affected by the trailing edge treatment in the frequencies dominated by gap noise, although a local minimum around 5.5 kHz can be seen for the TEF configuration in Fig. 2.26b. This analysis is based on the PWL extracted from the measurements of the spiral array but the same trends in terms of PSD levels and reductions have been found from the far-field measurements made on the suction side of the airfoil. However, the noise reduction minimum at 5.5 kHz does not appear on the pressure side ($\theta = -90$ deg.) and the same performance is observed for the baseline and feathered trailing edged configurations. The results presented here reinforce the point made in Section 2.3 that over-tip liners reduce the noise sources located close to the liner regardless of the noise generation mechanism.

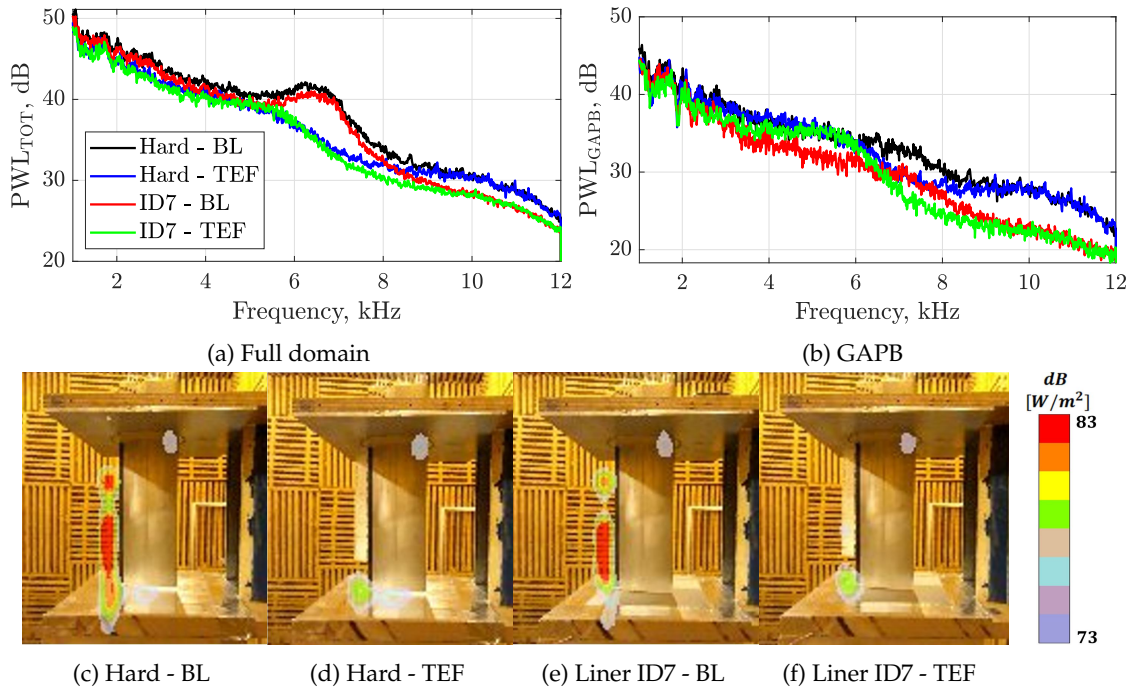

(a) Full domain (b) GAPB

(c) Hard - BL (d) Hard - TEF (e) Liner ID7 - BL (f) Liner ID7 - TEF

Figure 2.25: Noise localization and extraction for the baseline (BL,(c) and (e)) and feathered (TEF, (d) and (f)) trailing edged configurations. The PWL maps are rendered for the frequency range of f=[6-9] kHz.

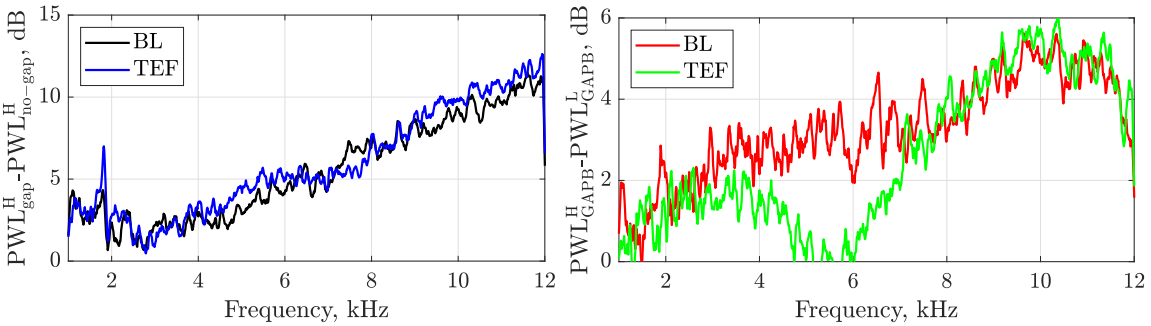

(a) Quantification of gap noise

(b) Over-tip liner noise reduction

Figure 2.26: Quantification of the gap noise generated by the tip leakage flow and PWL noise reductions by the over-tip liner in GAPB for the baseline (BL) and feathered (TEF) trailing edged configurations.

2.5 Comparison with point source analytical model

Analytical methods to model the tip gap noise generated by the turbulence in the cross-flow as they are scattered by the tip suction side edge and trailing edge have been explored previously [67]. A modified version of Amiet's theory [68] with spanwise attenuation to damp the perturbations away from the tip was suggested for the former mechanism and an adaptation of Dunne and Howe's [69] model of a vortex through a tip clearance gap for the latter. Neither of these methods is applicable here because our focus is not on the noise generation itself but the noise suppression by over-tip liners. Instead, a simpler approach based on a point source located over an infinite hard/lined plane has been used.

Analytical predictions have been obtained through a numerical implementation of the Thomasson formulation [70] of a monopole source over an infinite lined plane. A description of the formulation, the numerical implementation, the verification of an extension to account for dipoles and quadrupoles and the procedure to obtain comparable PWL to those captured by the spiral array are detailed in Appendix B. This section covers the comparison of the analytical predictions with the measured data, first for the more realistic configuration with the static airfoil and then for the no-flow artificial point source.

A. Static Airfoil

The predicted PSD IL evaluated at the far-field microphone position $(\phi, \theta) = (0, -90)$ deg. for a dipole normal to the chord of the airfoil (AoA=18 deg.) and located at the TE is shown in Fig. 2.27a. The three humps of PSD insertion loss (IL) with the resonances and anti-resonances are of course captured by the analytical model. The trend of lower IL as the gap size is increased can be clearly observed here and the rate of the loss of performance with the gap size increases with frequency: at 5 kHz $\sim$ 7 dB less IL is predicted

when the gap size changes from 5 mm to 25 mm whereas at 10 kHz the variation is of $\sim$ 10 dB and at 20 kHz soars up to 15 dB. The resonance peaks become higher but narrower as the gap size increases, causing the trends outlined here and observed in Section 2.4.2. The same conclusions can be drawn from the PWL IL predictions shown in Fig. 2.27b, which are directly comparable to the PWL IL extracted from GAPB shown in Fig. 2.17b.

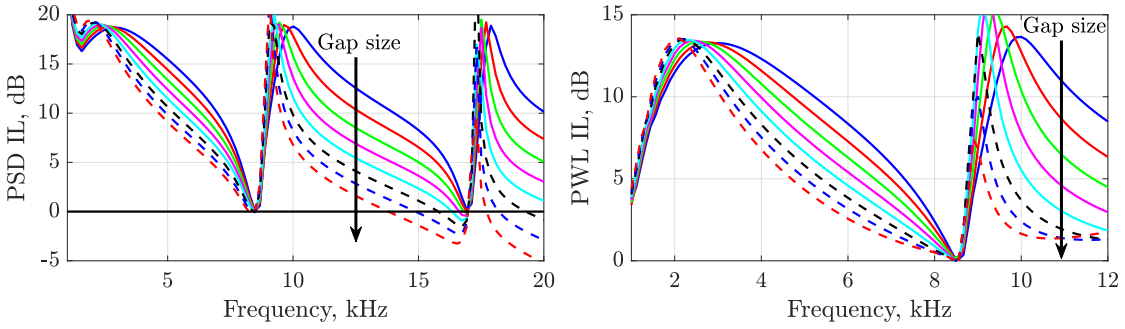

(a) PSD IL (b) PWL IL

Figure 2.27: Predicted (a) PSD and (b) PWL gap noise reduction for different gap sizes and a dipole perpendicular to the airfoil chord.

A comparison of the predicted PSD IL assuming different types of point source with the measured isolated gap noise PSD_{gap} IL is shown in Fig. 2.28 for a selection of gap sizes. Although the peak IL is generally overestimated, a qualitative agreement in the magnitude and spectral shape can be observed for the rest of the spectrum, especially in the second and third humps of noise reduction. The experimental results follow the trend of lower broadband noise reduction as the gap size increases and the agreement with the prediction gets better for bigger gaps, which can be linked to a stronger and more localised source. The spectral shape of the predicted PSD of a monople and a dipole are very different, but they collapse when performing the subtraction to obtain the PSD IL. The quadruple has a lower noise reduction as expected and would only be a candidate to represent the physical mechanisms if a jet-type source was measured. Based on the scaling of gap noise with the free-field velocity discussed in Section 2.4.1, a dipole-type source is the best candidate.

An equivalent comparison is made in Fig. 2.29 between the predicted PWL IL evaluated over the surface of the spiral array, and the PWL IL from the GAPB area extracted using the post-processing of the spiral array data. The prediction also overestimates the peak PWL IL but a better agreement than with the PSD IL is found at lower frequencies. Again, the predicted and measured data are closer for higher gap sizes and the monopole and dipole present some agreement both in magnitude and spectral shape for almost the full frequency range in Fig. 2.29c and 2.29d. The quadrupole source, as expected, is not a good candidate for the modelling of gap noise reduction in the current experiment as observed with large differences with the measured data as the gap size is increased.

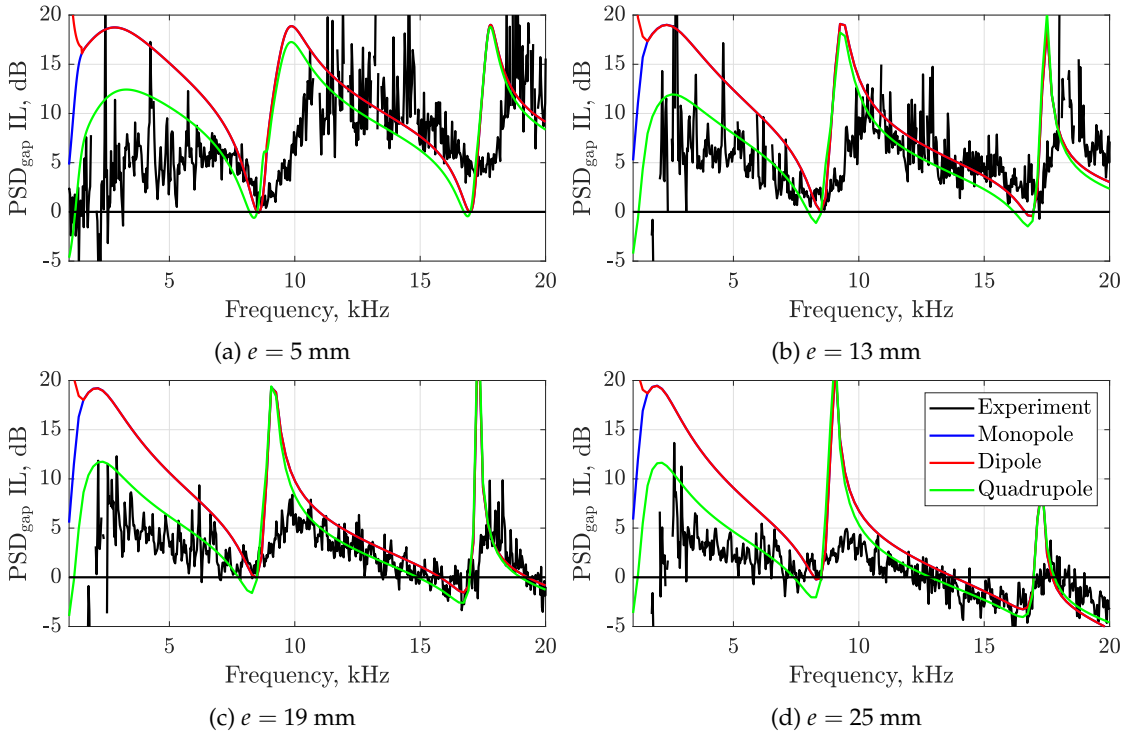

(a) $e = 5$ mm (b) $e = 13$ mm

(c) $e = 19$ mm (d) $e = 25$ mm

Figure 2.28: Measured and predicted gap noise PSD IL for different gap sizes.

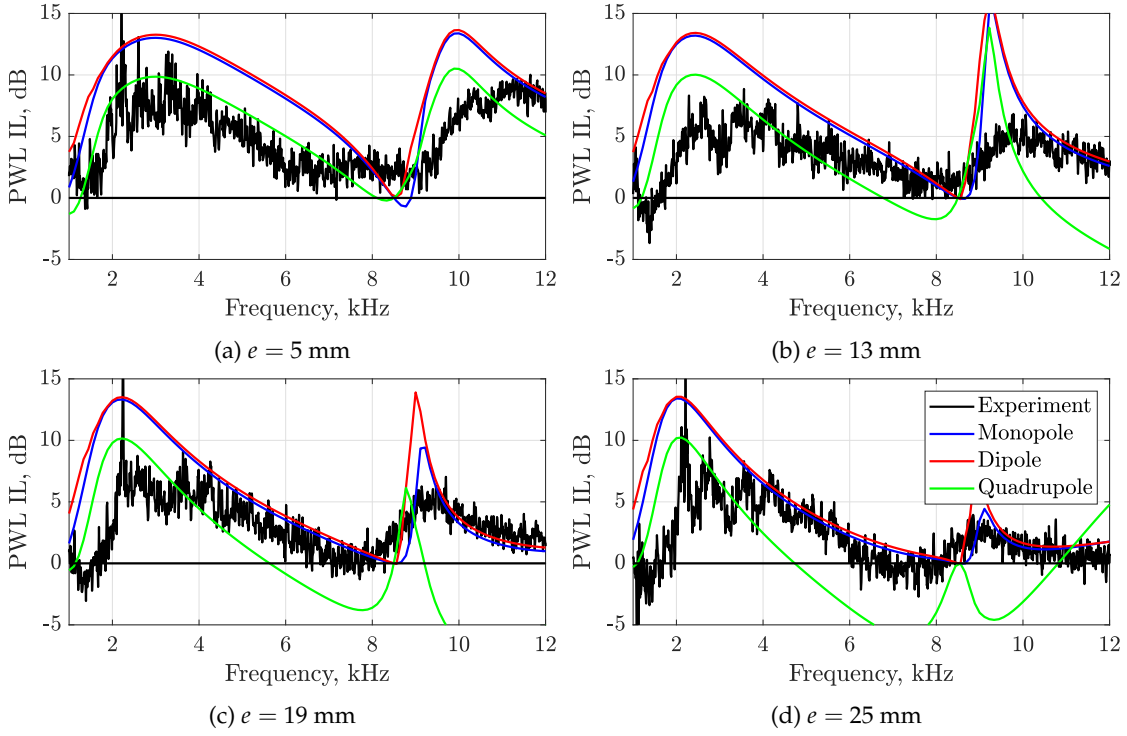

(a) $e = 5$ mm (b) $e = 13$ mm

(c) $e = 19$ mm (d) $e = 25$ mm

Figure 2.29: Measured and predicted gap noise PWL IL for different gap sizes.

B. No-flow artificial point source

The frequencies tested in this test were $f = [3, 4, 5]$ kHz, corresponding to wavelengths of $\lambda = [113, 85, 68]$ mm respectively. This provides at least one wavelength of propagation over the lined surface before the field encounters the end of the lower plate. For each excitation frequency, a sweep along a range of gap sizes was performed with increasingly small spacing as the source gets closer to the surface, cases of higher interest for real applications of tip leakage noise. The gap sizes measured for each excitation frequency are specified in Table 2.2 rounded to mm. The far-field measurements were all taken at an angle of θ=-90 deg. with respect to the nozzle exit, with the spiral array located at θ=+90 deg.. The tests at 4 kHz were also performed at azimuthal angles of θ=-45 deg and θ=0 deg to assess the omnidirectional radiation of the point source and to check any scattering effects associated to the finite plate and the nozzle.

Table 2.2: Test matrix for the no-flow point source test. Gap size e from the source to the bottom plane.

	Target e/λ						
	0.025	0.05	0.1	0.2	0.4	0.8	1
f (kHz)	Gap size e (mm)						
3	3	6	11	23	45	91	113
4	2	4	9	17	34	68	85
5	2	3	7	14	27	54	68

The measured PSD spectra of the far-field measurements is dominated in all cases, as expected, by the source excitation frequency, as shown in Figure 2.30a. The measured spectrum is post-processed to isolate the PSD level at the source excitation frequency to be able to assess the effect of the problem variables and to compare the measurements to analytical models. The tone amplitude is integrated over a small bandwidth to account for variations of the excitation frequency such as in Fig. 2.30b.

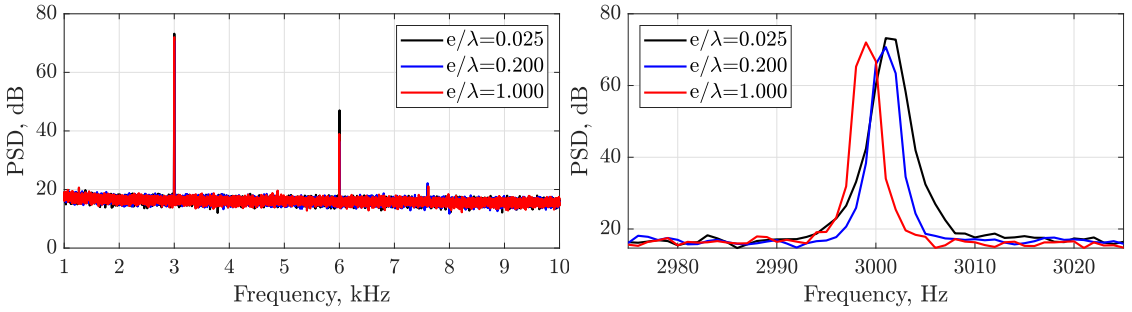

(a) Full Spectrum (b) Tonal detail

Figure 2.30: PSD spectra at different gaps (e/λ) for a source excited at 3 kHz and hard wall configuration.

Equivalent sound power maps can be obtained for each test case and prescribed frequency range by using the data acquired with the spiral array and the CIRA post-processing technique. A power map is shown in Fig. 2.31a for the hard wall configuration with e=7 mm and f=5 kHz. The equivalent sources of acoustic power from the probe termination can be defined as a selected spatial area, indicated with the red square, to obtain the spectrum of the power radiated by the sources within that region. The extracted PWL spectra is also dominated by the tone excitation frequency, as observed in Fig. 2.31b, and is integrated over a certain bandwidth to obtain a single PWL value for each frequency and gap size as in the far-field data. The main advantage of the PWL extraction technique for this particular application is that it minimises the effects of leakage noise sources from the tube junction and reflections from the upper support plate, the nozzle, edges and from the tube itself on the measured data.

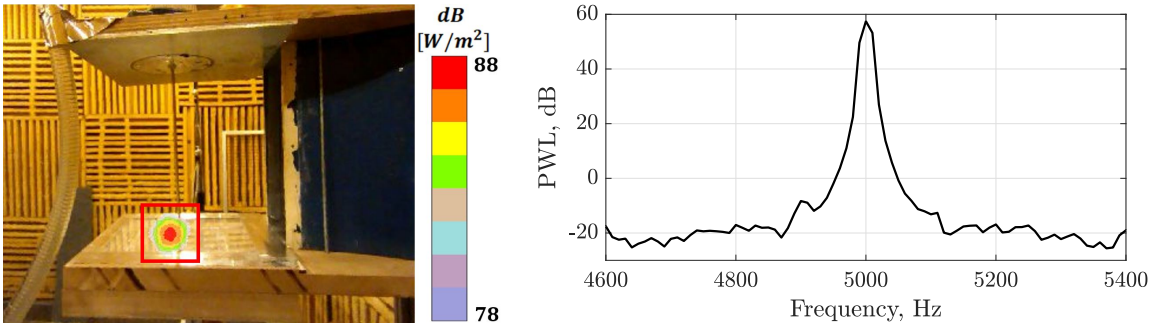

(a) PWL map

(b) Extracted PWL spectrum

Figure 2.31: PWL map and power extracted from equivalent sources in the red area for the hard wall configuration with e=7 mm and f=5 kHz.

B.1. Far-field measurements

The directivity of a monopole source over an infinite plane is azimuthally omnidirectional. However, the measured far-field in the current set-up can be contaminated by leakage sources and scattering effects associated with the finite support plates, the nozzle and the tube itself. The far-field PSD measured for three azimuthal positions of the arc array, θ=[-90, -45, 0] deg., are presented in Fig.2.32 and compared with the analytical predictions for the hard wall and lined configurations. Note that the polar angles ϕ_{mic} are in the coordinates of the arc array, centred in the mid-point between the upper and bottom support plates and measured from the equator and not the zenith. The microphone positions in the spherical coordinate system used for the analytical predictions (r,θ,ϕ), with the origin on the bottom plate and below the point source, can be readily obtained with a translation in the z-direction.

The measured data in Fig.2.32 should ideally collapse on the green analytical solution. However, variations between measured data within +/- 5 dB for the hard wall and +/- 15 dB for the lined case can be observed. The highest deviations such as for θ=-90 deg

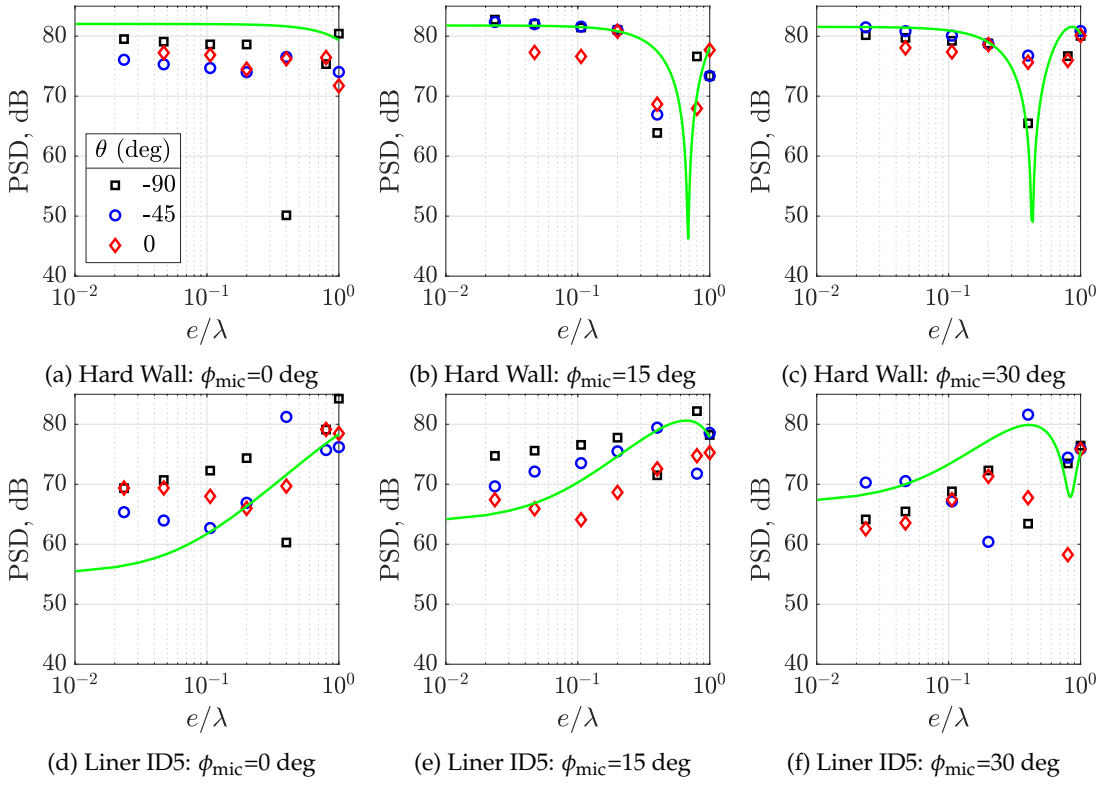

(a) Hard Wall: ϕ_{mic}=0 deg (b) Hard Wall: ϕ_{mic}=15 deg (c) Hard Wall: ϕ_{mic}=30 deg

(d) Liner ID5: ϕ_{mic}=0 deg (e) Liner ID5: ϕ_{mic}=15 deg (f) Liner ID5: ϕ_{mic}=30 deg

Figure 2.32: PSD variation with non-dimensional gap distance measured at each microphone at various azimuthal position of the microphone arc array for hard wall and ID5 configurations and f=4 kHz. Symbols: measured data; Solid line: analytical solution.

and e/λ=0.4 in Fig. 2.32a may be attributed to changes in the directivity lobes due to the interference with reflective surfaces. The higher variability in the lined case is likely caused by spurious leakage sound sources at the junction observed in the noise localisation maps. The sound levels of the leakages are small in comparison to those of the point source in the hard wall case but increase its relative strength once the liner insert is present. This first set of data should be used as a reference for the expected variability in the rest of the PSD results and highlights the need of noise localisation and extraction methods to isolate the noise radiated from the probe termination. Therefore, the rest of the analysis of the far-field results is based on the analytical predictions and a qualitative comparison with the measured PSD data focused on the trends.

The PSD measured at each microphone location for the azimuthal position of $\theta = -90$ deg. is shown in Fig. 2.33 for the three frequencies tested and the hard and lined configurations. To support the analysis of the data in Fig. 2.33, analytical directivity plots for the source located at particular e/λ values are presented in Fig. 2.34. The normalisation used in the directivity plots is different for the hard wall and liner cases for illustration purposes and the polar angles ϕ are expressed in the spherical coordinate system used for the analytical predictions, for which ϕ=90 deg. is normal to the infinite plane. Note that

the impedance of the liner varies with frequency and hence the measured and predicted PSD and the directivity plots.

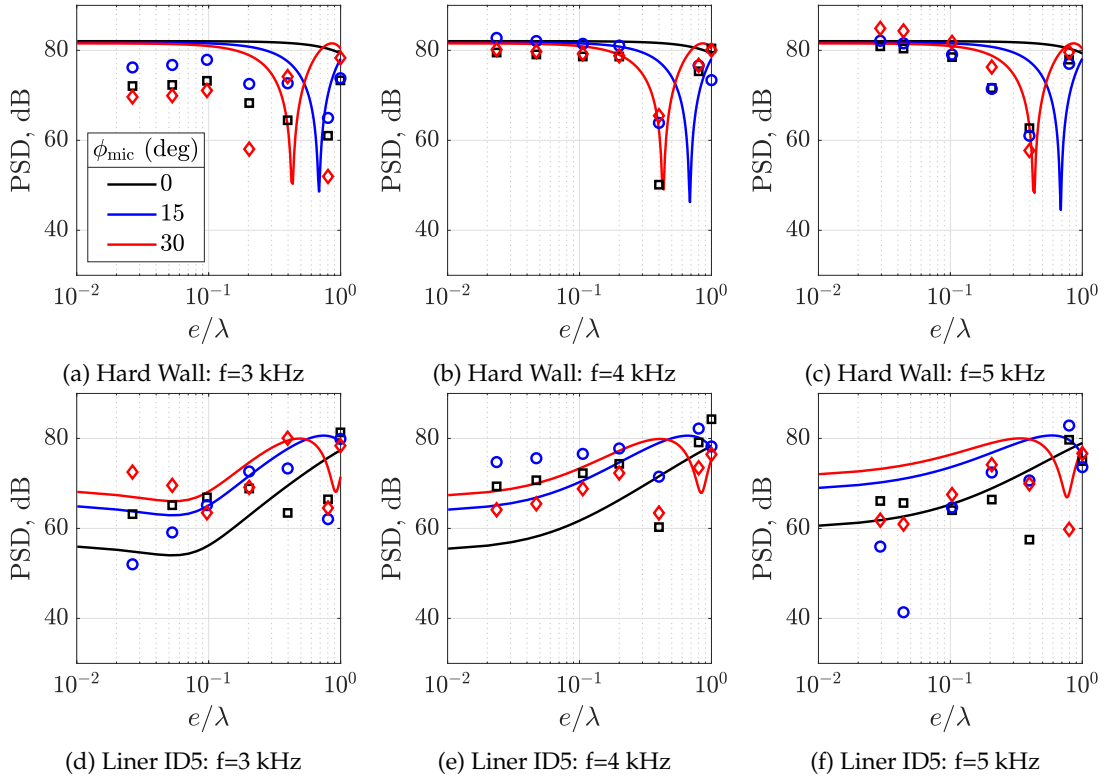

(a) Hard Wall: f=3 kHz (b) Hard Wall: f=4 kHz (c) Hard Wall: f=5 kHz

(d) Liner ID5: f=3 kHz (e) Liner ID5: f=4 kHz (f) Liner ID5: f=5 kHz

Figure 2.33: Comparison of measured and predicted PSD at each microphone location for the hard wall and lined configurations. Symbols: measured data; Solid line: analytical solution.

The main features of the source radiation over a hard wall surface observed in Fig. 2.34 are (1) the tendency towards a fully omnidirectional source as it gets closer to the surface and (2) the presence of well-defined radiation lobes as the source moves away from it caused by cancellations of the direct and reflected contributions. The radiation lobes cause the zeros at e/λ=0.4 for ϕ_{mic}=30 deg. and e/λ=0.7 for ϕ_{mic}=15 deg. in Fig. 2.33a-2.33c. Although the trends in the measured data show some agreement with the analytical predictions the lobes do not agree and reinforce the idea of directivity modifications caused by the experimental set-up. The directivity pattern changes significantly when the liner insert is introduced, the predictions in Fig. 2.34 show that the components radiating at small angles from the surface, close to grazing, are practically cancelled. The steep pressure gradient results in a vertical dipole-like radiation when the source is very close to the liner and shifts the radiation lobes upwards for source locations further away from the surface. These trends on the effect of the liner on the source directivity have been already reported in [71] and can be also observed in the predicted curves of Fig. 2.33.

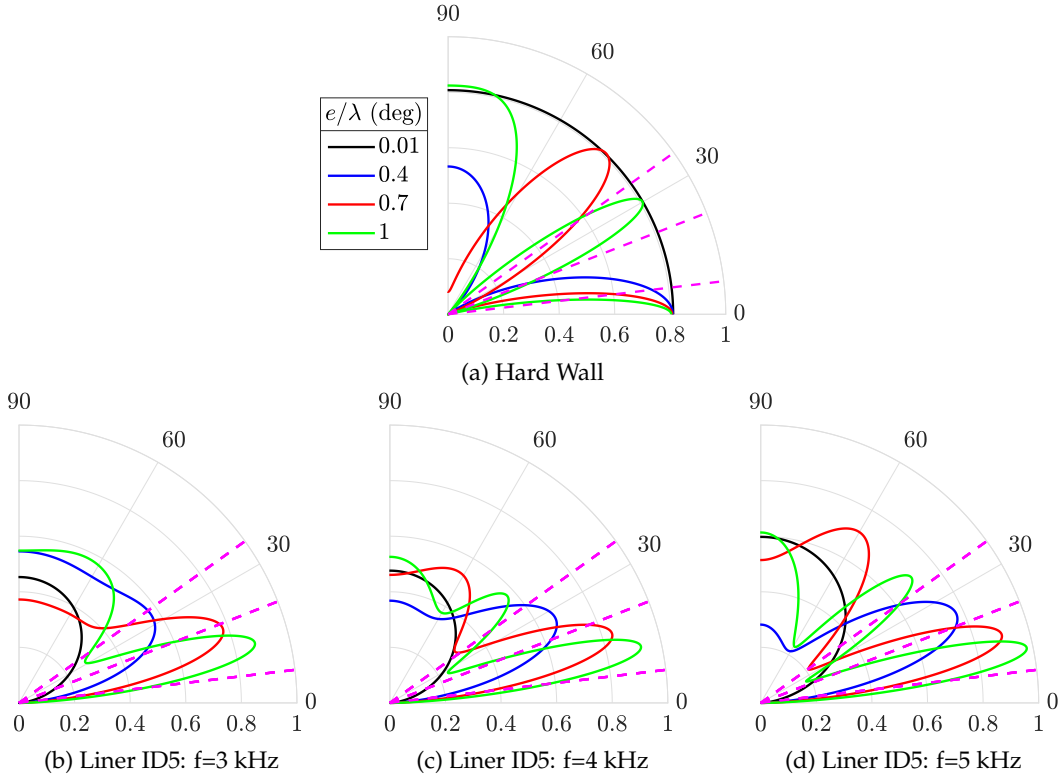

(a) Hard Wall

(b) Liner ID5: f=3 kHz

(c) Liner ID5: f=4 kHz

(d) Liner ID5: f=5 kHz

Figure 2.34: Predicted directivity plots at particular source locations for the (a) hard wall and (b)-(d) lined configurations. The magenta dashed lines indicate the positions of the arc array microphones.

The PSD Insertion Loss (IL) is computed for all three microphones as the difference, in dB scale, between the PSD in the hard wall configuration and with the liner insert. The measured PSD IL and the analytical estimates are shown for each source excitation frequency in Fig. 2.35. Despite the mismatch in the amplitude of the IL between the measured data and the analytical estimates, both datasets indicate that the noise reduction increases when the source is located closer to the acoustic treatment.

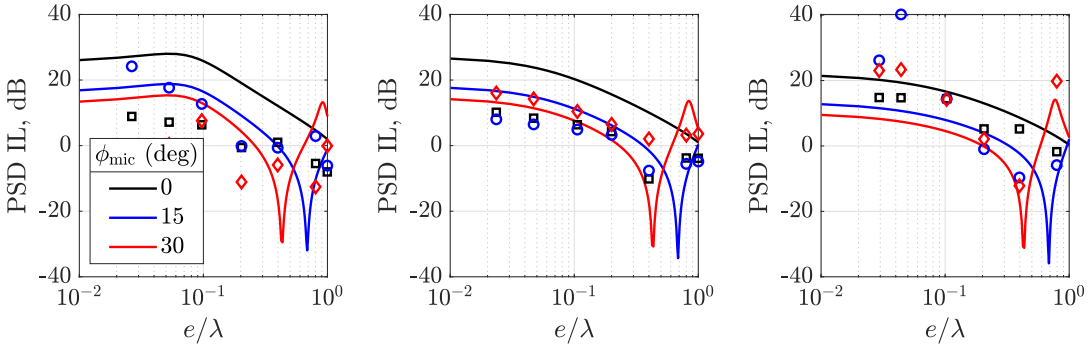

(a) f=3 kHz

(b) f=4 kHz

(c) f=5 kHz

Figure 2.35: Comparison of measured and predicted PSD IL at each microphone location. Symbols: measured data; Solid line: analytical solution.

B.2. Noise localisation and extraction

The analysis of the far-field results has shown that discrimination of the acoustic field generated by the artificial source is necessary to minimise the contamination of leakage noise sources and reflections from other elements of the set-up. Therefore, equivalent sound power maps have been obtained for each test case and prescribed frequency range. The selected spatial areas to extract the spectrum of the power radiated by the artificial source are shifted vertically in accordance with the gap size. The analytical predictions of the acoustic power incident on the spiral array are computed by the numerical integration described in Appendix B.

The comparison of the measured and predicted PWL for the hard wall and liner ID5 is shown in Fig. 2.36. The missing points for the hard wall at 4 kHz are due to faulty data-files. The predicted PWL for the hard wall configuration presents only small variation with frequency, which is due to the different relative location of the source with respect to the spiral array for a given e/λ. The agreement of the extracted PWL with the predictions has generally improved both for the hard wall and lined configurations with respect to the PSD comparison. However, the hard wall data at 3 kHz still presents high discrepancies that are still under investigation. The drastic improvement, especially in the lined configuration, between the predicted and measured PWL supports the hypothesis of spurious sources and reflections contaminating the far-field data. The same trends can be observed in terms of the PWL IL, shown in Fig.2.37, confirming that the liner can reduce the power output of the artificial point source up to 20 dB when located well within the near-field of the source.

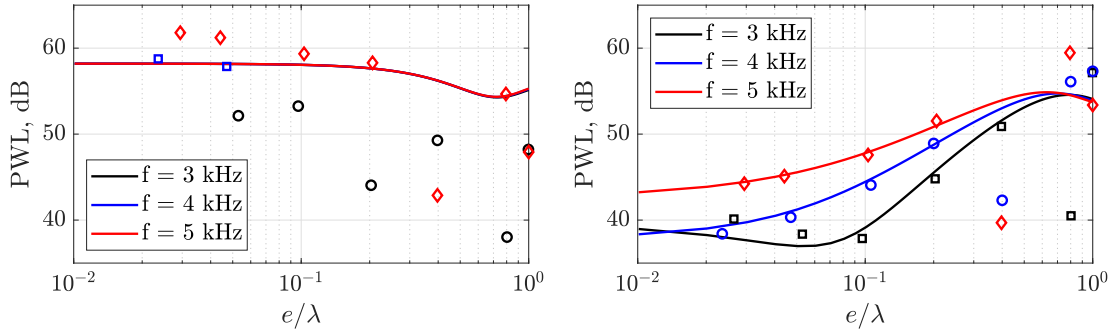

(a) Hard Wall

(b) Liner ID5

Figure 2.36: Comparison of measured and predicted PWL captured by the spiral microphone array. Symbols: measured data; Solid line: analytical solution.

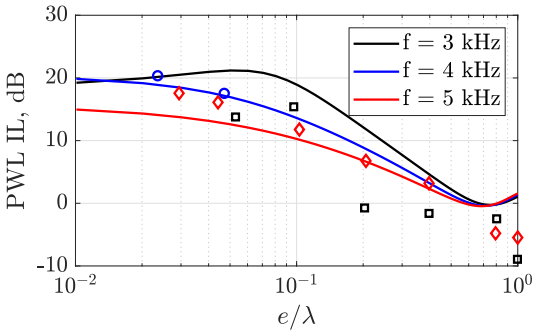

Figure 2.37: Comparison of measured and predicted PWL IL captured by the spiral microphone array. Symbols: measured data; Solid line: analytical solution.

The semi-logarithmic scale used along this part of the section emphasises the source locations closer to the liner surface, which generally presents a better agreement with the analytical model. The reason for using this scale is that the comparison with the analytical model is more meaningful for those small values, as illustrated in Fig. 2.38, where L_L=250 mm and L_S=350 mm are the width of the liner insert and the bottom support plate. The three outermost source positions are depicted for f=3 kHz, in red, and f=5 kHz, in green, which corresponds to values of e/λ=[0.4 0.8 1]. The angle ϑ for e/λ=1 is 42 deg. for f=3 kHz and 29 deg. for f=5 kHz, showing that the assumption of an infinite plane is quickly diminished away from the surface and that it can vary significantly with frequency.

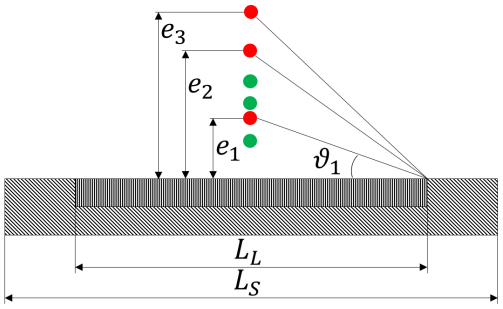

Figure 2.38: Geometric representation of the finite liner insert.

2.6 Summary and conclusions

Summary

- This chapter has focused on improving the understanding of the physical mechanisms of noise reduction of the Over-Tip-Rotor (OTR) liner concept by means of wind tunnel experiments with two simplified set-ups. The first experiment consisted of a static airfoil mounted vertically between two flat plates and separated from the lower one by a small gap. The pressure difference between the suction side and the pressure side of the airfoil creates a jet-like flow through the tip gap that resembles the noise generation mechanism of a tip vortex. The second uses an artificial single-frequency monopole-like source in the absence of flow. In both cases, a hard wall or a SDOF liner insert is flush mounted in the lower plate representing an over-tip liner. Differences of measured far-field sound spectra and sound power from spiral microphone-array measurements have been used to isolate and quantify the noise sources and the noise reduction benefits of over-tip liners.

- A series of parametric studies have been presented: the scaling of gap noise with the free-stream velocity; the directivity of the dominant sources; the effect of gap size and airfoil loading in gap noise generation and the noise reduction of the over-tip liner; modified lined configurations to study source modification effects and the use of trailing edge feathers.

- Analytical predictions of the over-tip liner noise reduction have been obtained through a discrete evaluation of Thomasson formulation [70] for a monopole point source located over an infinite lined plane. The analytical predictions are compared with the measured PSD IL and PWL IL, both for the gap noise and the artificial source, for various gap sizes.

- Source localization results from the spiral array show that the over-tip liner reduces the noise radiated in the vicinity of the liner, which can be dominated by gap noise or trailing edge noise depending on the frequency range. The over-tip liner gap noise reduction spectra obtained using differences of far-field sound spectra and differences of source-power spectra show peak broadband reduction of gap noise by 5-10 dB, corresponding to 2-3 dB of noise reduction in the full domain.

- The results suggest that the interaction of turbulence with the tip edges is the dominant source of gap noise in the current tests, with a PSD dependence of the 5^{th} power of the free-stream velocity. The gap noise generally increases with the gap size, although it can saturate at low frequencies (f$<$6 kHz) and remain unaffected at high frequencies (f$>$12 kHz).

- The increase of airfoil loading results in an apparent greater noise reduction of the over-tip liners. However, it is argued that this is a result of the weakening of trailing edge noise sources along the span when increasing the loading and not an enhanced reduction of gap noise sources.
- Measurements with various liner configurations might suggest weak source modification effects but the results are inconclusive. Additional measurements of the unsteady pressure fluctuations on the airfoil surface could give more insight on source modification effects caused by the over-tip liner.
- The use of TE feathers concentrate the dominant noise sources towards the tip of the airfoil for an extended range of frequencies and the results reinforce the point that over-tip liners attenuate the noise sources located close to the liner regardless of the noise generation mechanism.

Conclusions

- It has been found that the performance of the over-tip liner is not significantly modified by the tip-leakage flow, which suggests that the liner suppresses the noise sources located in its vicinity, irrespective of the dominant source (i.e. TE or gap noise sources). This result highlights the potential of over-tip liners in turbo-machinery applications even if the role of gap noise is not fully quantified.
- The noise reduction benefits of the over-tip liners are reduced when increasing the gap size, observed both in the static airfoil and the artificial source tests, in agreement with the analytical prediction model evaluated here. This confirms the impact of the proximity of the noise sources to the liner, which can significantly modify the radiated acoustic field with measured PWL broadband gap noise reductions of 5-10 dB and PWL tonal noise reductions of up to 20 dB.
- Although the peak IL is usually overestimated by the analytical predictions, a qualitative agreement has been obtained for the gap noise reduction performance of over-tip liners, the match improving for larger gap sizes or more localised sources. This shows that simple analytical models can provide guidance on the design of over-tip liners and encourages the development of the analytical OTR prediction models for fan noise reduction described in subsequent chapters.

Chapter 3

Impedance Modelling

Contents

Solving the wave equation in the fan duct requires not only a source model but also the imposition of appropriate boundary conditions at the duct walls. The modelling of the impedance boundary conditions is essential to solve the acoustic problem. The analytical Green's function of the acoustic field in a circular hollow duct described in Chapter 4 requires the impedance boundary condition as an input. The definition and the impedance model used in this research are presented in Section 3.1 alongside a brief review of the literature.

Acoustic liners are widely used in turbofan engines and are the most common technology used to reduce its noise emissions. Liner design relies on the modelling of the acoustic treatment as an equivalent acoustic impedance that can be used as a boundary condition in the propagation problem. Determining this impedance such that it behaves like the real acoustic treatment installed in the engine ducts is a broad topic by itself. The aim of Section 3.2 is to present the most common liner designs used in industry and its modelling. The main original contribution of this chapter is Section 3.3, which contains the derivation and verification of two analytical impedance models to predict the equivalent impedance of acoustically treated circumferential grooves.

3.1 Impedance boundary conditions for acoustics

In the absence of flow, the acoustic impedance in a point of the boundary, i.e. the wall of the duct, is defined as the ratio of acoustic pressure and acoustic particle velocity normal

to the wall:

$$z(\omega) = \frac{\hat{p}(\omega)}{\hat{\boldsymbol{u}}(\omega) \cdot \boldsymbol{n}} \tag{3.1}$$

with complex pressure and particle velocity of the form $p = \hat{p}e^{j\omega t}$ and $u = \hat{u}e^{j\omega t}$ and where $\boldsymbol{n}$ is a unit vector normal to the wall and pointing *into* it.

This expression is valid under the assumption of locally reacting liner, also called point reacting liner, which considers that the response of the liner can be obtained at each point using the acoustic pressure and particle velocity at that point. This is achieved by preventing the propagation of sound within the treatment. In the case of non-locally reacting liners, the acoustic impedance at a point depends on the acoustic field in other points of the wall and the propagation inside the liner [60].

It is convenient to non-dimensionalise the acoustic impedance using the fluid characteristic impedance $\rho_0 c_0$, resulting in the specific acoustic impedance:

$$Z(\omega) = \frac{z(\omega)}{\rho_0 c_0} = R(\omega) + jX(\omega) \tag{3.2}$$

where R is the specific acoustic resistance and X the specific acoustic reactance, which in general are related to the liner dissipation and stiffness respectively. Their physical meaning is briefly outlined in the next section for cavity liners.

In the presence of flow, the boundary layer of the grazing flow will modify the acoustic field acting on the liner. The standard model for the impedance boundary condition in the presence of uniform mean flow over a flat lined surface was derived by Ingard [72] assuming (1) an infinitely thin boundary layer modelled by a vortex sheet that separates the mean flow and a vanishingly small region of zero flow within the boundary layer and (2) continuity of the normal displacement (ξ) and pressure across the vortex sheet. These assumptions are depicted in Figure 3.1.

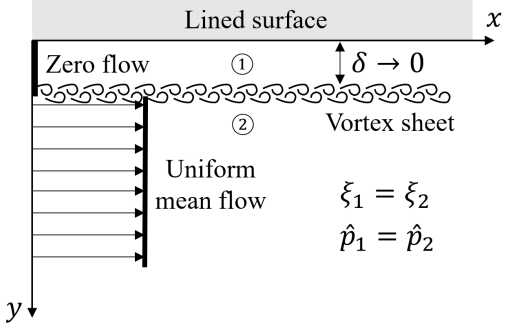

Figure 3.1: Assumptions in Ingard's impedance condition for a uniform mean flow slipping over a locally reacting acoustic liner.

Ingard's impedance condition at the wall is given by

$$\hat{\boldsymbol{u}} \cdot \boldsymbol{n} = \left(j\omega + \boldsymbol{u}_0 \cdot \boldsymbol{\nabla}\right) \frac{\hat{p}}{j\omega z} \tag{3.3}$$

which can be expressed in terms of pressure by using Euler's momentum equation

$$\rho_0 \left(j\omega + \boldsymbol{u}_0 \cdot \boldsymbol{\nabla}\right)^2 \hat{p} + j\omega z \frac{\partial \hat{p}}{\partial n} = 0 \tag{3.4}$$

or

$$\left(jk + \boldsymbol{M}_0 \cdot \boldsymbol{\nabla}\right)^2 \hat{p} + jkZ \frac{\partial \hat{p}}{\partial n} = 0 \tag{3.5}$$

Ingard's impedance model was generalised for a curved surface and non-uniform mean flow by Myers [73], giving

$$\hat{\boldsymbol{u}} \cdot \boldsymbol{n} = \left(j\omega + \boldsymbol{u}_0 \cdot \boldsymbol{\nabla} - \boldsymbol{n} \cdot \left(\boldsymbol{n} \cdot \boldsymbol{\nabla} \boldsymbol{u}_0\right)\right) \frac{\hat{p}}{j\omega z} \tag{3.6}$$

The vortex sheet used in Ingard and Myers boundary conditions can become unstable when grazing flow is present under certain impedance and Mach number conditions. Such instabilities were first identified by Tester [74] and later described analytically by Rienstra [75], who called them hydrodynamic surface waves, for high Helmholtz numbers (He) and azimuthal orders $m \ll He$ and later extended to arbitrary azimuthal orders by Brambley and Peak [76]. The existence of the instabilities was confirmed experimentally by Aurégan and Lereoux [77] and Marx et al. [78] and were explained by Brambley [79], concluding that the Myers boundary condition leads to an ill-posed problem in the time domain due to an unbounded maximum temporal growth rate. Discrepancies between experimental measurements and the predictions with the Ingard and Myers boundary condition suggest that it may be inadequate for impedance eduction techniques [80].

The ill-posed problem can be avoided while significantly improving the accuracy of the predictions by considering a finite boundary layer. Modified versions of the Myers conditions considering a thin but finite boundary layer have been proposed by Rienstra and Darau [81], Brambley [82] and Khamis and Brambley [83]. A review and benchmark of modified Myers conditions considering a finite boundary layer is given by Gabard [84], who assessed the accuracy of these conditions by comparison to a numerical solution of the Pridmore-Brown equation [85] governing the propagation of sound through the boundary layer. Recent developments in the impedance boundary conditions with shear flow include the viscous effects on the stability of the shear layer [86] and the effects of swirling flow [87].

The Ingard-Myers boundary condition has been used in this work in line with the objective of providing simple prediction methods for fan proximity liners and to enable the use of established eigenvalue solvers. This approach is taken with the awareness of the instabilities studied in the literature and choosing to ignore those solutions if they appear. Future improvements of the tools described in this thesis could include using published models for a thin finite boundary layer for fan case/OTR liners and the corrected boundary condition for swirling flow proposed by Masson et al. [87] for the modelling of OTR/interstage liners.

3.2 Locally reacting SDOF/DDOF cavity liners

The aim of this section is to present well-established models for Single-Degree-Of-Freedom (SDOF) and Double-Degree-Of-Freedom (DDOF) locally reacting cavity liners, widely used in the inlet and bypass areas of turbofan engines and hence a realistic estimate for fan proximity liners. Typical cavity liner designs are shown in Figure 3.2. Bulk absorbing non-locally reacting liners are not considered in this work. Extensive research [86, 88–96] has been carried out to model the effect of grazing flow in the impedance of locally reacting cavity liners, the non-linear losses in the facing sheet due to high-level excitation and multiple tone liner response. However, these effects are out of the scope of this research and a detailed review of the state-of-the-art impedance models to predict them is not presented here. The impedance models used throughout the thesis follow the formulation presented for SDOF/DDOF in this section and for acoustically treated grooves in the next. The prediction model for the acoustic performance of fan proximity liners proposed in this thesis could a priori accept any locally reacting impedance model as long as it allows for an analytical solution of the eigenvalue problem in the duct. Therefore, it could be readily used in conjunction with some of the semi-empirical impedance models proposed in the literature to include those effects of special relevance such as high-level excitation.

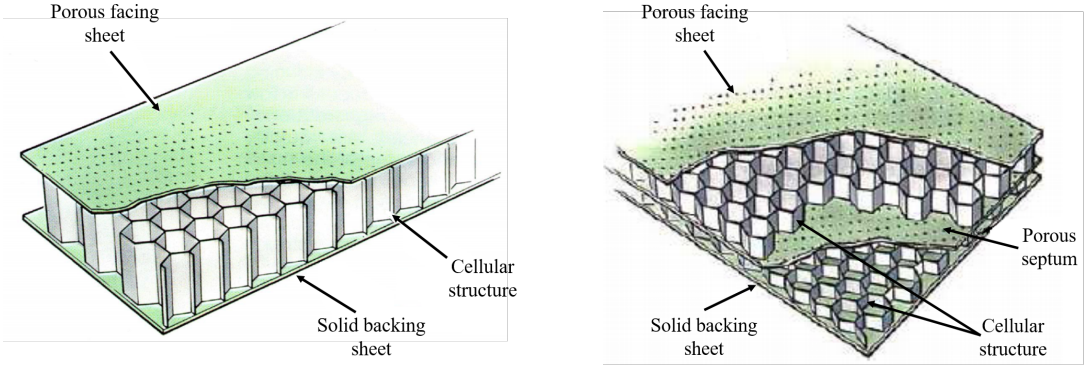

(a) SDOF (b) DDOF

Figure 3.2: Typical design of cavity liners, adapted from [4]

Single-Degree-of-Freedom Liners

SDOF cavity liners consist of a porous facing sheet, perforated with or without a wire mesh, over a cell structure, usually honeycomb, mounted on a solid fully reflective backing sheet, see Figure 3.2a. The acoustic behaviour of a single orifice over a cavity can be regarded as a Helmholtz resonator or a mass-spring damper, with damping due to the energy dissipation in the orifice, the mass being the air oscillating in the neck inside the orifice and the spring being the air in the cavity. Motsinger and Kraft [60] modelled the specific impedance of a SDOF liner as

$$Z = R + j\left(X_m + X_c\right) \quad , \tag{3.7}$$

where R is the facing sheet resistance, X_m the facing sheet mass reactance and X_c the cavity reactance. The facing sheet resistance can be obtained experimentally and accounts for the energy dissipation (acoustic energy converted into heat) in the orifices of the facing sheet due to friction (viscous dissipation) and vortices (at high sound amplitudes). The mass and cavity reactance are expressed as follows:

$$X_m = \frac{k(t + \epsilon d_h)}{\sigma} \quad , \tag{3.8}$$

where k is the wave number, t and d_h are the facing sheet thickness and hole diameter respectively, ϵ the non-dimensional end correction and σ the facing sheet porosity or Percentage Open Area (POA), and

$$X_c = -\cot(kh) \quad , \tag{3.9}$$

where k is again the wave number and h the cavity depth. This cavity reactance corresponds to a quarter wavelength resonator ($kh = \pi/2$). Therefore, the minimum tuning frequencies will be limited by the maximum depth of the cavity.

Approximate expressions to guess the resistance and to include the effect of grazing flow with Mach number (M) in the end correction are given in [60] as:

$$R = \frac{0.3M}{\sigma} \quad , \tag{3.10}$$

$$\epsilon = 0.85\frac{\left(1 - 0.7\sqrt{\sigma}\right)}{1 + 305M^3} \quad . \tag{3.11}$$

Double-Degree-of-Freedom Liners

The DDOF cavity liners consist of a porous facing sheet, again perforated with or without a wire mesh, over two layers of cell structure separated by a porous septum sheet

and mounted on a solid fully reflective backing sheet, see Figure 3.2b. Advantages with respect to the SDOF include (1) the resistance is dominated by the septum (reducing the effects of grazing flow) and (2) the impedance can be tuned for a wider range of frequencies. The impedance of a DDOF liner can be modelled as shown in Eq. 3.12 [97]. For liners with more than two panels, Rschevkin [97] derived an expression for a liner with n degrees of freedom.

$$Z = Z_{\text{fs}} + \frac{Z_{\text{sp}} \frac{\cos(kh_1)\sin(kh_2)}{\sin(kh)} - jcot(kh)}{1 + jZ_{\text{sp}} \frac{\sin(kh_1)\sin(kh_2)}{\sin(kh)}} \quad , \tag{3.12}$$

where Z_{fs} and Z_{sp} are the impedances of the facing sheet and septum respectively, h_1 and h_2 the depth of the upper and lower cells (assuming facing sheet at the bottom) and $h = h_1 + h_2$ is the total cavity depth. The impedance of the facing sheet and septum being of the form

$$Z_{\text{fs,sp}} = R_{\text{fs,sp}} + jX_{m_{\text{fs,sp}}} \quad . \tag{3.13}$$

3.3 Modelling of acoustically treated circumferential grooves

The analytical prediction models developed in this thesis are assessed against the experimental data from the OTR circumferential groove array tested in the NASA-GRC W-8 fan rig [5]. An analytical impedance model equivalent to the acoustically treated circumferential grooves used in the experiments is required as an input to our OTR prediction models.

The modelled OTR fan case configurations consist of circumferential grooves extending over an axial length equal to the axial projection of the fan chord. The grooves are formed of upper and lower parts, this arrangement is illustrated in Figure 3.3b where the lower and upper parts of the groove are labelled ① and ② respectively. The upper part ② is open at the top and terminated at the base with a 'septum'. Below the septum the lower part of the groove ① is partitioned azimuthally and can also be filled with acoustically absorbing material. This means that the upper portion of the groove in which the propagation is permitted in the azimuthal direction is bounded by a porous interface to the lower portion which is truly locally reacting due to the azimuthal partitions. The particular case of a hard 'septum' is also considered, in which part ② is terminated by a hard wall and therefore part ① is not modelled, as illustrated in Figure 3.3a. The case where the septum is acoustically hard can be considered as a particular case of the annular partitioned bulk-reacting liner model published by Rienstra [98], where the bulk properties match those of air, or as a limiting case of the spiralling non-locally reacting liner of Sijtsma et al. [99], when the spiral angle is set to zero.

This section details the formulation and underpinning assumptions of two analytical groove impedance models as semi-locally reacting liners and a verification against high-order FEM simulations performed with the commercial software Simcenter 3D Acoustics [100]. A number of numerical case studies are presented to demonstrate the acoustic response of the groove to incident duct modes. Single and multiple groove configurations are used for modal solutions in the airway and for the W-8 groove geometry excited by a point source. Numerical results for the pressure and radial particle velocity are evaluated at the interface between the groove/s and the main duct, and these are used to obtain an equivalent impedance which is directly comparable to that obtained from the analytical models.

3.3.1 Formulation of the analytical models for the groove liner impedance

The analytical impedance models presented here aim at characterising the acoustic behaviour of the OTR circumferential groove array tested in the NASA W-8 fan rig. In particular, two configurations are considered taken directly from the experimental datasets [5]. Both treatments consist of circumferential grooves that cover the axial projection of the fan chord, with the base of the upper portion of the grooves terminated by a hard or porous septum as indicated in Figure 3.3. A photograph of the actual treatment tested in the W-8 rig is shown in Figure 3.4a. Note that the lower partitioned portion of the groove is filled in this case with metal foam.

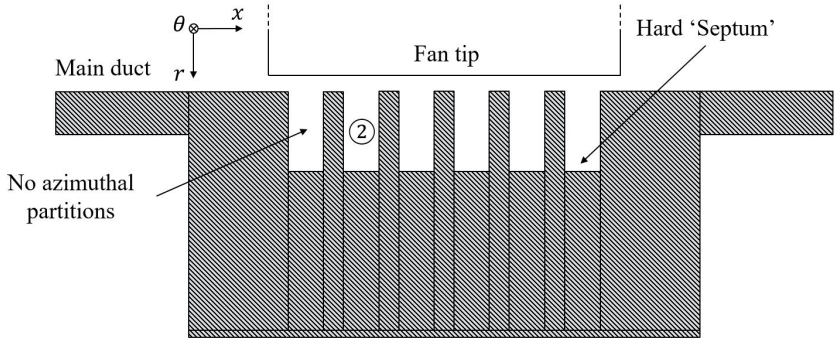

(a) Hard 'septum'

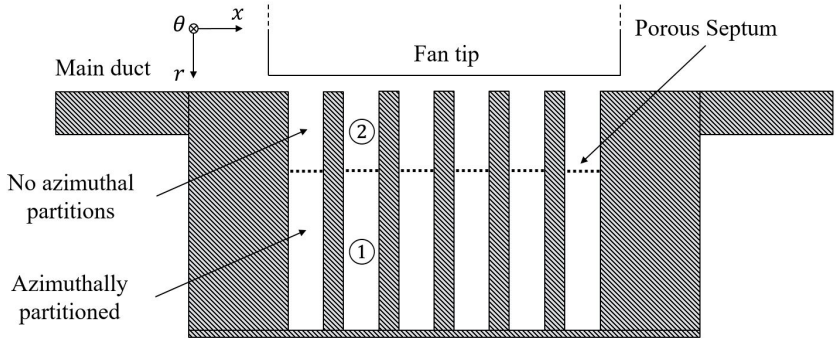

(b) Porous 'septum'

Figure 3.3: OTR circumferential groove array as tested in NASA W-8 fan rig.

A dimensional diagram of a single groove and the nomenclature used in the derivation of the equivalent acoustic impedance is shown in Figure 3.4b. Regions ① and ② refer to the portions of the groove below and above the septum, of depth $\tilde{h}$ and $\tilde{d}$ respectively. $\tilde{l}_g$ and $\tilde{l}_s$ denote the width of the groove and the (hard wall) separation between two consecutive grooves and $\tilde{a}$ is the radial distance of the liner surface from the duct axis. In all that follows distances will be non-dimensionalised with respect to a reference length $\tilde{l}_{ref} = \tilde{a}$ giving non-dimensional quantities: $d = \tilde{d}/\tilde{l}_{ref}$, $h = \tilde{h}/\tilde{l}_{ref}$, etc. Note that the non-dimensional radius of the duct is consequently equal to unity. The frequency, pressure and particle velocity are also non-dimensionalised by using reference values: $\omega = \tilde{\omega}\tilde{l}_{ref}/\tilde{c}_0$, $p = \tilde{p}/(\tilde{\rho}_0\tilde{c}_0^2)$ and $u = \tilde{u}/\tilde{c}_0$ ($\tilde{\rho}_0$ and $\tilde{c}_0$ are the density and speed of sound in the airway). Note that the $e^{j\omega t}$-convention is used here.

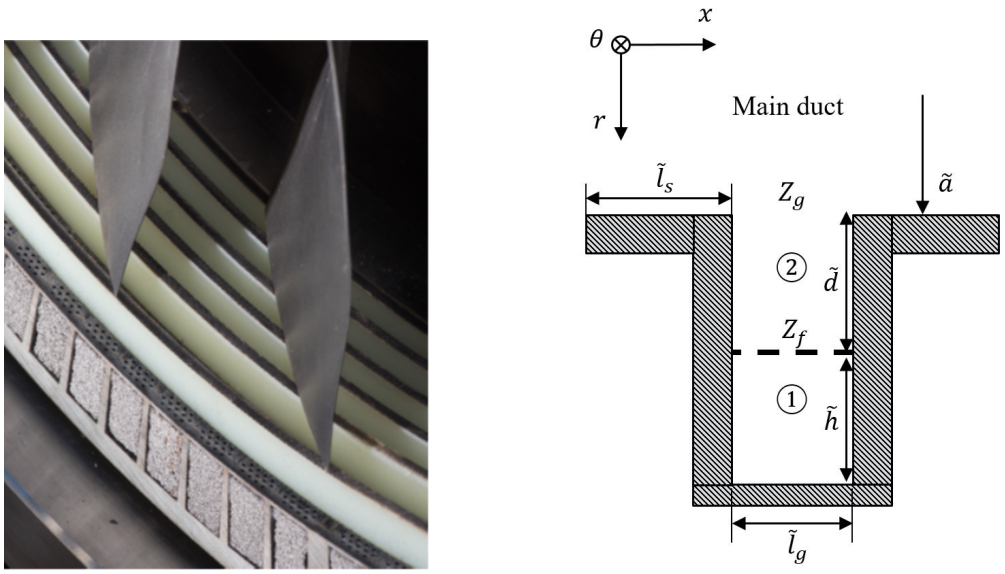

(a) (b)

Figure 3.4: OTR fan case liner: (a) View of the OTR fan case liner installed in the NASA W-8 fan rig [5] and (b) dimensional diagram of the problem and nomenclature.

Two models will be presented; an exact 'annular' model and an approximate 'Cartesian' model. The groove area of the treatment is annular, but if the groove depth is small in comparison to the radius, it can be 'unwrapped' and approximated by a rectangular channel, as indicated in Figure 3.5. Clearly the 'annular' representation is more accurate than the 'Cartesian' approximation but both will be shown to give very similar results for the frequencies and test geometry studied here. In both cases the mean axial flow in the groove, and the mean azimuthal flow in the groove induced by the rotation of the fan blades, is currently neglected.

Annular groove model

The pressure field in the upper portion (region ②) of the annular groove can be expressed as a separable solution of the Helmholtz equation in cylindrical coordinates:

$$p(x,r,\theta) = \sum_{m=-\infty}^{\infty} e^{-jm\theta} \sum_{n=0}^{\infty} f_n(x) g_{mn}(r) \quad , \tag{3.14}$$

where

$$f_n(x) = \cos(\kappa_n x) \quad , \quad \kappa_n = \frac{n\pi}{l_g} \tag{3.15}$$

$$g_{mn}(r) = A_{mn} J_m(\alpha_n r) + B_{mn} Y_m(\alpha_n r) \tag{3.16}$$

and

$$\alpha_n = \pm\sqrt{\omega^2 - \kappa_n^2} \quad . \tag{3.17}$$

Here, A_{mn} and B_{mn} are arbitrary constants to be determined by boundary conditions at the septum. If it is assumed also that all higher-order modes are cut-off in the groove, which is true in the test geometry for all frequencies of interest (below 30 kHz), contributions to expression 3.14 for $n \neq 0$ can be neglected. Expression 3.14 then reduces to

$$p(x,r,\theta) = \sum_{m=-\infty}^{\infty} e^{-jm\theta} \left[A_{m0} J_m(\omega r) + B_{m0} Y_m(\omega r) \right] \quad . \tag{3.18}$$

The boundary condition at the septum is:

$$\frac{p|_{r=1+d}}{u_r|_{r=1+d}} = Z_f \quad , \tag{3.19}$$

where Z_f is the locally reacting impedance of the septum and azimuthally partitioned cavity ①.

The radial particle velocity can be obtained by using the non-dimensional linearised momentum equation in the radial direction:

$$u_{r_n}(r) = \frac{j}{\omega}\frac{\partial p}{\partial r} = j \sum_{m=-\infty}^{\infty} e^{-jm\theta} \left[A_{m0} J'_m(\omega r) + B_{m0} Y'_m(\omega r) \right] \quad . \tag{3.20}$$

By substituting Eq. 3.18 and Eq. 3.20 into Eq. 3.19 and rearranging the summations over m yields, for each azimuthal mode number,

$$K_m = \frac{B_{m0}}{A_{m0}} = -\frac{J'_m(\omega[1+d]) + j\frac{J_m(\omega[1+d])}{Z_f}}{Y'_m(\omega[1+d]) + j\frac{Y_m(\omega[1+d])}{Z_f}} \quad . \tag{3.21}$$

Finally, the total effective impedance of a component of the acoustic field varying as $e^{-jm\theta}$ at the interface between the groove and the airway is given by

$$Z_g(\omega, m) = \frac{p|_{r=1}}{u_r|_{r=1}} = -j\frac{J_m(\omega) + K_m Y_m(\omega)}{J'_m(\omega) + K_m Y'_m(\omega)} \quad . \tag{3.22}$$

The dependence of this quantity on 'm', the azimuthal mode number, demonstrates that this 'impedance' is not locally reacting in the sense that each azimuthal fourier component of the sound field in the airway experiences a different impedance. It is also worth noting that for the case of a hard septum ($Z_f \to \infty$), K_m is real and the impedance Z_g is purely reactive, as would be expected in the absence of any absorbing elements.

Cartesian groove model

An approximate expression can be obtained by assuming that the groove depth is sufficiently small ($d \ll 1$) such that the annular casing can be approximated by a rectangular channel as indicated in Figure 3.5. The pressure field in the upper portion of the groove repeats itself over a distance $z = 2\pi a (= 2\pi)$ and may be written as a separable solution in Cartesian coordinates as

$$p(x, y, z) = \sum_{m=-\infty}^{\infty} e^{-jk_z z} \sum_{n=0}^{\infty} \cos(k_n x) \left[A_{mn} \cos(\beta_{mn} y) + B_{mn} \sin(\beta_{mn} y)\right] \quad , \tag{3.23}$$

where

$$k_z = m, \quad k_n = \frac{n\pi}{l_g} \quad \text{and} \quad \beta_{mn} = \pm\sqrt{\omega^2 - k_n^2 - k_z^2} \quad . \tag{3.24}$$

Once again, only terms corresponding to $n = 0$ need to be considered giving

$$p(x, y, z) = \sum_{m=-\infty}^{\infty} e^{-jmz} \left[A_{m0} \cos(\beta_m y) + B_{m0} \sin(\beta_m y)\right] \quad . \tag{3.25}$$

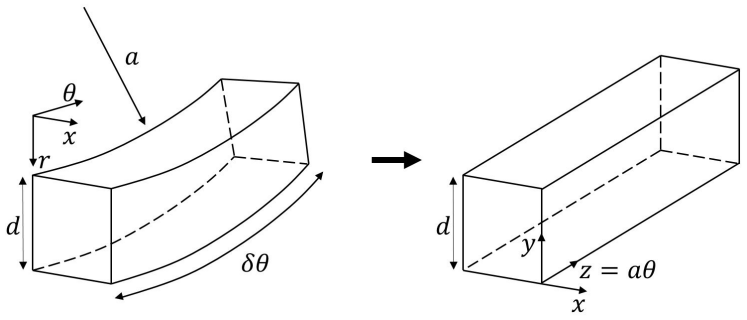

Figure 3.5: Approximation of the annular grooves into a rectangular section when $d \ll 1$.

Following an analogous procedure to that for the annular groove, the expression for the effective impedance of the treatment (Eq. 3.26) can be obtained by applying the boundary condition at the bottom of the groove ($y = 0$) and evaluating the pressure and particle velocity at the interface with the main duct ($y = d$). Note that the y-axis is defined in the opposite direction to the radius. This yields

$$Z_g(\omega, m) = -\frac{j\omega}{\beta_m}\left[\frac{\cot(\beta_m d) + \frac{j\omega}{Z_f \beta_m}}{1 - \frac{j\omega}{Z_f \beta_m}\cot(\beta_m d)}\right] \quad . \tag{3.26}$$

Once again, the configuration with hard septum can be modelled by setting $Z_f \to \infty$ in Eq. 3.26. As observed in expression 3.22, the acoustic impedance Z_g is not only a function of frequency but also of the azimuthal mode number m.

Comparison of groove models

To assess the accuracy of the approximation of the annular grooves by a rectangular channel, Figure 3.6 shows a comparison of the impedance obtained with each model for a range of frequencies corresponding to the experimental data ($0 \leq \omega \leq 50$) and for the liner parameters shown in Table 3.1. In the case of the W-8 rig the duct radius is $\tilde{a} = 279.4$ mm, giving a non-dimensional groove depth of 0.045. The impedance at the septum (Z_f) is obtained by using the standard non-dimensional expression for a SDOF cavity liner [60].

$$Z_f = R_{fs} + j\left[\omega m_r - \cot(\omega h)\right] \quad , \tag{3.27}$$

where R_{fs} and m_r denote the non-dimensional resistance and mass reactance of the septum and $\cot(\omega h)$ is the reactance of the cavity.

Table 3.1: Numerical values used for the impedance parameters.

R_{fs}	$\tilde{m}_r$	$\tilde{h}$	$\tilde{d}$
0.5	2.39 cm	2.54 cm	1.27 cm

Results are shown in Figure 3.6 for the cases of a hard and porous septum for $m = 22$. The agreement shown between the annular and Cartesian predictions is consistent with the results obtained at lower and higher azimuthal mode numbers. The two impedance models show good agreement for the whole range of frequencies used in this study. However, the annular model is used for the analytical predictions presented in the rest of the section.

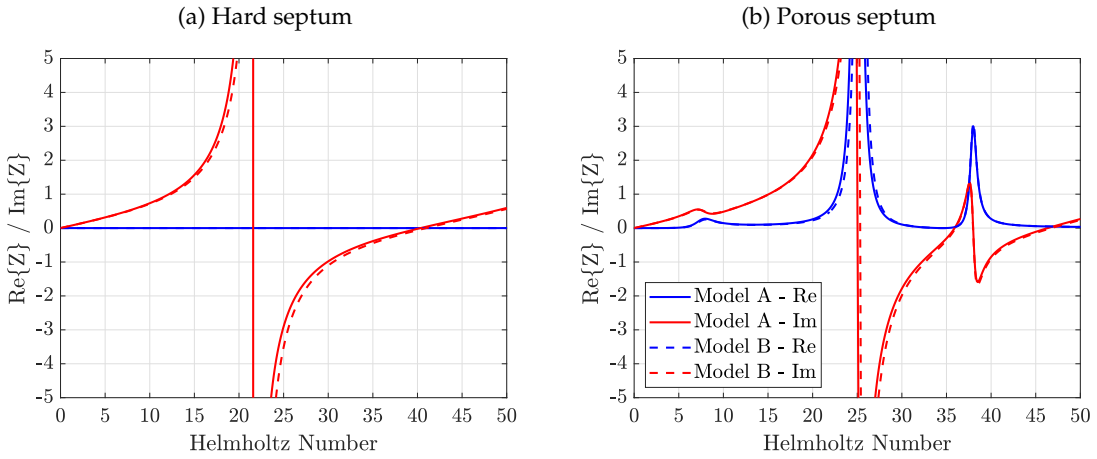

Figure 3.6: Comparison of the impedance models based on the annular (Model A) and Cartesian groove (Model B) for $m = 22$.

Qualitative behaviour of the equivalent groove impedance

As indicated previously, the equivalent impedance for the case of a groove with a hard septum is obtained by setting $Z_f \to \infty$ in Eq.3.26, yielding

$$Z_g = -\frac{j\omega}{\beta_m}\cot(\beta_m d) \quad . \tag{3.28}$$

The following implications about the groove behaviour can be immediately drawn

- The liner presents a purely reactive response.
- If $m = \omega$, $Z_g = \pm j\infty$ (hard wall).
- If $m = 0$, $Z_g = -j\cot(\omega d)$ (simple reactance behaviour).
- If $m < \omega$ and $\omega = \sqrt{m^2 + \left(\frac{\pi}{2d}\right)^2}$, $Z_g = 0$ (pressure-release surface).

The behaviour with the porous septum is not as straightforward as in the hard septum case. The resistance, reactance and the normal incidence absorption coefficient of the groove with porous septum are shown in Figure 3.7 for a range of frequencies $0 \leq \omega \leq 50$, azimuthal mode numbers $0 \leq m \leq 50$ and for the impedance parameters in Table 3.1. The normal incidence absorption coefficient of the impedance at the septum is also shown in Figure 3.7 as reference. The resistance of the lined groove, provided by septum, is no longer constant and depends on the frequency and azimuthal mode number. Both the resistance and the reactance show peaks around $m = \omega$ of a finite magnitude ($Z_g \approx 20$) influenced by the impedance at the septum and the azimuthal propagation within the groove. However, the absorption coefficient of the groove is not substantially modified with respect to a SDOF cavity, the maximum attenuation in both cases occurs for $Im(Z) =$

0, that is at $\omega = 10$ and $\omega = 38$ in this example. The low-frequency limit shows that the impedance tends to $-\infty$ for the plane wave and to zero otherwise for both hard and porous septum.

The radial propagation within the groove depends on the frequency and azimuthal mode number. The line $m = \omega$ separates two regions in the colormaps of Figure 3.7 that determine the propagation in the radial or y-direction that also apply to the hard grooves. If $m < \omega$, k_y is real and waves are propagative in the radial direction (cut-on); if $m > \omega$, k_y is imaginary and waves are exponentially decaying in the radial direction (cut-off).

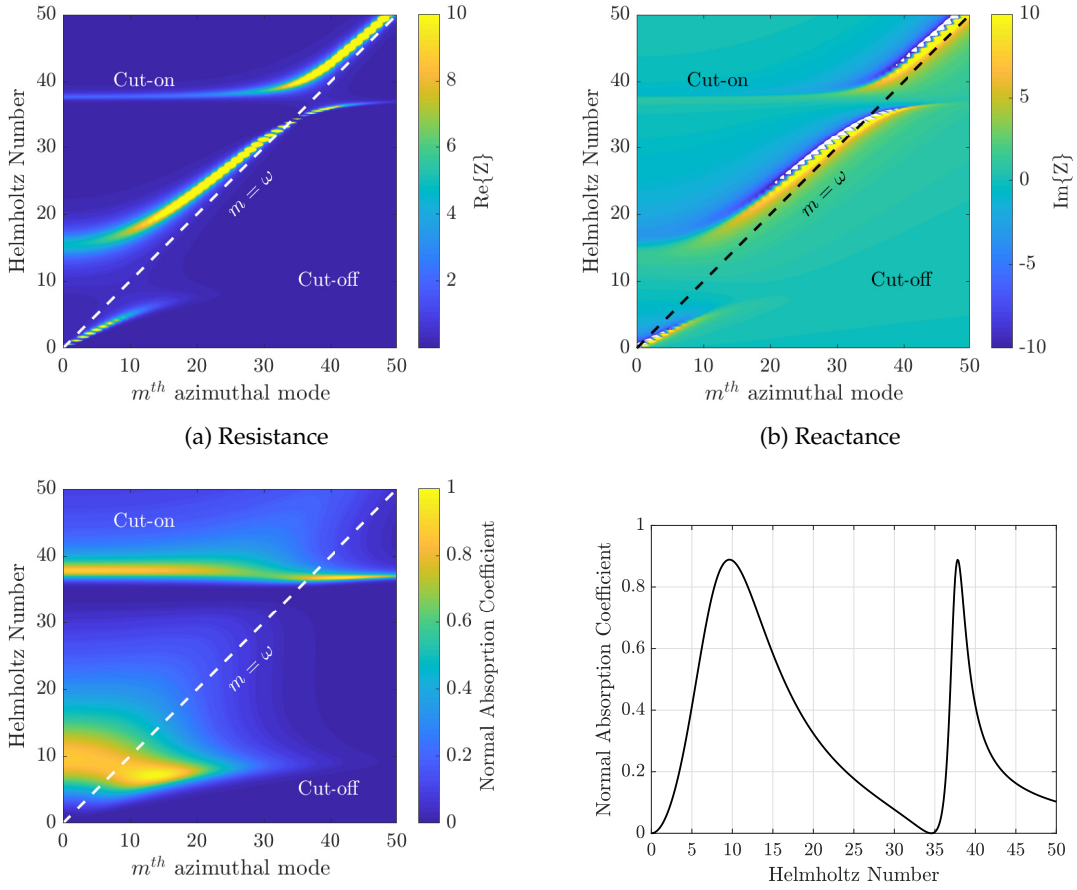

(a) Resistance

(b) Reactance

(c) Absorption coefficient - groove

(d) Absorption coefficient at septum

Figure 3.7: Groove impedance and normal incidence absorption coefficient for a range of frequencies $0 \leq \omega \leq 50$ and azimuthal mode numbers $0 \leq m \leq 50$.

3.3.2 High fidelity FEM simulations

A number of FEM computations have been conducted to cross-verify with the analytical models in terms of predicting the equivalent impedance of the circumferential grooves both for hard and absorbing septums. The numerical simulations have been performed

using the FEM commercial software Simcenter 3D Acoustics [100]. A high-order FEM formulation is used within Simcenter, which uses adaptive polynomial order (p-refinement) in each element based on an *a priori* error indicator. The solver selects automatically the polynomial order in each element to obtain a target accuracy while minimizing the computational cost. This approach, described in Beriot et al. [101], is designed to tackle realistic large-scale 3D problems over a large number of frequencies and only requires a single mesh.

The mesh creation process used in this instance follows the guidelines given in [101]. The mesh element size is selected as large as possible, constrained by the highest frequency of interest and the maximum polynomial order available. A target accuracy of 0.5% has been used. It should be noted that smaller elements are still required to ensure that the geometry at the boundaries is well represented and in regions where singularities are present.

Three test cases have been performed, as shown in Figure 3.8:

(a) **Single groove with incident modes**: the aim is to obtain the acoustic impedance within the open groove and at the interface with the main duct when excited by incoming duct modes of azimuthal and radial mode orders (m, n).

(b) **Multiple grooves with incident modes**: extension of the first case to six grooves, as used in the W-8 rig, to assess the variations on the impedance of each groove due to the interaction with adjacent grooves.

(c) **Multiple grooves with a monopole source**: consists of the full groove geometry and a monopole point source located at 95% of the radius. The aim is to assess the suitability of the analytic groove impedance model as an input wall impedance for OTR analytical prediction models described in [102].

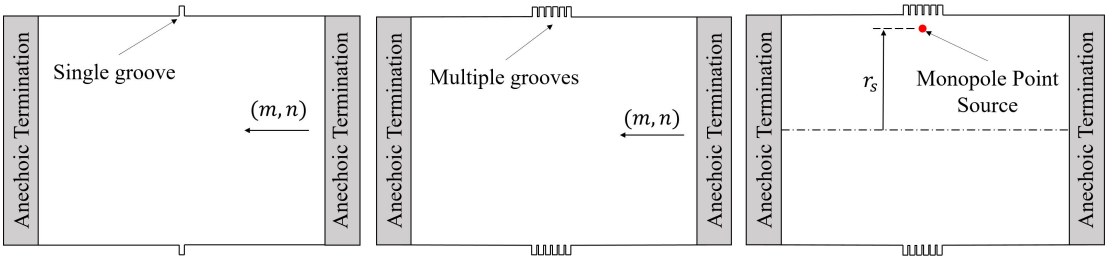

(a) Single groove with incident modes (b) Multiple grooves with incident modes (c) Application to OTR liners

Figure 3.8: Diagrams of the FEM cases used for the verification of the analytical groove models.

All cases have been defined as 3D finite ducts, numerically modelled by using a PML-type anechoic boundary condition at each end of the duct section [100]. The geometry of each circumferential groove is consistent with the dimensions of the grooves tested in the NASA W-8 fan rig. A hard septum and a SDOF locally reacting cavity impedance are imposed at the bottom of the open groove/s for the 'hard' and 'lined' groove configurations respectively.

A convergence study has been carried out for the single and multiple groove cases focusing on the refinement of the mesh close to the groove neck, of special interest to evaluate the equivalent impedance of the groove, and around the point source location. The cross-section of the mesh used for case (c) and a zoom around the groove region are shown in Figure 3.9.

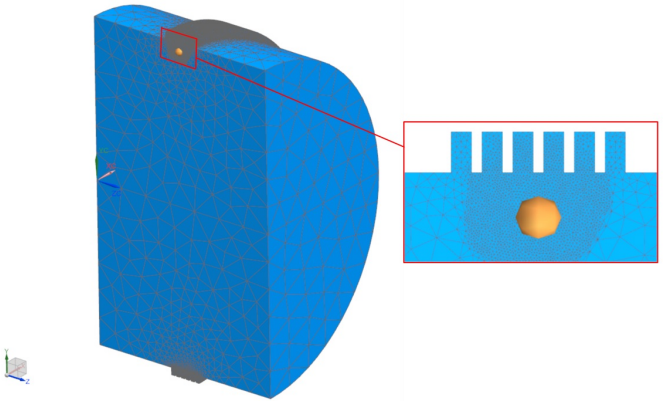

Figure 3.9: Cross-section of the mesh used for case (c) and a zoom around the groove region.

3.3.3 Cross-verification of the analytical model with FEM results

Single groove with incident duct modes

In both of the analytical impedance models an assumption is made that the acoustic field is uniform across the width of the groove, i.e. that only the plane wave can propagate within the groove in the radial direction. However, it is expected that evanescent 'cut-off' components may contribute to the acoustic field at the open end of the groove where it matches to the external acoustic field in the airway. The standard deviation in acoustic pressure across the groove at a particular normalised depth, $(r-a)/a$, measured from the open end, is defined as

$$s(p) = \frac{\sqrt{\frac{1}{N}\sum_{i=1}^{N}|p_i - \overline{p}|^2}}{|\overline{p}|} \quad , \tag{3.29}$$

where N is the number of nodes across the groove, p_i is the nodal value, and the mean value ($\overline{p}$) is given by

$$\overline{p} = \frac{1}{N}\sum_{i=1}^{N} p_i \quad . \tag{3.30}$$

The standard deviation across the groove of the pressure and radial particle velocity magnitudes in the FEM solution are shown in Figure 3.10 to assess the validity of the above assumption. The plots only show the results for the lined groove but the same behaviour has been observed for the hard groove. It can be observed that, as expected, the standard deviation is higher at the groove 'neck' (groove depth = 0), specially for the radial particle velocity: $s(p) \approx 10\%$ and $s(u_r) \approx 100\%$, and is monotonically reduced when moving to the groove bottom (groove depth = 1): $s(p)(\%) \approx \mathcal{O}(10^{-2})$ and $s(u_r)(\%) \approx \mathcal{O}(10^{-2})$.

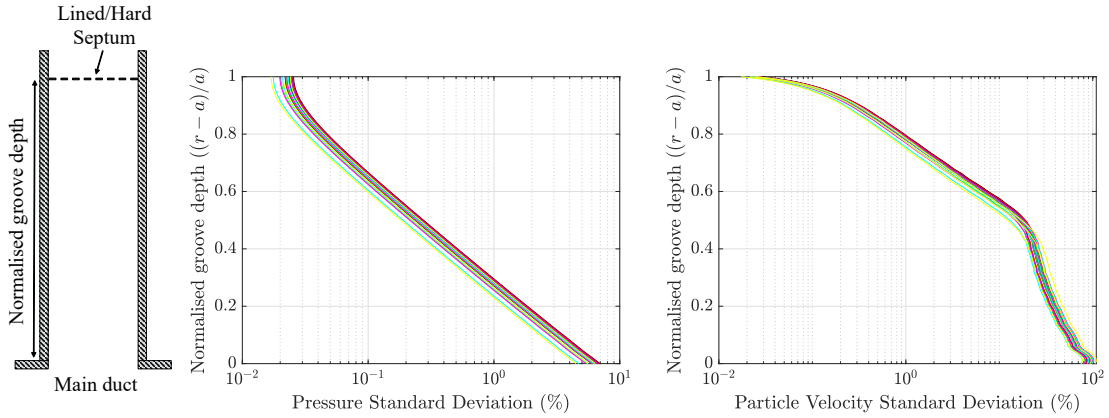

Figure 3.10: Axial standard deviation (in %) of the pressure and radial particle velocity within the lined groove for different incident modes (m=1-18) at 3900 Hz. Each colour represents a different azimuthal mode number and results are shown for the first three radial modes.

These results indicate that standard deviation in pressure and particle velocity is small across the groove and that an average value can therefore be compared to the analytical predictions. The equation of the groove effective impedance derived from the semi-locally reacting analytical model is based on a continuous solution of the wave equation throughout the groove and therefore the radial impedance at any point *within* the groove can be computed by evaluating the pressure and radial particle velocity at any radius, giving

$$Z_g(\omega, m, r) = -j\frac{J_m(\omega r) + K_m Y_m(\omega r)}{J'_m(\omega r) + K_m Y'_m(\omega r)} \quad . \tag{3.31}$$

A comparison of the analytical and numerical effective impedance is shown in Figure 3.11 for a hard and lined duct, limited to modes (5,1), (15,1) and (20,1). In the hard groove case, the resistance is zero and the reactance results are in good agreement, tending to minus infinity when moving towards the hard wall boundary condition. In the lined groove case, both the resistance and the reactance satisfy the imposed boundary condition at the septum and generally present a satisfactory agreement.

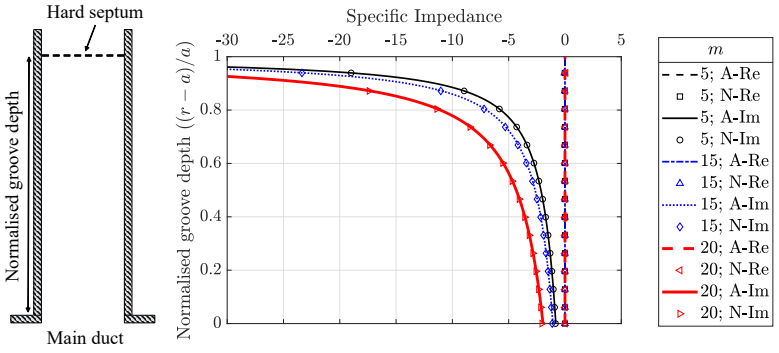

(a) Hard groove

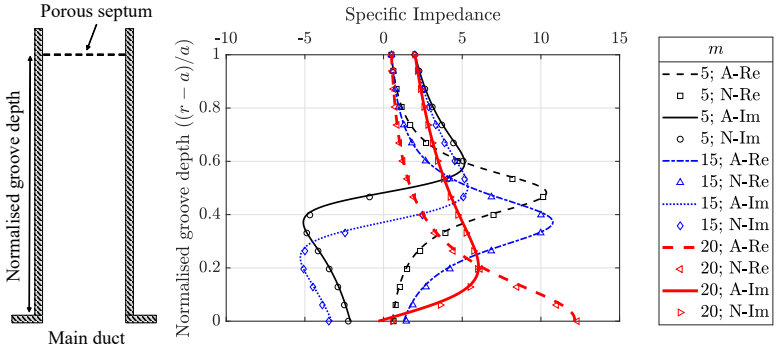

(b) Lined groove

Figure 3.11: Radial impedance within the groove for different incident azimuthal modes: comparison of analytical annular model and numerical results at 3900 Hz. In the legend, A refers to Analytical and N to Numerical.

It is reassuring that the agreement between the analytical models and the FEM results is close within the groove. However, a good match of the equivalent impedance at the interface between the main duct and the groove, i.e. at normalised groove depth of zero, for the whole range of frequencies of interest and azimuthal mode numbers is the main objective. This comparison is shown in Figure 3.12 for the lined groove and modes (5,1), (15,1) and (20,1). The numerical results are plotted for each mode only for the cut-on frequencies. Very good agreement can be observed, which has been shown to hold for other azimuthal mode numbers and for the hard groove case.

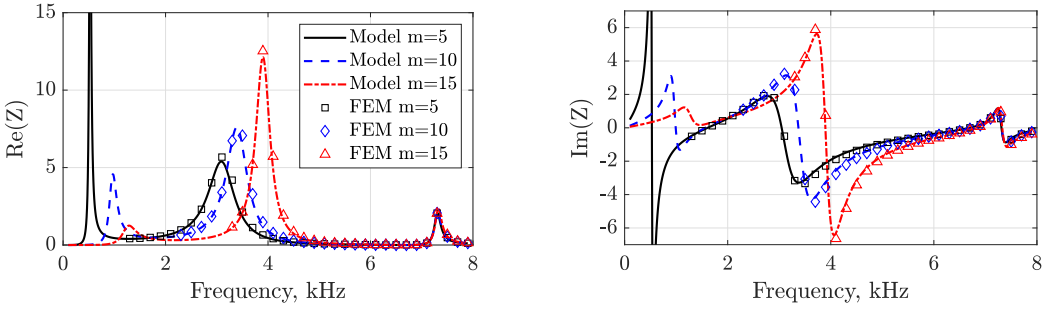

(a) Resistance (b) Reactance

Figure 3.12: Frequency dependence of the effective groove impedance: comparison of analytical model and numerical results for the lined groove case.

This cross-verification of the FEM and analytical model for the single groove means that the latter can be used with confidence to predict the impedance boundary condition for the uniform-duct propagation models used in later chapters.

Multiple grooves with incident duct modes

The analytical impedance models are derived for a single groove but, in practice, multiple grooves are usually present, as in the fan casing tested in the W-8 rig. The extent to which the effective impedance of each groove is affected by the presence of adjacent grooves is now investigated using model (b) of Figure 3.8. Following a procedure analogous to that for the single groove, the numerical effective acoustic impedance $Z_{\text{num}}(\omega, m, n, r)$ is evaluated at each of the six grooves considered in the geometry of Figure 3.8b.

A comparison of the impedance predicted by the analytical single groove model with the numerical effective acoustic impedance obtained for the 6 grooves FEM model is shown Figure 3.13. The numerical values of the resistance/reactance at the interface of each of the six grooves are shown with the same symbol. It can be observed that the numerical impedance of each groove tends to cluster around the 'single groove' prediction with fairly small variations except at the peaks, where the impedance of the grooves is similar to that of a hard wall. In terms of relative error with respect to the single groove prediction, the results in Figure 3.13 range from 1% to 15%. This indicates that reasonable acoustic predictions can be expected if a multiple groove case is treated by assuming the effective impedance of a single groove applied to an extended duct length equivalent to that of the multiple groove liner.

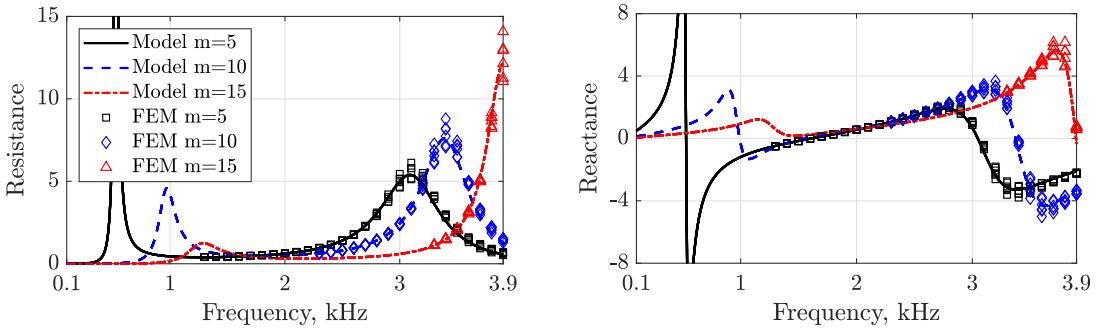

(a) Resistance

(b) Reactance

Figure 3.13: Frequency dependence of the effective groove impedance for multiple grooves: comparison of analytical model and numerical results for each groove for the lined groove case.

Application to OTR liners: multiple grooves excited by a point source

The ultimate aim of the groove impedance models is their application in predicting OTR liner fan noise suppression performance so that the analytical and numerical prediction models can be compared directly to the NASA W-8 rig experimental data. The description of the OTR analytical prediction model for propagation in the fan duct and a comparison with the experimental data is covered in Chapter 6. The model relies on a Green function approach for a point source close to the liner surface. This study is a check of the validity of representing the grooved liner in the Green's function model by an equivalent local impedance at the groove/airway interface derived from the theoretical impedance model described in section 3.3.1. This is done by comparing the Green's function solution for a source close to the liner to a full FE prediction for the same problem in which the grooves are explicitly modelled. The comparison also quantifies the effect on axial sound power reduction of applying the single groove impedance when multiple grooves are present in the geometry.

The OTR analytical model, called Green/FINF, represents a cylindrical finite lined section connected to infinite hard wall duct extensions. The acoustic field is excited by a monopole or dipole point source located close to the lined surface. This is a simplification of a more realistic configuration where an OTR liner (modelled by the lined section) is used to suppress fan sources (modelled with equivalent point sources above the liner). The simplified problem is shown in Fig.3.14. The acoustic field is calculated in Green/FINF by imposing continuity of mass and momentum at the two interfaces, I-II and II-III, and has been cross-verified for a constant impedance in the lined section against FEM simulations for zero and uniform mean flow (thus verification is described in Chapter 5). The numerical FEM model in the current study is that shown Figure 3.8c. This represents the full geometrical character of the six grooves and their hard or lined septums. A monopole source is used both in the analytical estimates and in the FEM solution. It is located at the middle of the lined section and at 95% of the duct radius: $(x_s, r_s, \theta_s) = (0.5l_L, 0.95a, 0)$.

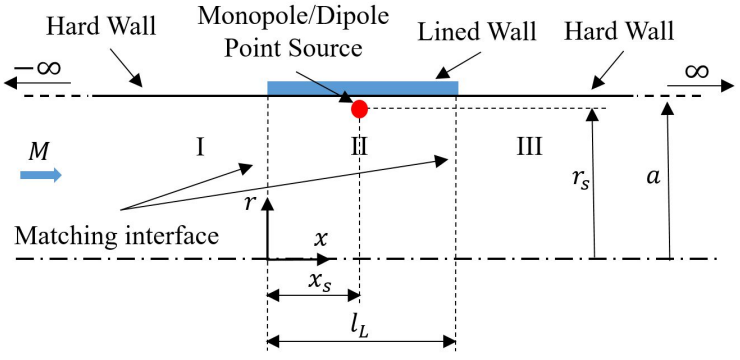

Figure 3.14: Diagram of the OTR analytical prediction model.

The lined circumferential grooves are defined in the Green/FINF model by a corrected impedance obtained from the analytical groove models and taking account of the length of the treatment (l_L). Two alternatives have been explored and compared to the FEM results. These are:

(a) The impedance of a single groove is used over a shortened liner length equal to the groove open area or groove-duct interface. This approach does not account for the effect of the hard walls between grooves. i.e. define

$$Z_{\text{eff}} = Z_g, \quad l_L = 6l_g \quad . \tag{3.32}$$

(b) A corrected impedance is used based on the continuity of mass in the radial direction to account for the rigid surfaces between the groove cavities. i.e. the length of the liner is defined as the total length of the acoustic treatment and a porosity correction is used with $\sigma = l_t/l_g$, which in this case is $\sigma = 3/2$. i.e. define

$$Z_{\text{eff}} = \sigma Z_g, \quad l_L = l_t = 6(l_g + l_s) \quad . \tag{3.33}$$

The computation of the non-dimensional acoustic axial power and the definition adopted for the PWL IL is as described in Section 4.5. The PWL IL obtained with the analytical prediction model and the two alternatives described above are compared to the FEM results in Figure 3.15. Although both methods of estimating the impedance generally show a close agreement, the use of a corrected impedance applied to the total length of the acoustic treatment (alternative (b)) is marginally closer to the FEM solution, especially in the region of higher attenuation (1-2.5 kHz). The differences between the analytical prediction (b) and the FEM solution are less than 0.2 dB for the whole frequency range. The alternative impedance prediction (a) without the porosity correction over-predicts the IL of the acoustic treatment by up to 1 dB relative to the FEM solution. This result was expected since the porosity assumption is a better representation of the physical problem and has been widely used in liner modelling [60].

A key factor of the existence of grazing flow over the grooves is the excitation of cavity resonances. Additional groove or cavity noise in the presence of the OTR grooves treatment was measured at certain frequency ranges in the tests conducted in the W-8 rig [5]. Testing of the same OTR casing treatments in the NASA Grazing Flow Impedance Tube showed the generation of cavity noise at the same frequency range than when installed over a turbofan rotor [37]. The lengthwise tones caused by the feedback loop of the unstable shear layer over the cavity [103] cannot be predicted in the analytical groove impedance model nor the FEM solver due to the inviscid nature of the Helmholtz equation and it is outside the scope of this work.

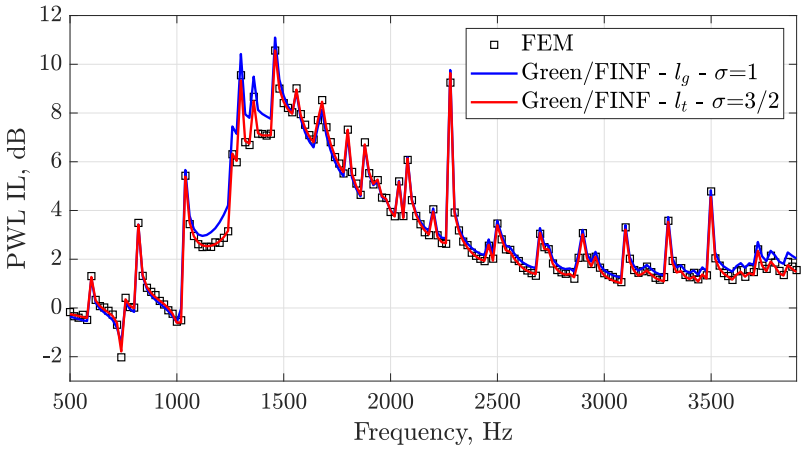

Figure 3.15: Comparison of PWL Insertion Loss analytical predictions against the FEM results for a monopole point source.

3.3.4 Inclusion of mean swirling flow in the groove impedance model

Swirling flow characterised by a non-zero azimuthal component of the base flow is usually negligible in the intake but is significant in the fan and interstage sections induced by the rotation of the fan blades. Numerical simulations indicate that a transition from a purely axial base flow upstream of the fan to an axial and swirling base flow downstream of the fan occurs along the blade passage. Therefore, a natural extension of the work presented in this thesis could include the Green's function for swirling flow [36] in the fan section and a mode-matching between the duct sections with different swirling flow characteristics.

It can be argued that the rotation of the fan blades could also induce a steady mean flow within the grooves in the azimuthal direction. In fact, different modal wall SPL Insertion Loss (IL) for the positive and negative spinning modes has been measured in tests conducted in the W-8 rig [5]. The experimental data was acquired with an azimuthal array installed at the duct wall 2.2 radii upstream of the fan stacking axis as described in [5]. Fig. 3.16a-3.16b show the measured SPL for the hard wall datum and the acoustically treated grooves. Fig. 3.16c shows the modal IL obtained by subtracting the SPL in Fig. 3.16b from that in Fig. 3.16a. All contours are plotted against frequency and azimuthal (or spinning) mode number. The measurements indicate that the plane wave is dominant at low frequencies and that the modes co-rotating with the fan ($m > 0$) are dominant for the rest of the frequency range, as previously reported in [5]. The first two BPFs (at 2.32 kHz and 4.64 kHz) can also be observed, possibly suggesting strong flow distortion. It can be observed from the slightly asymmetric contours of SPL IL (Fig. 3.16c) that the noise reduction is higher for the co-rotating modes.

Possible mechanisms to explain the bias towards co-rotating modes are (1) the 'direct' effect of mean flow swirl in the duct on the modes attenuation and, (2) the 'indirect' effect of swirl in modifying the effective impedance due to induced swirl in the grooves. Since swirl in the airway has not been implemented in this thesis the effect of (1) cannot be analysed. However, mechanism (2) is explored here by assuming that the positive and negative azimuthal Fourier components of the sound field in the airway experience different effective impedances. The difference originates from the fact that the azimuthal propagation in groove occurs in the same or opposite direction to that of the induced mean swirling flow.

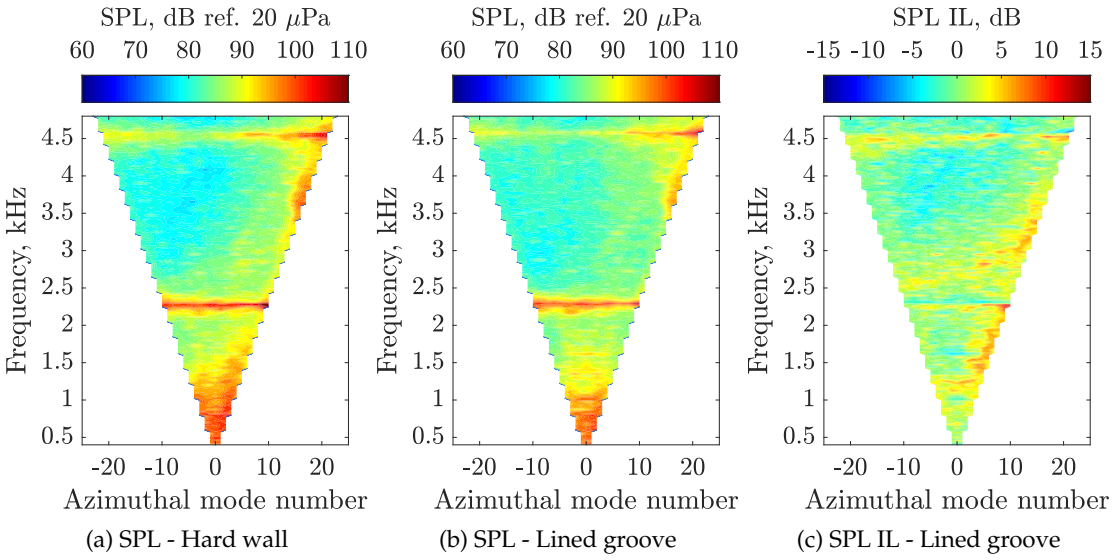

(a) SPL - Hard wall (b) SPL - Lined groove (c) SPL IL - Lined groove

Figure 3.16: Measured SPL and SPL IL spectrum as a function of azimuthal mode order at 50% fan speed, based on measured time history data supplied by R. Bozak (NASA GRC).

The Cartesian groove model assumes that the groove depth is sufficiently small ($d \ll 1$) such that the annular casing can be approximated by a rectangular channel, as indicated in Figure 3.5. Uniform axial flow in the airway is considered with $\boldsymbol{M} = (M_x, 0, 0)$. It is also assumed here that the swirl Mach number, $M_\theta(r) = \frac{U_\theta(r)}{c_0}$, is constant within the groove and equal to the azimuthal component of the tip Mach number $M_\theta(r = 1) = M_{\text{tip}}$. A diagram of the Cartesian groove model with the inclusion of 'swirling' flow and the assumed shear layers is shown in Fig. 3.17. The base flow conditions in the groove and the airway have been divided into regions to clarify the formulation that follows and are summarised in Table 3.2. Region ① is in the groove, immediately above the cavity liner and below the vortex sheet caused by the azimuthal flow. Region ② is where the azimuthal propagation within the groove occurs and is connected to the airway (region ④) through a 'double' shear layer: ② to ③ and ③ to ④. The effective impedance of the groove Z_g is derived at region ③ since the shear layer from ③ to ④ is already modelled in the formulation of the Green's function of a lined duct with uniform axial mean flow presented in Chapter 4.

Table 3.2: Base flow conditions in each region of the groove model.

Region	Axial mean flow	Azimuthal mean flow
①	0	0
②	0	M_{tip}
③	0	0
④	M_x	0

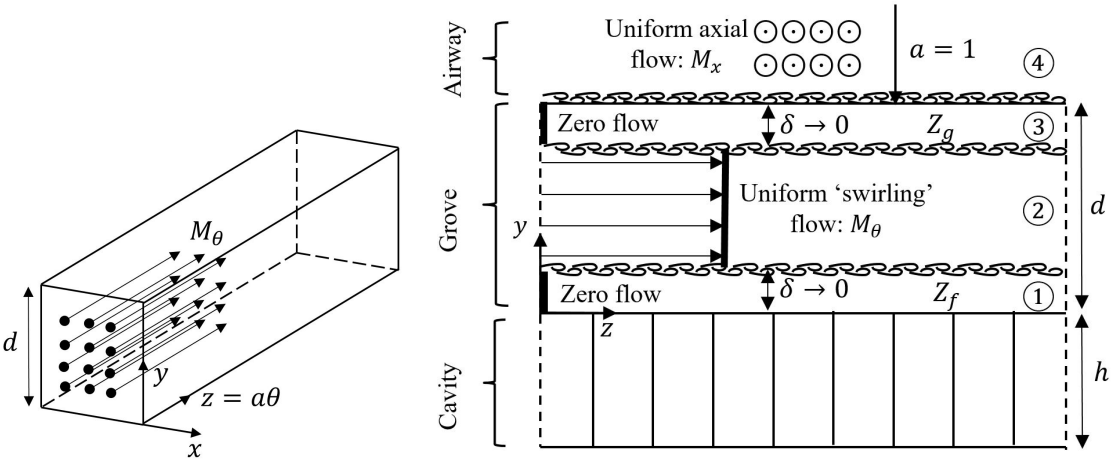

(a) Groove with 'swirling' mean flow

(b) Non-dimensional diagram and nomenclature

Figure 3.17: Diagrams of the Cartesian groove impedance model with 'swirling' mean flow.

The material derivative in the groove with swirling mean flow is expressed as

$$\frac{D_0}{Dt} = \frac{\partial}{\partial t} + \frac{M_\theta(r)}{r}\frac{\partial}{\partial \theta} \quad , \tag{3.34}$$

which can be simplified for the rectangular channel with constant $M_\theta = M_{\text{tip}}$ as

$$\frac{D_0}{Dt} = \frac{\partial}{\partial t} + M_{\text{tip}}\frac{\partial}{\partial z} \quad . \tag{3.35}$$

Therefore, the convective Helmholtz equation governing the sound propagation within the upper section of the groove is

$$\nabla^2 p - \left(j\omega + M_{\text{tip}}\frac{\partial}{\partial z}\right)^2 p = 0 \quad . \tag{3.36}$$

The solution of the non-dimensional Helmholtz equation for the pressure field can be written again as a separable solution in Cartesian coordinates (Eq. 3.23) but with a different dispersion relation:

$$(\omega - k_z M_{\text{tip}})^2 = k_n^2 + \beta_{mn}^2 + k_z^2 \quad , \tag{3.37}$$

resulting in the eigenvalues of Eq. 3.23 now given by

$$k_z = m, \quad k_n = \frac{n\pi}{l_g} \quad \text{and} \quad \beta_{mn} = \sqrt{(\omega - mM_{\text{tip}})^2 - k_n^2 - k_z^2} \quad , \tag{3.38}$$

where only $n = 0$ is considered as in the original formulation. Application of the Ingard-Myers boundary condition at the bottom of the groove ($y = 0$, ① to ②) yields

$$\left(\omega - mM_{\text{tip}}\right)^2 + j\omega Z_f \frac{\partial p}{\partial y} = 0 \quad , \tag{3.39}$$

and

$$B_{m0} = \frac{j\left(\omega - mM_{\text{tip}}\right)^2}{\omega \beta Z_f} A_{m0} \quad . \tag{3.40}$$

Similarly, the boundary condition is applied at the interface between the groove and the airway ($y = d$, ② to ③) to obtain

$$\left(\omega - mM_{\text{tip}}\right)^2 - j\omega Z_g \frac{\partial p}{\partial y} = 0 \quad , \tag{3.41}$$

and allowing to retrieve the groove effective impedance Z_g

$$Z_g(\omega, m, M_{\text{tip}}) = -\frac{j\Omega^2}{\omega \beta_m} \left[\frac{\cot(\beta_m d) + \frac{j\Omega^2}{\omega Z_f \beta_m}}{1 - \frac{j\Omega^2}{\omega Z_f \beta_m} \cot(\beta_m d)} \right] \quad , \tag{3.42}$$

where $\Omega = \omega - mM_{\text{tip}}$.

The expressions for the effective impedance of the Cartesian groove model derived earlier in the section for zero flow and here to include a uniform azimuthal flow are summarised in Table 3.3, which also includes the dispersion relations. The zero flow expressions are recovered if M_{tip} is set to zero and for $m = 0$.

Table 3.3: Summary of the expressions for the Cartesian groove model with and without azimuthal mean flow.

Groove conf.	Effective Impedance	Dispersion Relation
Zero flow	$Z_g = -\frac{j\omega}{\beta_m} \left[\frac{\cot(\beta_m d) + \frac{j\omega}{Z_f \beta_m}}{1 - \frac{j\omega}{Z_f \beta_m} \cot(\beta_m d)} \right]$	$\omega^2 = \beta_m^2 + m^2$
'Swirling' flow	$Z_g = -\frac{j\Omega^2}{\omega \beta_m} \left[\frac{\cot(\beta_m d) + \frac{j\Omega^2}{\omega Z_f \beta_m}}{1 - \frac{j\Omega^2}{\omega Z_f \beta_m} \cot(\beta_m d)} \right]$	$\Omega^2 = \beta_m^2 + m^2$

The sound propagation in the upper section of the groove is now different for $m > 0$ and $m < 0$ as dictated by the radial wavenumber β_m, which translates to a different value of impedance for each spinning direction for a given azimuthal mode number. The effective groove impedance with and without azimuthal flow is shown in Fig. 3.18 in a format analogous to that used in Fig. 3.7. The cut-off condition for the propagation in the groove is given by $\omega = (1 \pm M_{\text{tip}})|m|$ for modes $m = \pm|m|$ respectively, indicated with the dashed lines in Fig. 3.18.

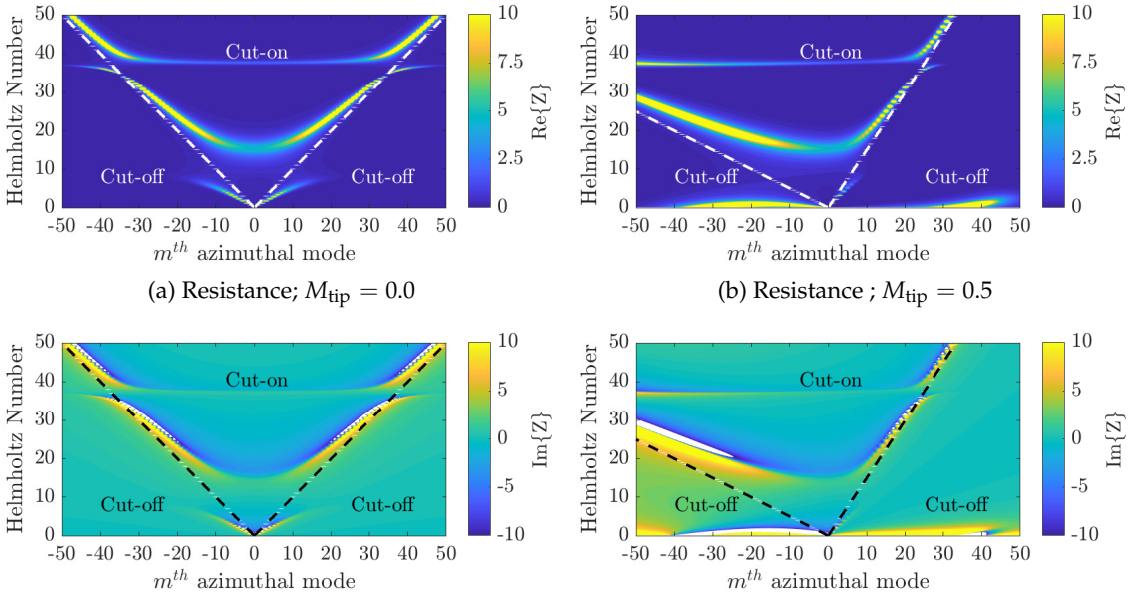

(a) Resistance; $M_{\text{tip}} = 0.0$

(b) Resistance ; $M_{\text{tip}} = 0.5$

(c) Reactance; $M_{\text{tip}} = 0.0$

(d) Reactance; $M_{\text{tip}} = 0.5$

Figure 3.18: Groove impedance with and without azimuthal flow in the groove region for a range of frequencies $0 \leq \omega \leq 50$ and azimuthal mode numbers $0 \leq m \leq 50$.

In a 'real' OTR configuration, e.g. the W-8 test, swirling flow will exist in the airway above the liner *and* in the open groove (induced by the flow in the airway). The performance of the liner will be affected, as suggested before, in two ways:

1. The effect of the impedance on the sound field will be modified by the mean swirling flow in the airway.
2. The effective impedance will be changed by the presence of the mean swirling flow in the groove.

Effect (1) cannot be modelled by the current Green's function, which has been formulated for axial flow without swirl, and effect (2) is modelled by expression 3.42. While both effects cannot be predicted by the current model, effect (2) can be studied in isolation by using the modified impedance with the current (non swirling) Green's function. This may indicate whether or not the modified impedance due to swirl in the groove, contributes independently to the asymmetry of the measured Insertion Loss form the W-8 test. To

this end, the predicted SPL IL for an axial dipole located at $(x_s, r_s, \theta_s) = (0.5l_L, 0.95a, 0)$ for M_x=0.236 and a range of M_{tip} is shown in Fig 3.19a, indicating that the overall noise reduction is marginally affected by the azimuthal flow in the groove. However, comparison of the predicted modal noise reduction with or without the azimuthal flow in Fig. 3.19b-3.19c shows a shift of the noise reduction towards the positive (co-rotating) spinning modes. These predictions can be qualitatively compared with the measurements of Fig. 3.16c and suggest that the modified groove impedance model is able to predict an asymmetry on the noise reduction of the co-rotating and counter-rotating spinning modes.

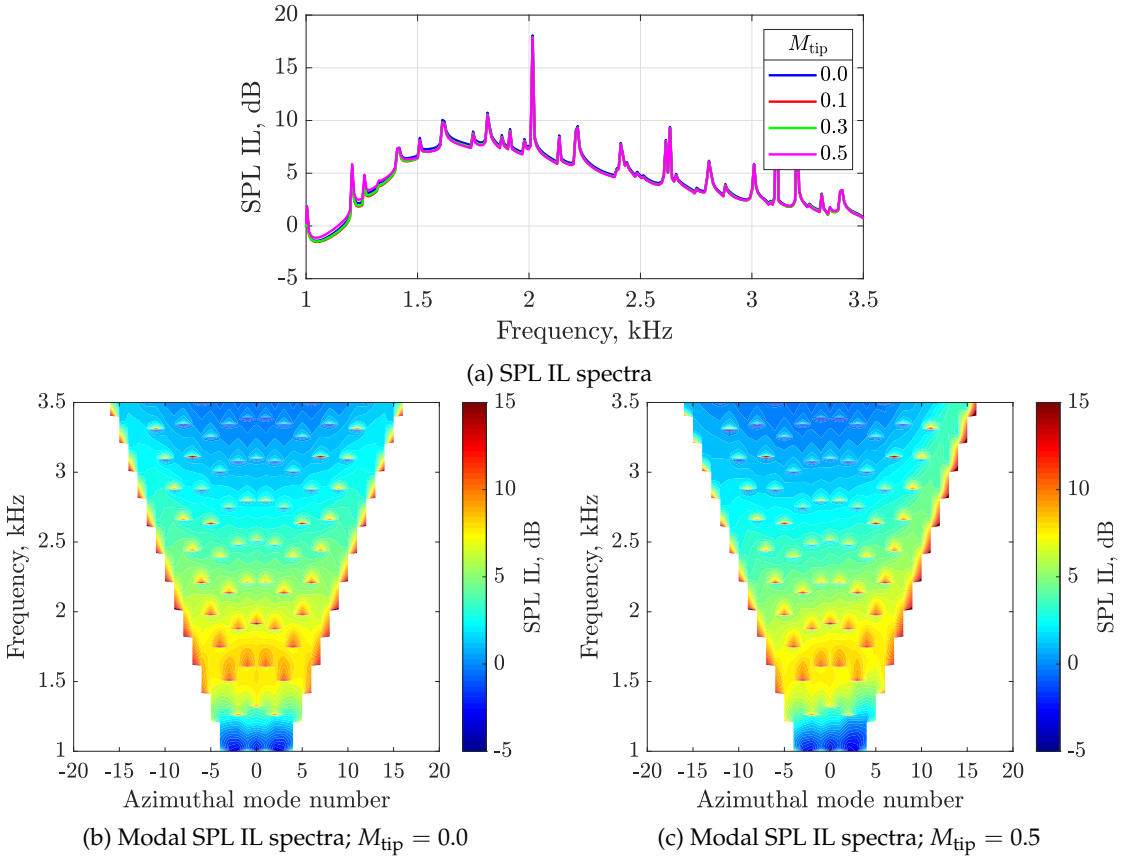

(a) SPL IL spectra

(b) Modal SPL IL spectra; $M_{\text{tip}} = 0.0$

(c) Modal SPL IL spectra; $M_{\text{tip}} = 0.5$

Figure 3.19: SPL IL spectra for a range of M_{tip} and modal SPL IL spectra with and without azimuthal mean flow in the groove.

The asymmetry in the noise reduction of the co- and counter-rotating modes is most pronounced for the near cut-off mode numbers ($\pm m_{max}$). This is used to obtain a measure of such asymmetry by subtracting the modal SPL IL in Fig. 3.19c for $m = \pm m_{max}$, which can also be computed for the experimental data in Fig. 3.16c. The resultant measured and predicted ΔSPL IL is shown in Fig. 3.20. As mentioned before, the modified impedance model with the current assumptions is able to qualitatively predict the asymmetry on the noise reduction but cannot capture the full physics, which requires further investigation.

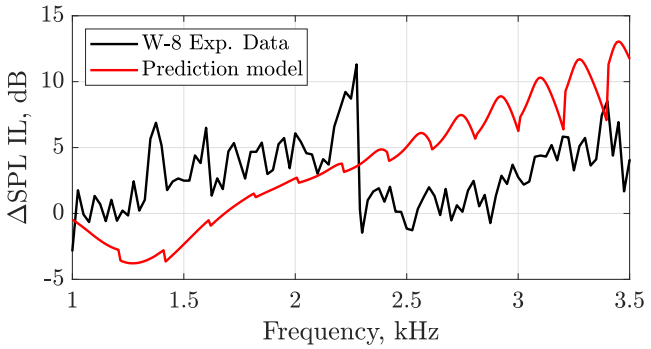

Figure 3.20: Measured and predicted ΔSPL IL spectra between $m = \pm m_{max}$.

The modified version of the impedance groove model has not been verified with FEM simulations due to the difficulties of recreating the underlying assumptions numerically. The verified annular impedance groove model without axial or annular flow in the groove is used in subsequent chapters.

3.4 Summary and conclusions

Summary

- A brief review of impedance boundary conditions used in the modelling of the sound propagation in turbofan engines has been presented and the formulation for the impedance of conventional SDOF and DDOF cavity liners used in this thesis has been described.
- The validation of the analytical predictions developed in this thesis against experimental data from a recent OTR circumferential groove array tested in the NASA W-8 fan rig requires an analytical model for the impedance of the OTR configurations used in the experiments.
- The OTR treatments modelled consist of circumferential grooves extending over the axial projection of the fan chord. Two analytical models have been developed, one exact and the other approximate. Both are 'semi-locally reacting' in the sense that local reaction is assumed in the axial direction, but non-local reaction in the azimuthal direction. That is to say, the impedance depends on the frequency and the azimuthal mode number. Good agreement between the two impedance models has been established for the geometry and frequencies of interest in this project.
- The locally/non-locally reacting behaviour assumed in the development of the analytical models have agreed with the FEM high-order, high-fidelity numerical simulations for the range of frequencies of interest, which consist of a 3D axisymmetric duct with a single groove and incident duct modes. Good agreement has

been found between the predicted analytical groove impedance and the numerical impedance evaluated in the groove-duct interface of the FEM model.

- An extension of the FEM model to include multiple grooves has indicated also that the effective impedance of each groove tends to cluster around the 'single groove' prediction with fairly small variations except at peak values, where the behaviour of the grooves is practically that of a hard wall. This suggests that the use of the analytical single groove impedance model in cases with multiples grooves can provide reasonable predictions.

- The groove model has been coupled with a simplified OTR liner analytical prediction model, Green/FINF. The test case consists of a cylindrical finite lined duct section matched to infinite hard wall duct extensions excited by a monopole point source located within the lined section. The analytical predictions for PWL insertion loss obtained by using the 'single groove' impedance corrected by a porosity factor have been compared to FEM predictions accounting for the full groove geometry. The predictions and FEM solutions agree within 0.2 dB for the whole frequency range.

- The groove impedance model has been extended to include a simplified swirling flow within the upper section of the groove that results in a different impedance for positive or negative spinning modes. The overall predicted SPL IL is marginally affected by the azimuthal flow in the groove. However, the noise reduction is enhanced for the modes co-rotating with the fan and diminished for those counter-rotating, as observed in the NASA W-8 measured data.

Conclusions

- The analytical groove impedance models have proven to most effectively represent the acoustic behaviour of the physical groove geometry in the absence of grazing flow by applying the corrected effective impedance of a single groove to an extended duct length equivalent to that of the multiple groove liner. This impedance model permits a comparison of our analytical OTR prediction model to the NASA W-8 measured data in Chapter 6.

- Additional noise generated by grazing flow over the grooved liner cannot be modelled within the analytical impedance models and is outside the scope of this work. It will be assumed that the mean flow in the airway does not interact with the grooves, whose existence is modelled by an equivalent continuous impedance at the duct wall.

- Future work in groove modelling could include a formal consideration of the effects of the swirling flow in the annular (rather than the simpler rectangular) groove

model induced by the rotation of the fan blades. A further more substantial improvement would be to also model the swirling flow in the Green's function for the main duct.

Chapter 4

Modelling of fan noise in circular lined ducts with uniform mean flow

Contents

The fan sources and the acoustic treatments are located and installed within a duct. Therefore, this chapter starts with a review in Section 4.1 of the formulation of time-harmonic acoustic propagation within infinite circular ducts with rigid or lined walls in the presence of uniform mean flow. This propagation is reduced to solving the homogeneous convective wave equation and applying the hard wall or lined boundary condition at the duct walls. Then, in Section 4.2, the Green's function for a point source within the duct is described as a solution of the inhomogeneous wave equation. The Green's function for a hard/lined circular duct with uniform mean flow is the basis for the noise generation and propagation modelling used in this thesis. The section also contains an overview of the method used to solve the eigenvalue equation and its challenges.

The modelling of the acoustic field of various types of static and rotating noise sources to represent the fan rotor blade is detailed in Section 4.3 and Section 4.4. Section 4.5 describes the definition and expressions to compute the axial acoustic power. Finally, Section 4.6 focuses on assessing the impact of the hard/lined duct boundary condition on the power output of simple noise sources and a comparison with a reference model of a point source over an infinite hard/lined plane. The study is focused on the effect of locating the sources in close proximity to the wall.

In all analytical expressions of this chapter, distances are normalised by the duct radius a, time by a/c_0, frequency by c_0/a, pressure by $\rho_0 c_0^2$, and particle velocity by c_0. The intensity is normalised by $\rho_0 c_0^3$ and the power by $\rho_0 c_0^3 a^2$. The $e^{j\omega t}$ convention has been used to define time-harmonic variables.

4.1 Sound propagation in a lined circular duct with uniform mean flow

4.1.1 Formulation

The time-harmonic sound propagation in an infinite circular hollow duct in the presence of mean flow is governed by the convective Helmholtz equation (Eq.1.14). A cylindrical coordinate system is used for convenience: the duct axis is defined in the x-direction and its cross-section in terms of the radial and circumferential coordinates r and θ. For reference, the Nabla and Laplace operators in cylindrical coordinates are

$$\nabla = \frac{\partial}{\partial x}\hat{x} + \frac{\partial}{\partial r}\hat{r} + \frac{1}{r}\frac{\partial}{\partial \theta}\hat{\theta} \quad , \tag{4.1}$$

$$\nabla^2 = \frac{\partial^2}{\partial x^2} + \frac{\partial^2}{\partial r^2} + \frac{1}{r}\frac{\partial}{\partial r} + \frac{1}{r^2}\frac{\partial^2}{\partial \theta^2} \quad , \tag{4.2}$$

where $\hat{x}$, $\hat{r}$ and $\hat{\theta}$ are the unit vectors in the axial, radial and circumferential direction.

The convective Helmholtz equation for uniform axial mean flow, $\boldsymbol{M} = (M, 0, 0)$, in cylindrical coordinates, can be expressed as

$$\frac{\partial^2 p}{\partial x^2} + \frac{\partial^2 p}{\partial r^2} + \frac{1}{r}\frac{\partial p}{\partial r} + \frac{1}{r^2}\frac{\partial^2 p}{\partial \theta^2} - \left(j\omega + M\frac{\partial}{\partial x}\right)^2 p = 0 \quad . \tag{4.3}$$

Modal solutions of the convective Helmholtz equation can be obtained by separation of variables [50, 53]. By assuming solutions of the form

$$p(x, r, \theta) = F(x)G(r)H(\theta) \quad , \tag{4.4}$$

Eq. 4.3 can be divided into three second order ordinary differential equations:

$$\left(1-M^2\right)\frac{d^2F}{dx^2} - 2j\omega M\frac{dF}{dx} + \left(\omega^2-\alpha^2\right)F = 0 \quad , \tag{4.5}$$

$$\frac{d^2G}{dr^2} + \frac{1}{r}\frac{dG}{dr} + \left(\alpha^2 - \frac{m^2}{r^2}\right)G = 0 \quad , \tag{4.6}$$

and

$$\frac{d^2H}{d\theta^2} + m^2H = 0 \quad , \tag{4.7}$$

where m and α are arbitrary complex constants to be determined by boundary conditions on the solution.

The solutions of Eq.4.5-4.7 are of the form:

- $F(x) = C_1e^{-j\kappa^+x} + C_2e^{-j\kappa^-x}$, where $\kappa^{\pm} = \frac{-\omega M \pm \sqrt{\omega^2-(1-M^2)\alpha^2}}{1-M^2}$
- $G(r) = C_3J_m(\alpha^{\pm}r) + C_4Y_m(\alpha^{\pm}r)$, where J_m and Y_m are the Bessel functions of first and second kind.
- $H(\theta) = C_5e^{-jm\theta}$.

Note that κ, α and m are the wavenumbers in the axial, radial and circumferential direction respectively.

Since the duct is assumed to be infinite in the positive and negative axial directions, the solution must radiate or decay as $x \to \pm\infty$. Hence, $C_2 = 0$ for $x > 0$ and $C_1 = 0$ for $x < 0$. Boundary conditions must also be satisfied in the radial and circumferential directions. These are :

- *Circumferential direction*: The solution must be periodic in θ at period 2π, giving

$$H(\theta) = H(\theta + 2m\pi) \quad m = 0, \pm1, \pm2, \quad \text{etc.} \tag{4.8}$$

- *Radial direction*: The pressure must be finite at $r = 0$, hence $C_4 = 0$, and condition 3.5 must be satisfied at the outer wall, giving

$$\left(j\omega + M\frac{\partial}{\partial x}\right)^2 p + j\omega Z\frac{\partial p}{\partial r} = 0 \quad \text{at} \quad r = 1 \quad . \tag{4.9}$$

The substitution of expressions for $F(x)$ and $G(r)$ into Eq. 4.9 above then gives

$$j\Omega^2J_m(\alpha) + \omega\alpha ZJ'_m(\alpha) = 0 \quad , \tag{4.10}$$

where $\Omega = \omega - \kappa M$ is obtained from the dispersion relation

$$\Omega^2 = \alpha^2 + \kappa^2 \quad . \tag{4.11}$$

The above generic solutions in each dimension can be recombined to recover expressions for the pressure of the form

$$p(x,r,\theta) = \left(C_1 C_3 e^{-j\kappa^+ x} J_m(\alpha^+ r) + C_2 C_3 e^{j\kappa^- x} J_m(\alpha^- r)\right) C_5 e^{-jm\theta} \quad . \tag{4.12}$$

This poses a coupled eigenvalue problem for α and κ. For each integer value of m (from $-\infty$ to $-\infty$) a set of eigenvalue pairs (α^+_{mn},κ^+_{mn}) and (α^-_{mn},κ^-_{mn}) satisfy Eq. 4.10 for $n = 1,2,3,...$

The eigenvalue statement is valid for any value of wall impedance Z, an input to the acoustic problem in the duct. The eigenvalue equation for a hard wall case can be obtained by setting $Z = \infty$ in Eq. 4.10 to give $J'_m(\alpha_{mn}) = 0$. The radial eigenvalues α_{mn} can then be directly obtained from the zeros of the derivative of the Bessel function of the first kind. All axial and radial eigenvalues have been expressed for $m = (0, \pm 1, \pm 2, ...)$ and $n = (1,2,3,...)$ since for each azimuthal mode number m there are infinite n solutions of the eigenvalue equation. Each combination of (m,n) is known as a duct mode and $\alpha^{\pm}_{mn}$ and $\kappa^{\pm}_{mn}$ are used for the right-running (+) and left-running modes (-). In the case of a hard wall or lined wall with zero mean flow the right and left-running modes are the same and no sign distinction is made. Finally, by superposition, the pressure solution of the wave equation can be written as the modal expansion

$$p(x,r,\theta) = \sum_{m=-\infty}^{\infty} e^{-jm\theta} \left(\sum_{n=1}^{\infty} \left[N^+_{mn} J_m(\alpha^+_{mn} r) e^{-j\kappa^+_{mn} x} + N^-_{mn} J_m(\alpha^-_{mn} r) e^{-j\kappa^-_{mn} x} \right] \right) \quad , \tag{4.13}$$

where N^-_{mn} and N^+_{mn} are complex modal amplitudes.

4.1.2 Numerical method to solve the eigenvalue equation

The description of the sound field in the lined duct requires determining the solutions α_{mn} and κ_{mn} of the eigenvalue equations (Eq. 4.10 and Eq. 4.11). It is not trivial to solve all the eigenvalue solutions for a lined case. A routine developed by Rienstra has been used in the current study and is outlined in this part of the section. The computational scheme is based on the dynamics of the eigenvalues in the complex plane described in [75]. The main steps involved in the routine are:

1. **Calculation of the hard-wall eigenvalues:** as mentioned before, these are the solutions of $J'_m(\alpha_{mn}) = 0$ which can be directly obtained from the zeros of the derivative of the Bessel function of the first kind j'_{mn}.

2. **Eigenvalue tracing to obtain the lined solution:** a contour in the complex impedance plane is defined from the hard wall condition $Z = \infty$ to the target impedance Z_{tar} and the eigenvalue equation is solved taking small steps along the contour and using the previous solution as starting values. Contours parallel to the imaginary axis are used of the form $Z = R + jX$ with a constant resistance R_{tar} and the reactance varying from $X = -\infty$ for $M > 0$ and $X = +\infty$ for $M = 0$ to $X = X_{\text{tar}}$. Starting at $Z = \infty$ ensures that all the surface waves are captured [75]. Two approaches have been used:

   A. Express the eigenvalue equation in terms of an admittance function of a dummy variable η such that $A(\eta = 0) = 0$ is the hard wall admittance and $A(\eta = \eta_{\text{tar}}) = A_{\text{tar}}$ is the target admittance. The eigenvalue equation can then be expressed in the form of an ordinary differential equation (ODE) and integrated numerically as an initial value problem for $\eta = [0, \eta_{\text{tar}}]$ to yield the solutions of the eigenvalue equation for the target impedance/admittance. The solution is then refined using a Newton-Raphson routine. A more detailed description including the formulation is given in [51].

   B. Solving directly the eigenvalue equation at each point of the impedance contour with a zero-finding routine, starting with the hard wall initial values and then using the solution of the previous step as the initial values of the current step until reaching the target impedance.

Both options permit the computation of the eigenvalues for a desired number of radial mode numbers for a given azimuthal mode number, frequency, wall impedance and mean flow Mach number. Solving the eigenvalue equation with a Newton-Raphson method with nearly hard wall eigenvalues as the initial condition was introduced by Ko [104] and the idea of tracing the eigenvalues by transforming the eigenvalue equation to an ODE was first proposed for a 2D duct by Eversman [105]. The main difference between the ODE strategies proposed by Eversman and Rienstra is the choice of the parametrisation of the impedance, which in the latter is based on the classification of modes as acoustic modes and surface waves.

The strategy adopted in this thesis has been the transformation of the eigenvalue equation into an ODE since it has proven to be a faster routine more suited for problems involving a large number of modes and frequencies. However, the groove impedance model described in Chapter 3 is purely reactive when a hard groove is considered and can lead to values of resistance close to zero even for the lined groove configuration. Strategy (A) can diverge under certain conditions with these zero/small resistances, for which strategy (B) with small steps along the contour appears to be more reliable. An alternative impedance contour has also been explored using strategy (B) and starting from the pressure-release condition $Z = 0$, with analytical solutions $J_m(\alpha_m n) = 0$, i.e. $\alpha_{mn} = j_{mn}$, instead of the hard wall solution, which has provided reliable solutions for $|Z| < 1$ even when $R = 0$.

The numerical integration of the ODE has been implemented with the MATLAB function *ode45* based on an explicit Runge-Kutta (4,5) solver and with *ode113*, a variable-step, variable-order (VSVO) Adams-Bashforth-Moulton PECE solver [106]. The latter has been found to be more stable at low resistances and hereby is used as default.

After the considerations outlined above, the ODE strategy has been used with automatic monitoring to (1) remove duplicated eigenvalue solutions, (2) remove modal solutions when appearing as convective instabilities [74], (3) flag if the solution has not reached convergence and (4) make sure that the surface waves with the analytical solution, i.e. for $M = 0$, have been captured by using the analytical solution as starting value and a zero finding routine. Only cases with null or very small resistance $R < 0.1$ have been an issue and are addressed with the use of an artificial resistance detailed in Chapter 6.

4.2 Green's function for a lined circular duct with uniform mean flow

The Green's function represents the impulse response of the wave equation for specific boundary and initial conditions. This section describes a tailored Green's function in the frequency domain for a lined circular duct with uniform mean flow adopted in this thesis. The infinite circular duct problem is sketched in Figure 4.1.

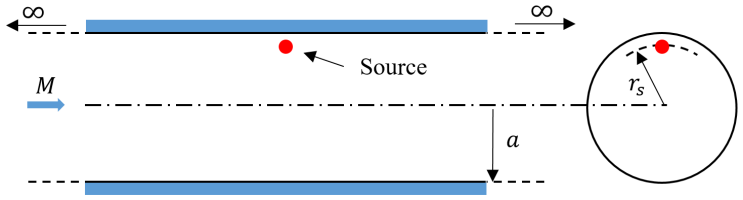

Figure 4.1: Lateral and cross-section of the infinite circular duct problem.

The Green function $G(\mathbf{x}|\mathbf{y})$ represents the pressure field generated at $\mathbf{x} = (x, r, \theta)$ by a point source located at $\mathbf{y} = (x_s, r_s, \theta_s)$. For an infinite lined cylindrical duct with uniform mean flow:

$$\frac{\partial^2 G}{\partial x^2} + \frac{\partial^2 G}{\partial r^2} + \frac{1}{r}\frac{\partial G}{\partial r} + \frac{1}{r^2}\frac{\partial^2 G}{\partial \theta^2} - \left(j\omega + M\frac{\partial}{\partial x}\right)^2 G = \delta(\mathbf{x}-\mathbf{y}) \quad , \tag{4.14}$$

with the impedance boundary condition at the wall:

$$\left(j\omega + M\frac{\partial}{\partial x}\right)^2 G + j\omega Z \frac{\partial G}{\partial r} = 0 \quad \text{at} \quad r = 1 \quad . \tag{4.15}$$

An analytic Green's function for this problem was proposed by Tester et al. [43, 107] based on a previous formulation for a 2D lined duct with uniform mean flow [74]. An

equivalent formulation was independently obtained by Zorumski [108], although some of the expressions were not given explicitly. Alonso et al. [109–111] derived a Green's function by solving a linear system of equations based on a modal expansion of the solution and enforcing continuity of the solution at the source plane.

The analytic Green's function adopted here is the version derived by Rienstra and Tester [51], expressed as a sum of non-orthogonal modes obtained by representing the solution as a Fourier integral evaluated as a summation over the residues. The formulation is explicit and agrees with the Green's function of Alonso et al. when a sufficient number of modes in both solutions are considered.

The Green's function is expressed as a sum of non-orthogonal modes

$$G(\mathbf{x}|\mathbf{y}) = \sum_{m=-\infty}^{\infty} e^{-jm(\theta-\theta_s)} G_m(r,x) \quad , \tag{4.16}$$

where

$$G_m(r,x) = -\frac{1}{2\pi j} \sum_{n=1}^{\infty} \frac{J_m(\alpha_{mn}^{\pm} r) J_m(\alpha_{mn}^{\pm} r_s)}{Q_{mn}^{\pm} J_m(\alpha_{mn}^{\pm})^2} e^{-j\kappa_{mn}^{\pm}(x-x_s)} \quad , \tag{4.17}$$

with

$$Q_{mn}^{\pm} = \pm \left[(\kappa_{mn}^{\pm} + \Omega_{mn}^{\pm} M) \left(1 - \frac{m^2}{\alpha_{mn}^{\pm 2}} - \frac{\Omega_{mn}^{\pm 4}}{(\omega \alpha_{mn}^{\pm} Z)^2} \right) - \frac{2jM\Omega_{mn}^{\pm}}{\omega Z} \right] \quad , \tag{4.18}$$

$Q_{mn}^{\pm}$, $\alpha_{mn}^{\pm}$ and $\kappa_{mn}^{\pm}$ are used for the right-running (+) and left-running modes (-), in the regions $x > x_s$ and $x < x_s$ respectively. The axial and radial modal wavenumbers can be obtained by finding the solutions of the eigenvalue equation (Eq.4.10). More details of the formulation and the analogous expressions for an annular section can be found in [51]. The expressions given by Eq. 4.16-4.18 are also valid for the semi-locally reacting impedance models described in Section 3.3, for which $Z = Z(\omega, m)$.

The delta function on the right hand side of Eq. 4.14 can also be understood as a monopole volume acceleration point source of constant unit strength, as explained in Section 4.3.1.

The axial particle velocity is a key variable to analyse the behaviour of the acoustic field and necessary to compute the in-duct sound power radiated by the source/s, as described in Section 4.5. The axial particle velocity, u_x, can be obtained from the modal expansion of the pressure field and the non-dimensional linearised momentum equation in the axial direction:

$$j\omega u_x + M\frac{\partial u_x}{\partial x} + \frac{\partial p}{\partial x} = 0 \tag{4.19}$$

which gives, for the Green's function pressure field,

$$u_x(\mathbf{x},\omega) = \sum_{m=-\infty}^{\infty} e^{-jm(\theta-\theta_s)} \left(-\frac{1}{2\pi j} \sum_{n=1}^{\infty} \frac{\kappa_{mn}^{\pm}}{\Omega_{mn}^{\pm}} \frac{J_m(\alpha_{mn}^{\pm} r) J_m(\alpha_{mn}^{\pm} r_s)}{Q_{mn}^{\pm} J_m(\alpha_{mn}^{\pm})^2} e^{-j\kappa_{mn}^{\pm}(x-x_s)} \right) \tag{4.20}$$

4.3 Acoustic field generated by ducted static sources

The non-dimensional inhomogeneous convective wave equation in uniform axial mean flow is:

$$\left(\frac{D^2}{Dt^2} - \nabla^2\right) p = q \quad , \tag{4.21}$$

where

$$\frac{D}{Dt} = \frac{\partial}{\partial t} + M\frac{\partial}{\partial x} \quad , \tag{4.22}$$

and q represents the source term.

In the acoustic analogy, the source term q represents the noise generation mechanism exciting the acoustic field. The main physical excitation mechanisms usually considered in aeroacoustics are unsteady volume acceleration, velocity and displacement, external forces and external stresses, which are represented by distributions of monopoles, dipoles and quadrupoles respectively. The expressions in this section and the next are limited to the volume velocity and the external force since these are the dominant mechanisms in rotor blade noise [50]: the so-called thickness noise and the unsteady loads normal to the fan surface respectively. These two source terms are defined as

$$q = \frac{DQ}{Dt} \quad , \tag{4.23}$$

where Q is the volume velocity per unit volume, and

$$q = \nabla \cdot \boldsymbol{f} \quad , \tag{4.24}$$

with the vector $\boldsymbol{f}$ defining the external force per unit volume. Although these are the only type of sources used in the thesis, Joseph et al. [7] showed that any ducted source could be generalised as a distribution of temporal and spatial derivatives. They provided the following general expression for the pressure modal amplitudes p_{mn} of an incoherent source distribution of arbitrary spatial order μ and temporal order ν in a hard wall duct

$$|p_{mn}^{(\mu,\nu)}|^2 \propto \frac{1}{\xi_{mn}^2}\left(\frac{M-\xi_{mn}}{1-M^2}\right)^{2\mu}\left(\frac{1-\xi_{mn}M}{1-M^2}\right)^{2\nu} \quad , \tag{4.25}$$

where

$$\xi_{mn} = \sqrt{1-(1-M^2)(\alpha_{mn}/\omega)^2} \quad . \tag{4.26}$$

These relations will be compared with the point source expressions formulated in this section.

4.3.1 Monopole point source

The solution of the inhomogeneous wave equation for the volume velocity source can be solved by using the Green's function. Goldstein [50] showed that the acoustic field, in the time domain, generated by the monopole source is of the form

$$p(\boldsymbol{x},t) = \int_{-\infty}^{\infty} \iint_{S} Q(\boldsymbol{y},\tau) \frac{Dg(\boldsymbol{x},t|\boldsymbol{y},\tau)}{D\tau} dS(\boldsymbol{y}) d\tau \quad , \tag{4.27}$$

where the sources are distributed over the blade surface S and Q is the non-dimensional unsteady flow velocity normal to the blade surface. Note that the material derivative is now applied to the time-domain Green's function instead of the source term. The time-domain Green's function is related to the frequency-domain form of Eq. 4.16 by the inverse Fourier transform:

$$g(\boldsymbol{x},t|\boldsymbol{y},\tau) = \frac{1}{2\pi} \int_{-\infty}^{\infty} G(\boldsymbol{x}|\boldsymbol{y}) e^{j\omega(t-\tau)} d\omega \quad . \tag{4.28}$$

In the frequency domain, the material derivative is transformed, for each modal component, to

$$\frac{D}{D\tau} = \left(\frac{\partial}{\partial \tau} + M \frac{\partial}{\partial x_s} \right) \rightarrow -j\left(\omega - M\kappa_{mn}\right) = -j\Omega_{mn} \quad , \tag{4.29}$$

leading to

$$p(\boldsymbol{x},t) = \int_{-\infty}^{\infty} \iint_{S} \frac{-j}{2\pi} \int_{-\infty}^{\infty} Q(\boldsymbol{y},\tau) e^{-j(\omega\tau} \Omega_{mn} G(\boldsymbol{x}|\boldsymbol{y}) e^{j\omega t} d\omega dS(\boldsymbol{y}) d\tau \quad . \tag{4.30}$$

The integral over emission time of the source strength is interpreted as a Fourier transform

$$\int_{-\infty}^{\infty} Q(\boldsymbol{y},\tau) e^{-j\omega\tau} d\tau = Q(\boldsymbol{y},\omega) \quad , \tag{4.31}$$

which allows writing the pressure field in the frequency domain as

$$p(\boldsymbol{x},\omega) = \iint_{S} -jQ(\boldsymbol{y},\omega) \Omega_{mn} G(\boldsymbol{x}|\boldsymbol{y}) dS(\boldsymbol{y}) \quad . \tag{4.32}$$

Note that the material derivative term Ω_{mn} is applied within the double summation over the azimuthal modes m and radial modes n inside the Green's function and has been placed outside only for conciseness. For a single point source, one can avoid the surface integral and write, now including the full Green's function,

$$p(\boldsymbol{x},\omega) = Q(\omega) \sum_{m=-\infty}^{\infty} e^{-jm(\theta-\theta_s)} \left(\frac{1}{2\pi} \sum_{n=1}^{\infty} \Omega_{mn}^{\pm} \frac{J_m(\alpha_{mn}^{\pm} r) J_m(\alpha_{mn}^{\pm} r_s)}{Q_{mn}^{\pm} J_m(\alpha_{mn}^{\pm})^2} e^{-j\kappa_{mn}^{\pm}(x-x_s)} \right) \quad . \tag{4.33}$$

It can be shown that the modal amplitudes of the above expression for a hard wall duct are of the form

$$|p_{mn}|^2 \propto \frac{1}{\xi_{mn}^2}\left(\frac{1-\xi_{mn}M}{1-M^2}\right)^2 \quad , \tag{4.34}$$

in agreement with the generalised formulation of Joseph et al. for the volume velocity source used here, i.e. with spatial and temporal orders (μ,ν)=(0,1).

The monopole representation in Eq. 4.33 has been used for the cross-verification with the FEM simulations with uniform mean flow since this is the monopole interpretation implemented in the software Simcenter 3D [100]. However, the physical interpretation used for the rest of analytical studies and predictions involving monopoles has been in terms of the volume acceleration of unit strength $q = 1$ with (μ,ν)=(0,0). This monopole source model does not involve the material derivative on the right hand side of the wave equation and permits a direct implementation of the pressure Green's function without any additional modification.

4.3.2 Dipole point source

A dipole source model is described here to account for the lift fluctuations due to the turbulence impinging on the fan blade and the trailing edge noise. The dipolar sources are regarded as the dominant contribution of rotor blade noise at subsonic tip speeds [50]. The dipole considered here is orientated at a certain angle γ relative to the duct axis as indicated in Fig. 4.2. The dipole is depicted at the leading edge for illustration purposes but any distribution of dipoles over the blade surface S can be modelled.

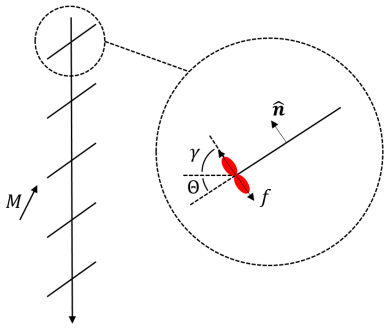

Figure 4.2: Row of fan blades as viewed over the tip and the dipole source model, with γ the angle relative to the duct axis, Θ the stagger angle and f the fluctuating lift force.

Again, the non-dimensional version of the Goldstein acoustic analogy is used to derive the pressure field of a dipole source distribution:

$$p(\boldsymbol{x},t) = \int_{-\infty}^{\infty}\iint_{S} f(\boldsymbol{y},\tau)\hat{\mathbf{n}}\cdot\nabla_y g(\boldsymbol{x},t|\boldsymbol{y},\tau)dS(\boldsymbol{y})d\tau \quad , \tag{4.35}$$

where f is the strength of the dipole normal to the blade surface S and located at $\mathbf{y} = (x_s, r_s, \theta_s)$. The normal $\hat{\mathbf{n}}$, and therefore the dipole alignment γ, could be defined as a function of $\boldsymbol{y}$ but a flat plate assumption is taken here such that it is constant and given by

$$\hat{\mathbf{n}} = [\hat{x}, \hat{r}, \hat{\theta}] = [\cos\gamma, 0, \sin\gamma] \quad . \tag{4.36}$$

An analogous procedure than for the volume velocity monopole source is followed and the integral over emission time of the dipole strength is again interpreted as a Fourier transform such that

$$\int_{-\infty}^{\infty} f(\boldsymbol{y}, \tau) e^{-j\omega\tau} d\tau = f(\boldsymbol{y}, \omega) \quad . \tag{4.37}$$

The pressure field generated at $\mathbf{x} = (x, r, \theta)$ by a dipole source in a lined circular duct with uniform mean flow can be then obtained by using the analytic Green's function solution of the wave equation with:

$$p(\mathbf{x}, \omega) = \iint_S f(\boldsymbol{y}, \omega) \hat{\mathbf{n}} \cdot \nabla_y G(\mathbf{x}|\mathbf{y}) dS(\mathbf{y}) \quad . \tag{4.38}$$

The nabla operator in cylindrical coordinates applied to the Green's function of Eq. 4.16 gives:

$$\nabla_y G = \frac{\partial G}{\partial x_s}\hat{x_s} + \frac{\partial G}{\partial r_s}\hat{r_s} + \frac{1}{r_s}\frac{\partial G}{\partial \theta_s}\hat{\theta_s} \quad , \tag{4.39}$$

resulting in the following expression of the pressure for a single point dipole in the frequency domain:

$$p(\mathbf{x}, \omega) = f(\boldsymbol{y}, \omega) \sum_{m=-\infty}^{\infty} e^{-jm(\theta-\theta_s)} \Bigg(-\frac{1}{2\pi} \sum_{n=1}^{\infty} \frac{J_m(\alpha_{mn}^{\pm} r) J_m(\alpha_{mn}^{\pm} r_s)}{Q_{mn}^{\pm} J_m(\alpha_{mn}^{\pm})^2} e^{-j\kappa_{mn}^{\pm}(x-x_s)} \left[\kappa_{mn}^{\pm}\cos\gamma + \frac{m}{r_s}\sin\gamma\right] \Bigg) \quad , \tag{4.40}$$

where $Q_{mn}^{\pm}$ and $\Omega_{mn}^{\pm}$ are the same as for the monopole Green's function. The sign logic and nomenclature also apply here.

Once again, it can be shown that the modal components of the above expression for an axial dipole (γ=0) in a hard wall duct are of the form

$$|p_{mn}|^2 \propto \frac{1}{\xi_{mn}^2} \left(\frac{M - \xi_{mn}}{1 - M^2}\right)^2 \tag{4.41}$$

in agreement with the generalised formulation of Joseph et al. for an axial dipole with spatial and temporal orders (μ,ν)=(1,0).

4.4 Acoustic field generated by ducted rotating sources

The expressions presented in the previous section always consider that the source/s are stationary in the reference frame relative to the duct. However, in reality, rotor-blade sources are spinning with the rotor. The modelling of free-field and in-duct rotor-blade noise has been often based on the formulation of the Goldstein's version of the acoustic analogy adapted for each target source type. In-duct prediction models based on Goldstein's formulation include the works of Ventres [112] and Meyer and Envia [113] for tonal interaction noise and of Glegg [114], Glegg and Jochault [115] and Lowis et al. [116] for broadband self noise amongst others. Alternative approaches based on the direct solution of the convective wave equation and including uniform mean flow have been proposed such as the formulation of McAlpine and Kingan [117] for modelling the noise of installed open rotors or Wang et al. for rotating dipoles in a plug jet flow [118].

This section describes the dipole formulation based on the Goldstein version of the acoustic analogy using the Green's function for a lined circular duct with uniform mean flow. Then, the approach based on the direct solution of the convective wave equation is adapted to the in-duct lined problem and it is shown that both approaches yield the same result if equivalent underlying assumptions are taken. The derivations can be formulated with an equivalent procedure for rotating monopoles but it has not been included in this manuscript. The last part of the section describes the modelling of the dipole source strength adopted in this thesis. The effects of considering static or rotating sources in the predicted noise generation and reduction are covered in Chapter 6.

4.4.1 Solution based on the Green's function

The effect of the dipole rotation is included in the Green's function formulation by expressing the azimuthal source position $\theta_s(\tau)$ in the stationary frame of reference relative to the duct as

$$\theta_s(\tau) = \tilde{\theta}_s + \bar{\Omega}\tau \quad , \tag{4.42}$$

where $\tilde{\theta}_s$ is the source azimuthal position in a rotating frame of reference spinning with the fan at a non-dimensional angular frequency $\bar{\Omega}$.

Substitution of Eq. 4.42 and the Green's function (Eq. 4.16) into the pressure expression in the time domain (Eq. 4.35) gives

$$p(\boldsymbol{x},t) = \int_{-\infty}^{\infty} \iint_{S} f(\tilde{\boldsymbol{y}},\tau)\frac{1}{2\pi}\int_{-\infty}^{\infty} \hat{\mathbf{n}}\cdot\nabla_y \left[\sum_{m=-\infty}^{\infty} e^{-jm(\theta-\tilde{\theta}_s)} G_m(\boldsymbol{x}|\tilde{\boldsymbol{y}}) e^{j\omega t} e^{-j(\omega-m\bar{\Omega})\tau}\right] d\omega dS(\boldsymbol{y}) d\tau \quad . \tag{4.43}$$

The integral over the emission time can now be solved as

$$\int_{-\infty}^{\infty} f(\tilde{\boldsymbol{y}},\tau)e^{-j(\omega-m\bar{\Omega})\tau}d\tau = f(\boldsymbol{y},\omega-m\bar{\Omega}) \quad , \tag{4.44}$$

which yields

$$p(\boldsymbol{x},t) = \iint_S \frac{1}{2\pi}\int_{-\infty}^{\infty} \hat{\mathbf{n}}\cdot\nabla_y\left[e^{-jm(\theta-\tilde{\theta}_s)}f(\tilde{\boldsymbol{y}},\omega-m\bar{\Omega})G_m(\boldsymbol{x}|\tilde{\boldsymbol{y}})e^{j\omega t}\right]d\omega dS(\boldsymbol{y}) \quad . \tag{4.45}$$

The pressure field for a single point rotating dipole in the frequency domain can then be obtained by taking the Fourier transform and applying the gradient as in Eq. 4.39:

$$p(\mathbf{x},\omega) = \sum_{m=-\infty}^{\infty} e^{-jm(\theta-\tilde{\theta}_s)}\left(-\frac{1}{2\pi}f(\tilde{\boldsymbol{y}},\omega-m\bar{\Omega})\sum_{n=1}^{\infty}\frac{J_m(\alpha_{mn}^{\pm}r)J_m(\alpha_{mn}^{\pm}r_s)}{Q_{mn}^{\pm}J_m(\alpha_{mn}^{\pm})^2}e^{-jk_{mn}^{\pm}(x-x_s)}\right.$$
$$\left.\left[\kappa_{mn}^{\pm}\cos\gamma+\frac{m}{r_s}\sin\gamma\right]\right) \quad . \tag{4.46}$$

Comparison of the equation above with its counterpart for a static dipole (Eq. 4.40) show that the effect of the source rotation is to shift the frequency of the source strength term f by $-m\bar{\Omega}$ but does not modify the propagation terms in the Green's function, which are still evaluated at ω. The physical interpretation of this result is that the steady loading, i.e. $\tilde{\omega} = \omega - m\bar{\Omega} = 0$, will only generate tonal noise at multiples of the shaft frequency $\omega = m\bar{\Omega}$ and the unsteady perturbations will generate broadband noise that will be perceived with a frequency ω in the static frame of reference and generated with a shift of $-m\bar{\Omega}$ in the rotating frame of reference, analogous to the Doppler factor. Therefore, the source strength and its propagation become coupled through the azimuthal mode number. An equivalent result for the hard wall Green's function has been derived in the literature by, amongst others, Ventres [112] and Lowis et al. [116]. Note that this solution requires the modelling or measurements of the dipole source strength spectrum, which is covered in more detail in Section 4.4.3.

4.4.2 Direct solution of the inhomogeneous wave equation

This formulation follows the approach taken by McAlpine and Kingan [117] based on the direct solution of the convective wave equation in free-field with uniform mean flow, which is extended here for an infinite circular lined duct. The derivation starts with the non-dimensional convective wave equation with a dipole source on the right hand side:

$$\frac{\partial^2 p}{\partial x^2}+\frac{\partial^2 p}{\partial r^2}+\frac{1}{r}\frac{\partial p}{\partial r}+\frac{1}{r^2}\frac{\partial^2 p}{\partial\theta^2}-\left(j\omega+M\frac{\partial}{\partial x}\right)^2 p = \nabla\cdot\boldsymbol{f} \quad . \tag{4.47}$$

The magnitude of the force is assumed to be harmonic with a source excitation frequency ω_0 and the direction given, as previously, by the normal to the blade surface $\hat{\mathbf{n}}$. Only the axial and azimuthal components are considered in the formulation. The source position is fixed in the axial and radial direction and rotates azimuthally with the fan such that

$$(x(t), r(t), \theta(t)) = (0, r_s, \bar{\Omega}t) \quad . \tag{4.48}$$

Therefore, the force term f can be expressed as

$$\boldsymbol{f}(x, r, \theta, t) = f_0 \hat{\mathbf{n}} e^{j\omega_0 t} \frac{\delta(r - r_s)}{r} \left(\sum_{\mu=-\infty}^{\infty} \delta(\theta - \bar{\Omega}t - 2\pi\mu) \right) \delta(x) \quad . \tag{4.49}$$

The solution of the convective wave equation is obtained by introducing the Fourier transform in x and t and Fourier series in θ given by

$$p_m(r, \kappa, \omega) = \int_{-\infty}^{\infty} \int_{-\pi}^{\pi} \sum_{-\infty}^{\infty} p(x, r, \theta, t) e^{j(\kappa x + m\theta - \omega t)} dx d\theta dt \quad , \tag{4.50}$$

and

$$p(x, r, \theta, t) = \frac{1}{(2\pi)^3} \sum_{m=-\infty}^{\infty} \left(\int_{-\infty}^{\infty} \int_{-\infty}^{\infty} p_m(r, \kappa, \omega) e^{-j(\kappa x - \omega t)} d\kappa d\omega \right) e^{-jm\theta} \quad . \tag{4.51}$$

This procedure transforms the derivatives such that

$$\frac{\partial}{\partial x} \rightarrow -j\kappa \quad , \quad \frac{\partial}{\partial \theta} \rightarrow -jm \quad , \quad \frac{\partial}{\partial t} \rightarrow j\omega \quad , \tag{4.52}$$

and the inhomogeneous wave equation transforms to

$$\frac{d^2 p_m}{dr^2} + \frac{1}{r}\frac{dp_m}{dr} + \left(\alpha^2 - \frac{m^2}{r^2} \right) p_m = \mathcal{F}_m \quad , \tag{4.53}$$

where

$$\alpha^2 = (\omega + \kappa M)^2 - \kappa^2 = \Omega^2 - \kappa^2 \tag{4.54}$$

is the radial wavenumber and the Fourier transform of the source term results in

$$\mathcal{F}_m = -j \left(\kappa \cos\gamma + \frac{m}{r} \sin\gamma \right) \frac{2\bar{\Omega}(-1)^{m+1} \sin \pi \frac{\omega - \omega_0}{\bar{\Omega}}}{m\bar{\Omega} - (\omega - \omega_0)} \frac{\delta(r - r_s)}{r} \sum_{\mu=-\infty}^{\infty} \delta(\omega - [\omega_0 + \mu\bar{\Omega}]) \quad . \tag{4.55}$$

Details of the integrations involved in the Fourier transform of the source term above can be found in [117]. The solution of Eq. 4.53 is found by using the method of variation of parameters and noting that the homogeneous version of Eq. 4.53 ($\mathcal{F}_m = 0$) has solutions

of the form $J_m(\alpha r)$ and $Y_m(\alpha r)$, i.e. Bessel functions of the first and second kind respectively. The method of variation of parameters is applied by taking $J_m(\alpha r)$ and $Y_m(\alpha r)$ as the linearly independent solutions of the homogeneous differential equation, which yields

$$p_m = J_m(\alpha r)\left[A_m(\kappa,\omega) - \frac{\pi}{2}\int_0^r \mathcal{F}_m(s)Y_m(\alpha s)sds\right] + Y_m(\alpha r)\left[B_m(\kappa,\omega) + \frac{\pi}{2}\int_0^r \mathcal{F}_m(s)J_m(\alpha s)sds\right] \quad . \quad (4.56)$$

After substitution of Eq. 4.55 and evaluation of the inegrals one gets

$$\begin{aligned} &p_m = A_m J_m(\alpha r) \quad \text{if} \quad r < r_s \\ &\text{or} \quad J_m(\alpha r)\left(A_m + \frac{\pi}{2}\tilde{\mathcal{F}}_m Y_m(\alpha r_s)\right) - Y_m(\alpha r)\left(B_m + \frac{\pi}{2}\tilde{\mathcal{F}}_m J_m(\alpha r_s)\right) \quad \text{if} \quad r > r_s \quad , \end{aligned} \quad (4.57)$$

where

$$\tilde{\mathcal{F}}_m = -j\left(\kappa\cos\gamma + \frac{m}{r_s}\sin\gamma\right)\frac{2\bar{\Omega}(-1)^{m+1}\sin\pi\frac{\omega-\omega_0}{\bar{\Omega}}}{m\bar{\Omega}-(\omega-\omega_0)}\sum_{\mu=-\infty}^{\infty}\delta(\omega-[\omega_0+\mu\bar{\Omega}]) \quad . \quad (4.58)$$

The constants $A_m(\kappa,\omega)$ and $B_m(\kappa,\omega)$ are now determined by applying the boundary conditions:

- p_m must remain finite as $r \to 0$. Since $Y_m(x)$ is singular as $x \to 0$ it immediately follows that
$$B_m(\kappa,\omega) = 0 \quad (4.59)$$
- The Ingard-Myers boundary condition is applied at the wall (r=1)
$$j\Omega^2 p_m + \omega Z\frac{\partial p_m}{\partial r} = 0 \quad (4.60)$$
which leads to
$$A_m(\kappa,\omega) = \frac{\pi}{2}\tilde{\mathcal{F}}_m\left[Y_m(\alpha r_s) - \frac{j\Omega^2 Y_m(\alpha) + j\omega Z\alpha Y_m'(\alpha)}{j\Omega^2 J_m(\alpha) + j\omega Z\alpha J_m'(\alpha)}J_m(\alpha r_s)\right] \quad (4.61)$$

Substitution of Eq. 4.59 and Eq. 4.61 back into Eq. 4.57 and rearranging the terms, the solution for p_m can be expressed as

$$p_m(r,\kappa,\omega) = \frac{\pi}{2}\tilde{\mathcal{F}}_m J_m(\alpha r_<)\frac{j\Omega^2 F_m(r_>,\alpha) + \omega Z H_m(r_>,\alpha)}{E_m(\kappa)} \quad , \quad (4.62)$$

where the nomenclature of Rienstra and Tester [51] has been adopted such that

$$E_m(\kappa) = j\Omega^2 J_m(\alpha) + \omega Z \alpha J_m'(\alpha) \quad , \tag{4.63}$$

$$F_m(r,\alpha) = J_m(\alpha)Y_m(\alpha r) - Y_m(\alpha)J_m(\alpha r) \quad , \tag{4.64}$$

$$H_m(r,\alpha) = \alpha J_m'(\alpha)Y_m(\alpha r) - \alpha Y_m(\alpha)J_m(\alpha r) \quad , \tag{4.65}$$

and

$$r_> = \max(r, r_s) \quad \text{and} \quad r_< = \min(r, r_s) \quad . \tag{4.66}$$

The inverse Fourier transform in x is defined as

$$p_m(x,r,\omega) = \frac{1}{2\pi} \int_{-\infty}^{\infty} p_m(r,\kappa,\omega) e^{-j\kappa x} d\kappa \quad . \tag{4.67}$$

The back transformation can be performed by noting the isolated poles of $E_m(\kappa^{\pm})$, $\kappa = \kappa_{mn}^{\pm}$. The integral is evaluated as a sum over the residues in the poles at $\kappa = \kappa_{mn}^{+}$ for $x > 0$ and $\kappa = \kappa_{mn}^{-}$ for $x < 0$ [51]. By noting that

$$\left.\frac{dE_m}{d\kappa}\right|_{\kappa=\kappa_{mn}} = -\omega Z J_m(\alpha) \left[(\Omega M - \kappa) \left(1 - \frac{m^2}{\alpha^2} - \frac{\Omega^4}{(\omega Z \alpha)^2} \right) - \frac{2jM\Omega}{\omega Z} \right] \quad , \tag{4.68}$$

introducing an equivalent quantity that in Eq. 4.18

$$Q_{mn} = \pm \left[(\kappa - \Omega M) \left(1 - \frac{m^2}{\alpha^2} - \frac{\Omega^4}{(\omega Z \alpha)^2} \right) - \frac{2jM\Omega}{\omega Z} \right] \quad , \tag{4.69}$$

and using the eigenvalue equation $E_m(\kappa_{mn}^{\pm}) = 0$ and the Wronskian to obtain

$$j\Omega^2 F_m(r_>, \alpha) + \omega Z H_m(r_>, \alpha) = -\frac{2\omega Z}{\pi J_m(\alpha)} J_m(\alpha r_>) \quad , \tag{4.70}$$

the integral of the inverse Fourier transform results in

$$p_m(x,r,\omega) = -j \sum_{n=1}^{\infty} \tilde{\mathcal{F}}_m \frac{J_m(\alpha_{mn} r_<) J_m(\alpha_{mn} r_>)}{Q_{mn} J_m(\alpha_{mn})^2} e^{-j\kappa_{mn} x} \quad . \tag{4.71}$$

So the distinction between $r_>$ and $r_<$ can be skipped to obtain

$$p_m(x,r,\omega) = -j \sum_{n=1}^{\infty} \tilde{\mathcal{F}}_m \frac{J_m(\alpha_{mn} r) J_m(\alpha_{mn} r_s)}{Q_{mn} J_m(\alpha_{mn})^2} e^{-j\kappa_{mn} x} \quad . \tag{4.72}$$

Finally, we define the inverse Fourier time-transform as

$$p_m(x,r,t) = \frac{1}{2\pi} \int_{-\infty}^{\infty} p_m(x,r,\omega) e^{j\omega t} d\omega \quad , \tag{4.73}$$

in which the integration over ω is performed by noting that the zeros of the delta function occur when $\omega = \omega_0 + \mu\bar{\Omega}$ and rewriting

$$\frac{2\bar{\Omega}(-1)^{m+1}\sin\pi\frac{\omega-\omega_0}{\bar{\Omega}}}{m\bar{\Omega}-(\omega-\omega_0)} = 2\pi\frac{\sin\left[m\pi-\pi\frac{\omega-\omega_0}{\bar{\Omega}}\right]}{\left[m\pi-\pi\frac{\omega-\omega_0}{\bar{\Omega}}\right]} \quad . \tag{4.74}$$

The evaluation of the inverse Fourier time-transform yields

$$p_m(x,r,\omega) = -f_0\sum_{\mu=-\infty}^{\infty}\left\{\sum_{n=1}^{\infty}\frac{\sin(m\pi-n\pi)}{(m\pi-n\pi)}\left(\kappa\cos\gamma+\frac{m}{r}\sin\gamma\right)\right. \\ \left.\frac{J_m(\alpha_{0mn}r)J_m(\alpha_{0mn}r_s)}{Q_{0mn}J_m(\alpha_{0mn})^2}e^{-j\kappa_{mn}x}e^{j(\omega_0+n\bar{\Omega})t}\right\} \quad , \tag{4.75}$$

in which the summation over μ is reduced to a single term by the fact that

$$\frac{\sin(m\pi-n\pi)}{(m\pi-n\pi)} = \begin{cases}1, & n=m\\ 0, & n\neq m\end{cases} \tag{4.76}$$

Therefore, the final time-domain expression for a rotating single-frequency dipole in a infinite lined duct with uniform mean flow writes

$$p_m(x,r,\theta,t) = -\frac{1}{2\pi}f_0\sum_{m=-\infty}^{\infty}e^{-jm\theta}\sum_{n=1}^{\infty}\left(\kappa\cos\gamma+\frac{m}{r}\sin\gamma\right) \\ \frac{J_m(\alpha_{0mn}r)J_m(\alpha_{0mn}r_s)}{Q_{0mn}J_m(\alpha_{0mn})^2}e^{-j\kappa_{mn}x}e^{j(\omega_0+m\bar{\Omega})t} \quad , \tag{4.77}$$

where the '0' subscripts in α_{0mn} and Q_{0mn} indicate that they are evaluated a the shifted frequency $\omega = \omega_0 + m\bar{\Omega}$.

An equivalent expression can be obtained by taking the approach based on Goldstein's acoustic analogy. Starting from Eq. 4.43 and taking the same assumption of an harmonic dipole source than for the current formulation, i.e. $f(\hat{\boldsymbol{y}},\boldsymbol{\tau}) = f_0 e^{j\omega_0\tau}$, the integral over the emission time is now of the form

$$\int_{-\infty}^{\infty} f_0 e^{-j(\omega-[\omega_0+m\bar{\Omega}])\tau}d\tau = f_0\delta(\boldsymbol{y},\omega-[\omega_0+m\bar{\Omega}]) \quad . \tag{4.78}$$

After the ω-integration, the pressure expression for the equivalent problem based on the former approach results in

$$p(\boldsymbol{x},t) = -\frac{1}{2\pi} f_0 \sum_{m=-\infty}^{\infty} e^{-jm(\theta-\tilde{\theta}_s)} \sum_{n=1}^{\infty} \left(\kappa_{mn}^{\pm} \cos\gamma + \frac{m}{r_s} \sin\gamma \right) \frac{J_m(\alpha_{mn}^{\pm} r) J_m(\alpha_{mn}^{\pm} r_s)}{Q_{mn}^{\pm} J_m(\alpha_{mn}^{\pm})^2} e^{-j\kappa_{mn}^{\pm}(x-x_s)} e^{j(\omega_0+m\bar{\Omega})t} \quad , \quad (4.79)$$

where α_{mn} and Q_{mn} are also evaluated at the shifted frequency $\omega = \omega_0 + m\bar{\Omega}$.

The former model based on the Goldstein's acoustic analogy and the Green's function is used in Chapter 6 since it has been conveniently derived in the frequency domain. This exercise has been a useful cross-verification of the two different approaches taken in the literature to model the effect of rotating sources and has shown that they yield the same expressions provided equivalent assumptions on the source model.

4.4.3 Modelling of the dipole source strength

It follows from the expressions in this section that the dipole strength function $f(\hat{\boldsymbol{y}},\omega)$ is required for the modelling of the effects of source rotation in the frequency domain. Indeed, a realistic estimate of this magnitude would also make the source modelling used for comparison with the OTR W-8 NASA data more representative of a rotor blade.

The modelling of fan self-noise is more suitably expressed, due to its broadband nature, in terms of the pressure cross-spectrum S_{pp} between two observer positions $\boldsymbol{x}$ and $\boldsymbol{x}'$ expressed as

$$S_{pp}(\boldsymbol{x},\boldsymbol{x}',\omega) = \lim_{T\to\infty} \frac{\pi}{T} E\{p(\boldsymbol{x},\omega) p^*(\boldsymbol{x}',\omega)\} \quad , \quad (4.80)$$

where * denotes the complex conjugate and $E\{\}$ the expectation value.

For a distribution of dipole sources given by the generalisation of Eq. 4.43, the pressure cross-spectrum in a lined cylindrical duct with uniform mean flow can be expressed as

$$S_{pp}(\boldsymbol{x},\boldsymbol{x}',\omega) = \iint_{\tilde{S}} \iint_{\tilde{S}'} \sum_{m=-\infty}^{\infty} \sum_{m'=-\infty}^{\infty} S_{ff}(\tilde{\boldsymbol{y}},\tilde{\boldsymbol{y}}',\omega-m\bar{\Omega},\omega-m'\bar{\Omega}) G_m(\boldsymbol{x},\tilde{\boldsymbol{y}},\omega) G_{m'}^*(\boldsymbol{x}',\tilde{\boldsymbol{y}}',\omega) e^{-jm(\theta-\tilde{\theta}_s)} e^{jm'(\theta'-\tilde{\theta}'_s)} d\tilde{S}(\tilde{\boldsymbol{y}}) d\tilde{S}'(\tilde{\boldsymbol{y}}') \quad , \quad (4.81)$$

where

$$G_m(\boldsymbol{x},\tilde{\boldsymbol{y}},\omega) = -\frac{1}{2\pi} \sum_{n=1}^{\infty} \frac{J_m(\alpha_{mn}^{\pm} r) J_m(\alpha_{mn}^{\pm} r_s)}{Q_{mn}^{\pm} J_m(\alpha_{mn}^{\pm})^2} e^{-j\kappa_{mn}^{\pm}(x-x_s)} \left[\kappa_{mn}^{\pm} \cos\gamma + \frac{m}{r_s} \sin\gamma \right] \quad , \quad (4.82)$$

and

$$S_{ff}(\tilde{\boldsymbol{y}}, \tilde{\boldsymbol{y}}', \omega, \omega') = \lim_{T\to\infty} \frac{\pi}{T} E\{f(\tilde{\boldsymbol{y}}, \omega) f^*(\tilde{\boldsymbol{y}}', \omega')\} \quad , \tag{4.83}$$

is the source spatial and frequency cross-spectrum, which is often based on models of the boundary layer pressure fluctuations on the blade surface [114–116, 119] due to Amiet's theory [68] of trailing edge noise in isolated blades.

The simplifying assumptions for the fan noise model that follows are based in the approach of Lowis et. al [116] and can be summarised as:

1. The acoustic sources of each blade are concentrated at the trailing edge ($x_s = x_s'$).
2. The fan consists of B identical uncorrelated blades.
3. Each rotor blade is considered a flat plate with zero pressure gradient.
4. The surface pressure fluctuations are assumed to be concentrated at the trailing edge and the scattering of the hydrodynamic pressure field as it sweeps past the trailing edge is not considered.

The source cross-spectrum can be rewritten from assumptions (1) and (2) as

$$S_{ff}(\tilde{\boldsymbol{y}}, \tilde{\boldsymbol{y}}', \omega, \omega') = S_{ff}(r_s, r_s', \tilde{\theta}_{s_0}, \omega, \omega') \delta(\theta_{s_p} - \theta_{s_p}') \delta(\theta_{s_p} - 2\pi p/B) \quad , \tag{4.84}$$

where θ_{s_p} is the azimuthal position of the trailing edge of each pth rotor blade.

An additional assumption (5) has been taken here to consider a homogeneous turbulent boundary layer such that

$$S_{ff}(\tilde{\boldsymbol{y}}, \tilde{\boldsymbol{y}}', \omega, \omega') = S_{ff}(\tilde{\boldsymbol{y}}, \tilde{\boldsymbol{y}}', \omega) \delta(\omega - \omega') \quad . \tag{4.85}$$

The flat plate turbulence model used here to describe the spatial cross-spectrum follows assumptions (3)-(5) and is given by Blake [120] as

$$S_{ff}(r_s, r_s', \omega) = \phi_{ff}(r_s, \omega) e^{-\bar{\gamma} \frac{\omega |r_s - r_s'|}{U_c}} \quad , \tag{4.86}$$

where ϕ_{ff} is the single-point spectrum of wall pressure fluctuations beneath the turbulent boundary layer, $\bar{\gamma}$ is an experimental constant (typically 0.7 [116]) and U_c is the non-dimensional turbulent eddy convection velocity given by

$$U_c(r_s) = 0.7 \sqrt{(\bar{\Omega} r_s)^2 + M^2} \quad . \tag{4.87}$$

The expressions implemented for ϕ_{ff} are the non-dimensional version of those provided by Blake [120], that is

$$\phi_{ff}(\omega, r_s) \propto \begin{cases} U_\tau^4 \left(\frac{\delta}{U_c}\right) \left(\frac{\omega\delta}{U_c}\right)^2 & \text{for} \quad \frac{\omega\delta}{U_c} \leq 1 \\ U_\tau^4 \omega^{-1} & \text{for} \quad 1 < \frac{\omega\delta}{U_c} \leq \frac{\frac{1}{30} U_\tau \delta}{\nu} \\ U_\tau^4 \omega^{-1} \left(\frac{\omega\delta}{U_c}\right)^{-4} & \text{for} \quad \frac{\omega\delta}{U_c} > \frac{\frac{1}{30} U_\tau \delta}{\nu} \end{cases} , \tag{4.88}$$

where U_τ, δ and ν are the non-dimensional hydrodynamic friction velocity, boundary layer thickness, and kinematic viscosity. The non-dimensional boundary layer thickness δ is estimated as [120]

$$\delta = \frac{c}{Re_c^{0.2}} \quad , \tag{4.89}$$

where c is the non-dimensional rotor-blade chord and Re_c the Reynolds number $U_\infty c/\nu$. The three ranges of $\frac{\omega\delta}{U_c}$ in Eq. 4.88 correspond to the regions where the dominant convected eddies are in the outer region of the boundary layer, the logarithmic region and the viscous sublayer respectively. Note that the variables involved in Eq. 4.88 vary for each radial source position, which means that the radial distribution of source strength is affected by $\bar{\Omega}$, the spanwise rotor-blade chord distribution and frequency.

The final expression for the pressure cross-spectrum for the fan self-noise model adopted in this thesis can be obtained by substitution of Eq. 4.84-4.86 in Eq. 4.81 to yield

$$S_{pp}(\boldsymbol{x}, \boldsymbol{x}', \omega) = B \int_{r_s} \int_{r_s'} \sum_{m=-\infty}^{\infty} \phi_{ff}(r_s, \omega - m\bar{\Omega}) e^{-\tilde{\gamma} \frac{(\omega - m\bar{\Omega})|r_s - r_s'|}{U_c}} G_m(\boldsymbol{x}, \tilde{\boldsymbol{y}}, \omega) G_m^*(\boldsymbol{x}', \tilde{\boldsymbol{y}}', \omega) e^{-jm(\theta - \tilde{\theta}_s)} r_s r_s' dr_s dr_s' \quad . \tag{4.90}$$

The integrals over the source region S and S' in the pressure cross-spectrum of Eq. 4.81 are reduced to integrals over the radial source position due to assumptions (1) and (2) expressed in Eq. 4.84 and assumption (5) reduces the double summation over m and m' to a single sum over m. The two integrals are discretised and evaluated numerically for a source separation distance that provides a converged solution for the frequency range, axial Mach number and non-dimensional shaft rotation frequency of interest.

This model allows for a radial variation of the rotor blade chord as well as variable twist by modifying the dipole stagger angle Θ in the Green's function. The impact of these variables in the predicted OTR noise reduction is analysed in Chapter 6.

4.5 In-duct sound power

The non-dimensional acoustic axial power at each axial cross-section (S) can be used to assess the performance of liners. It is computed by integrating the intensity field over the duct cross-section, resulting in [121–124]:

$$P(x) = \int_S I_x dS = \frac{1}{2} \int_S Re\left\{ pu_x^* \left(1 + M^2\right) + Mpp^* + Mu_x u_x^* \right\} dS \tag{4.91}$$

The power computation can be done either fully numerically using the pressure and particle velocity resultant of the mode summation, or by considering that the total power can be computed as the sum of individual modal powers. The second approach is more accurate because the circumferential integration can be obtained analytically, leaving only the radial integration to be computed numerically. It is common to analyse the liner acoustic performance using the Sound Power Level (PWL) Insertion Loss (IL) or just IL, defined as the power relative to the hard wall case in dB scale.

$$\mathrm{IL}(x) = 10 \log_{10} \frac{P_H(x)}{P_L(x)} \quad [dB] \tag{4.92}$$

where P_H and P_L are the acoustic power for the hard wall and lined configurations obtained using Eq.4.91.

As usual, the infinite number of modes that define the analytical solution of the acoustic field cannot be computed. Therefore, a parameter to control the series truncation is used, which determines the number of modes considered in the computation. This parameter is called Cut-Off Ratio (COR) and the definition that has been used is:

$$\mathrm{COR} = \frac{\alpha \sqrt{1 - M^2}}{\omega} \tag{4.93}$$

The radial wave number increases with the mode order, which means that for a given COR all the modes with α smaller than $\frac{\omega \mathrm{COR}}{\sqrt{1-M^2}}$ are included in the modal summation. Note that COR=1 corresponds to only cut-on modes and that COR>1 will include a certain number of evanescent modes. The evanescent modes play an important role in the near-field of the source [51] and therefore CORs sensibly higher than one have been used.

4.6 Effect of the boundaries in the source power output

In this section, an analysis is presented of the effects that the impedance boundary condition, the source radial position and excitation frequency have on the acoustic power generated by a monopole and axial dipole point source in an infinite hard and lined duct with and without axial uniform mean flow. The axial acoustic power is computed at the

source plane by integrating the axial intensity over the cross-section of the duct using Eq. 4.91. The intensity field is obtained from the Green's function modal expansion of the pressure (Eq. 4.14) and the axial particle velocity (Eq. 4.20). Hence, in practice, the intensity field is truncated to a finite number of modal contributions and can be integrated analytically. The total power radiated by the source P is obtained by adding the absolute power radiated upstream $|P^-|$ and downstream $|P^+|$, as indicated in Fig. 4.3.

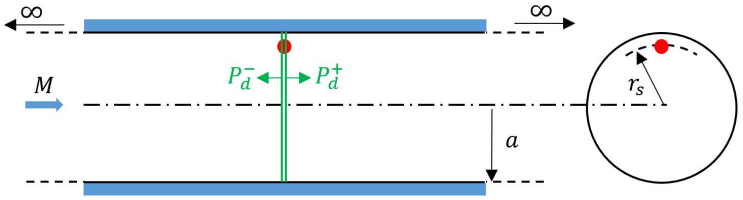

Figure 4.3: Lateral and cross-section of the infinite circular duct problem and axial acoustic power evaluation *at* the source plane.

Any axial position upstream and downstream of the source would be sufficient in the case of a hard wall duct because there is no energy loss as the modes propagate axially. However, the evaluation of the power *at* the source plane is key for the lined case because it omits any energy dissipated by propagation over the lined walls. The axial power results of this section are normalised by the power radiated by a monopole/dipole source in free-field and zero flow. That is, P_d/P_f, the subscripts d and f referring to ducted and free-field respectively. A similar analysis for monopoles and dipoles has been previously published for a hard wall duct [125], which is extended here to lined ducts. The total non-dimensional power radiated in free-field by a volume acceleration monopole of unit strength and a dipole point source without flow are:

- Monopole: $P_f = \frac{1}{8\pi}$
- Dipole: $P_f = \frac{\omega^2}{24\pi}$

The power output of a monopole source over an infinite plane is included in the analysis of this section and compared to the results obtained with the in-duct expressions. The analytical solutions of Levine [6] described in Appendix B are used for the comparison with the in-duct results presented here. The first part of the section deals with a hard wall duct, which also includes a cross-verification with FEM numerical solutions. The second part is focused on a lined duct and the comparison with the half-space problem. The third combines the hard wall and lined results to assess the source modification effects in terms of Insertion Loss.

4.6.1 Source power output in a hard wall duct

Cross-verification with FEM numerical results

The numerical solutions in this section were obtained using the FEM commercial software Simcenter 3D Acoustics [100]. A brief description of the FEM formulation used has been outlined earlier in Section 3.3.2. An 'infinite' 3D duct has been numerically modelled by using a finite duct terminated with a PML-type anechoic boundary condition at each end of the duct section [100]. A diagram of the problem and a cross-section of the unstructured tetrahedral mesh used is shown in Fig. 4.4. The white spheres indicate the different source radial locations tested. As in Section 3.3.2, the mesh has been created following the guidelines given in [101], including smaller elements in the cylinder surface to ensure that the geometry at the boundaries is well represented and around the source locations.

This cross-verification is limited to the hard wall case with and without mean flow. The total power radiated by a monopole source is computed analytically and numerically for different excitation frequencies, radial source positions and base mean flow Mach numbers. This comparison does not target high-resolution computations that minimise the relative error between the numerical and analytical results but aims to ensure that the trends observed in the analytical solutions are also present in the FEM solution.

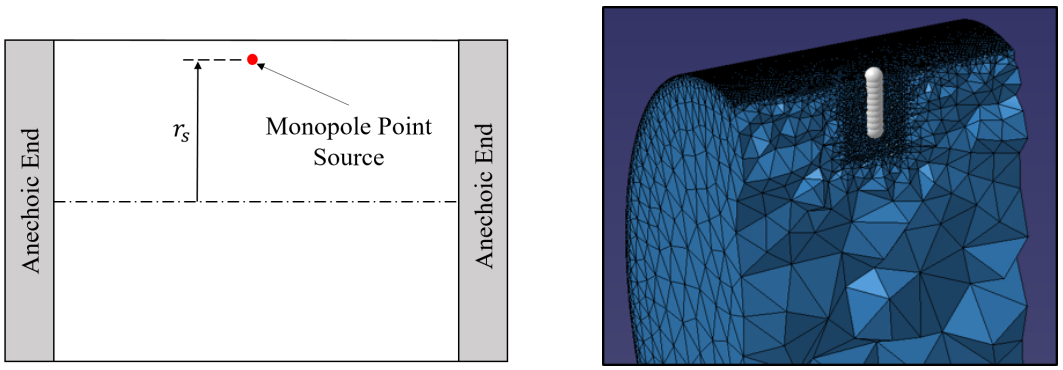

(a) Diagram of the problem

(b) Cross-section of the mesh

Figure 4.4: (a) Numerical implementation of the infinite duct and (b) cross-section of the tetrahedral mesh with refinement in the source region.

A sample of this comparison is showed in Figure 4.5. The total power radiated by the monopole source is plotted against the radial source position at different excitation frequencies, the solid lines are analytical solutions and the symbols the numerical results. The agreement in the absence of mean flow is excellent (Figure 4.5a). The addition of mean flow introduces some errors in the solution, but the trends are still well modelled (Figure 4.5b). This agreement holds for other frequencies and Mach numbers tested, only giving higher errors if the mode is near cut-off, where the numerical solution becomes ill-conditioned.

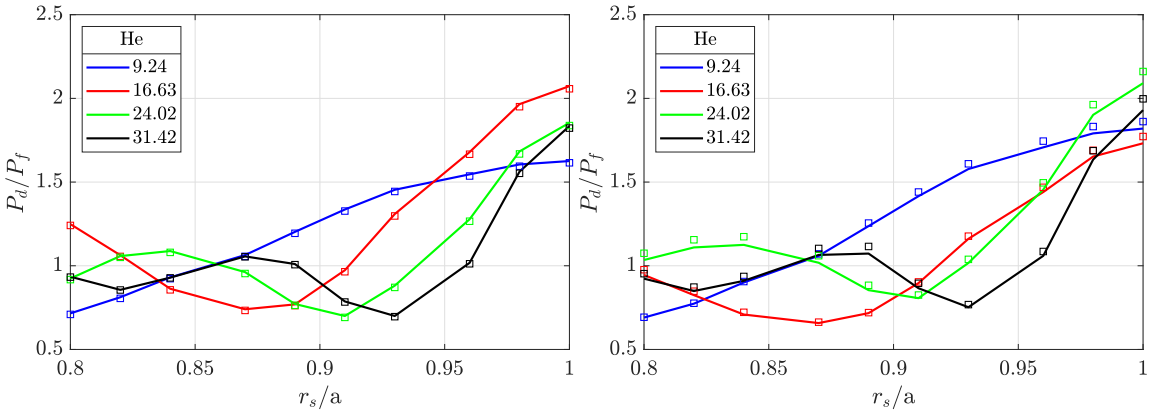

(a) $M = 0.0$ (b) $M = 0.2$

Figure 4.5: Power radiated by a monopole source at different source radial positions: analytical (solid line) and numerical (symbols) results: (a)$M = 0.0$ and (b)$M = 0.2$.

Parametric analytical analysis

The effect of the source radial position and the excitation frequency in the normalised power output is shown in Fig.4.6 considering a hard wall case. The results indicate that the power tends to the free-field value when the source is located away from the wall and tends to twice this value when located at the wall itself. It can be seen that the wall acts as an image source if the source is located very close to it. The variation in radiated power gets progressively confined to the vicinity of the wall as the frequency is increased. However, the effects of the source position are minimal in the low frequency range, where the power spectrum is dominated by the cutting-on process. The power output of the source at high frequency tends to be that of a source over an infinite rigid plane. This behaviour occurs both for a monopole and a dipole source, the latter not being included here for brevity.

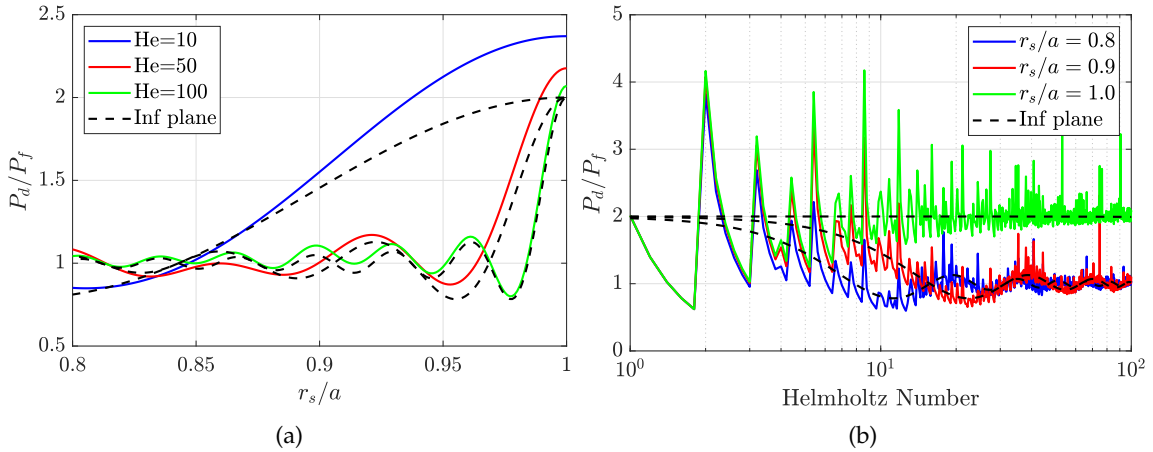

(a) (b)

Figure 4.6: Power generated by a monopole in a hard duct for various radial source positions and excitation frequencies with COR=5 and $M = 0$ and comparison with a half-space equivalent problem [6].

The results in Fig.4.6 are plotted in Fig.4.7 in terms of the radial distance from the source to the wall ($e = 1 - r_s$) normalised by the wavelength (λ). The curves collapse and show the relation between the source radial location and frequency outlined above. The same trends can be observed for the ducted solution and the half-space problem and the agreement improves at higher frequencies.

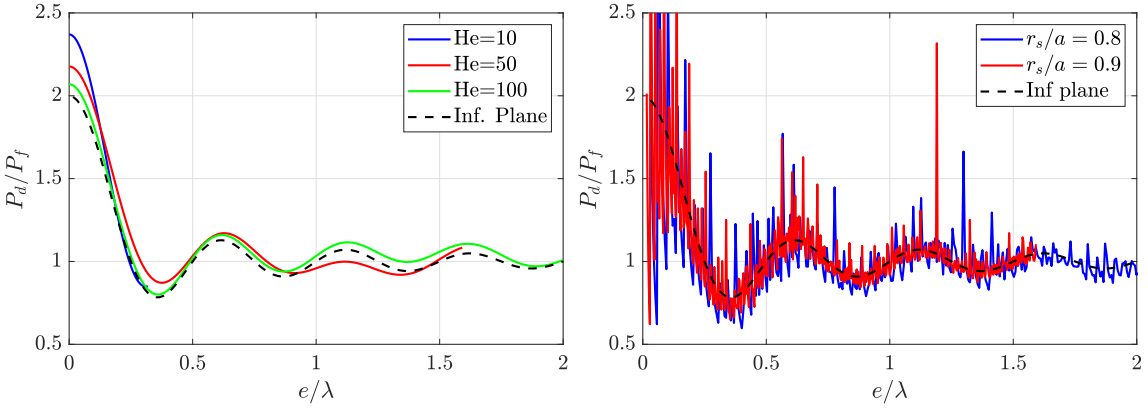

(a) (b)

Figure 4.7: Power generated by a monopole in a hard duct for various normalised radial source positions ($e = 1 - r_s$) and excitation frequencies with COR=5 and $M = 0$ and comparison with a half-space equivalent problem [6].

The total power generated by a monopole and an axial dipole source for various base flow Mach numbers is shown in Figure 4.8. The results obtained here are compared with the multi-mode high-frequency Mach number expressions of Joseph et al. [7] relating the dependence of axial sound power with and without flow for an incoherent uniform distribution of sources of arbitrary spatial and temporal order over the duct cross-section. In particular, for the monopole ($(\mu,\nu) = (0,0)$) and axial dipole ($(\mu,\nu) = (1,0)$) considered in this section:

$$\frac{P^+(M)}{P^+(0)} = \begin{cases} 1+M, & (\mu,\nu) = (0,0) \\ \frac{3[M^4+M^3-M^2-2M-2(1-M^2)\ln(1+M)]}{M^3(1-M^2)}, & (\mu,\nu) = (1,0) \end{cases} \tag{4.94}$$

Note that these expressions are for the acoustic axial power radiated downstream and that to obtain the total power radiated by the source one should add the contributions of $P^+ = P^+(+M)$ and $P^- = P^+(-M)$.

It can be observed in Fig 4.8a that the effect of the Mach number in the power generated by a monopole is minimal, especially at high frequencies. The differences observed at lower frequencies are attributed to a different number of modes being cut-on, since the cut-off frequency of each mode changes with Mach number. However, the total power radiated by an axial dipole increases with Mach number, as shown in Figure 4.8b. These

trends agree with the high-ω expressions of Eq. 4.94, shown in both figures as dashed lines.

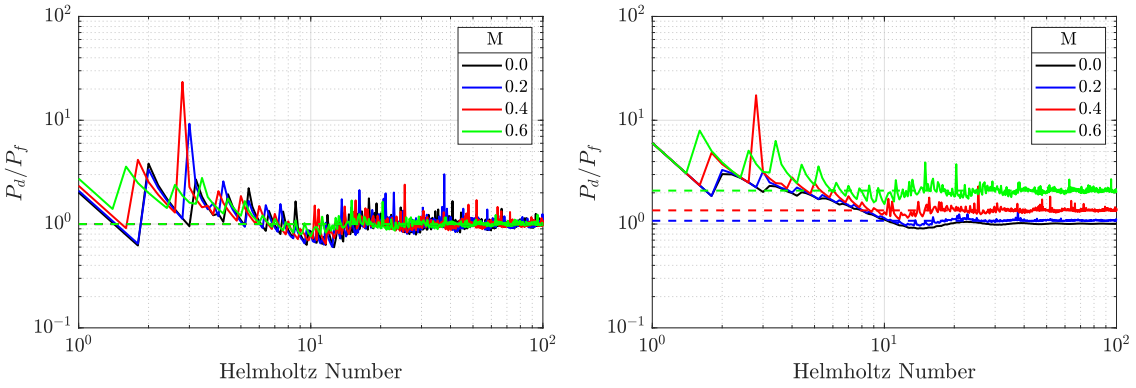

(a) Monopole (b) Axial dipole

Figure 4.8: Power spectra of a monopole/dipole source for various base flow Mach numbers and $r_s/a = 0.8$. Dashed line: multimode high-ω limit [7].

The monopole and axial dipole show the opposite behaviour regarding the ratio of power radiated downstream and upstream as indicated in Fig. 4.9. The monopole radiates more power downstream than upstream and, on the contrary, the dipole radiates more power upstream than downstream. It can be shown that Eq. 4.94 can be rearranged to obtain the ratio of downstream to upstream power in the high-frequency limit (Eq. 4.95), shown as the dashed lines in Fig. 4.9 and in good agreement with the point source tendency presented here.

$$\frac{P^+(M)}{P^-(M)} = \begin{cases} \frac{1+M}{1-M}, & (\mu,\nu) = (0,0) \\ -\frac{M^4+M^3-M^2-2M-2(1-M^2)\ln(1+M)}{M^4-M^3-M^2+2M-2(1-M^2)\ln(1-M)}, & (\mu,\nu) = (1,0) \end{cases} \tag{4.95}$$

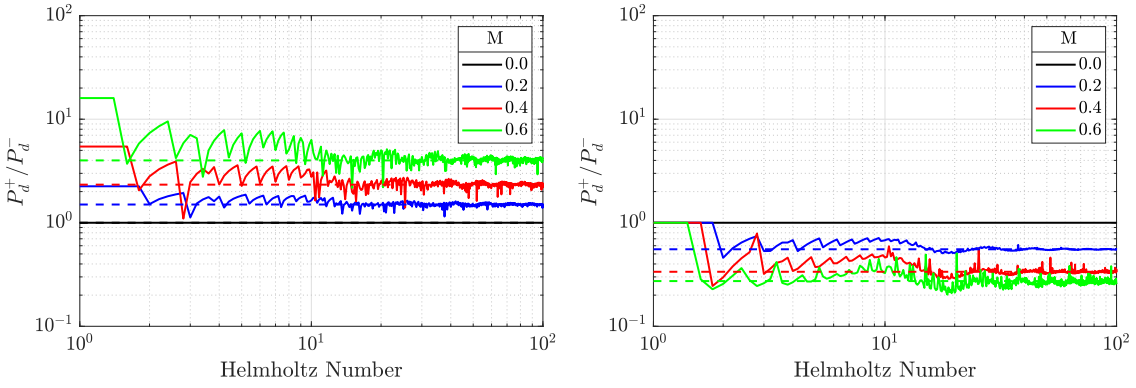

(a) Monopole (b) Axial dipole

Figure 4.9: Spectra of the ratio of power radiated downstream and upstream by a monopole/dipole source for various base flow Mach numbers and $r_s/a = 0.8$. Dashed line: multimode high-ω limit [7].

4.6.2 Source power output in a lined duct

This part of the section aims at extending the analysis of Section 4.6.1 to lined ducts, for which three values of impedance have been used to assess the impact of this parameter on the trends observed in Fig.4.6-4.7. As mentioned before, the power is evaluated at the source plane to capture the power *generated* by the source before it starts decaying as the modes propagate over the lined surface. Note that the acoustic field in a lined duct at the source plane is a singularity formed by an infinite summation of modes with complex axial wavenumber. A consistent comparison of the power at the source plane is obtained by limiting the number of modes in the solution (truncating the infinite mode summation) and maintaining the COR constant for all cases. The effect of the COR in the predicted trends is also addressed.

The effect of the lined surfaces is shown in Fig.4.10, where the results are again plotted in terms of e/λ. The trends are similar to those for the hard wall case: the duct wall has almost no effect in the power output provided that the distance between the source and the wall is large enough, this distance depending on the source excitation frequency. That is, the source proximity to the wall is only important if the source is located within $1/2$ a wavelength from it. This result holds for all values of impedance tested and is also applicable to a dipole source. The same trend has been measured experimentally and discussed in Section 2.5. However for $e/\lambda < 0.5$ the value of the impedance has a significant impact on the source power output, which is up to 10 times higher than in free-field when e/λ tends to zero. In those circumstances, the solution given by Levine and the in-duct Green's function start diverging unless the number of cut-off modes in the in-duct solution is substantially increased.

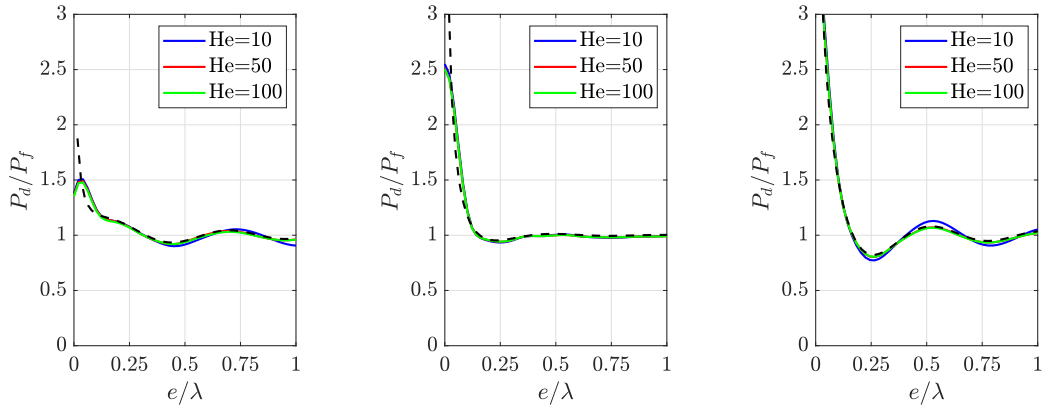

(a) $Z = 1 + j$ (b) $Z = 1$ (c) $Z = 1 - j$

Figure 4.10: Power generated by a monopole in a lined duct for various impedance values, normalised radial source positions ($e = 1 - r_s$) and excitation frequencies with COR=5 and $M = 0$ and comparison to a half-space equivalent problem [6].

As pointed out in the last paragraph, the number of modes considered in the solution, controlled with the COR, has a significant impact on the predicted power output for source positions acoustically close to the lined wall. The results in Fig. 4.11 show how the progressive increase of COR moves the solution closer to Levine's solution for a half-space problem. The power output in the case of a source over a lined plane tends to infinity for $e/\lambda \to 0$ but the power absorbed by the lined plane too in such a way that the actual radiated power in the hemisphere remains finite. The interpretation in the lined duct is that an infinite number of modes with a non-zero real part of the axial wavenumber are present at the source plane, but these are highly evanescent and have little effect away from the source plane. The maximum azimuthal mode order and the total number of modes included in the calculations for a He=10 are indicated in Table 4.1 for reference.

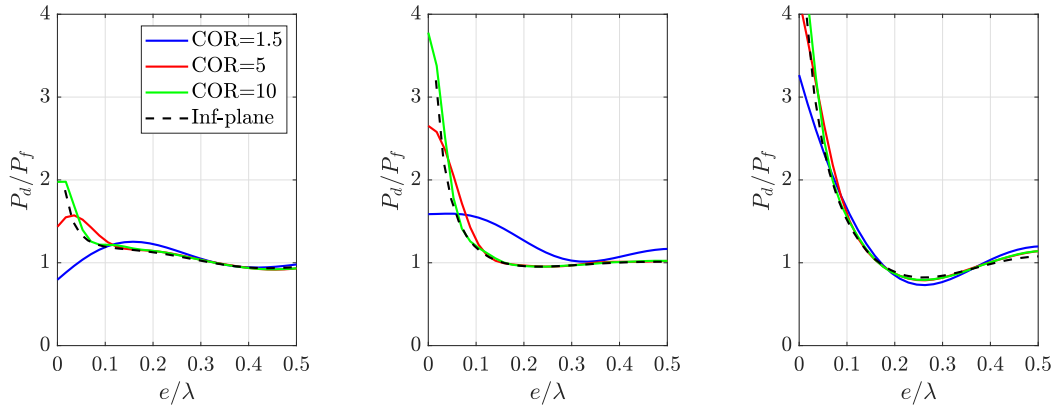

(a) $Z = 1 + j$ (b) $Z = 1$ (c) $Z = 1 - j$

Figure 4.11: Power generated by a monopole in a lined duct for various impedance values, normalised radial source positions ($e = 1 - r_s$) and CORs with $He = 10$ and $M = 0$ and comparison to a half-space equivalent problem [6].

Table 4.1: Modes included in the solution for $He = 10$ and various COR.

COR	$m_{\max}$	N
1	9	17
5	48	333
10	97	1294

The main implication of this section is that the power generated by simple point sources is modified if the source is located in the proximity of a lined surface. The power modification will vary for each combination of impedance, source location and source excitation frequency, especially for $e/\lambda < 0.5$. Therefore, the predictions of power IL will combine the effects of the liner attenuation when the sound propagates over the lined surface *and* the variation in the power *generated* by the source due to the wall impedance. This idea is addressed in greater detail in the next part of the section.

4.6.3 Implications on PWL Insertion Loss

This part of the section aims at evaluating the implications of the power modifications described in Sections 4.6.1-4.6.2 in the context of predicting the acoustic performance of Over-Tip-Rotor liners. To this end, the ducted axial power is no longer normalised by the source power output in free field but compared for a hard and lined configurations.

The axial variation of the absolute PWL for a hard and lined wall is shown in Fig. 4.12 for two radial locations of the source e/λ=[0.1,0.3] corresponding to r_s/a=[0.94,0.81] respectively. The PWL IL at each axial position is obtained, as defined in Eq. 4.92, by subtracting the PWL obtained with a hard wall and a lined configuration. The former is constant and does not vary in different axial locations since there is no dissipative process but the latter decays as the waves propagate upstream away from the source due to the liner absorption. It has been observed earlier in this section that the source power output varies with the wall impedance and frequency. Therefore, the PWL IL can be separated into two contributions as follows

$$\mathrm{IL}(x) = \mathrm{TL}(x) + \Delta P_s = 10\log_{10}\frac{P_L(x_s)}{P_L(x)} + 10\log_{10}\frac{P_H}{P_L(x_s)} \tag{4.96}$$

where $\mathrm{TL}(x)$ is the Transmission Loss, measuring the liner *attenuation*, and ΔP_s accounts for the variation in the source power *generation* due to a different boundary condition and the back-reaction effects. Note that the axial dependence in the hard wall power (P_H) is omitted because is constant along the duct and that $P_L(x_s)$ refers to the axial acoustic power evaluated at the source plane for the lined duct. This separation of the IL into two components is indicated graphically in Fig. 4.12a for the absolute PWL and in Fig. 4.12b directly for the PWL IL.

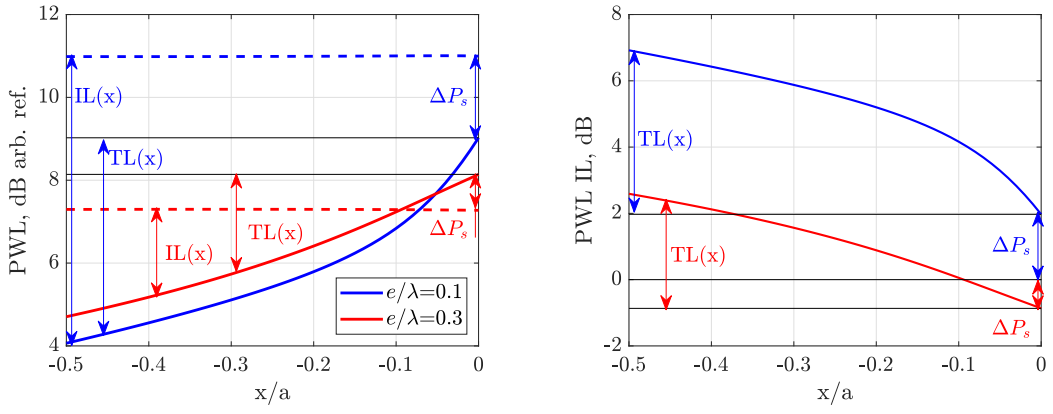

(a) Sound Power Level

(b) Insertion Loss

Figure 4.12: Axial variation of the PWL and PWL IL for a monopole source located at $x_s/a = 0$ in a lined (solid lines) or hard wall (dashed lines) duct for $Z = 1 + j$, COR=5, $He = 10$ and $M = 0$.

As discussed previously, the source power output in a hard wall duct is bounded to twice the free-field power but it can be larger for a lined duct. Hence, close to the source plane, the PWL in a lined duct can exceed, under certain conditions, that in a hard wall, leading to noise *amplification* (negative IL). Noise amplification near the source plane can be observed both in Fig. 4.12a comparing the hard and lined PWL at the source, and explicitly in Fig. 4.12b, when the source is located at e/λ=0.3.

The effect of the source proximity to the wall in the power output can be presented in terms of the PWL IL evaluated at the source plane, providing insight on the noise modification component. This is readily obtained by combining the results of Fig. 4.7a and Fig. 4.11, as shown in Fig. 4.13. The noise modification effects tend to produce a positive IL when placed away from the source (large e/λ) but can lead to up to 3 dB of noise amplification as $e/\lambda \to 0$. As long as enough liner surface can be acoustically treated, the transmission loss will eventually compensate for a negative ΔP_s. However, it may not always be the case for a short lined section, such as in OTR applications, when negative IL can be obtained. The implications of this phenomena in the mode-matching technique and the related challenges are described in Section 5.2.2.

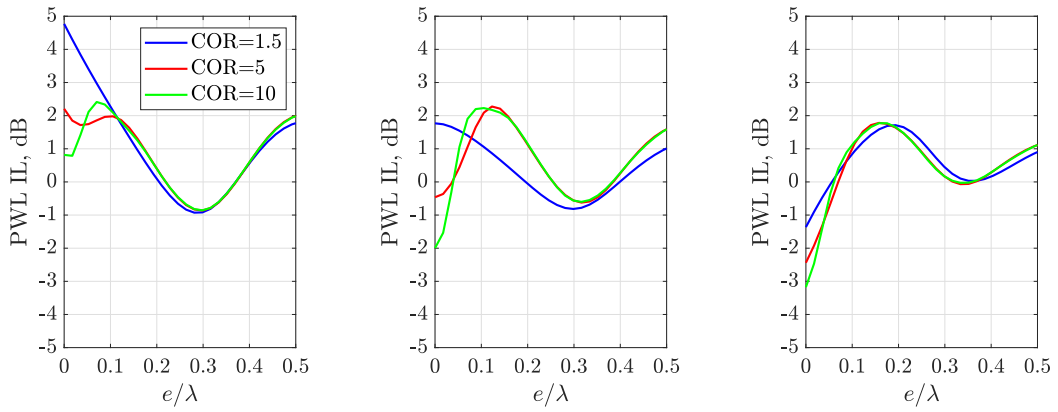

(a) $Z = 1 + j$ (b) $Z = 1$ (c) $Z = 1 - j$

Figure 4.13: PWL IL evaluated at the source plane for a monopole in a lined duct for various impedance values and CORs with $He = 10$ and $M = 0$.

4.7 Summary and conclusions

4.7.1 Summary

- The formulation adopted in this thesis to model the acoustic field of static monopoles and dipoles in a lined circular duct with uniform mean flow has been presented as well as the approach taken to solve the eigenvalue equation.
- The static expressions for dipole sources have been adapted to rotating dipoles using two approaches based on the Goldstein acoustic analogy and the direct solution of the inhomogeneous wave equation.
- The model of a point rotating dipole source is extended under certain simplifying assumptions to provide a model for the pressure cross-spectrum of in-duct rotor-blade fan noise that is compared with OTR NASA experimental data in Chapter 6.
- The definition and expressions to compute the axial acoustic power and to control the number of modes included in the solution of the acoustic field are given.
- The impact of the hard and lined boundary conditions, the source frequency and the Mach number of the base flow on the power output of in-duct point monopoles and dipoles is assessed. The analytical axial acoustic power is cross-verified with FEM solutions and compared with the analytical formulation of Levine [6] for a half-space problem.

4.7.2 Conclusions

- It is found that the two approaches for the modelling of rotating in-duct sources yield equivalent expressions if the same assumptions on the source strength are taken. The approach based on the Goldstein's acoustic analogy is used in Chapter 6 since it has been conveniently derived in the frequency domain.
- The in-duct source power output is dominated by the cutting-on process of the modes at low frequencies and tends to the free-field at the high frequency limit. The effects of the source proximity to the wall are more pronounced when the source is very close to the wall ($e/\lambda < 0.5$), in agreement with the experiments of Section 2.5.
- The in-duct power is found to tend to the half-space solution as the number of modes included in the modal summation is increased. The results suggest that predicted in-duct PWL IL combine the effects of the liner attenuation and the variation in the power *generated* by the source due to the wall impedance, which can lead to a negative liner insertion loss (IL) for some parameter combinations.

Chapter 5

Mode-matching in circular ducts with uniform mean flow

Contents

This chapter describes the mode-matching method implemented in this thesis to compute the acoustic field in circular ducts with an axially-segmented wall impedance and uniform mean flow. Two types of impedance discontinuities are presented: (1) a simple lined-hard discontinuity, which is effectively a cylindrical semi-infinite lined duct matched with a semi-infinite hard wall duct, and (2) a hard-lined followed by a lined-hard discontinuity, which represents an infinite cylindrical duct containing a finite lined section.

The first section of the chapter reviews two alternative formulations of the mode matching method for a single interface and a generic time-harmonic acoustic field. The second section includes a point source within the duct that excites the acoustic field and extends the single interface to a two interface problem, i.e. a finite length liner. The inclusion of a duct termination in the mode-matching method is described in the third section.

5.1 The mode-matching method

The mode-matching technique is a well-known method to compute the acoustic field in ducts with changes in wall impedance. It has been used in the field of aircraft engines since the 70s, when it was introduced by Lansing and Zorumski [126] to study the effect of axially-segmented liners on the transmission loss in jet engines. Similar matching methods are described in the literature [126, 127], including a comprehensive formulation in a more recent publication of McAlpine et. al. [128]. The standard approach of the mode-mode matching method is based on the continuity of acoustic pressure and axial particle velocity on the matching interface. Then, a Galerkin method of weighted residuals is often applied using the inner product of duct eigenfunctions with chosen test functions to transform the problem into a set of algebraic equations.

An alternative mode-matching technique based on the continuity of mass and momentum across the matching interface was formulated by Gabard and Astley [129]. This approach results in a finite contribution from the contour of the interface that, in the presence of flow, improves the accuracy of the solution in the vicinity of the impedance discontinuity. The contour term vanishes in the absence of flow and the standard continuity of pressure and axial particle velocity is recovered.

More recently a new mode-matching method was devised by Oppeneer et al. [130] based on closed-form analytical integrals of the modal solutions of the Pridmore-Brown equation allowing for parallel non-uniform mean flow. However, since uniform mean flow is assumed throughout the thesis only the classical mode-matching forms will be considered in the formulation that follows.

5.1.1 Formulation based on the continuity of pressure and particle velocity

The conventional formulation of the matching equations is based on the continuity of pressure (dynamic condition) and acoustic particle velocity (kinematic condition) at the interface between the lined and hard duct sections, i.e. at the impedance discontinuity. Alternatives to the acoustic particle velocity for the kinematic continuity condition have been proposed, such as continuity of axial acoustic displacement or a hybrid condition that lies between the two [131]. A diagram of the interface and the nomenclature used are depicted in Figure 5.1.

The time-harmonic pressure field in a generic cylindrical duct can be expressed as the superposition of right-running (+) and left-running (-) duct modes, see Section 4.1 for the derivation of this expression.

$$p(x,r,\theta) = \sum_{m=-\infty}^{\infty} e^{-jm\theta} \left(\sum_{n=1}^{\infty} A_{mn}^{+} J_m(\alpha_{mn}^{+} r) e^{-j\kappa_{mn}^{+} x} + A_{mn}^{-} J_m(\alpha_{mn}^{-} r) e^{-j\kappa_{mn}^{-} x} \right) \quad . \tag{5.1}$$

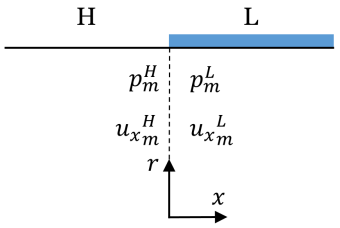

Figure 5.1: Detail of the matching interface and nomenclature.

The impedance of the liner is assumed to be axisymmetric, which restricts any scattering between azimuthal modal orders. Under this condition, scattering is only possible between radial modes. Therefore, the matching problem can be solved separately for each azimuthal mode number m. The pressure field in the hard and lined ducts for each m is given by Eq. 5.2-5.3. Note that the radial eigenvalues in the hard section are the same for both axial propagation directions ($\alpha_{mn}^{H+} = \alpha_{mn}^{H-} = \alpha_{mn}^{H}$).

$$p_m^H(x,r,\theta) = \sum_{n=1}^{\infty} \left(A_{mn}^{H+} J_m(\alpha_{mn}^H r) e^{-j\kappa_{mn}^{H+} x} + A_{mn}^{H-} J_m(\alpha_{mn}^H r) e^{-j\kappa_{mn}^{H-} x} \right) e^{-jm\theta} \quad . \tag{5.2}$$

$$p_m^L(x,r,\theta) = \sum_{n=1}^{\infty} \left(A_{mn}^{L+} J_m(\alpha_{mn}^{L+} r) e^{-j\kappa_{mn}^{L+} x} + A_{mn}^{L-} J_m(\alpha_{mn}^{L-} r) e^{-j\kappa_{mn}^{L-} x} \right) e^{-jm\theta} \quad . \tag{5.3}$$

The axial particle velocity can be obtained from the modal expansion of the pressure field and the non-dimensional linearised momentum equation in the axial direction:

$$j\omega u_x + M\frac{\partial u_x}{\partial x} + \frac{\partial p}{\partial x} = 0 \quad , \tag{5.4}$$

resulting for the hard and lined duct sections as

$$u_{x_m}^H(x,r,\theta) = \sum_{n=1}^{\infty} \left(\frac{\kappa_{mn}^{H+}}{\Omega_{mn}^{H+}} A_{mn}^{H+} J_m(\alpha_{mn}^H r) e^{-j\kappa_{mn}^{H+} x} + \frac{\kappa_{mn}^{H-}}{\Omega_{mn}^{H-}} A_{mn}^{H-} J_m(\alpha_{mn}^H r) e^{-j\kappa_{mn}^{H-} x} \right) e^{-jm\theta} \quad , \tag{5.5}$$

$$u_{x_m}^L(x,r,\theta) = \sum_{n=1}^{\infty} \left(\frac{\kappa_{mn}^{L+}}{\Omega_{mn}^{L+}} A_{mn}^{L+} J_m(\alpha_{mn}^{L+} r) e^{-j\kappa_{mn}^{L+} x} + \frac{\kappa_{mn}^{L-}}{\Omega_{mn}^{L-}} A_{mn}^{H-} J_m(\alpha_{mn}^{L-} r) e^{-j\kappa_{mn}^{L-} x} \right) e^{-jm\theta} \quad . \tag{5.6}$$

Imposing continuity of pressure and particle velocity at the interface implies:

$$p_m^H\Big|_{x=0} = p_m^L\Big|_{x=0} \quad , \tag{5.7}$$

$$u_{x_m}^H\Big|_{x=0} = u_{x_m}^L\Big|_{x=0} \quad . \tag{5.8}$$

The Galerkin method of weighted residuals is used to solve the above matching equations for a truncated value of radial modes N. This method uses the property that if a function is orthogonal to all members of a complete set, then the function must be zero [127].

The hard wall eigenfunctions can be used as weighting functions because they form a complete set and are orthogonal to each other both in the absence and in the presence of uniform mean flow. Using the Galerkin method, the matching equations result in

$$\int_{r=0}^{1} J_m(\alpha_{mn'}^H r) \left[p_m^L(0,r,\theta) - p_m^H(0,r,\theta) \right] r dr = 0, \quad n' = 1 \text{ to } N \quad , \tag{5.9}$$

$$\int_{r=0}^{1} J_m(\alpha_{mn'}^H r) \left[u_{x_m}^L(0,r,\theta) - u_{x_m}^H(0,r,\theta) \right] r dr = 0, \quad n' = 1 \text{ to } N \quad . \tag{5.10}$$

The expressions above (Eq. 5.9-5.10) can be expanded to 2N algebraic equations. Assuming that two sets of amplitudes are known, then the other two can be calculated by solving the resultant matrix equation. This derivation is explained in detail for cases with a point source within the duct in Section 5.2.1.

5.1.2 Formulation based on the continuity of mass and momentum

An alternative mode-matching technique starting from the first principles of continuity of mass and momentum at the matching interface was proposed by Gabard and Astley [129].

The method deals with the impedance discontinuity at the junction between the hard and lined sections at x=0, say, by introducing a transition region [-ϵ, +ϵ] over which the impedance is continuous and varies from Z_1 (at x=-ϵ) to its final value Z_2 (at x= +ϵ). The Ingard-Myers boundary condition then holds at all points in this region with no ambiguity at the previous liner discontinuity. The momentum and continuity equations are multiplied by a continuous weighting function and then integrated over the corresponding transition volume of the duct. The Ingard-Myers condition is incorporated weakly into these volume integral equations by applying Green's theorem to volume integrands involving the divergence of the acoustic velocity, introducing an additional boundary contribution. Finally, the transition volume is made vanishingly small by taking the limit as ϵ approaches zero.

The detailed derivation is not included here and can be consulted in reference [129], but the resultant non-dimensional corrected matching conditions with uniform mean flow can be written as

$$\int_S \overline{W}(p_2 - p_1) dS = -\frac{jM^2}{1-M^2} \frac{1}{\omega} \int_\Gamma \overline{W} \left(\frac{p_2}{Z_2} - \frac{p_1}{Z_1} \right) d\Gamma \quad , \tag{5.11}$$

$$\int_S \overline{W}(u_{x_2} - u_{x_1}) dS = \frac{jM}{1-M^2} \frac{1}{\omega} \int_\Gamma \overline{W} \left(\frac{p_2}{Z_2} - \frac{p_1}{Z_1} \right) d\Gamma \quad , \tag{5.12}$$

where S is the cross-sectional surface of the duct, Γ its contour, $\overline{W}$ a weighting function and the subscripts $1,2$ refer to each side of the matching plane. The terms on the right-hand side show a finite contribution of the contour at the matching plane in the presence of mean flow. These additional terms improve the accuracy of the mode-matching scheme when compared to reference FE solutions, especially at the vicinity of the impedance discontinuity [129].

Gabard [132] showed that the additional contour or boundary terms can be linked to the normal flux of mass and momentum across the vortex sheet and are consistent with the additional term of acoustic power proposed by Eversman [133] accounting for the acoustic power contained within the vortex sheet. It was also shown that the agreement between the analytical mode-matching schemes and the FE formulations rely on the underlying assumptions regarding the continuity of the impedance across the interface. That is, the mode-matching based on the continuity of mass and momentum with a continuous transition of impedance matches well with the variational FE formulation assuming a smooth variation of the impedance; but equally the conventional continuity of pressure and particle velocity agrees with the FE formulation for an abrupt change in impedance, obtained evaluating the contour integral from [134] in the lined section.

Analogous matching equations to Eq. 5.9-5.10 for a hard-lined interface can be obtained by substitution of the generic solutions of pressure and axial particle velocity into the expressions above. The hard wall eigenfunctions have been used again as weighting functions in this instance. The corrected matching equations for each azimuthal mode number m assuming a truncated value of radial modes N can be expressed as

$$\int_{r=0}^{1} J_m(\alpha_{mn'}^H r)\left[p_m^L(0,r,\theta) - p_m^H(0,r,\theta)\right] r dr = -\frac{jM^2}{1-M^2}\frac{1}{\omega} J_m(\alpha_{mn'}^H)\frac{p_m^L(0,1,\theta)}{Z} \quad , \tag{5.13}$$

$$\int_{r=0}^{1} J_m(\alpha_{mn'}^H r)\left[u_{x_m}^L(0,r,\theta) - u_{x_m}^H(0,r,\theta)\right] r dr = \frac{jM}{1-M^2}\frac{1}{\omega} J_m(\alpha_{mn'}^H)\frac{p_m^L(0,1,\theta)}{Z} \quad , \tag{5.14}$$

where in both equations $n' = 1$ to N. Eq. 5.13-5.14 can be expanded to 2N algebraic equations in the same way than Eq. 5.9-5.10. The resultant coefficients in the matrix equation will be modified with respect to Eq.5.9-5.10 by the contributions of the discontinuity contour terms. This derivation is also explained in more detail in Section 5.2.1.

5.2 The inclusion of a point source in the mode-matching method

The mode-matching formulation outlined in the previous section assumes that 2 out of the 4 sets of unknown modal coefficients are known. In fan noise applications is common to assume that the incoming modes from the fan are known (from a CFD solution or particular duct modes) and that the amplitudes of the incoming modes from the inlet are

zero (anechoic termination). Therefore, the matching equations result in 2N equations with 2N unknowns: the reflected and transmitted modal coefficients at the matching plane.

In the context of over-tip-rotor liners, the noise sources are located within a finite length liner. In this section, the matching equations are applied for a given source model described in terms of a tailored Green's function. A similar approach was proposed by Zorumski [108] for a circular duct without flow and a monopole source located at the duct axis, hence considering only azimuthal modes with $m = 0$. The description of the mode-matching matrix equations for a semi-infinite lined-hard duct is shown in the first part of the section and the expressions are then extended to a finite length liner (two matching interfaces). The coefficients of the matrix equations are detailed for the two approaches described in the previous section: based on the continuity of pressure and axial particle velocity and based on the continuity of mass and momentum.

5.2.1 Analytical formulation

Semi-infinite lined-hard duct

The problem considered here consists of a cylindrical semi-infinite lined duct matched with a semi-infinite hard wall duct in which the pressure field is generated by a monopole/dipole point source. A diagram of the problem is shown in Fig. 5.2. The acoustic field generated by the source can be obtained by using Eq. 4.16(monopole)/Eq. 4.40(dipole) and solving the matching problem at the interface between the lined and hard regions. By using this approach, one can modify the radial and axial position of the source to define the tip clearance and lined surface available respectively. Then, the axial power radiated into the upstream hard wall section can be computed to assess the performance of the liner. Furthermore, it allows to study any 'back-reaction' effects on the source that the proximity of the matching interface may cause.

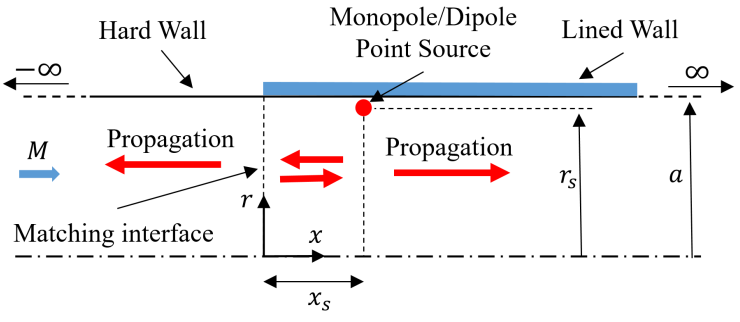

Figure 5.2: Semi-infinite hard-lined duct.

The pressure and particle velocity at the hard and lined section evaluated at the matching plane are:

$$p_m^H(0,r,\theta) = \sum_{n=1}^{N} \left(A_{mn}^{H+} J_m(\alpha_{mn}^H r) e^{-j\kappa_{mn}^{H+} x_a} + A_{mn}^{H-} J_m(\alpha_{mn}^H r) \right) e^{-jm\theta} \quad , \tag{5.15}$$

$$p_m^L(0,r,\theta) = \sum_{n=1}^{N} \left(A_{mn}^{L+} J_m(\alpha_{mn}^{L+} r) + A_{mn,s}^{L-} J_m(\alpha_{mn}^{L-} r) e^{+j\kappa_{mn}^{L-} x_s} \right) e^{-jm\theta} \quad , \tag{5.16}$$

$$u_{x_m}^H(0,r,\theta) = \sum_{n=1}^{N} \left(\frac{\kappa_{mn}^{H+}}{\Omega_{mn}^{H+}} A_{mn}^{H+} J_m(\alpha_{mn}^H r) e^{-j\kappa_{mn}^{H+} x_a} + \frac{\kappa_{mn}^{H-}}{\Omega_{mn}^{H-}} A_{mn}^{H-} J_m(\alpha_{mn}^H r) \right) e^{-jm\theta} \quad , \tag{5.17}$$

$$u_{x_m}^L(0,r,\theta) = \sum_{n=1}^{N} \left(\frac{\kappa_{mn}^{L+}}{\Omega_{mn}^{L+}} A_{mn}^{L+} J_m(\alpha_{mn}^{L+} r) + \frac{\kappa_{mn}^{L-}}{\Omega_{mn}^{L-}} A_{mn,s}^{L-} J_m(\alpha_{mn}^{L-} r) e^{+j\kappa_{mn}^{L-} x_s} \right) e^{-jm\theta} \quad , \tag{5.18}$$

where x_s is the axial distance from the source to the matching plane and x_a the distance from the anechoic condition to the matching plane. The value assigned to x_a in this case is irrelevant because the anechoic condition implies that $A_{mn}^{H+} = 0$. The coefficients of the incoming modes from the source plane can be obtained by direct comparison with Eq.4.16 for a monopole source or Eq.4.40 for a dipole source:

- Monopole point source:

$$A_{mn,s}^{L-} = -\frac{1}{2\pi j} \frac{J_m(\alpha_{mn}^{L-} r_s)}{Q_{mn}^{L-} J_m(\alpha_{mn}^{L-})^2} \quad , \tag{5.19}$$

- Dipole point source:

$$A_{mn,s}^{L-} = -\frac{1}{2\pi} \frac{J_m(\alpha_{mn}^{L-} r_s)}{Q_{mn}^{L-} J_m(\alpha_{mn}^{L-})^2} \left[\kappa_{mn}^{L-} \cos\gamma + \frac{m}{r_s} \sin\gamma \right] \quad , \tag{5.20}$$

with

$$Q_{mn}^{L-} = -\left([\kappa_{mn}^{L-} + \Omega_{mn}^{L-} M] \left[1 - \left(\frac{m}{\alpha_{mn}^{L-}} \right)^2 - \frac{\Omega_{mn}^{\pm 4}}{(\omega \alpha_{mn}^{L-} Z)^2} \right] - \frac{2jM\Omega_{mn}^{L-}}{\omega Z} \right) \quad . \tag{5.21}$$

Substitution of Eq. 5.15-5.18 into the matching equations[1] leads to 2N sets of equations which can be used to obtain the 2N unknown coefficients, corresponding to the reflected (A_{mn}^{L+}) and transmitted (A_{mn}^{H-}) modes. The equations can be solved directly if arranged in the following form adopted from [128]:

$$\begin{bmatrix} A_{mn}^{H-} \\ A_{mn}^{L+} \end{bmatrix} = TD \begin{bmatrix} A_{mn}^{L-} \\ A_{mn}^{H+} \end{bmatrix} \quad , \tag{5.22}$$

[1] Eq. 5.9-5.10 if using continuity of pressure and particle velocity or Eq. 5.13-5.14 if using continuity of mass and momentum across the matching interface.

where T and D are 2Nx2N transfer matrices. T is a square matrix which describes the pressure-velocity modal relations and the analytic integrals of the products of the Bessel functions. D is a diagonal matrix which contains the axial decay rates at the hard and lined duct sections. The matrices are given by:

$$T = \left[\begin{array}{c|c} a & -c^+ \\ \hline b^- & -d^+ \end{array}\right]^{-1} \left[\begin{array}{c|c} c^- & -a \\ \hline d^- & -b^+ \end{array}\right] \quad , \tag{5.23}$$

where each element (i, j) of the matrix is defined as

$$a_{ij} = \begin{cases} \int_{r=0}^{1} J_m^2(\alpha_{mi}^H r) r dr & \text{if} \quad i = j \\ 0 & \text{if} \quad i \neq j \end{cases} \quad , \tag{5.24}$$

$$b_{ij}^{\pm} = \begin{cases} \dfrac{\kappa_{mj}^{H\pm}}{\Omega_{mj}^{H\pm}} a_{ij} & \text{if} \quad i = j \\ 0 & \text{if} \quad i \neq j \end{cases} \quad , \tag{5.25}$$

$$c_{ij}^{\pm} = \int_{r=0}^{1} J_m(\alpha_{mi}^H r) J_m(\alpha_{mj}^{L\pm} r) r dr + M\varsigma_{ij}^{\pm} \quad , \tag{5.26}$$

$$d_{ij}^{\pm} = \frac{\kappa_{mj}^{H\pm}}{\Omega_{mj}^{H\pm}} \left[J_m(\alpha_{mi}^H r) J_m(\alpha_{mj}^{L\pm} r) r dr \right] - \varsigma_{ij}^{\pm} \quad , \tag{5.27}$$

and

$$D_{ii} = \begin{cases} e^{j\kappa_{mi}^{L-} x_s} & \text{if} \quad i = 1, ..., N \\ e^{-j\kappa_{mi}^{H+} x_a} & \text{if} \quad i = N+1, ..., 2N \end{cases} \quad . \tag{5.28}$$

The term $\varsigma_{ij}^{\pm}$ represents the additional contributions one gets by using the continuity of mass and momentum at the matching interface instead of the standard condition of continuity of pressure and particle velocity. Therefore, this term is zero in the standard approach and is defined as follows when using continuity of mass and momentum:

$$\varsigma_{ij}^{\pm} = \frac{jM}{1 - M^2} \frac{1}{\omega Z} J_m(\alpha_{mi}^H) J_m(\alpha_{mj}^{L\pm}) \quad . \tag{5.29}$$

The integrals of the products of the Bessel functions can be solved analytically by using [135]:

$$\int_0^a J_m^2(\alpha r_s) r_s dr_s = \frac{1}{2} J_m^2(\alpha a) \left(1 - \frac{m^2}{\alpha^2}\right) \quad , \tag{5.30}$$

$$\int_0^a J_m(\alpha r_s) J_m((\beta r_s) r_s dr_s = \frac{a}{\alpha^2 - \beta^2} \left\{ \beta J_m(\alpha a) J_m'(\beta a) - \alpha J_m'(\alpha a) J_m(\beta a) \right\} \quad . \tag{5.31}$$

Finite length liner within an infinite hard wall duct

The semi-infinite lined-hard case is extended to a finite length liner within an infinite hard wall duct. This configuration is more representative of the problem targeted here: the modelling of OTR liners. In particular, this model is a simplification of a rotor-alone arrangement with (1) an OTR liner modelled by the lined section and (2) the fan noise modelled with point sources *within* the lined section. A diagram of the problem is shown in Fig. 5.3. Note that this arrangement can be easily extended to model the noise reduction of fan case liners by placing the noise sources just downstream of the lined section and in the hard wall semi-infinite duct. Although this work does not include the noise predictions of fan case liners the mode-matching equations for such configurations are summarised at the end of this section.

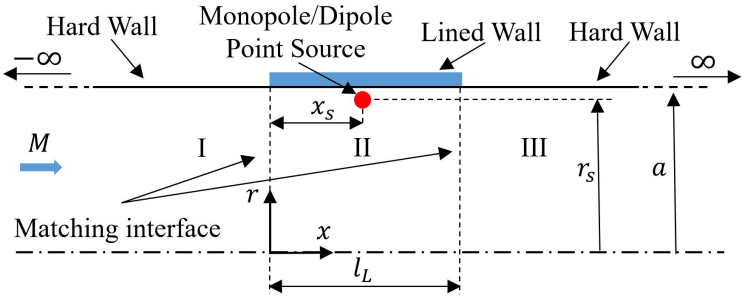

Figure 5.3: Finite length liner within an infinite hard wall duct.

The pressure field and particle velocity at each section are evaluated at the matching interfaces I-II and II-III. The contributions of the point source can be added in region II by using the superposition principle. This contribution is represented by the sets of known coefficients $A^{\mathrm{II}\pm}_{mn,s}$. Note that $A^{\mathrm{II}-}_{mn,s}$ and $A^{\mathrm{II}+}_{mn,s}$ only exist for $0 \leq x \leq x_s$ and $x_s \leq x \leq l_L$ respectively. The axial particle velocity expressions are omitted to shorten this derivation. However, they can be easily recovered given that

$$u^{\pm}_{x_{mn}} = \frac{\kappa^{\pm}_{mn}}{\Omega^{\pm}_{mn}} p^{\pm}_{mn} \quad . \tag{5.32}$$

- Pressure field evaluated at $x = 0$ (I-II):

$$p^{\mathrm{I}}_m(0,r,\theta) = \sum_{n=1}^{N} \left(A^{\mathrm{I}+}_{mn} J_m(\alpha^H_{mn} r) e^{-j\kappa^{H+}_{mn} x_a} + A^{\mathrm{I}-}_{mn} J_m(\alpha^H_{mn} r) \right) e^{-jm\theta} \quad . \tag{5.33}$$

$$p^{\mathrm{II}}_m(0,r,\theta) = \sum_{n=1}^{N} \left(A^{\mathrm{II}+}_{mn} J_m(\alpha^{L+}_{mn} r) + J_m(\alpha^{L-}_{mn} r) \left[A^{\mathrm{II}-}_{mn} e^{+j\kappa^{L-}_{mn} l_L} + A^{\mathrm{II}-}_{mn,s} e^{+j\kappa^{L-}_{mn} x_s} \right] \right) e^{-jm\theta} \quad . \tag{5.34}$$

- Pressure field evaluated at $x = l_L$ (II-III):

$$p_m^{\mathrm{II}}(l_L, r, \theta) = \sum_{n=1}^{N} \left(J_m(\alpha_{mn}^{L+} r) \left[A_{mn}^{\mathrm{II}+} e^{-j\kappa_{mn}^{L-} l_L} + A_{mn,s}^{\mathrm{II}+} e^{-j\kappa_{mn}^{L-}(l_L - x_s)} \right] + A_{mn}^{\mathrm{II}-} J_m(\alpha_{mn}^{L-} r) \right) e^{-jm\theta} \quad . \tag{5.35}$$

$$p_m^{\mathrm{III}}(l_L, r, \theta) = \sum_{n=1}^{N} \left(A_{mn}^{\mathrm{III}+} J_m(\alpha_{mn}^{H} r) + A_{mn}^{\mathrm{III}-} J_m(\alpha_{mn}^{H} r) e^{-j\kappa_{mn}^{H-}(l_L - x_a)} \right) e^{-jm\theta} \quad . \tag{5.36}$$

Substitution of the above expressions into the matching equations[2] leads to 2N sets of equations at each matching interface, totalling 4N sets of equations:

$$\begin{bmatrix} A_{mn}^{\mathrm{I}-} \\ \hline A_{mn}^{\mathrm{II}+} \end{bmatrix} = T_1 D_1 \begin{bmatrix} A_{mn}^{\mathrm{II}-} \\ \hline A_{mn}^{\mathrm{I}+} \end{bmatrix} + T_{1,s} D_{1,s} \begin{bmatrix} A_{mn,s}^{\mathrm{II}-} \end{bmatrix} \quad , \tag{5.37}$$

$$\begin{bmatrix} A_{mn}^{\mathrm{III}+} \\ \hline A_{mn}^{\mathrm{II}-} \end{bmatrix} = T_2 D_2 \begin{bmatrix} A_{mn}^{\mathrm{II}+} \\ \hline A_{mn}^{\mathrm{III}-} \end{bmatrix} + T_{2,s} D_{2,s} \begin{bmatrix} A_{mn,s}^{\mathrm{II}+} \end{bmatrix} \quad . \tag{5.38}$$

As in the single matching interface, T_1, T_2, D_1 and D_2 are 2Nx2N transfer matrices. However, the introduction of noise sources within the lined section results in the additional terms $T_{1,s}$, $T_{2,s}$, with dimensions of 2NxN, and $D_{1,s}$, $D_{2,s}$, with dimensions of NxN. These matrices are given by

$$T_1 = \left[\begin{array}{c|c} a & -c^+ \\ \hline b^- & -d^+ \end{array} \right]^{-1} \left[\begin{array}{c|c} c^- & -a \\ \hline d^- & -b^+ \end{array} \right] \quad , \tag{5.39}$$

$$T_2 = \left[\begin{array}{c|c} a & -c^- \\ \hline b^+ & -d^- \end{array} \right]^{-1} \left[\begin{array}{c|c} c^+ & -a \\ \hline d^+ & -b^- \end{array} \right] \quad , \tag{5.40}$$

$$T_{1,s} = \left[\begin{array}{c|c} a & -c^+ \\ \hline b^- & -d^+ \end{array} \right]^{-1} \left[\begin{array}{c} c^- \\ \hline d^- \end{array} \right] \quad , \tag{5.41}$$

$$T_{2,s} = \left[\begin{array}{c|c} a & -c^- \\ \hline b^+ & -d^- \end{array} \right]^{-1} \left[\begin{array}{c} c^+ \\ \hline d^+ \end{array} \right] \quad , \tag{5.42}$$

where each element (i, j) of the matrix is defined as per Eq.5.24-5.27, and

$$D_{1,ii} = \begin{cases} e^{j\kappa_{mi}^{L-} l_L} & \text{if} \quad i = 1, ..., N \\ e^{-j\kappa_{mi}^{H+} x_a} & \text{if} \quad i = N+1, ..., 2N \end{cases} \quad , \tag{5.43}$$

[2] Again, Eq. 5.9-5.10 if using continuity of pressure and particle velocity or Eq. 5.13-5.14 if using continuity of mass and momentum.

$$D_{2,ii} = \begin{cases} e^{-j\kappa_{mi}^{L+} l_L} & \text{if} \quad i = 1, ..., N \\ e^{-j\kappa_{mi}^{H-}(l_L - x_a)} & \text{if} \quad i = N+1, ..., 2N \end{cases} \quad , \tag{5.44}$$

$$D_{1,s,ii} = e^{j\kappa_{mi}^{L-} x_s} \quad , \tag{5.45}$$

$$D_{2,s,ii} = e^{-j\kappa_{mi}^{L+}(l_L - x_s)} \quad . \tag{5.46}$$

The known sets of coefficients are those defined by the source model ($A_{mn,s}^{\text{II}\pm}$) and those resultant of assuming anechoic conditions at both infinite duct sections ($A_{mn}^{\text{I}+} = A_{mn}^{\text{III}-} = 0$). The unknown coefficients are $A_{mn}^{\text{I-}}$ and $A_{mn}^{\text{III}+}$, corresponding to the transmitted modes upstream and downstream into the hard wall sections, and $A_{mn}^{\text{II}\pm}$, related to the reflections at the matching interfaces. This results in a system of 4N algebraic equations with 4N unknowns. The source coefficients are given by

- Monopole point source:

$$A_{mn,s}^{\text{II}\pm} = -\frac{1}{2\pi j} \frac{J_m(\alpha_{mn}^{L\pm} r_s)}{Q_{mn}^{L\pm} J_m(\alpha_{mn}^{L\pm})^2} \quad , \tag{5.47}$$

- Dipole point source:

$$A_{mn,s}^{\text{II}\pm} = -\frac{1}{2\pi} \frac{J_m(\alpha_{mn}^{L\pm} r_s)}{Q_{mn}^{L\pm} J_m(\alpha_{mn}^{L\pm})^2} \left[\kappa_{mn}^{L\pm} \cos\gamma + \frac{m}{r_s} \sin\gamma \right] \quad , \tag{5.48}$$

  with

$$Q_{mn}^{L\pm} = -\left([\kappa_{mn}^{L\pm} + \Omega_{mn}^{L\pm} M] \left[1 - \left(\frac{m}{\alpha_{mn}^{L\pm}} \right)^2 - \frac{\Omega_{mn}^{\pm 4}}{(\omega \alpha_{mn}^{L\pm} Z)^2} \right] - \frac{2jM\Omega_{mn}^{L\pm}}{\omega Z} \right) \quad . \tag{5.49}$$

The system of equations formed by Eq. 5.37-5.38 can be solved by using simple iterative schemes. The routine used in this instance is depicted with the diagram in Figure 5.4, where Eq. I-II and Eq. II-III refer to Eq. 5.37 and Eq. 5.38 respectively. An equivalent routine used for this purpose is outlined in the literature [136]. In this case, the scheme starts with $A_{mn}^{\text{II}-}$ initially set to zero and computing $A_{mn}^{\text{I}-}$ and $A_{mn}^{\text{II}+}$ using Eq.5.37. Then, $A_{mn}^{\text{II}+}$ is used to obtain $A_{mn}^{\text{III}+}$ and the new value of $A_{mn}^{\text{II}-}$. This loop is repeated until the coefficients converge, i.e. the variation of each coefficient with respect to the previous iteration is lower than a specified tolerance δ.

As mentioned previously, an analogous formulation can be adapted to model a fan case liner configuration or a conventional intake liner by placing the point source downstream of the lined section ($x > l_L$). Eq. 5.37-5.38 can then be re-written as

$$\begin{bmatrix} A_{mn}^{\text{I}-} \\ A_{mn}^{\text{II}+} \end{bmatrix} = T_1 D_1 \begin{bmatrix} A_{mn}^{\text{II}-} \\ A_{mn}^{\text{I}+} \end{bmatrix} \quad , \tag{5.50}$$

$$\begin{bmatrix} A_{mn}^{\mathrm{III}+} \\ \hline A_{mn}^{\mathrm{II}-} \end{bmatrix} = T_2 D_2 \begin{bmatrix} A_{mn}^{\mathrm{II}+} \\ \hline A_{mn}^{\mathrm{III}-} \end{bmatrix} + T_{2,s} D_{2,s} \begin{bmatrix} A_{mn,s}^{\mathrm{III}-} \end{bmatrix} \quad , \tag{5.51}$$

where all the matrices are the same except for the source contributions $T_{2,s}$ and $D_{2,s}$ now given as

$$T_{2,s} = \begin{bmatrix} a & -c^- \\ \hline b^+ & -d^- \end{bmatrix}^{-1} \begin{bmatrix} -a \\ \hline -b^- \end{bmatrix} \quad , \tag{5.52}$$

$$D_{2,s,ii} = e^{-jk_{mi}^{H+}(l_L - x_s)} \quad . \tag{5.53}$$

The hard wall source amplitudes $A_{mn,s}^{\mathrm{III}-}$ can be obtained using Eq. 5.19-5.19 with the hard wall eigenvalues and setting $Z \to \infty$ in Eq 5.21.

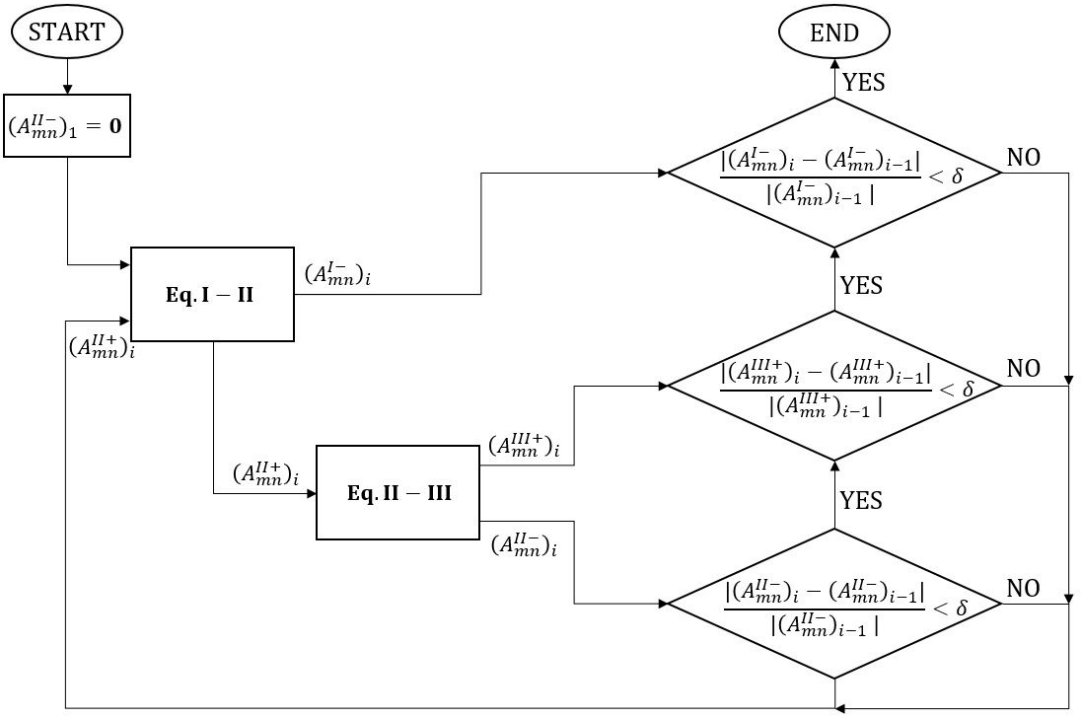

Figure 5.4: Iterative scheme used to solve the matching equations.

5.2.2 Source proximity to the matching interface

Analytical mode-matching techniques are a well-known method to model the propagation in ducts with lined sections and simple geometries and assess the noise attenuation of inlet and bypass liners. For such applications, the source is often assumed to be a prescribed duct mode propagating from the source plane, such as the fan section. However, for an OTR application, it has been argued that a modal Green's function representation is preferred in order to compute the mode amplitudes excited by a realistic fan noise source distribution and to allow for back-reaction effects due to the close proximity to the lined surface. The relatively short length of OTR liners, usually limited to the axial projection

of the tip fan chord, involves the modelling of the fan noise source distribution located acoustically close to the matching interface. The problem poses a number of challenges with respect to conventional mode-matching applications outlined below and analysed in this part of the section.

It has been shown in Section 4.6.2 that an increasingly higher number of evanescent modes are required to capture the back-reaction effects in the power output of a source within a lined duct as it is moved closer to the wall. Therefore, the mode-matching must consider, at least, as many radial terms as those included in the point source representation. The current implementation is controlled with the COR and uses the same number of modes for the source terms and the mode-matching, i.e. $N = n_{\max}$. The inclusion of cut-off modes in the matching equations generally increases the accuracy of the computations and allows for a more accurate representation of the near-field close to the matching plane. However, the large number of evanescent components included in the solution to represent the near-field of the source can also compromise the conditioning of the matrices.

In practice, if the source is located relatively far from the matching plane, the amplitude of the evanescent modes excited by the source are highly attenuated when evaluated at the impedance discontinuity and have a small effect in the solution. Conversely, for a leading edge or trailing edge source located in close proximity to a matching interface the cut-off modes can significantly affect the mode-matching calculations. To illustrate this issue, the PWL of the field propagating upstream of the OTR liner in the hard wall section is evaluated for a range of source positions and CORs as shown in Fig. 5.5. The non-dimensional length of the OTR liner used for this study is that of the NASA W-8 test rig [5] $l_L = 0.2045$ and the point source an axial dipole. Apart from source positions within the lined section, two additional cases are included where the source is downstream of the lined section and close to the interface (fan case liner config.) and well downstream as a reference case.

It can be observed in Fig. 5.5 that a COR=5 is generally sufficient to obtain a converged solution unless the source is very close to the matching interface, regardless of the technique used in the mode-matching, i.e. the conventional continuity of pressure and particle velocity, referred here as 'conv.' or the corrected equations based on continuity of mass and momentum, referred as 'corr.'. The convergence is faster for the reference case (x_s/l_L=10), which is not affected by the source proximity, and both matching formulations provide PWL estimates within 0.1 dB. The back-reaction effects on the source power caused by the proximity to the matching interface can be observed by comparing the PWL^{I} for source positions x_s/l_L=[1.25,10]. Even though both source locations are in the downstream hard wall section, the axial power reaching the upstream section can be up to 7 dB lower for the 'fan case' position (see curves for x_s/l_L=[1.25,10] in Fig. 5.5d), suggesting potential benefits of this liner configuration.

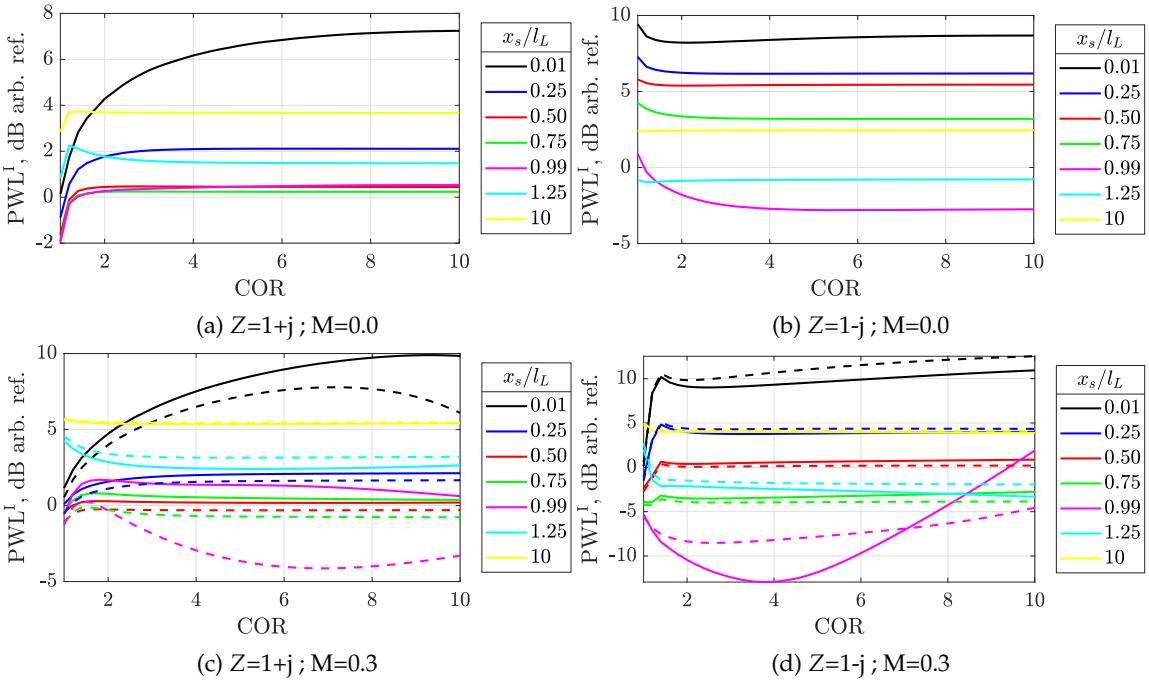

(a) Z=1+j ; M=0.0 (b) Z=1-j ; M=0.0

(c) Z=1+j ; M=0.3 (d) Z=1-j ; M=0.3

Figure 5.5: PWL in the duct section I for ω=15, $r_s/a = 0.99$, a range of source positions x_s/l_L and CORs. Solid line: corrected ; Dashed line: conventional

When the source is located at 1% or 99% of the liner length a converged solution has not been always achieved with non-zero uniform flow. It has been found that this limitation can be related to the distance from the source to the nearest matching plane relative to the wavelength, resulting in a more stringent constraint at low frequencies. A value of COR=5 appears to be sufficient for sources located 0.1λ or more from a matching plane. For a practical implementation of the proposed methodology, it is suggested that the liner be slightly extended beyond the leading/trailing edge position to avoid this issue.

Note that the lack of convergence at the limiting conditions is related to the modal point source representation; the evaluation of the PWL in an infinite lined duct at an axial plane in the near field of the source presents an analogous behaviour. All lined modes carry energy, even if they are highly evanescent, leading to a slower convergence rate of the solution closer to the source plane. This reasoning is illustrated in Fig. 5.6 by showing the PWL along an infinite lined duct for various COR. The asymptotic axial decay away from the source is of course that given by the least attenuated mode, but the higher-order modes dominate the near-field and cause the slower convergence of the solution when the power is evaluated close to the axial source location.

The accuracy of the mode-matching is assessed in terms of the continuity of axial power across the matching plane with the power defined as in Section 4.5. The power discontinuity in dB terms is shown in Fig. 5.7. The continuity of power in the converged solutions is always within 0.1 dB for a COR=5 and generally improves with COR and with the distance between the source and the matching plane.

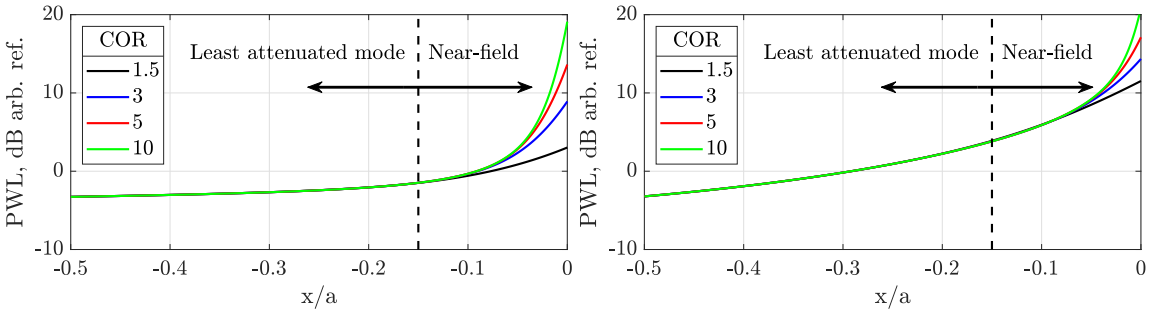

(a) Z=1+j (b) Z=1-j

Figure 5.6: PWL in an infinite lined duct for ω=15, $x_s/a = 0$, $r_s/a = 0.99$, M=0.0, and a range of CORs.

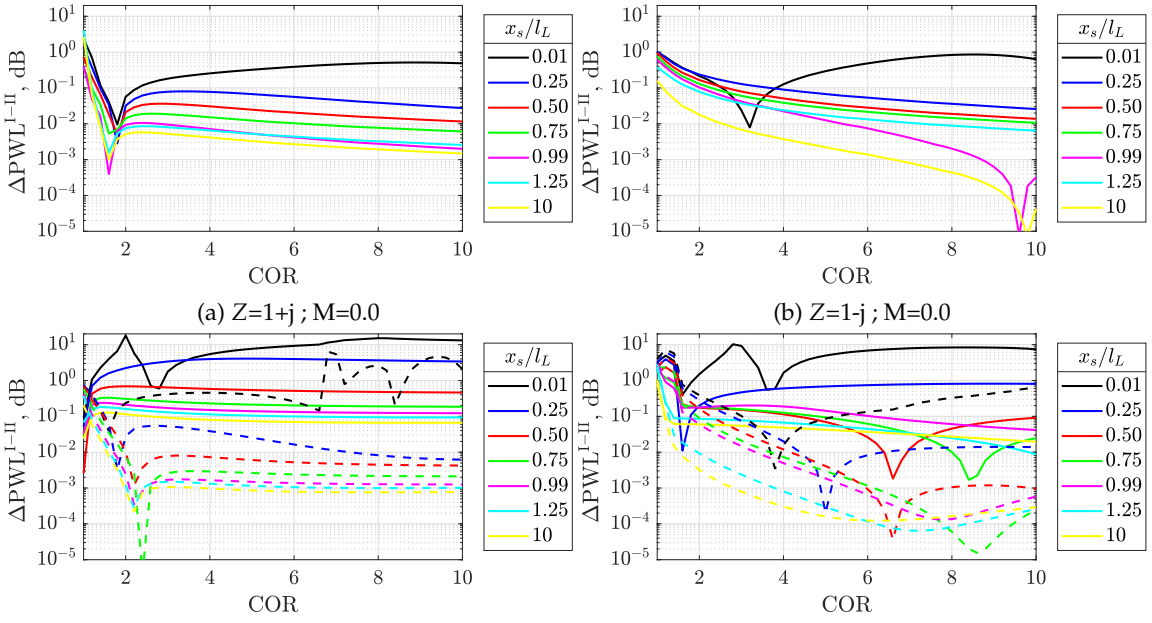

(a) Z=1+j ; M=0.0 (b) Z=1-j ; M=0.0

(c) Z=1+j ; M=0.3 (d) Z=1-j ; M=0.3

Figure 5.7: PWL continuity across the interface I-II for ω=15, $r_s/a = 0.99$, a range of axial source positions x_s/l_L and CORs. Solid line: corrected ; Dashed line: conventional

The higher power discontinuities observed in Fig. 5.7 with flow when using continuity of mass and momentum have been reported by Gabard [132], who justified the different behaviour when using the two mode-matching techniques by linking the boundary terms of the mass and momentum formulation to an additional term of the axial power accounting for the energy contained within the vortex sheet in the lined section. This additional power term was derived by Tester [137] using Möhring's [138] definition of intensity for shear flow by taking the limit of vanishing boundary layer thickness and was later derived from energy conservation principles by Eversman [133]. Since the additional term is null for a hard wall section and the OTR noise reduction predictions presented in this thesis are based on the PWL evaluated in the duct region I this topic is not discussed further.

5.2.3 Cross-verification with FEM results

Reference FE computations have been performed to cross-verify with the analytical solutions obtained with the mode-matching methodologies presented in this section. As in previous chapters, the numerical simulations have been obtained using the FEM commercial software Simcenter 3D Acoustics with adaptive polynomial order [100]. The domain used for the computations is shown in Fig. 5.8, which consists of a 3D hard walled duct terminated at each end with a PML-type anechoic boundary condition and a lined section, highlighted in orange, containing a monopole point source. The mesh has been refined around the source position ($r_s/a = 0.95$) and in the interface between the hard and lined duct sections.

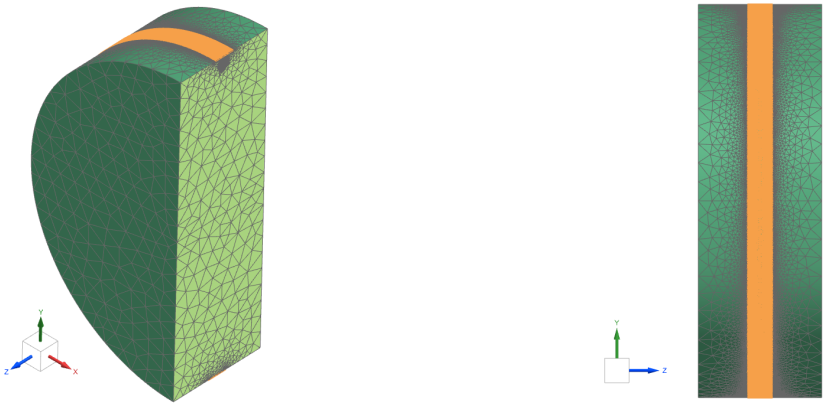

(a) Isometric view with lateral section

(b) Lateral view

Figure 5.8: Isometric and lateral view of the mesh used in the FEM simulations for the cross-verification with the mode-matching scheme.

A number of cases have been considered for the frequencies ω=[5,10,15], specific acoustic impedances Z=[1+j,1,1-j] and source positions in OTR and fan case configurations x_s/l_L = [0.25,0.50,0.75,1.25]. This test matrix has been repeated with zero mean flow and M=0.3. Only the results for ω=15 and Z=[1+j,1-j] are presented here for conciseness but a similar agreement has been found in most cases. The analytical results are computed for the volume displacement monopole with the convective source term since this is the interpretation of the monopole source in the FEM software. Both the conventional mode-matching technique based on the continuity of pressure and particle velocity and the corrected based on continuity of mass and momentum are included in this cross-verification.

The analytical and numerical solutions are compared in terms of the sound pressure level along the duct wall, shown in Fig. 5.9 for the zero flow case and in Fig. 5.10 for $M = 0.3$, where the vertical dashed lines indicate the position of the source plane in each case. Note that no difference is made between the two mode-matching formulations in the cases with zero uniform mean flow because both reduce to the same set of equations under these conditions. In all analytical results presented in this comparison, a COR=5 has been used

since it provides converged solutions for the cases presented here. The analytical and FE solutions show an excellent agreement both with and without flow except in the vicinity of the point source and the matching plane. It is in the latter where, with uniform flow, the two matching techniques differ more significantly and the continuity of mass and momentum results in a better match with the FE solution close to the matching plane, as previously reported [129, 132].

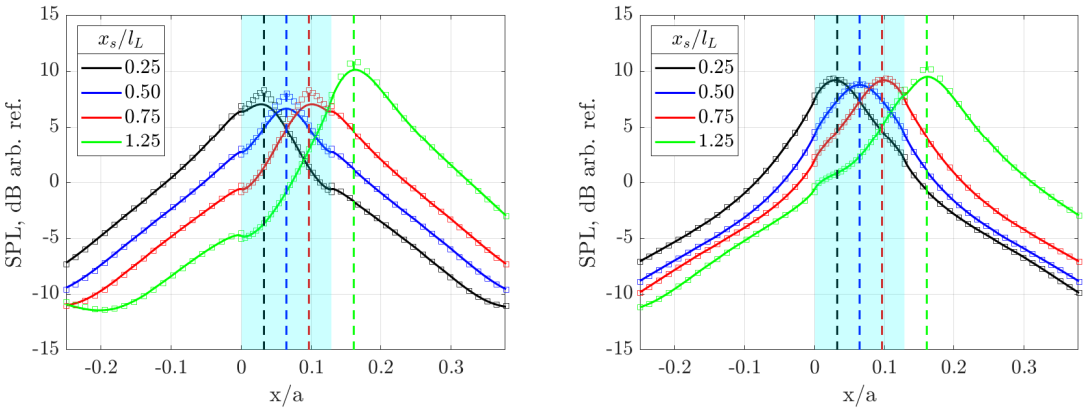

(a) Z=1+j (b) Z=1-j

Figure 5.9: Sound pressure level along the duct wall for ω=15, M=0.0 and COR=5. Solid line: FE solution; Squares: analytical; Blue-shaded area: lined section.

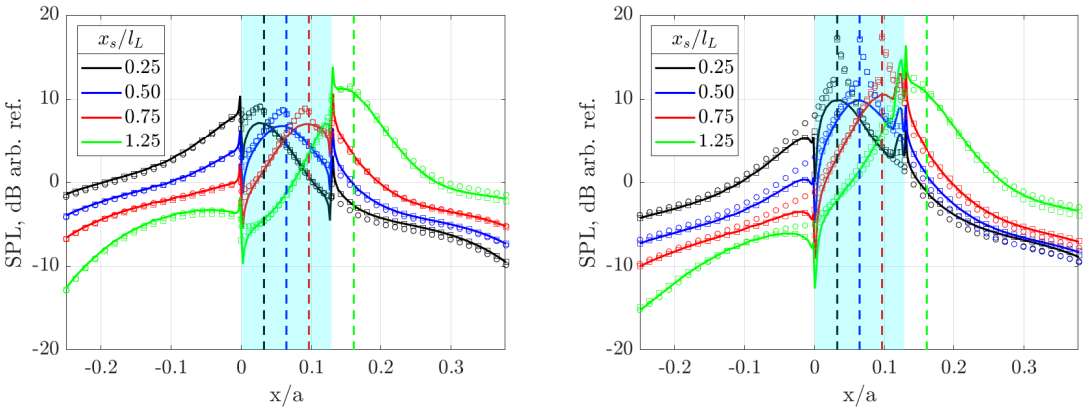

(a) Z=1+j (b) Z=1-j

Figure 5.10: Sound pressure level along the duct wall for ω=15, M=0.3 and COR=5. Solid line: FE solution; Squares: analytical-corrected; Circles: analytical-conventional ; Blue-shaded area: lined section.

The above results are compared in Fig. 5.11 in terms of the relative error in pressure between the analytical solutions and the FE results and in Fig. 5.12 as the SPL difference, in dB's. The relative error in the hard wall section falls within 1 % in the absence of flow or up to 5 % when flow is included using the continuity of mass and momentum. The error is higher for the conventional matching conditions, especially close to the matching interface as expected, but falls within 10 % further away.

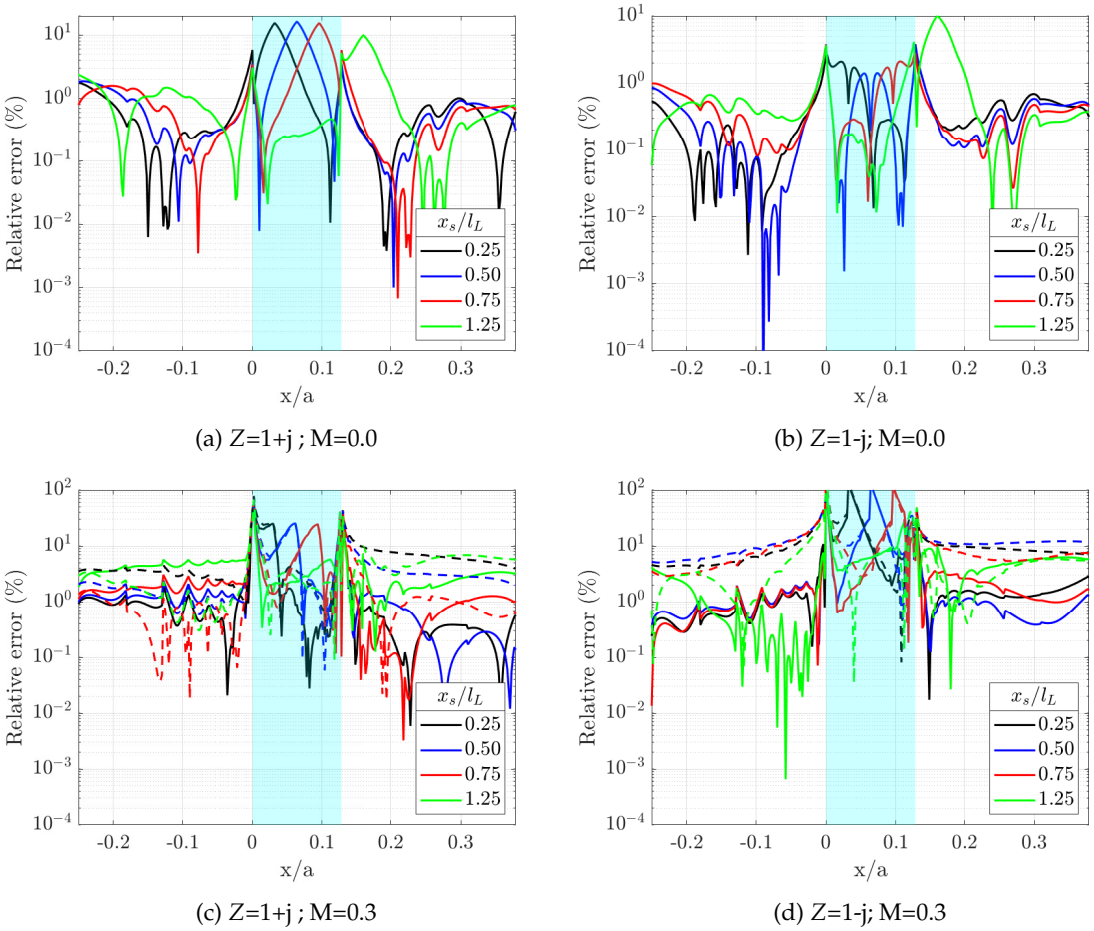

(a) Z=1+j ; M=0.0

(b) Z=1-j; M=0.0

(c) Z=1+j ; M=0.3

(d) Z=1-j; M=0.3

Figure 5.11: Relative error of the pressure magnitude at the duct wall for ω=15 and COR=5. Solid line: corrected ; Dashed line: conventional

The same observations can be made in terms of the difference in SPL. The results in Fig. 5.12 indicate errors within 0.2 to 0.5 dB away from the source using the corrected mode-matching conditions and up to 1 dB when using the continuity of pressure and particle velocity. Apart from the matching plane, the most significant discrepancies are in the immediate vicinity of the source, accounting for errors over a 100 % or 7 dB at the source position itself. This is attributed to the numerical modelling of the point source and the mesh size when using an adaptive polynomial order solver (FEMAO) based on an *a priori* error indicator. This approach allows the use of a single mesh for a wide range of frequencies and the polynomial order is suitably adjusted for each frequency for an efficient calculation while ensuring a target accuracy. However, as mentioned earlier in the thesis, the adaptive order does not account for singularities such as a point source and then the element size of the mesh (h-refinement) around the source must be small enough to capture the high gradients with a polynomial order of $p = 1$.

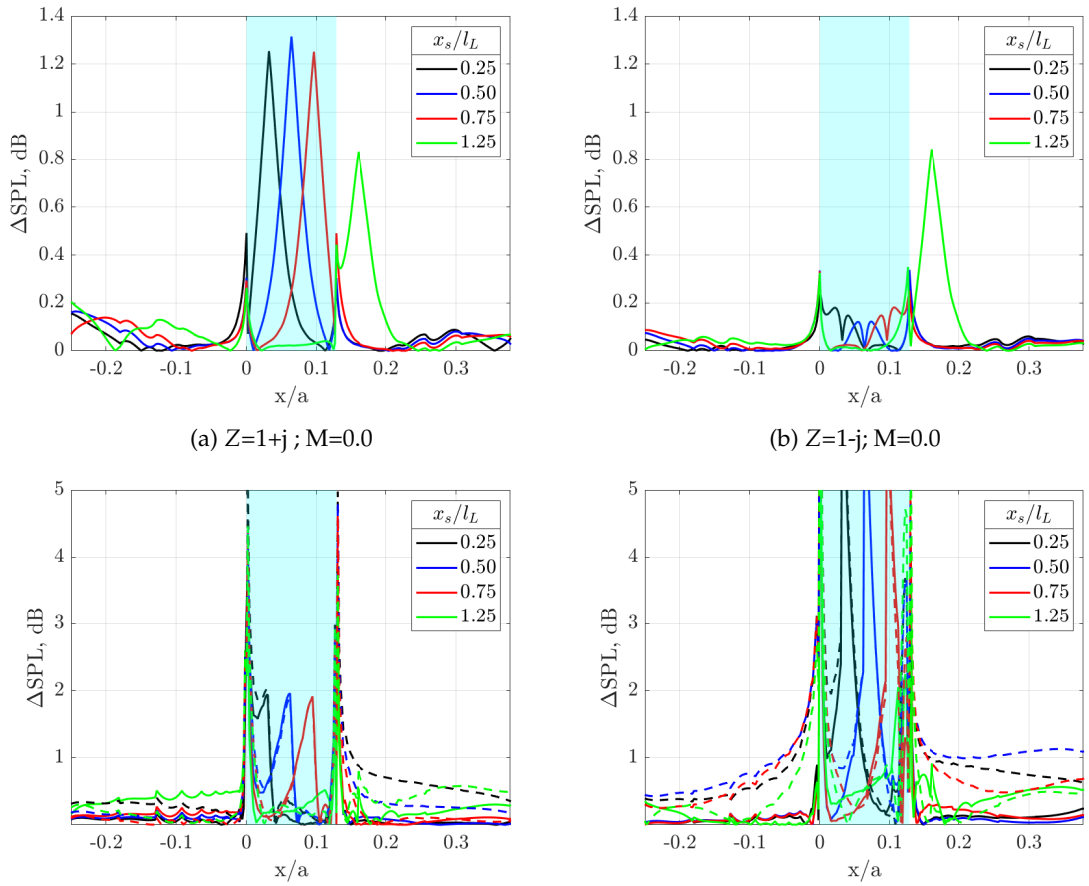

(a) Z=1+j ; M=0.0

(b) Z=1-j; M=0.0

(c) Z=1+j ; M=0.3

(d) Z=1-j; M=0.3

Figure 5.12: SPL error at the duct wall in dB for ω=15 and COR=5. Solid line: corrected ; Dashed line: conventional

Although a local mesh refinement is implemented in the mesh used in this section around x_s/l_L=0.5 and r_s/a=0.95 it does not seem to provide a significantly better agreement. Again, since the OTR prediction models proposed in the next chapter are based on the PWL and SPL evaluated at the hard wall section upstream of the OTR liner, where the agreement with the FE solution is below 1-5 %, a detailed refinement to capture the near field in the FE solution has not been pursued.

Two additional numerical cases have been considered to confirm the superposition principle applies when a mode-matching procedure with potential back reaction effects is involved. In particular, the aim is to ensure that multiple sources within the lined section can be modelled by computing analytically the acoustic field in the duct caused by each source separately and then superimpose the solutions. The first case, in Fig. 5.13, considers 3 sources distributed axially along the lined section at x_s/l_L = [0.25,0.50,0.75] and the second, in Fig. 5.14, distributed radially for r_s/a=[0.8,0.9,0.99]. All three sources are considered simultaneously in the FE solution (axially or radially distributed).

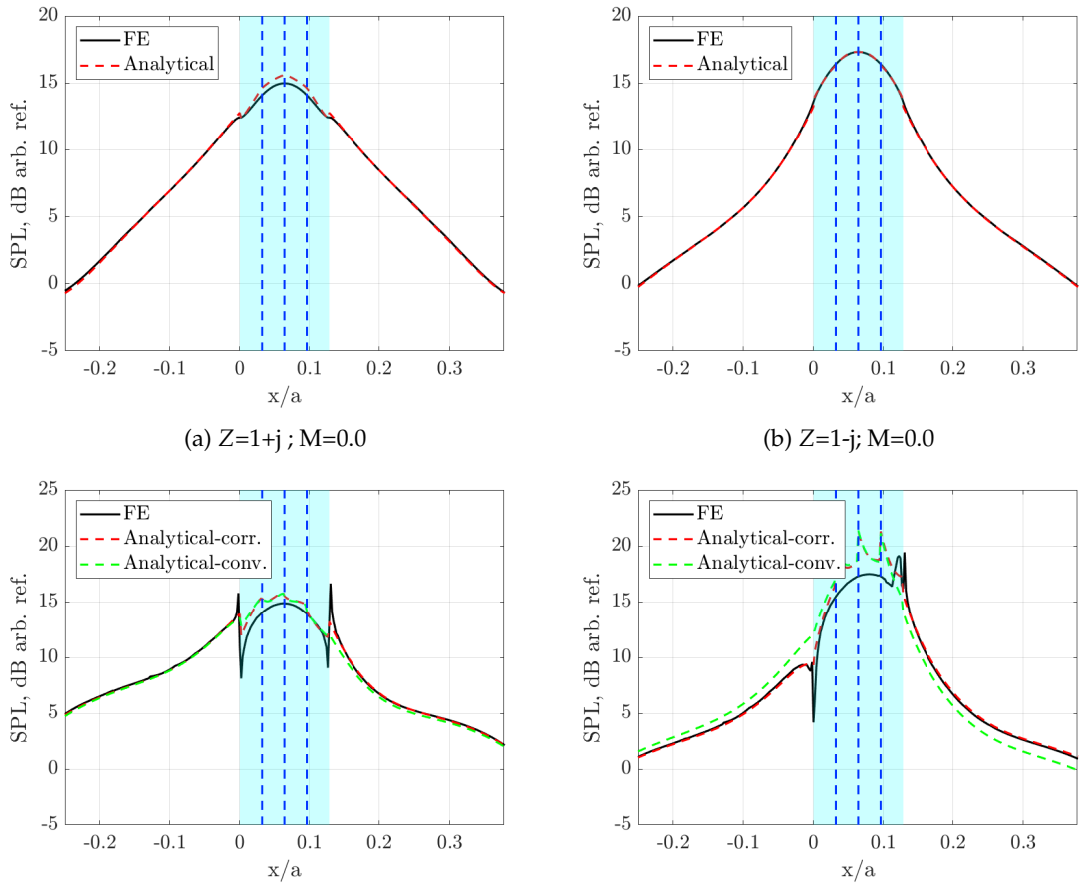

(a) Z=1+j ; M=0.0

(b) Z=1-j; M=0.0

(c) Z=1+j ; M=0.3

(d) Z=1-j; M=0.3

Figure 5.13: Comparison of the predicted sound pressure level along the duct wall for ω=15 and COR=5 and the FE solution with multiple axial sources. Blue-shaded area: lined section.

An excellent agreement is achieved between the FE solution with multiple sources and the analytical predictions based on the superposition of the acoustic fields of each separate source, both for the axial and radial distributions. As mentioned before, the higher discrepancies observed in Fig. 5.13 and 5.14 in the near-field of the sources can be expected and is not a problem for the OTR liner prediction model proposed in this thesis. The results with uniform mean flow show clearly how the mode-matching technique based on the continuity of mass and momentum (corr.) yields results closer to the FE solutions, especially in the vicinity of the matching interface.

This cross-verification with multiple sources provides confidence in applying the analytical mode-matching techniques described in this chapter for a single point source to cases where the source is modelled as a distribution of point sources in the fan region, whether they are distributed axially or radially.

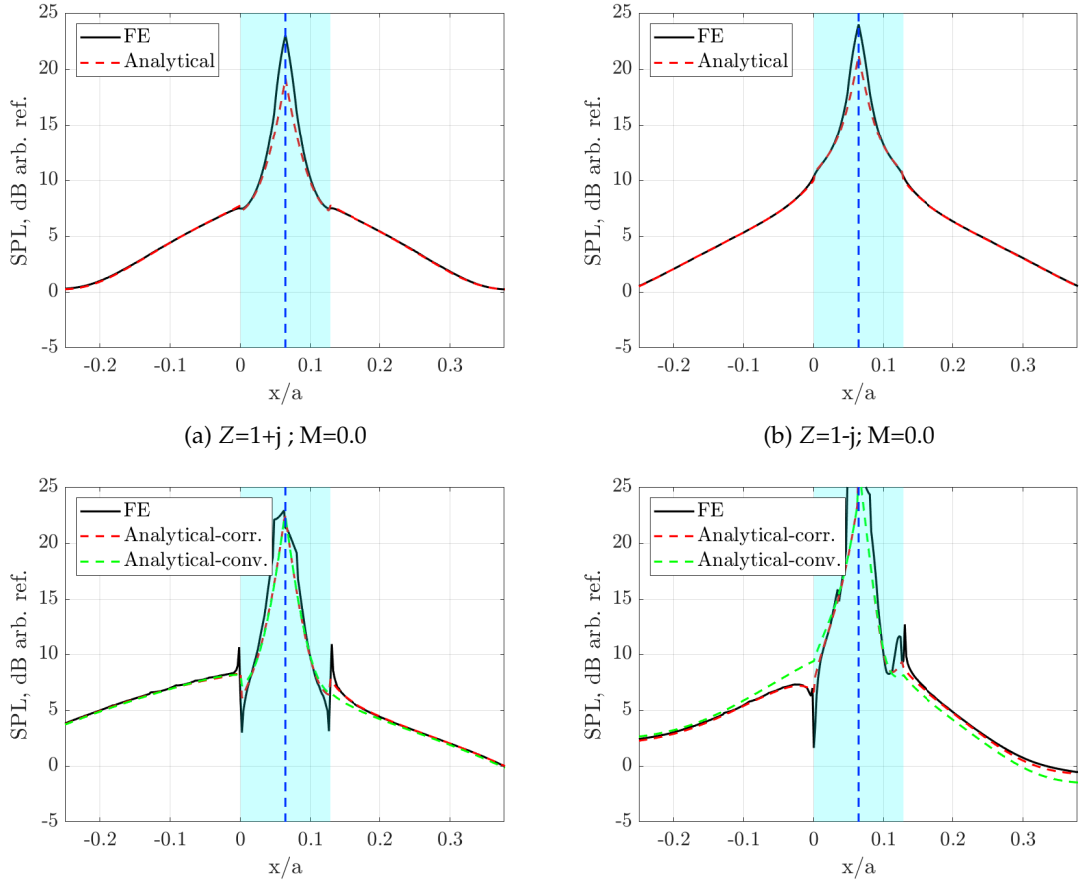

(a) Z=1+j ; M=0.0

(b) Z=1-j; M=0.0

(c) Z=1+j ; M=0.3

(d) Z=1-j; M=0.3

Figure 5.14: Comparison of the predicted sound pressure level along the duct wall for ω=15 and COR=5 and the FE solution with multiple radial sources. Blue-shaded area: lined section.

5.3 The inclusion of a duct termination in the mode-matching method

The modal representation of the acoustic field excited by a point source in an infinite hard wall duct can contain a singularity at the cut-on frequency of each mode depending on the source type and the presence of mean flow. This behaviour is shown explicitly in Eq. 4.34 and 4.41 for a monopole, with and without flow, and a dipole with flow since $\xi_{mn} \to 0$ at cut-on. This is also an issue in 'lift' dipoles without flow due to the azimuthal component. This singularity can also be observed in the Green's function approach taken here (Eq. 4.16 and Eq. 4.40) by noting that $(\kappa_{mn} + \Omega_{mn}M) \to 0$ at cut-on and hence $Q_{mn} \to 0$ for a hard wall. However, this is not an issue for a source within a lined section due to the last term in Q_{mn} remaining finite at cut-on. This singularity has been identified frequently in the literature [7, 50, 115, 139] with some suggesting the coupling of the

source strength with the blade response function of a rectilinear cascade [115], which tends to zero at the cut-on frequency [50], to mitigate the problem.

The approach taken here to address this issue and to improve the physical model is to include reflections from an inlet termination[3], specifically an unflanged duct termination for which a coded model was readily available. The addition of this termination has been found to effectively nullify the hard wall singularity at the cut-off/cut-on transition since at this condition the just cut-on mode is completely reflected at the duct termination. In a fully hard wall duct the reflected acoustic field can be added coherently to the acoustic field generated by the source in an infinite duct using superposition and in a hard-lined-hard configuration the reflections need to be included in the mode-matching formulation. This section describes the extension of the expressions in Section 5.2.1 to include the reflected modes from the inlet termination and shows the impact of the reflections in the cut-on/cut-off singularities.

5.3.1 Analytical formulation

The inclusion of reflections from a duct termination is implemented in the current mode-matching model by assuming that the incident and reflected modes at the duct termination are linked by a reflection coefficient C_{mnl}. The complex amplitude of the reflected right-running modes can be obtained from the complex amplitudes of the left-running incident modes evaluated at the duct termination ($x = x_t$) as

$$A_{ml}^{I+} = \sum_{n=1}^{N} C_{mnl} A_{mn}^{I-} e^{-jk_{mn}^{H-} x_t} \quad . \tag{5.54}$$

C_{mnl} relates the complex amplitude of the *incident* mode of azimuthal and radial order (m, n) with that of the *reflected* mode (m, l). Hence, the amplitude of the reflected mode (m, l), A_{ml}^{I+}, is the summation over all the contributions of the incident modes (m, n) allowing for radial scattering.

The problem modelled in this section is sketched in Fig. 5.15 and is concerned with the resultant acoustic field inside the duct and not the radiation to the far-field. Therefore, the assumption on the type of duct termination would only affect the model required to compute the reflection coefficients, described below.

The model adopted to obtain the reflection coefficients for an unflanged termination is that of Gabard and Astley [8] for the modal propagation and radiation through a semi-infinite unflanged duct exhaust, based on a Wiener-Hopf approach, which is an extension of the solutions of Munt [140, 141] and Rienstra [142]. The problem modelled in [8] is shown in Fig. 5.16 and consists of an annular (or hollow) duct with an unflanged

[3]Suggested by Professor Morfey (Personal Communication).

termination containing a uniform jet flow (M_0) and surrounded by an ambient uniform flow (M_∞). The model has been applied to the inlet problem by setting the hub-to-tip ratio to zero, using the inlet flow as the ambient and jet flows, $M_0 = M_\infty = -M_{\text{inlet}}$, and deactivating the Kutta condition at the edge controlling the vortex shedding since it is now assumed to be a leading edge. An existing routine has been used to obtain the reflection coefficients using this model, which are then included in the mode-matching scheme described here.

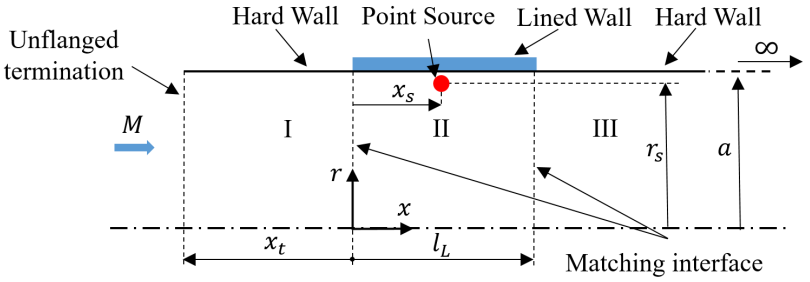

Figure 5.15: Finite length liner within a semi-infinite hard wall duct with an unflanged/flanged termination at $x = x_t$.

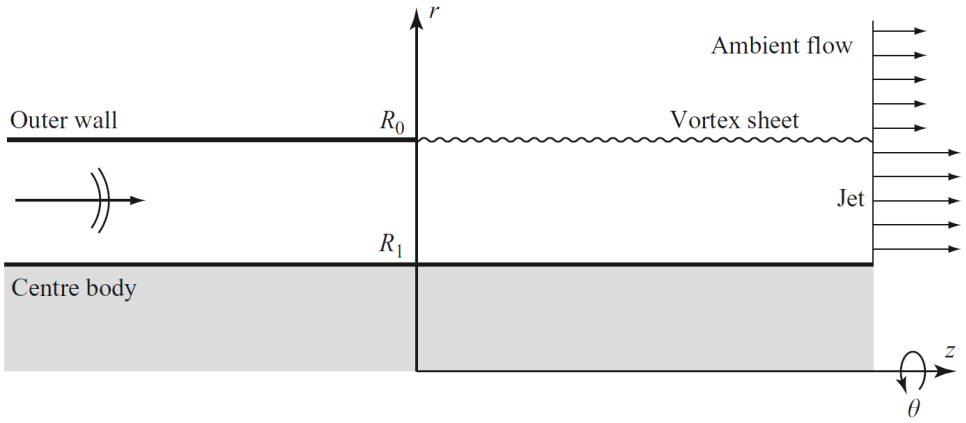

Figure 5.16: Sketch of the unflanged termination modelled in Gabard and Astley [8] .

The introduction of a duct termination in terms of a matrix of reflection coefficients in the mode-matching scheme has been previously explored in the literature. Gabard and Astley [129] integrated their mode-matching formulation based on continuity of mass and momentum with the unflanged duct exhaust model outlined above, but with the focus on assessing the noise reduction in the far-field directivity rather than in the in-duct power. More recently, Yang et al. [143] proposed an analytical model for a semi-infinite rectangular hard-lined-hard duct, which was targeted at impedance eduction techniques and included the mode-matching based on continuity of mass and momentum and reflections from a termination. However, they argued that the influence of the duct termination in the eduction results is small and hence assumed to be zero throughout.

The approach implemented here simply adds a set of equations to the system formed by Eq. 5.37-5.38 to account for the new set of unknowns A_{mn}^{I+} previously set to zero. That is

$$\left[A_{mn}^{I+}\right] = \mathcal{R}\left[A_{mn}^{I-}\right] \quad , \tag{5.55}$$

where $\mathcal{R}$ is a full square matrix with dimensions of N x N and

$$\mathcal{R}_{ij} = C_{mji} e^{-jk_{mj}^{H-} x_t} \quad . \tag{5.56}$$

The system formed by Eq. 5.37-5.38 and Eq. 5.55 is solved following an equivalent iterative scheme to that outlined in Fig. 5.4.

5.3.2 Effect of the reflections on the predicted noise reduction

The experimental data for the OTR liners tested in the W-8 NASA rig [5] used to compare with the prediction model developed in this thesis is in the form of the SPL of the azimuthally averaged pressure at the duct wall. The predicted SPL for an OTR liner of l_L equal to that in the W-8 geometry, evaluated at the position of the W-8 azimuthal array ($x_{\text{array}} = -2.2a$) is shown in Fig. 5.17a for an anechoic and unflanged inlet and for the lined and hardwall baseline. The position of the termination is estimated as $x_t/a = -3$, which is the upstream end of the cylindrical duct and the beginning of the inlet 'flare' or bellmouth in the W-8 rig [5]. The impedance model used for the lined configuration is that of the lined grooves derived in Chapter 3. The predictions are also presented in terms of the axial PWL evaluated at the position of the azimuthal array in Fig. 5.17b.

The singularities at the cut-on frequencies can be clearly observed in the hard wall SPL prediction in Fig. 5.17a by the narrow high amplitude spikes. The dashed vertical lines indicate the cut-on frequencies of the first radial order modes (m,1) but the singularities occur for the higher radial orders too as it can be observed in other 'secondary' spikes. As mentioned in the introduction of the section, the predictions with the OTR liner are free from singularities because, even if the SPL is evaluated in the hard wall region, the source is located within the lined section and therefore the modal amplitudes are not singular at the cut-off/cut-on transition. The duct termination proves effective in cancelling the mathematical singularity in the hard wall baseline due to a complete reflection of the cutting-on mode at the termination. The same observations apply to the hard wall PWL spectrum in Fig. 5.17b, where the issue of the singularities is hardly visible when the termination is included.

The high-amplitude spikes appearing in the SPL spectrum and to a lesser extent in the PWL spectrum for the lined configuration are attributed to axial resonances enhanced by the reflections at the impedance discontinuity of the right-running reflected modes originating from the duct termination. In fact, a sensitivity study for a range of values

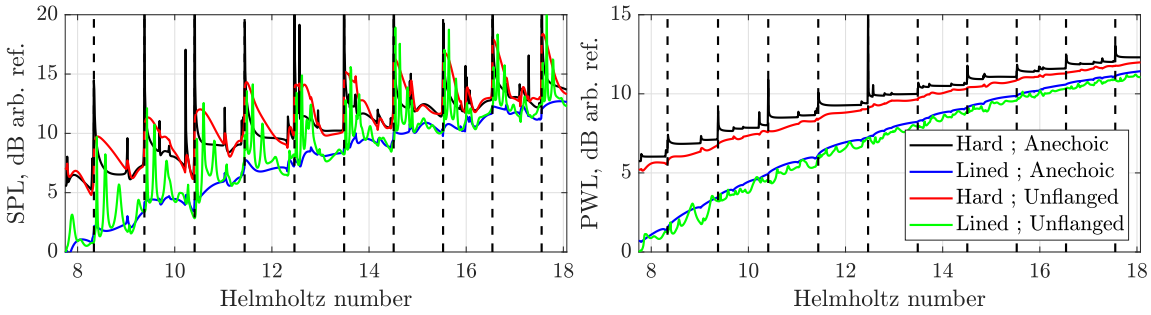

(a) SPL spectrum (b) PWL spectrum

Figure 5.17: Predicted (a) SPL and (b) PWL spectrum at the axial position of the W-8 azimuthal array for a hard wall and lined configuration and an anechoic and unflanged termination.

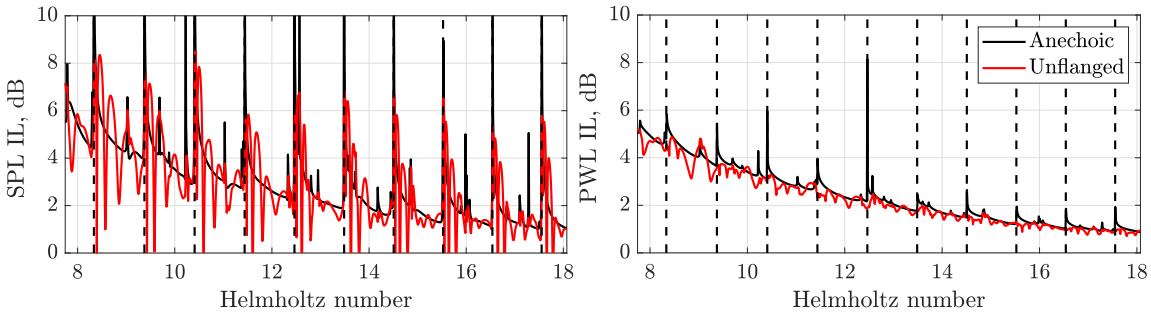

(a) SPL IL spectrum (b) PWL IL spectrum

Figure 5.18: Predicted (a) SPL IL and (b) PWL IL spectrum at the axial position of the W-8 azimuthal array for a hard wall and lined configuration and an anechoic and unflanged termination.

of the duct termination location (x_t) has shown that the frequency and magnitude of the spikes depend on x_t and the standing wave patterns created in the duct. The predictions with the unflanged termination yield SPL and PWL IL spectra centred in the anechoic results but free from the cutting-on singularities, as observed in Fig. 5.18.

The analysis presented in Section 5.2.2 is repeated for the configuration with the duct termination to ensure that the axial resonances do not compromise the continuity of power across the matching plane. Only a subset of cases is shown in Fig. 5.19 using the continuity of pressure and particle velocity but the same conclusion apply for all the cases tested in Section 5.2.2: the trends in the continuity of power are barely affected by the introduction of the duct termination.

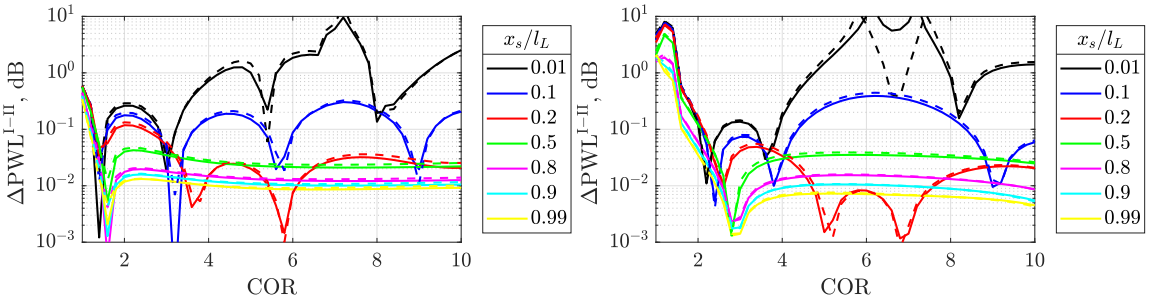

(a) Z=1+j ; M=0.3 (b) Z=1-j ; M=0.3

Figure 5.19: PWL continuity across the interface I-II for ω=15, $r_s/a = 0.95$, a range of source positions x_s/l_L and CORs. Solid line: anechoic; Dashed line: unflanged.

5.4 Summary and conclusions

5.4.1 Summary

- The main mode-matching techniques in the literature used to model noise propagation in ducts with uniform mean flow and changes in wall impedance have been reviewed and the model adopted in this thesis is described in detail.
- The existing formulations for mode-matching have been integrated with the point source representation described in Chapter 4 to enable the modelling of OTR liners and include back-reaction effects. The implications of the source proximity to the matching plane have been studied and the models cross-verified with reference FE solutions.
- The adopted mode-matching technique is extended to include an unflanged duct termination and coupled with a Wiener-Hopf-based routine to model the reflection coefficients at the duct inlet. The aim of including a duct termination being to cancel the point source singularities appearing in wall SPL predictions at the cut-on/cut-off transition in an infinite hard walled duct.

5.4.2 Conclusions

- The rate of convergence of the proposed model to predict the noise reduction of OTR liners is affected by source proximity to the matching plane. It is found that a COR=5 is generally sufficient as long as the source is separated from the matching plane by at least 0.1 wavelengths since the rate of convergence is rapidly reduced as the source gets closer to the matching plane.

- The agreement between the prediction model and the FE solutions in the hard wall section upstream of the OTR liner has been found to be within 1-5% in terms of relative error of the pressure at the wall or 0.5 dB in terms of ΔSPL.
- Comparison of analytical solutions with FE simulations containing multiple sources has confirmed that a source distribution can be modelled analytically as the superposition of the acoustic field of the individual sources, even when the mode-matching process with back reaction effects is involved.
- The inclusion of an unflanged termination successfully cancels the hard wall point source singularity at the cut-on/cut-off transition. However, in a hard-lined-hard configuration the reflections can cause axial resonances in an otherwise smooth spectrum. Overall, the unflanged termination provides predicted SPL/PWL IL spectra centred in the anechoic results but free from the cutting-on singularities. The choice of termination for the modelling of the W-8 bellmouth is discussed in Section 6.1.5.

Chapter 6

Acoustic modelling of OTR liners

Contents

The modelling efforts described in the preceding chapters to represent the liner impedance, the fan noise sources, mode-matching techniques and the duct termination are combined in this chapter to provide a prediction model for the noise reduction of OTR liners. In the first section, the main features of the analytical model are summarised and predictions are compared with experimental measurements available from the NASA W-8 test rig. In the second section, the prediction model is applied to a liner design study for a UHBR engine to show the potential benefits of OTR liners and guide the choice of liner parameters for their implementation in the next generation of turbofan engines.

6.1 Comparison of the OTR prediction model with NASA W-8 data

6.1.1 Summary of the prediction model

The outcomes of the previous chapters are combined here to obtain an analytical Green's function model of a Finite length liner connected to INFinite hard wall extensions, Green/FINF, for the prediction of the acoustic noise suppression of Over-Tip-Rotor liners. This model provides a simplification of a rotor-alone configuration with (1) the OTR liner modelled

by a finite lined section and (2) the fan noise modelled with point or distributed sources *within* the lined section based on Green's functions for lined cylindrical ducts. A diagram of the problem is shown in Fig. 6.1 and the modelling options of the main features are summarised below.

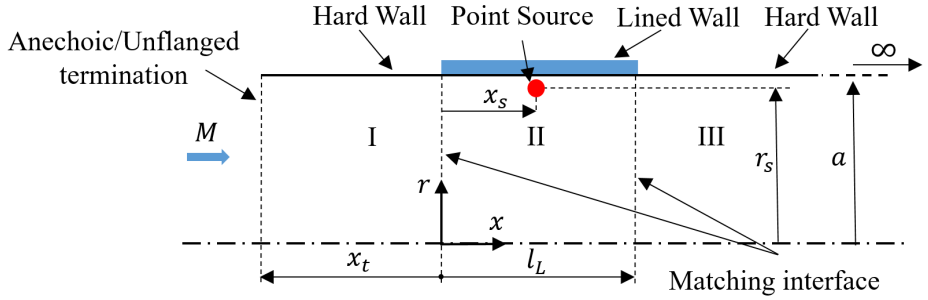

Figure 6.1: Diagram of the simplified Over-Tip-Rotor problem considered for the Green/FINF model.

1. **Liner modelling**: the liner impedance is applied using the Ingard-Myers boundary condition. Any locally reacting SDOF/MDOF model predicting the frequency dependent impedance or the semi-locally reacting equivalent impedance, such as the groove model described in Chapter 3, can be coupled with the current approach.

2. **Source modelling**: the fan noise sources are prescribed *within* the lined section based on the Green's function expressions presented in Chapter 4. Point/distributed static/rotating monopoles and dipoles have been considered, with constant or radially varying source strength. The ability to model the back-reaction effects of the source when it is located in close proximity to the liner surface is a key feature of the model.

3. **Mode-matching technique**: existing formulations for mode-matching wall impedance discontinuities have been integrated with the Green's function point source representation, both based on continuity of pressure and particle velocity and continuity of mass and momentum.

4. **Termination modelling**: any type of inlet termination can be included provided that a model to predict the matrix of reflection coefficients at the duct termination is available. The two options considered in this work are a purely anechoic (or infinite duct) and an unflanged termination. An existing model for the latter has been coupled with the mode-matching technique described in Chapter 5.

6.1.2 Modelling of the liner configurations

This part of the section describes the choice of parameters for the modelling of the acoustically treated grooves tested in the NASA W-8 rig [5]. A detailed description of this liner arrangement and the formulation of analytical models to predict the equivalent impedance of lined grooves is described in Section 3.3. However, a brief summary is given below and Fig. 3.4a-3.4b are repeated in Fig. 6.2 to support the explanation in this section.

The acoustically treated circumferential grooves cover the axial projection of the fan chord, as shown in Fig. 6.2a. The grooves are formed of upper and lower parts as indicated in the diagram in Fig. 6.2b. The upper part ② is open at the top and terminated at the base with a hard or porous 'septum'. Below the septum, the lower part of the groove ① is partitioned azimuthally. The equivalent groove impedance at the main duct - groove interface Z_g obtained using the annular groove model is given by Eq. 3.22 and repeated below.

$$Z_g(\omega, m) = -j\frac{J_m(\omega) + K_m Y_m(\omega)}{J'_m(\omega) + K_m Y'_m(\omega)} \quad , \tag{6.1}$$

where

$$K_m = -\frac{J'_m(\omega[1+\tilde{d}]) + j\frac{J_m(\omega[1+\tilde{d}])}{Z_f}}{Y'_m(\omega[1+\tilde{d}]) + j\frac{Y_m(\omega[1+\tilde{d}])}{Z_f}} \quad , \tag{6.2}$$

Z_f is the locally reacting impedance at the septum and $\tilde{d}$ the groove depth.

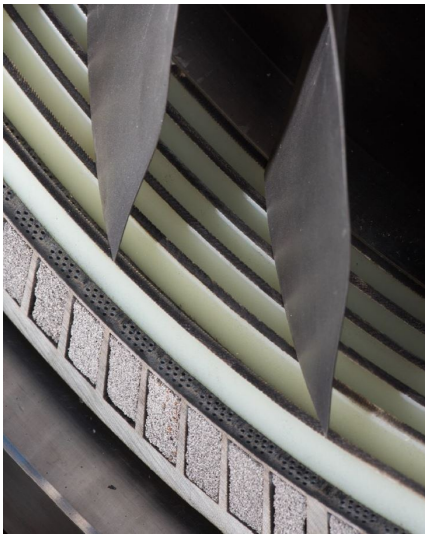

(a)

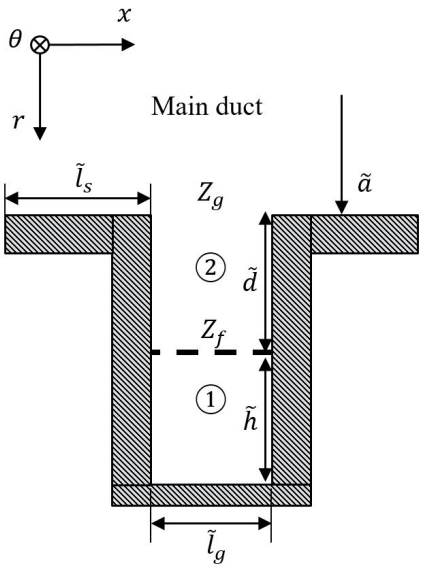

(b)

Figure 6.2: OTR fan case liner: (a) View of the OTR fan case liner installed in the NASA W-8 fan rig [5] and (b) dimensional diagram of the problem and nomenclature.

Diagrams of the actual OTR liners tested in the W-8 rig are shown in Fig. 6.3. Note that a lateral cross-section parallel to the duct axis is used in Fig. 6.2b, i.e. the flow goes from left to right, whereas a transversal cross-section perpendicular to the duct axis is adopted in Fig. 6.3 such that the flow direction is normal to the paper. The configuration in Fig. 6.3a is referred to as 'hard grooves' or 'hard septum' since there is no acoustic treatment in ①. An SDOF cavity liner is used with a 'thin' and 'thick' perforate in the configurations shown in Fig. 6.3b-6.3c. The configuration with the thin perforate was also tested with a Foam Metal Treatment inside the cavity ① (Fig. 6.3d), and an expansion chamber (Fig. 6.3d).

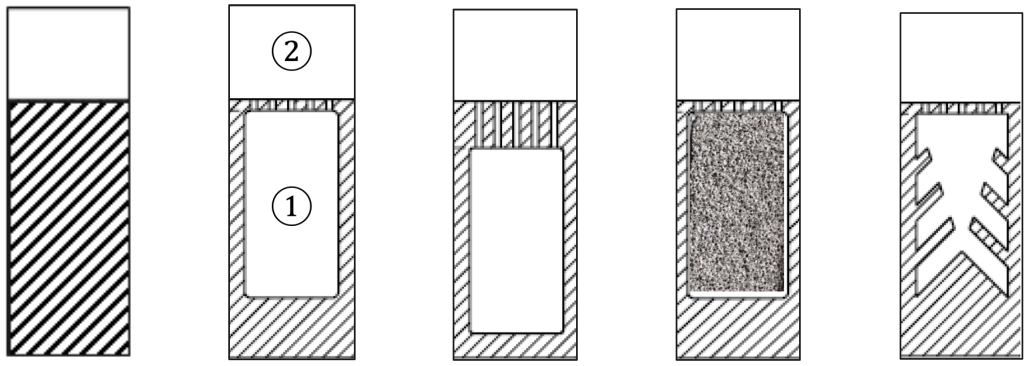

Figure 6.3: Cross-sections of the OTR fan case liners tested in the W-8 rig [5]:(a) Hard grooves, (b) Thin Perforate, (c) Thick Perforate, (d) Foam Metal Treatment, and (e) Expansion Chamber.

The comparisons in this section are limited to configurations (b)-(c), although it could be extended to the configuration with the metal foam treatment by changing the properties of the air in the cavity to those of the metal foam. The groove impedance model predicts vanishing values of resistance for some combinations of frequency and azimuthal mode number, which can lead to technical difficulties in the eigensolver described in Section 4.1.2. This can be overcome by postulating a small artificial resistance R_a at the groove neck adding to the groove impedance Z_g. A value of $R_a = 0.1$ has been used in the predictions of this section. The technical difficulty is particularly pronounced for the purely reactive 'hard grooves' (Fig. 6.3a). Predictions of configuration (a) are not included since the measured groove effect in the range of frequencies of interest is minimal and of less engineering interest than the lined cases.

It has been assumed that the impedance at the septum (Z_f) for the 'thin' and 'thick' perforates can be obtained by using the standard non-dimensional expression for a SDOF cavity liner [60]

$$Z_f = R_{fs} + j\left[\omega\frac{t+\varepsilon d_h}{\sigma} - \cot(\omega h)\right] \quad , \tag{6.3}$$

where R_{fs} denotes the resistance of the septum, t and d_h are the facing sheet thickness and hole diameter respectively, ϵ the end correction, σ the facing sheet porosity and h is the cavity depth. All variables are non-dimensional unless specified with a tilde.

The geometry of the grooves is specified in [5] and summarised in Table 6.1. The groove depth d is common for all configurations and the facing sheet and cavity parameters are also common for the 'thin' and 'thick' perforates, except for the facing sheet thickness, indicated as t_1 and t_2 respectively.

Table 6.1: Dimensional parameters of the acoustically treated grooves.

$\tilde{l_s}$	$\tilde{l_g}$	$\tilde{d}$	$\tilde{h}$	$\tilde{t}_1$	$\tilde{t}_2$	$\tilde{d_h}$	σ
1/8″	1/4″	1/2″	1″	0.06″	1/4″	0.035″	0.1

The missing variable required in the analytical groove models is the facing sheet resistance R_{fs}, for which the predicted groove impedance for a range of values of resistance has been compared to the measured impedance in the NASA Langley Normal Incidence Tube (NIT) [20]. The measured data in Fig. 6.4-6.5 was obtained using a tonal source for frequencies between 400 to 3000 Hz and at various SPL levels from 120 dB to 150 dB to assess the non-linearity effects [20]. The liner samples tested in the NIT are rectangular, which restricts the azimuthal propagation in the groove section ② that would normally occur when mounted in the fan casing. Hence, the predicted curves in Fig. 6.4-6.5 are obtained using $m = 0$. The predictions include the porosity correction of Eq. 3.33 to account for the rigid surfaces of width l_s between the grooves of width l_g.

The results in Fig. 6.4 show a reasonable agreement between the measurements and predictions for the tested range of resistances, especially for the thick perforate. The effect of additional non-linear losses at high SPL excitation corresponds, as expected, to higher values of facing sheet resistance. Measurements of the dynamic SPL at the fan leading edge for a tip Mach number of M=0.596, corresponding to the 50% fan speed data used in this section, can be as high as 160 dB [144]. However, data of the SPL at the septum position with the fan in operation, which could be lower, is not available.

The choice of the facing sheet resistance for the model is also supported by the measured and predicted normal incidence absorption coefficient, the latter obtained using the groove impedance model and Eq. 2.2. Based on the impedance and absorption coefficient comparisons a compromise of $R_{fs} = 0.5$ is taken for the 'thin' perforate and $R_{fs} = 0.7$ for the 'thick'. A sensitivity study around the chosen resistances showed very limited variability in the PWL IL spectrum and provided confidence in the current choice of parameters.

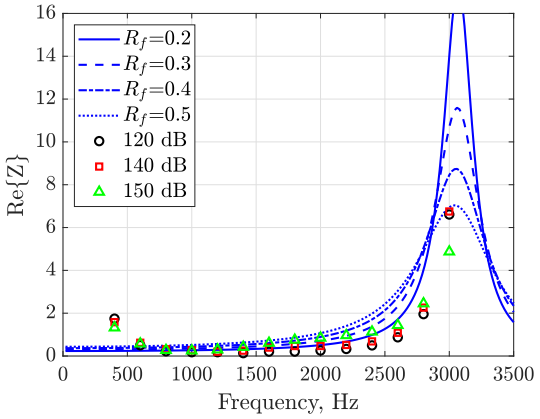

(a) Resistance ; 'Thin' perforate

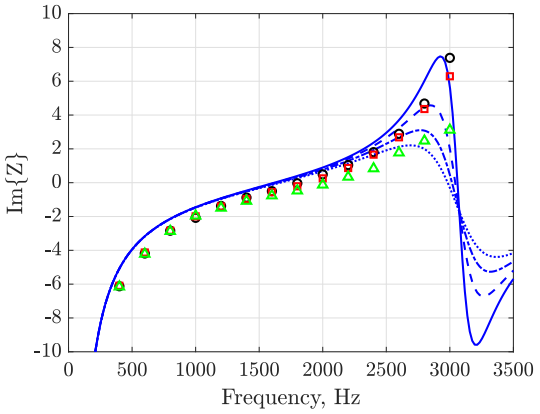

(b) Reactance ; 'Thin' perforate

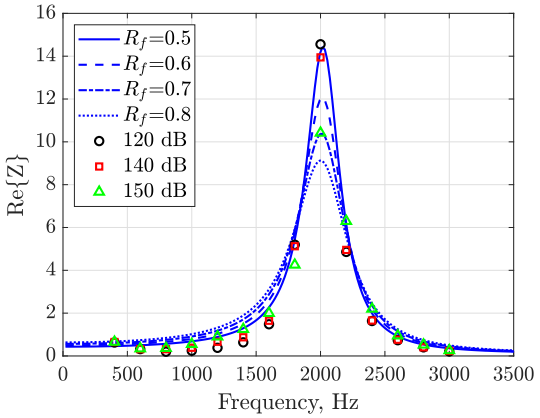

(c) Resistance ; 'Thick' perforate

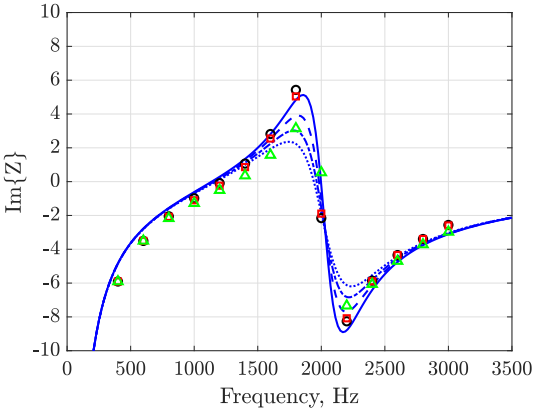

(d) Reactance ; 'Thick' perforate

Figure 6.4: Comparison of the predicted (lines) and measured (symbols) impedance of two lined grooves for a range of facing sheet resistances (R_{fs}).

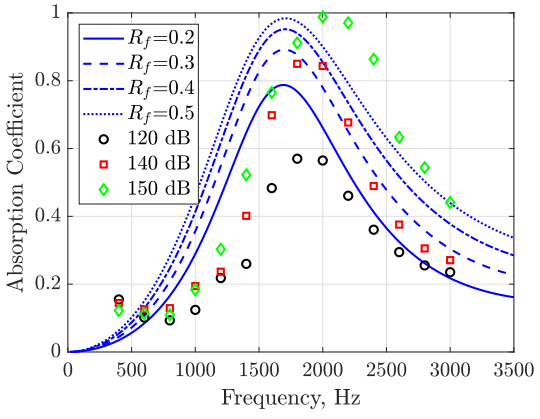

(a) 'Thin' perforate

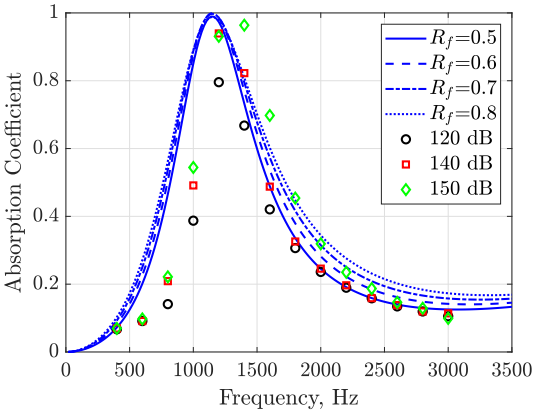

(b) 'Thick' perforate

Figure 6.5: Comparison of the predicted (lines) and measured (symbols) normal incidence absorption coefficient of lined grooves for a range of facing sheet resistances (R_{fs}).

6.1.3 Measured noise reductions and implications on the OTR model

This part of the section reviews the main features of the OTR NASA W-8 test [5] and the measured data, used for the comparisons with the prediction model described in this thesis. The tests were performed at the W-8 Single-Stage Axial Compressor Facility at the NASA Glenn Research Center using the Source Diagnostic Test (SDT) fan rotor R4, which consist of 22 blades, 22″ in diameter and a design speed of 12657 rpm.

The W-8 test rig is an internal flow facility in which the flow is conditioned in a plenum chamber upstream of the fan and guided through a bellmouth into the cylindrical section containing the instrumentation, the fan and the acoustic treatments. Two types of exhaust can be used, atmospheric and altitude, which can lead to additional background noise as described below. A schematic of the facility is provided in Fig. 1 of [5]. The data used in this section were acquired using a circumferential array of microphones located at 2.2 radii upstream of the fan.

The SDT fan rotor R4 was previously tested in a Rotor Alone Nacelle (RAN) hard wall configuration in the Low Speed Wind Tunnel at NASA GRC, as documented in [9, 145]. Bozak and Dougherty [5] compared the averaged in-duct SPL measured in the W-8 azimuthal ring and that acquired in the RAN configuration, in which an in-duct azimuthal array of microphones upstream of the fan was also installed. Their comparison for a hard wall case is shown in Fig. 6.7 to highlight two features of the W-8 data which are key for the comparison with the analytical predictions. Published pictures of the SDT RAN and W-8 rig are shown in Fig.6.6 to support the description below.

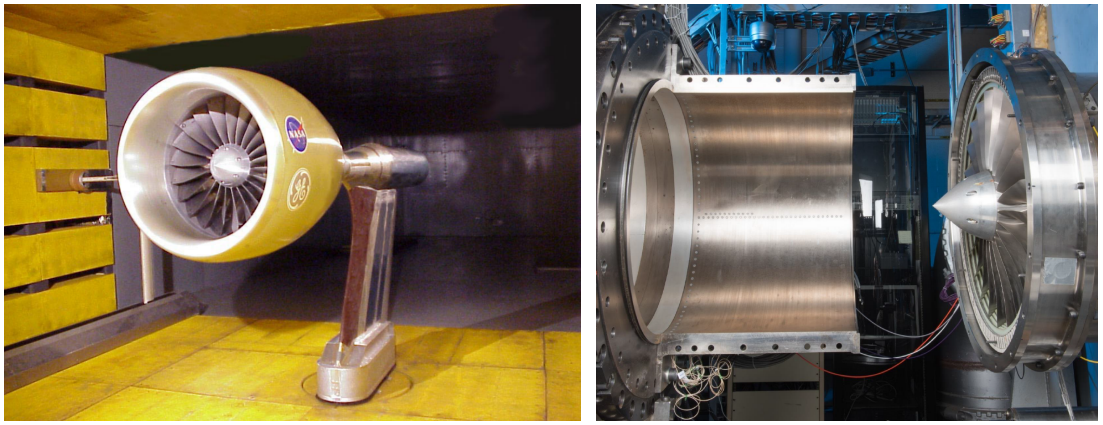

(a) SDT RAN (b) W-8 rig

Figure 6.6: Pictures of (a) the NASA SDT RAN in the Low Speed Wind Tunnel at NASA GRC [9] and (b) the NASA W-8 test rig with the fan and case acoustic treatment on the right and the inlet in-duct array on the left [5].

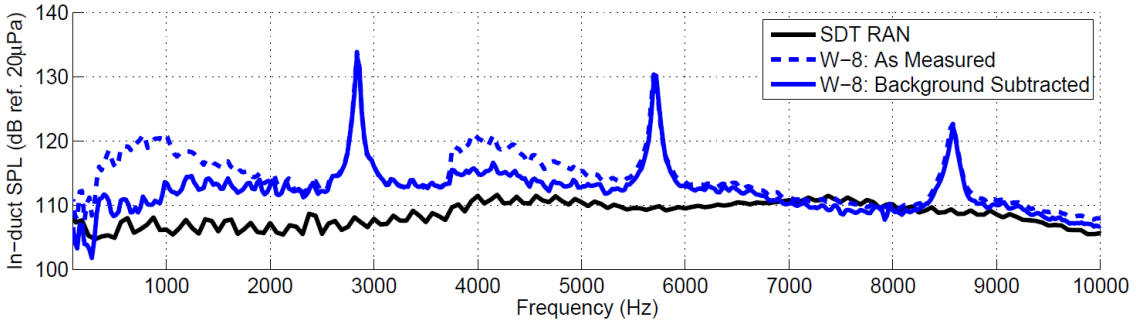

Figure 6.7: Comparison of the SPL spectrum measured with the fan rotor R4 in the SDT RAN and W-8 rigs at 61.7 % speed [5].

Noise contamination: comparison of the measured spectra with the atmospheric or altitude exhaust showed that, with the former, an additional broadband noise source around 800 Hz and 4 kHz is contaminating the data. This exhaust noise source is referred to as a 'background' source in [5] and can be observed in Fig. 6.7 by comparing the solid and dashed blue lines. All the measured data with the acoustic treatments contains exhaust noise contamination, which can be attenuated by the OTR liners. Therefore, the reduction of fan noise cannot be easily extracted at the contaminated frequencies and predicted analytical fan noise reductions could be masked by the exhaust noise in the experiments. This additional source could potentially be included in the prediction model by using an analytical source distribution located downstream of the fan and considering the relative strength of the fan and exhaust noise sources. However, this is out of the scope of this work and the approach taken here has been to restrict the comparisons to frequencies which lie outside the contaminated frequency range.

Dominant noise sources: broadened or 'haystacked' cut-on tones are observed at Blade Passing Frequency (BPF) in the W-8 in-duct SPL spectra which do not appear in the SDT RAN results (Fig. 6.7). This feature is linked to the thicker inlet boundary layer in the W-8 rig [146], with higher turbulence intensity and length scales than in the SDT RAN wind tunnel tests, interacting with the fan rotor blades. Differences in the inlet boundary layer characteristics are expected due to the significantly distinct geometry of the bellmouth in the W-8 rig and the flight inlet used in the SDT RAN wind tunnel tests. Besides, the thicker W-8 boundary layer also causes the fan broadband noise in the W-8 to be about 3 dB higher than that in the SDT up to 6.5 kHz. As a consequence, leading edge (LE) broadband sources should be included in the OTR prediction model when comparing with the W-8 experimental data to include the interaction noise as well as other main sources such as trailing edge (TE) noise. Depending on the relative strength of the LE and TE sources, the OTR liner benefits could be significantly lower than if a TE source were dominant, which could be the case for a cleaner inlet flow such as in the case of the SDT RAN tests. These considerations are assessed by using the analytical OTR prediction model in section 6.1.4.

The pressure measurements are obtained with flush-mounted wall microphones and hence both fan broadband acoustic noise and boundary layer broadband pressure fluctuations are present in the in-duct measured signals. The boundary layer noise in the SDT RAN tests is probably lower than in the W-8 rig due to a thinner boundary layer associated with the flight inlet nacelle, which can also contribute to the differences in the broadband noise spectra of the two rigs, in addition to the BL-fan interaction noise mentioned above. The noise reduction benefits of the OTR liners could therefore be masked, depending on the relative strength of the BL and fan noise. Since BL broadband spectra typically decay monotonically with frequency, this could be a reason for over-prediction of the measured insertion loss data at low frequencies but not at the higher frequencies.

The noise reduction performance of the OTR liners tested in the W-8 rig was assessed in [5] in terms of the PWL Insertion Loss by processing the measured wall pressures with a modal beamforming method [147]. It was found that the repeatability of the PWL results was within 1 dB and that the circumferential grooves can have a noise penalty of 2.5-6 dB. Grazing Flow Impedance Tube tests at NASA suggested that the groove noise can be attributed to cavity tones/resonances clipped by the fan [37]. An additional complication was that the hard wall and grooved configurations tested in the W-8 rig had a different tip clearance, in the former a nominal (0.000") tip clearance was used whereas in the later was 0.030". The effect of tip clearance was estimated from processing far-field data of the SDT RAN tests, showing up to 1 dB PWL additional noise for the larger tip gap at frequencies above 2 kHz [5]. The combined effect of the tip clearance and the additional noise generated by the circumferential grooves were treated separately and assumed independent from the noise reduction of the OTR liners. The resultant PWL IL (with a hard wall datum) due to the tip clearance and the effect of the grooves and the PWL IL (with a hard groove datum) of the acoustic treatments were presented in the form of contour plots for 1/12 octave frequencies and % fan speed.

The processed PWL data was not available for the current project but the measured pressure at the microphone arrays was provided by NASA. Therefore, the comparisons between the measured and predicted noise reductions in section 6.1.4 are based on the azimuthally averaged SPL at the wall instead of the more conventional PWL IL assessment.

The measured SPL at the duct wall is shown in Fig. 6.8 for the hard wall datum, the hard groove configuration and the two OTR liners ('thin' and 'thick' perforates) described in section 6.1.2. The two broadband humps of exhaust Background Noise ('BN') contaminating the data are roughly indicated at 50 % fan speed with the 'BN' blue arrows. At this fan speed, the hard grooves generate additional broadband noise that becomes dominant at frequencies above 4 kHz, attributed to the aerodynamic interaction of the flow in the fan tip region and the grooves. The acoustic treatments in the lined grooves can reduce

the additional noise. However, the SPL is still higher than in the hard wall case for frequencies above 5 kHz in the 'thin' perforate and above 4 kHz for the 'thick' one. The area dominated by groove noise is indicated in Fig. 6.8 with the red arrow.

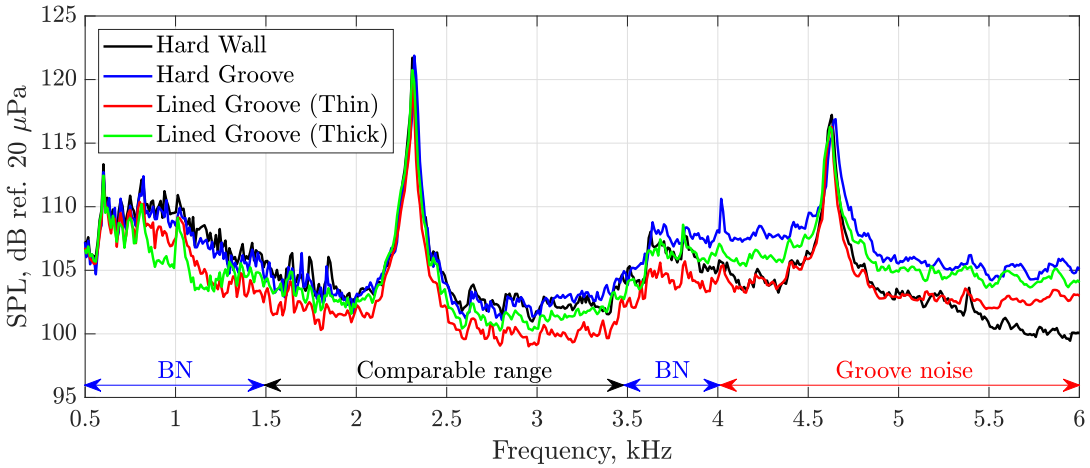

Figure 6.8: W-8 SPL spectra at 50 % fan speed (analysis bandwidth of 5 Hz).

The noise due to grazing flow over the grooves is not modelled by the analytical impedance groove models of Section 3.3, in which it is always assumed that the uniform mean flow in the duct does not interact with the grooves. It can be argued that additional uncorrelated axially distributed sources at the vicinity of the wall could be included to approximate the additional groove noise by adjusting their relative source strength based on the hard wall - hard groove measurements. However, this involves additional major assumptions on the source model and would complicate the understanding of the predictions. Instead, it is noted from Fig. 6.8 that the effect of the hard grooves in the range of 1.5-3.5 kHz is minimal and relatively free from the exhaust noise. Hence, the comparisons between the measured and predicted noise reductions in section 6.1.4 are restricted to this frequency range to avoid including additional noise sources other than fan noise in the current prediction model.

The measured SPL IL based on the hard wall or hard groove datum are shown in Fig. 6.9a - Fig. 6.9b respectively. Note that the tip clearance effect is not taken into account when using the hard wall datum since this data is not currently available. However, as mentioned before, this variation is within 1 dB PWL, which is also the repeatability of the experiments. The noise reduction spectrum in Fig. 6.9a shows more clearly the minimal impact of the hard grooves up to 3.5 kHz and supports the choice of the frequency range for the comparison with the model. Above this frequency, the additional groove noise dominates and masks the benefits of the OTR liners. However, by assessing the SPL IL with the hard groove datum (Fig. 6.9b) it can be observed that the OTR liners are indeed also reducing the noise in the tip area, where both fan and groove noise are confined, at frequencies above 3.5 kHz with broadband 2-4 dB SPL IL.

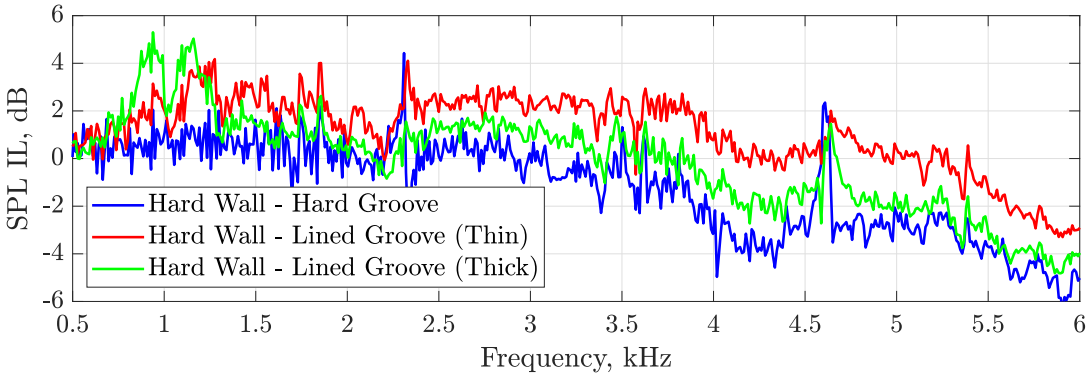

(a) SPL IL - hard wall datum

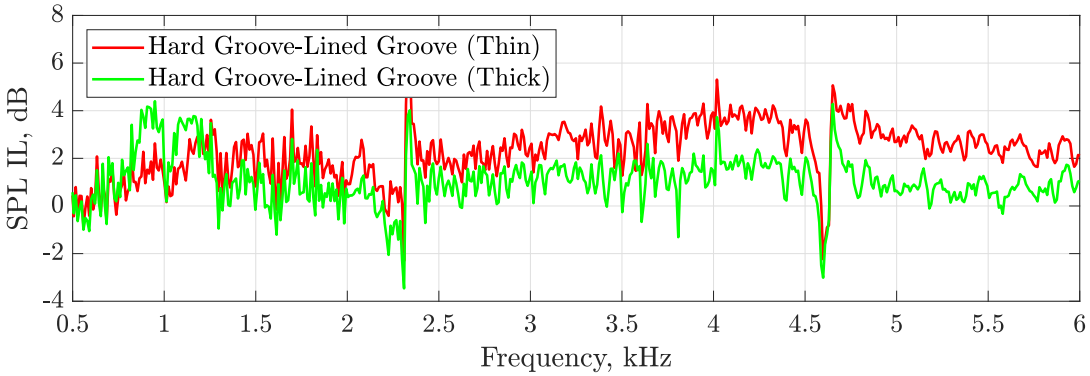

(b) SPL IL - hard groove datum

Figure 6.9: W-8 SPL IL spectra based on (a) the hard wall datum and (b) the hard groove datum at 50 % fan speed (analysis bandwidth of 5 Hz).

6.1.4 Comparison of predicted and measured Insertion Loss

Of the fan source models described in Chapter 4, arguably the most physically representative is the distribution of rotating dipoles coupled with Blake's model [120] for the pressure spectrum of the turbulent boundary layer on the rotor blade surface. The description of the model in Section 4.4.3 is given for a fixed fan stagger angle and without indications on the assumed fan chord at each source radial location. Hence, the following assumptions are introduced and compared in Fig. 6.11:

- **Stagger angle distribution $\Theta(r_s)$:** the fan chord at each radial location is assumed to be parallel to the incident flow (Fig. 6.10a with AoA≈0) such that

$$\Theta(r_s) = \text{atan}\left(\frac{\bar{\Omega} r_s}{M_x}\right) \quad . \tag{6.4}$$

- **Chord distribution $c(r_s)$:** the axial projection of the fan chord remains constant along the radius and equal to the OTR liner length l_L (Fig. 6.10b):

$$c(r_s) = \frac{l_L}{\cos[\Theta(r_s)]} \quad . \tag{6.5}$$

The measured axial mean flow at the fan section, $M_x = 0.236$, and the non-dimensional shaft rotation (or tip Mach number) at 50% fan speed, $\bar{\Omega} = 0.545$ have been used to determine the radial distribution of stagger angle and chord. In practice, for the OTR liner length in the W-8 test of $\tilde{l}_L$=57.2 mm, this results in Θ=30 deg. and $\tilde{c}$=66.0 mm at 25 % radius and Θ=66.6 deg. and $\tilde{c}$=143.9 mm at the fan tip.

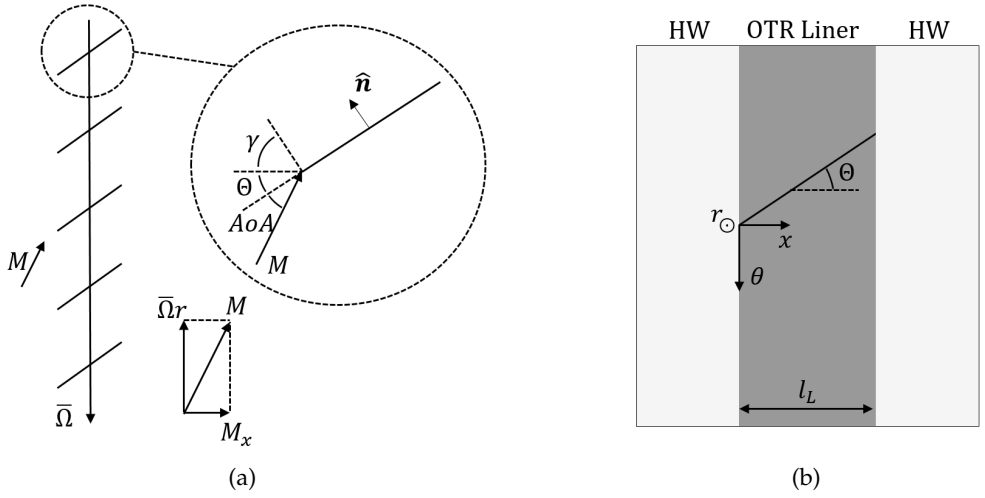

Figure 6.10: (a) fan row diagram with nomenclature and (b) definition of the radial fan chord distribution.

All predictions in this part of the section assume an anechoic inlet termination. The frequency range presented in the comparisons of the predicted and measured noise reductions is 1-3.5 kHz, even though 1-1.5 kHz is contaminated by the exhaust noise and not included in the discussion. This choice of frequencies is to show the expected peak noise reduction of the 'thick' perforate configuration.

The effect on the SPL IL predictions of considering a twisted flat plate (radially varying stagger angle) with a constant or variable chord distribution in the source model is shown in Fig. 6.11 by comparing with a case of constant stagger angle and chord. For all three curves the relative Mach number at each radial position has been used to compute the eddy convection velocity required in Blake's model and for the local stagger angle and fan chord, when applicable. However, the frequency shift in the source cross-spectrum due to source rotation is omitted here but considered in the next step. The effective impedance of the lined grooves is shown in Fig.6.12 for different azimuthal mode orders to support the analysis of the results in Fig. 6.11.

Comparison of the predictions with constant chord and constant or variable stagger angle in Fig. 6.11 shows a minor effect on the predicted noise reductions ($<$ 0.1 dB). However, a radially varying chord in accordance to the fan twist yields up to 0.6 dB of additional noise reduction due to a concentration of the source strength towards the tip

region (larger chord) and closer to the OTR liner, which leads to higher noise suppression. This source model is used in the rest of the comparisons in this part of the section unless specified otherwise.

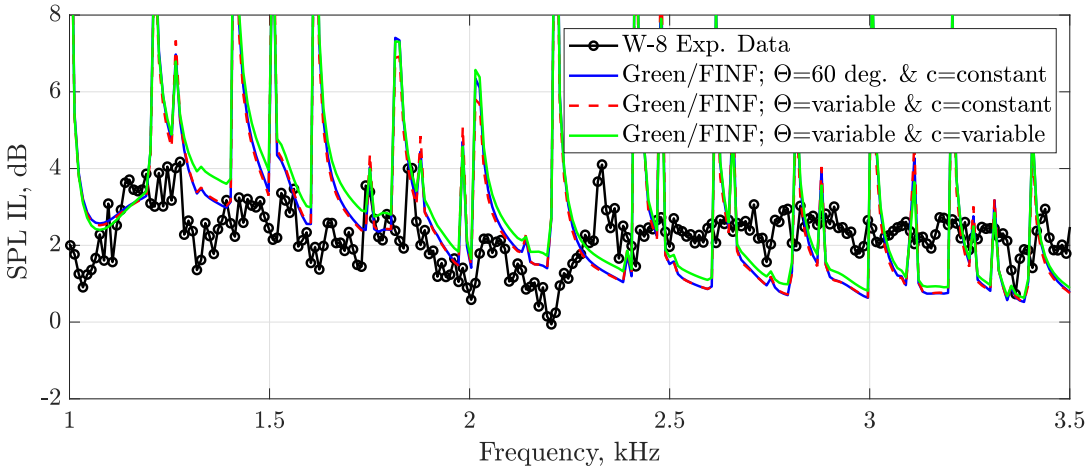

Figure 6.11: Effect of variable stagger angle and chord in the predicted SPL IL for the 'thin' perforate and a distribution of static dipoles at mid-chord position with M=0.236, $\bar{\Omega} = 0.545$ and COR=5.

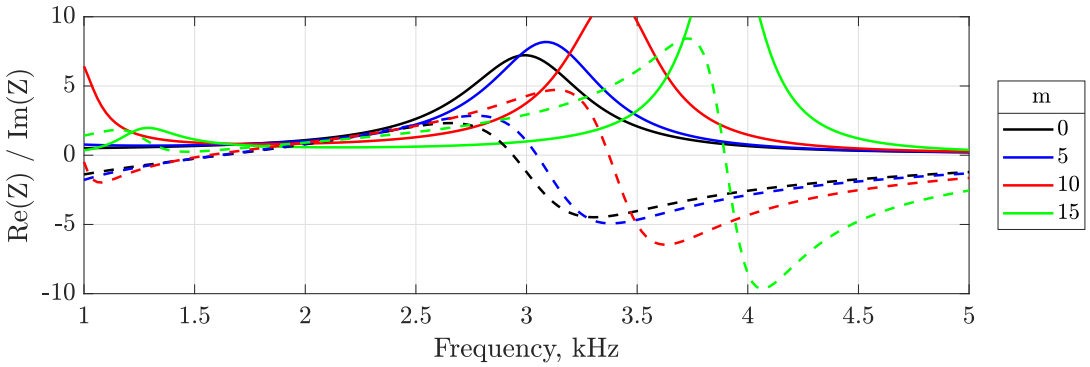

Figure 6.12: Impedance of the 'thin' perforate OTR liner for different azimuthal mode orders m. Key: solid lines - Re(Z), dashed lines - Im(Z).

The effect of the source rotation in the predicted noise reduction is now analysed. To this end, the SPL spectrum for the hard wall and lined configurations (thin perforate) are shown in Fig. 6.13 assuming static or rotating sources. The hard wall spectrum is marked by the cut-off/cut-on singularities while the lined curve is free from spikes due to a complex Lorentz wavenumber in the OTR liner section. The frequency shift in the source strength caused by the source rotation yields additional/reduced 0.5-1 dB SPL below/above 2.8 kHz. However, when computing the SPL IL, shown in Fig. 6.14, the effect of the rotation is reduced due to the similar shifting trends in the SPL spectral shape of the hard and lined configurations, leading to differences of less than 0.5 dB.

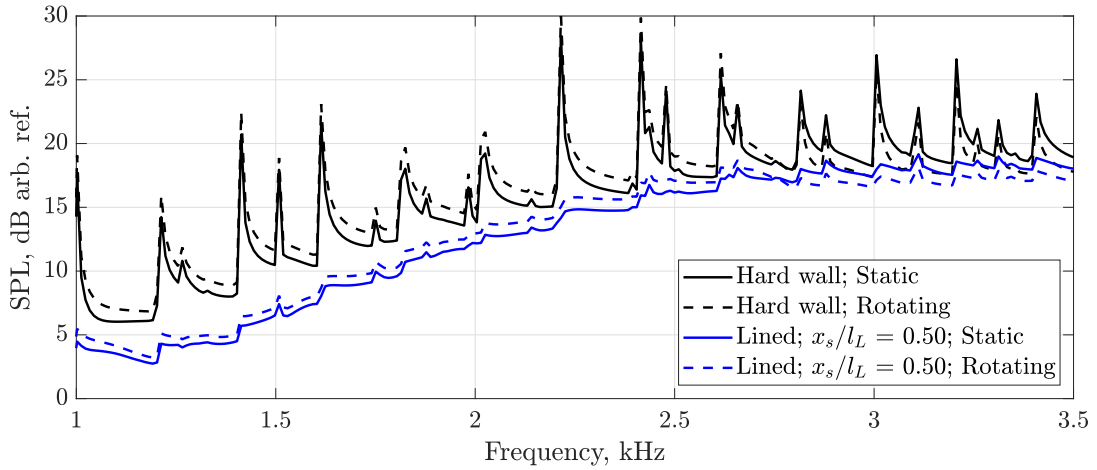

Figure 6.13: Effect of the source rotation in the predicted SPL for a distribution of dipoles at mid-chord position with M=0.236, $\bar{\Omega} = 0.545$ and COR=5.

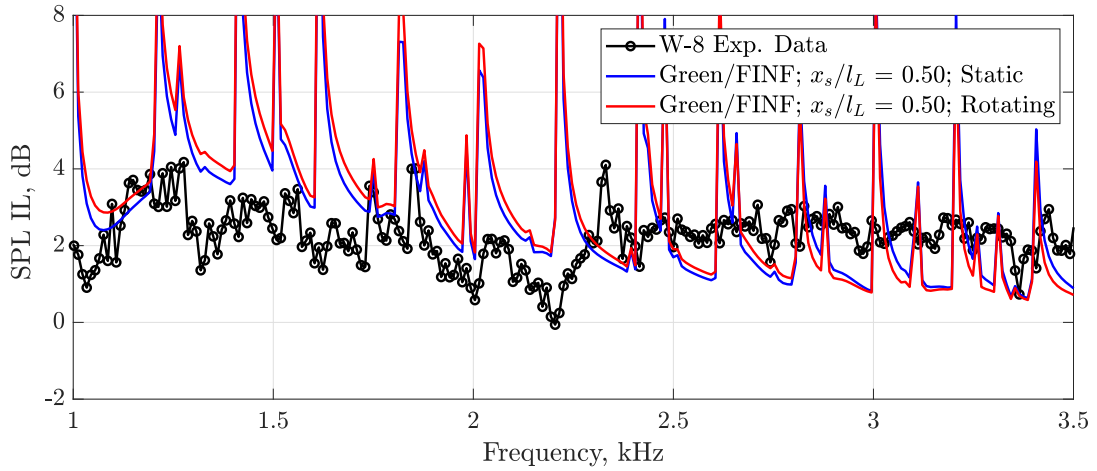

Figure 6.14: Effect of the source rotation in the predicted SPL IL for a distribution of dipoles at mid-chord position with M=0.236, $\bar{\Omega} = 0.545$ and COR=5.

The main features of the measured data have been highlighted in the previous part of the section. It has been argued that LE noise may well be a major source contributor in the W-8 experiments. Therefore, noise predictions have been obtained for a source distribution located at $x_s = 0.75l_L$, 'close' to the TE, and at $x_s = 0.25l_L$, 'close' to the LE. The choice of axial locations is conservative to avoid COR-convergence issues. Both source distributions are assumed to have the same strength and to be uncorrelated.

The predictions for the 'thin' and 'thick' perforates are compared with the W-8 measured data in Fig. 6.15. Leaving the singularity-induced spikes aside, broadband noise reductions of up to 6 dB are predicted in Fig. 6.15a when the source plane is located closer to the TE due to a higher lined surface available, overpredicting the measured IL by up to 4 dB over 1.5-2.5 kHz. However, if LE sources are included in the model, the predicted IL is reduced and gets closer to the measured data due to the LE sources being less attenuated by the OTR liner. Naturally, the impact of the assumed axial location of the sources

is more pronounced around the peak attenuation but has a lower effect at frequencies above 2.5 kHz, where the analytical model underpredicts the SPL IL by 1-2 dB.

Analogous trends can be observed in Fig. 6.15b for the 'thick' perforate configuration, although the predicted and measured IL present a closer agreement. The causes of the spikes have been discussed in Section 5.3 and motivated the inclusion of a duct termination in the Green/FINF model. The choice of anechoic or unflanged inlet termination is discussed in greater detail in the next part of the section by comparison with an FE model of the W-8 geometry. Therefore, at this point of the analysis, ignoring the spikes and keeping in mind the ± 1 dB repeatability of the experiments and the differences in tip clearance (also accounting for up to 1 dB), a reasonable agreement in magnitude and spectral shape can be drawn from the comparisons of the predicted and measured data consistent across the two liner configurations.

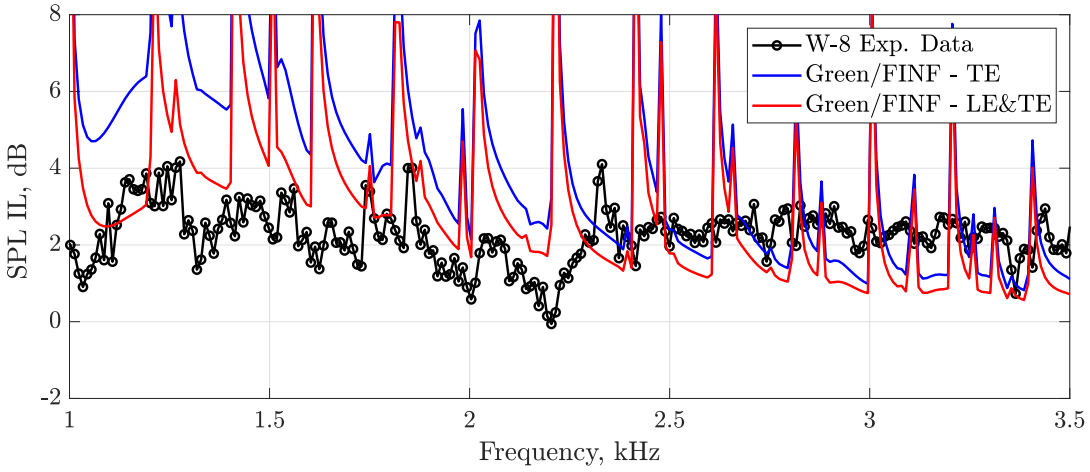

(a) 'Thin' perforate OTR configuration

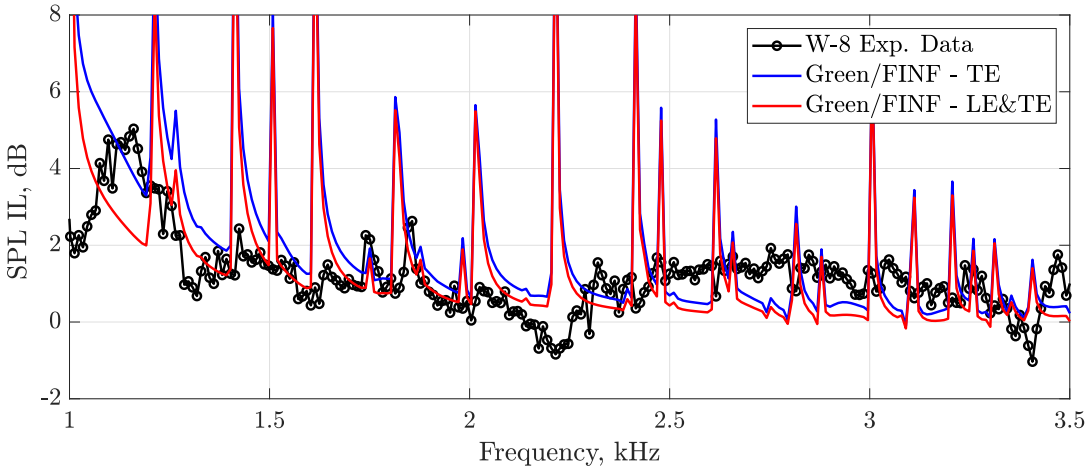

(b) 'Thick' perforate OTR configuration

Figure 6.15: Comparison of the measured and predicted SPL IL for a distribution of dipoles located at $x_s = 0.75 l_L$ (TE) and $x_s = 0.25 l_L$ (LE) with M=0.236, $\bar{\Omega} = 0.545$ and COR=5.

Based on the results shown here for the 'thin' perforate, it can be concluded that the key parameter controlling the peak noise reductions is the chordwise location of the dominant source mechanism, followed by the radial distribution of source strength, the maximum noise suppression benefit coming from close proximity to the OTR liner. The stagger angle and the source rotation would follow, being the parameters with the lowest impact on the SPL IL predictions. The latter could be expected due to the relatively flat spectrum of fan broadband noise over the range of frequencies of interest.

The PWL is less affected by the singularities at the cut-on frequency of each mode, as discussed in Section 5.3. Joseph et. al. [7] defined expressions that relate the axial acoustic power in a hard wall duct with the averaged pressure across the duct cross-section for various distributions of uncorrelated sources. They also proposed a relationship between the averaged pressure across the duct and that measured at the wall but showed some variability for monopoles and dipoles with flow. Therefore, a conversion from SPL IL to PWL IL is not attempted here but there is evidence that the former is a good representation of the latter for distributed noise sources. Both the SPL IL and the PWL IL are computed for the 'thin' perforate and compared with the measured SPL IL in Fig. 6.16. Although the broadband peak attenuation between the two predicted curves differs up to 1 dB, the PWL IL spectrum presents the same behaviour as the SPL IL prediction with the benefit of lower spikes at the cut-on frequency of each duct mode.

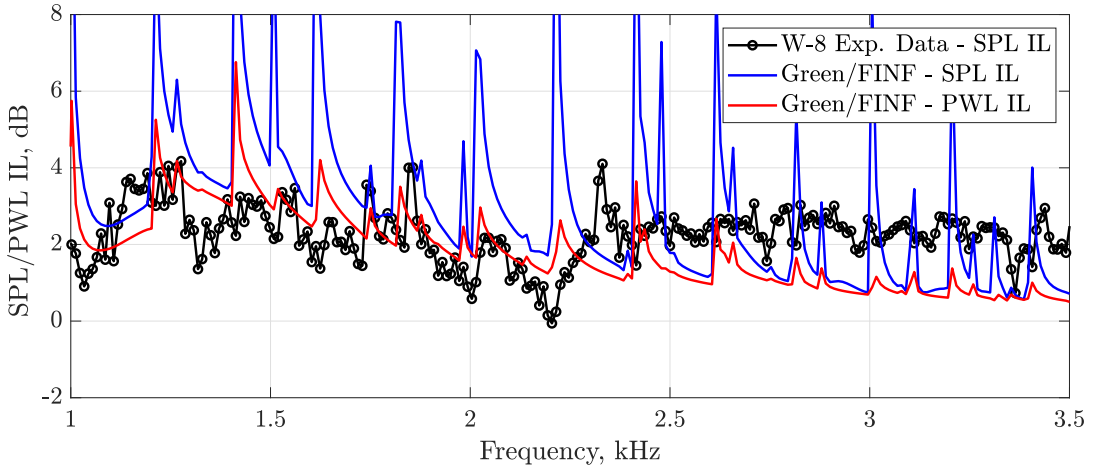

Figure 6.16: Comparison of the measured SPL IL and predicted SPL IL and PWL IL for the 'thin' perforate and a distribution of LE and TE dipoles with M=0.236, $\bar{\Omega} = 0.545$ and COR=5.

6.1.5 FE solutions of the W-8 rig and modelling of the termination

Inspection of the W-8 test facility schematic in Fig. 1 of [5] shows that the rig consists of a bellmouth guiding the flow into a cylindrical section containing the instrumentation and the fan itself. The choice of duct inlet in Green/FIFN to closer predict the bellmouth termination, either anechoic or unflanged, may not be immediate. Hence, a FE model of the W-8 rig, shown in Fig. 6.17, has been developed to guide the choice of the inlet duct termination. A 3D FE model is used to reproduce the W-8 geometry and with a PML-type boundary condition at the termination of the cylinder and a spherical PML at the end of the bellmouth. The same guidelines and procedures to generate the mesh and set-up the cases described in Section 3.3.2 have been applied here.

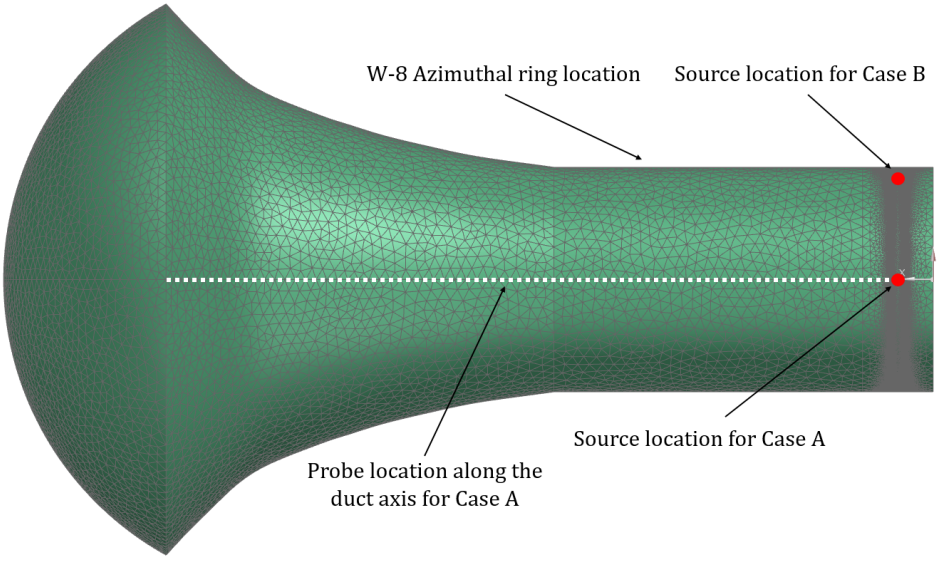

Figure 6.17: Diagram of the FE model to study the reflections of the W-8 geometry.

Two test cases are described and compared with the analytical predictions in this part of the section. This exercise is focused on the hard wall configuration since it is responsible for the singularities in the SPL/PWL IL predictions. However, it could be easily extended to the OTR lined configurations to assess the issue of the axial resonances when considering an unflanged termination. The two cases described here are for zero flow and hence a point volume velocity monopole is used to retain the cut-on/cut-off singularities. The location of the source and the probes for the cases described below is also indicated in Fig. 6.17.

- **Case A:** it represents the simplest case and aims at providing fundamental understanding of the reflections induced by the bellmouth. The point source is located at the duct axis such that it can only excite modes with $m = 0$ and at mid-chord position, $(x_s, r_s, \theta_s) = (l_L/2, 0, 0)$ in Green/FINF coordinates, and probes are located along the duct axis.

- **Case B:** it aims at reproducing a simplified version of the W-8 experimental arrangement by placing the source at 95% radius, $(x_s, r_s, \theta_s) = (l_L/2, 0.95a, 0)$ in Green/FINF coordinates, and the probe at the wall ($r = a$) and axial location of the azimuthal microphone array ($x = -2.2a$).

The predicted SPL spectrum evaluated on the duct axis at $x = -2.2a$ for case A is shown in Fig. 6.18. This figure shows the behaviour of the cutting-on process for an infinite duct (anechoic inlet termination), with the sharp high amplitude singularity at the cut-on frequency of a particular mode $\mathrm{He}_{(0,2)} = 3.832$. The coloured squares only indicate the frequencies at which the FE solution is compared with the analytical results for an anechoic or unflanged inlet termination in Fig. 6.19, to easily identify at which point of the cutting-on process the comparisons are being made.

Two distinct axial locations are key in the predicted SPL when reflections are included in the solution: the relative position of the termination and the azimuthal array. In this section, it is assumed that the termination is located at the end of the cylindrical part and beginning of the bellmouth ($x_t \approx -3a$). The position of the termination and azimuthal array are indicated with black and blue dashed lines in Fig. 6.19. The predictions using Green/FINF are only plotted for the cylindrical section of the duct $x_t < x < 0$.

It can be observed that the FE solution and the anechoic results present an excellent agreement at frequencies well away from cut-on/cut-off, as observed in Fig. 6.19a and Fig. 6.19f. At those frequencies, the FE W-8 does not show any signs of reflections, marked by the oscillations in the predicted solution with an unflanged duct. However, at frequencies immediately before and at cut-on (Fig. 6.19b-6.19c) the W-8 results lay closer to the unflanged duct configuration. The singularity with the anechoic termination is clearly observed in Fig. 6.19c with an SPL 20-40 dB higher than in the FE or unflanged results. Once cut-on, the FE solution initially falls somewhere in between the unflanged and anechoic predictions (Fig. 6.19d- 6.19e) but tends to an anechoic solution (it flattens) within the cylindrical section. The difference between the predictions and the FE solution at each frequency at the axial location of the azimuthal array are summarised in Table 6.2.

Table 6.2: Difference between the FE and predicted SPL at $x = -2.2a$ for Case A.

	He					
	2.800	3.275	3.832	3.835	3.875	4.400
Inlet termination	ΔSPL (dB)					
Anechoic	0.06	7.51	33.80	8.01	0.57	0.04
Unflanged	0.76	1.25	2.56	7.76	6.13	1.93

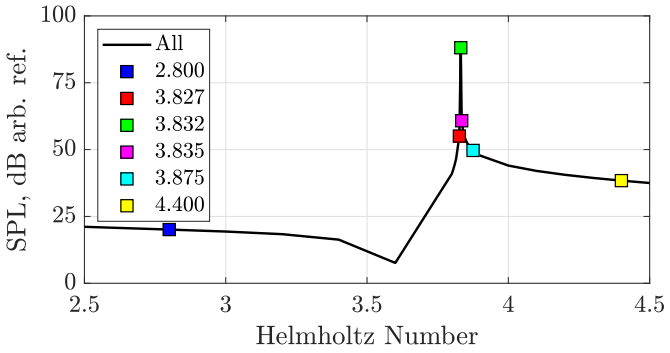

Figure 6.18: SPL of mode (0,2) cutting-on. Squares show the frequencies at which the FE and analytical predictions are evaluated in Fig. 6.19.

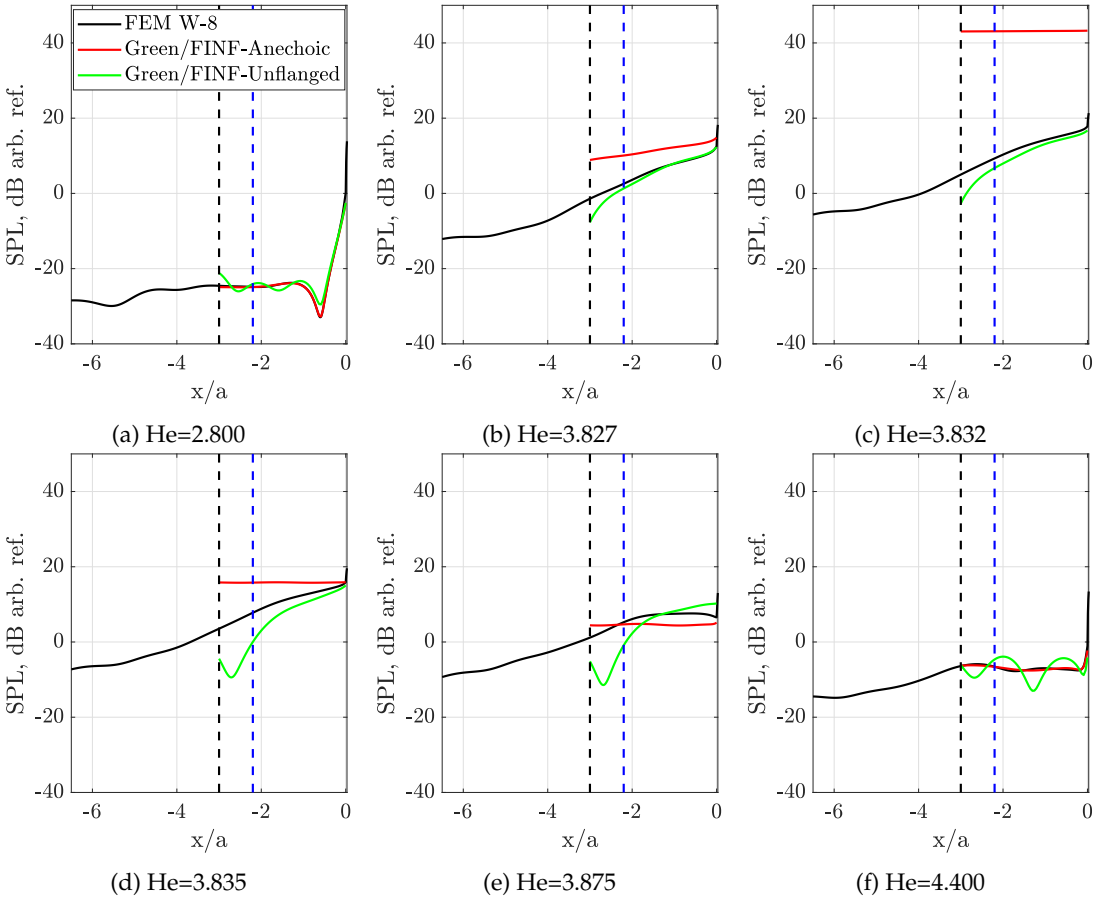

(a) He=2.800 (b) He=3.827 (c) He=3.832

(d) He=3.835 (e) He=3.875 (f) He=4.400

Figure 6.19: Comparison of the FE and predicted SPL along the duct axis for Case A. Key for dashed lines: black - end of the cylindrical section and start of the bellmouth (x/a=-3), blue - axial location of the azimuthal array in the W-8 rig (x/a=-2.2).

The comparison of the analytical solution and the FE results for Case B is shown in Fig. 6.20 for a wider frequency range that includes the cutting-on process of four modes. The solution is computed at intervals of 5 Hz since the small Δf used to capture the detail of the cut-on process in Fig. 6.18 is rarely used in practical applications due to the computational cost. In practice, the wider intervals result in reduced singularity-induced

spikes (solution evaluated at frequencies further away from the exact cut-on/cut-off) and therefore the FE and anechoic solution seems to show a better agreement for most of the spectrum. However, as mentioned earlier, a closer evaluation in the vicinity of the cut-on/cut-off frequency would show that at those conditions the FE W-8 bellmouth cancels the singularity as in the case of an unflanged duct. Overall, the FE W-8 bellmouth results seem to be in closer agreement to an anechoic termination but without the inherent singularities of the infinite duct representation.

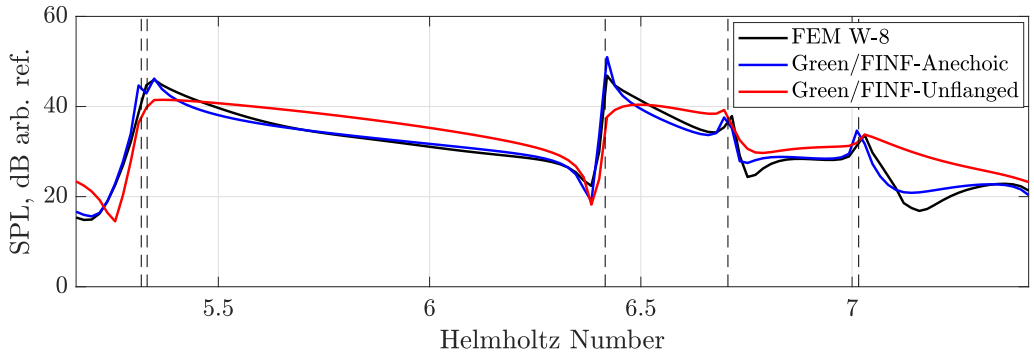

Figure 6.20: Comparison of the FE and predicted SPL spectra with an anechoic or unflanged termination for Case B.

The predicted SPL IL and the PWL IL computed for the 'thin' perforate and the distribution of dipoles of Fig. 6.16 are recomputed for an unflanged inlet termination and shown in Fig. 6.21. The predicted SPL IL spectrum suffers from the axial resonances in the inlet hard wall section described in Section 5.3. However, the PWL IL predictions show the benefits of including an unflanged termination in reducing the cut-on singularity spikes. The unflanged duct termination is therefore useful for realistically suppressing the cut-off/cut-on singularity, as shown above by comparing with the FEM solutions, but is unrealistic in that it causes much larger modal reflections, in general, than would be expected to occur with the slowly varying W-8 bellmouth intake.

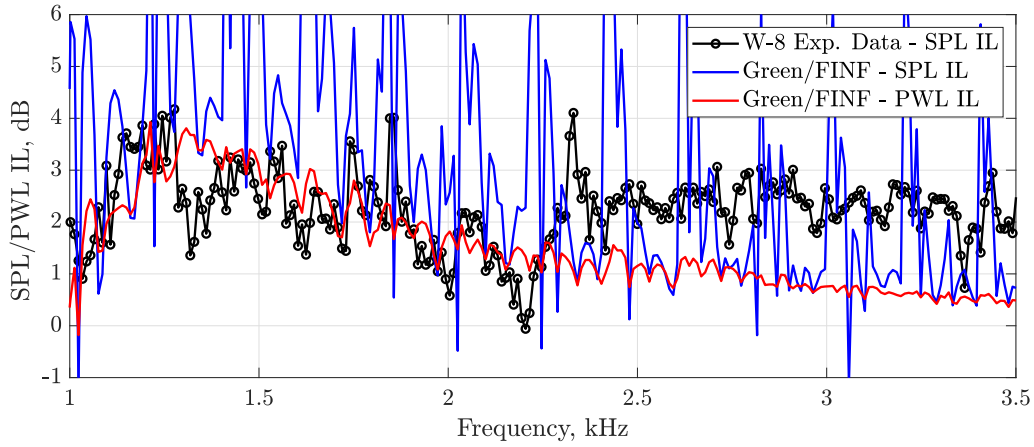

Figure 6.21: Comparison of the measured SPL IL and predicted SPL IL and PWL IL for the 'thin' perforate and a distribution of LE and TE dipoles with M=0.236, $\bar{\Omega} = 0.545$ and COR=5.

Even though there are no signs of the aforementioned cut-on/cut-off spikes in the measured W-8 hard wall data, the SDT RAN test may suggest evidence of this phenomenon. The measured hard wall SPL spectra at the wall for the SDT RAN test are compared with Green/FINF predictions with anechoic and unflanged inlet in Fig.6.22. The source model used in the predictions is a static axial dipole located at mid-chord position and 95% radius. The azimuthal microphone ring used in the SDT RAN test was installed much closer to the fan, only 0.55 radii upstream of the fan stacking axis, and the termination is estimated at $x_t/a = -1$. The actual SPL level is not predicted by the analytical model and an arbitrary reference is used in each subfigure for comparison purposes only. The unflanged termination is a better representation of the flight inlet used in the wind tunnel experiment than the bellmouth of the W-8 rig. Distinct humps can be observed in the measured data, appearing with a similar periodicity to that of the cut-on/off spikes in the predicted spectra, which can be more clearly observed in the predictions with the unflanged inlet. The amplitudes of the predicted singularities are limited when including the reflections at the termination and not far from those of the measured humps. The similar periodicity and amplitudes might suggest evidence of the cut-on singularities in the measured data that could be masked in the W-8 test by the noise of the thicker boundary layer.

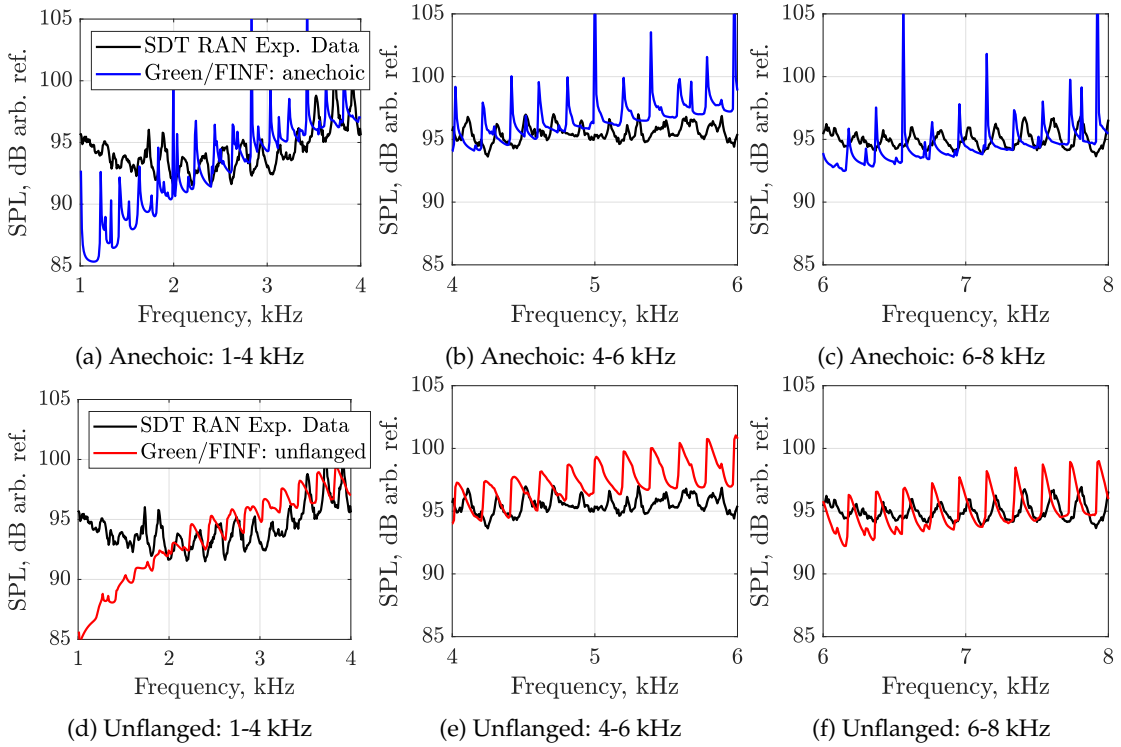

(a) Anechoic: 1-4 kHz (b) Anechoic: 4-6 kHz (c) Anechoic: 6-8 kHz

(d) Unflanged: 1-4 kHz (e) Unflanged: 4-6 kHz (f) Unflanged: 6-8 kHz

Figure 6.22: Comparison of measured hard wall SPL spectra in the SDT RAN wind tunnel test with predictions for an (a)-(c) anechoic inlet and (d)-(e) unflanged inlet and a static axial dipole at $(x_s, r_s, \theta_s) = (0.5l_L, 0.95a, 0)$ with M=0.236 and COR=5.

The section concludes with a simple comparison of the measured SPL IL in the W-8 rig and the predicted SPL IL (Fig. 6.23) and PWL IL (Fig. 6.24) for a static axial dipole located at mid-chord position and 95% radius, both for the anechoic and unflanged inlet terminations. As mentioned earlier in Fig. 6.21 and explained in Section 5.3, even though the hard wall spikes are reduced by the introduction of the termination, axial resonances can appear in the OTR configuration, leading to the high variability shown in Fig. 6.23. However, both the SPL IL and the PWL IL predictions indicate that using either an anechoic or an unflanged termination the broadband levels of noise reduction and spectral shape remains unchanged. In addition, such a simple point source representation can predict within roughly 3 dB the measured noise reductions and is computationally cheaper than distributed dipole point sources. This last point is used in the next section for a liner design study to guide the choice of future OTR liner configurations, using PWL insertion loss as the liner performance parameter. It is interesting to note that the PWL IL spectra in Fig. 6.24 are similar in shape to that of conventional liners.

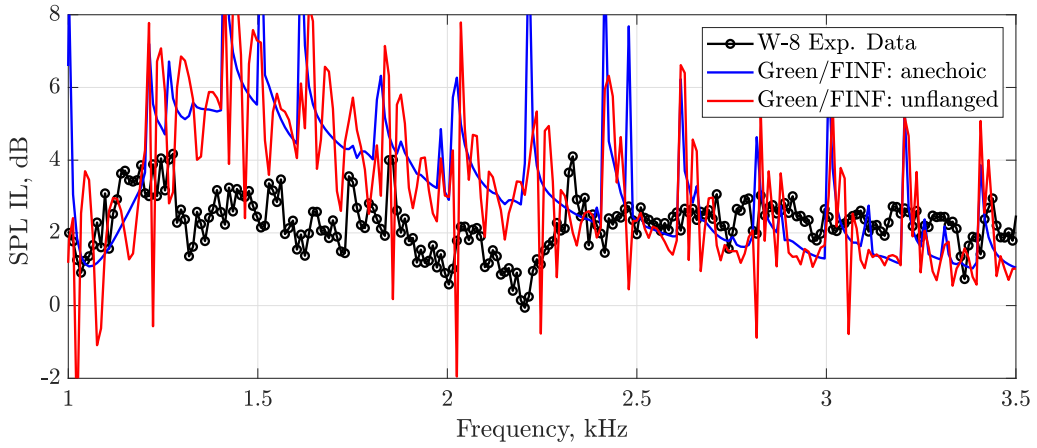

Figure 6.23: Comparison of the measured SPL IL and predicted SPL IL for the 'thin' perforate and a static axial dipole at $(x_s, r_s, \theta_s) = (0.5l_L, 0.95a, 0)$ with M=0.236 and COR=5.

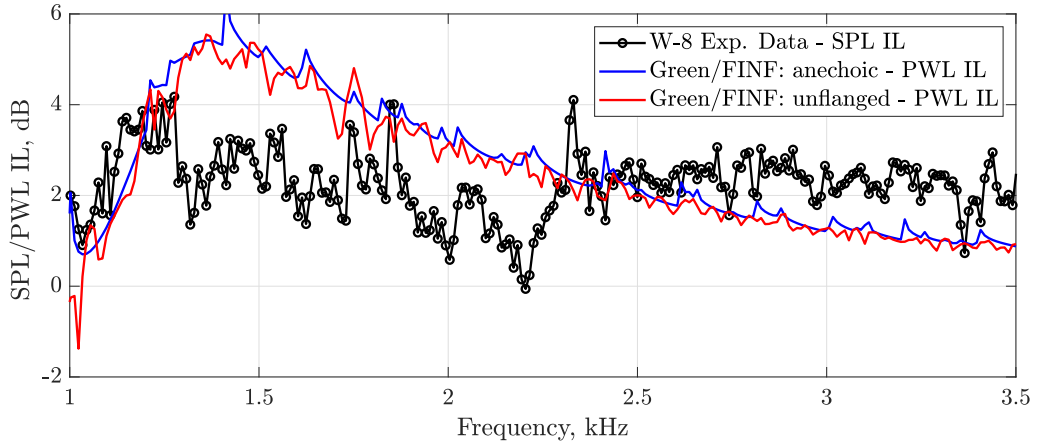

Figure 6.24: Comparison of the measured SPL IL and predicted PWL IL for the 'thin' perforate and a static axial dipole at $(x_s, r_s, \theta_s) = (0.5l_L, 0.95a, 0)$ with M=0.236 and COR=5.

6.2 OTR liner design study

The Green/FINF model is applied in this section to guide the design of Over-Tip-Rotor liners for the next generation of Ultra-High-By-pass-Ratio (UHBR) engines. The expected increase in fan diameter can lead to relatively shorter nacelles [2, 23] and reduced noise attenuation performance of intake liners [24, 25]. OTR liners have the potential to compensate for these reductions and maintain fan noise levels.

The UHBR 'design' engine considered in this section is supposed to have a diameter of 140" and slower shaft speed such that the Blade Passing Frequency is assumed at BPF=250 Hz (He=8.2). The study is performed over f=[50-1000] Hz and evaluated at the 1/3 octave frequencies. The non-dimensional liner length l_L is assumed to be that of the W-8, implying that the axial projection of the fan chord scales with radius. A Mach number of 0.3 is used through the section.

The use of circumferential grooves as part of the OTR acoustic treatments has been adopted as the OTR liner technology has developed at NASA due to the benefits in reducing losses in the fan aerodynamic performance while protecting the structural integrity of the rotor blades and the liner. Therefore, the first part of the section assumes a grooved liner modelled with the impedance groove model of Section 3.3 for a selection of parameters. Then, in the second part of the section, PWL IL predictions are obtained for a range of resistances and reactances to find the optimum impedance at each 1/3 octave frequency. In both cases a stationary point axial dipole source is used, located at 95% of the radius and multiple axial locations.

6.2.1 Design study of a grooved liner

Once again, the septum impedance within the analytical groove model is assumed to be that of an SDOF cavity liner. The mass reactance (m_r) of the facing sheet is kept constant for all cases and equal to the same non-dimensional value as for the 'thin' perforate configuration tested in the W-8 tests, $m_r = \frac{t+\varepsilon d_h}{\sigma} = 1.36 \cdot 10^{-2}$. Three cavity depths are considered, $\tilde{h} = [1,3,6]$", and three values of facing sheet resistance, $R = [0.5,1,1.5]$.

Three scenarios have been considered for the choice of the axial source location within the lined section: high distorted inflow leading to a fan noise spectra dominated by Leading Edge Noise (LEN), for which $x_s = 0.1 l_L$, a clean inflow leading to dominant Trailing Edge Noise (TEN), by setting $x_s = 0.9 l_L$, and a combination of both with uncorrelated sources of equal strength. The predicted PWL IL for each range of parameters specified above and for each source scenario is shown in Fig. 6.25.

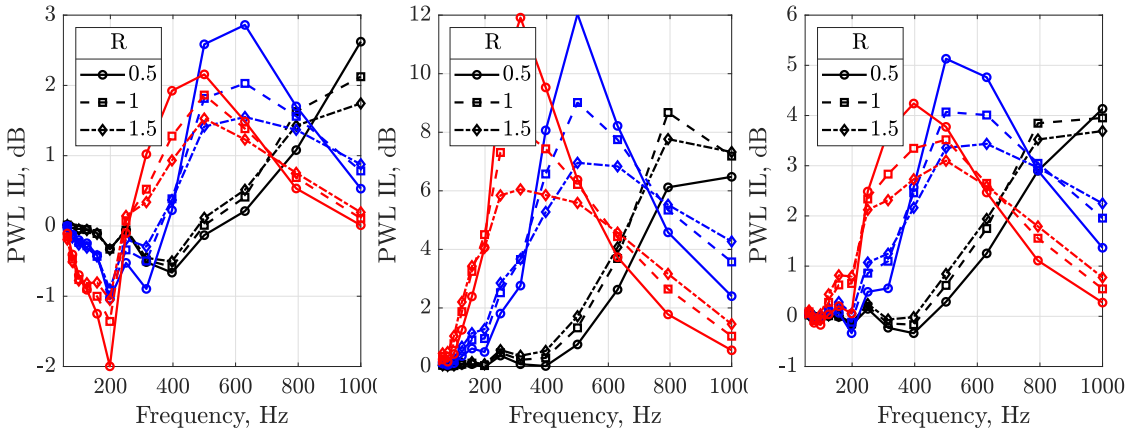

(a) LEN-dominated (b) TEN-dominated (c) LEN and TEN

Figure 6.25: PWL IL predictions using a grooved liner for a range of facing sheet resistance, cavity depths and source locations. Cavity depth of 1″ (black), 3″ (blue) and 6″ (red).

For a LEN-dominated fan, shown in Fig. 6.25a, there is very small room for liner attenuation and the source modification effects become significant, which become apparent at low frequencies with negative predicted values of IL. Likewise, additional noise reduction can also occur with predicted IL of up to 3 dB. An OTR lined grooved in a TEN-dominated fan (Fig. 6.25b) is predicted to yield up to 12 dB inlet PWL IL. In this scenario, any noise amplification linked to source modification is compensated by the axial attenuation along the (larger) liner length available. The benefits of OTR liners are reduced when a combination of LE and TE noise of equal strength are considered but could still provide up to 5 dB PWL IL for the right choice of parameters. A deeper cavity shifts the peak IL towards lower frequencies, as expected, with significant noise reductions at and above BPF for the 6″ cavity. The trend is that a low facing sheet resistance is beneficial, although it is not always the case for the shallow 1″ cavity.

6.2.2 Optimum impedance for OTR liners

This part of the section is not restricted to a particular liner design but explores the predicted PWL IL using OTR liners for a range of impedances $Z = R + jX$ at each 1/3 octave frequency. In particular, the evaluation space is for R varying from 0.5 to 5 and X from -5 to 5. The lower bound of resistance has been selected to avoid issues in the solution of the eigenvalue equation as $R \to 0$.

Contour plots of the predicted PWL IL for each source scenario in Section 6.2.1 are presented in Fig. 6.28-6.30. The impact of source modification effects mentioned earlier when $x_s = 0.1l_L$ can be observed in Fig. 6.28 by the large areas of noise amplification, especially at the lower frequencies. However, this is not an issue for $x_s = 0.9l_L$, in Fig. 6.29, when almost all impedances tested provide positive PWL IL with values up to 15

dB. When including both uncorrelated sources at $x_s = 0.1l_L$ and $x_s = 0.9l_L$ (Fig. 6.30) the source modification effects dominate once again but are not as severe due to the significant noise reductions of the TE noise source.

The impedance for maximum PWL IL at each frequency and scenario is shown in Fig. 6.26. As observed before, low resistance is beneficial in most cases. The predicted optimum reactance is reduced with increasing frequency, unlike the standard behaviour of SDOF/DDOF models, forcing to choose a target frequency range of peak attenuation to determine the liner design parameters.

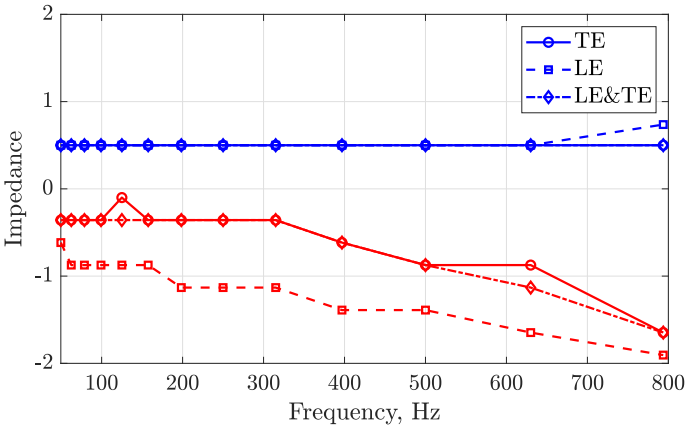

Figure 6.26: Resistance (blue) and reactance (red) for maximum PWL IL within the interrogated impedance space with $r_s = 0.95a$, M=0.236 and COR=5.

The two contributors to the PWL IL outlined in Section 4.6.3, the liner attenuation and the source modification, can be readily separated in the form of contour plots for zero mean flow, as illustrated in Fig. 6.27 for an axial dipole source at mid-chord and f=400 Hz. It can be observed that the liner attenuation or transmission loss is always positive, as expected since the liner is a passive device. Fig. 6.27c shows that the back-reaction effects can modify the power generated at the source plane by up to 1 dB of addition noise reduction and 10 dB of amplification. However, large values of amplification often appear in conjunction with pronounced noise attenuation. By adding the two contributions one recovers the power IL map shown in Fig. 6.27a. Furthermore, the region of large amplification only occurs when the resistance is very small, which is unlikely in practice, given the very high sound pressure levels present close to the tip of the fan rotor.

The evaluation of the acoustic power in the near field of the source in the presence of mean flow should include the finite contribution of the power contained within the vortex sheet, not considered in the definition of acoustic power adopted in this work. Hence, the separation between liner attenuation and source modification with flow is not included here but is suggested for future work on this topic.

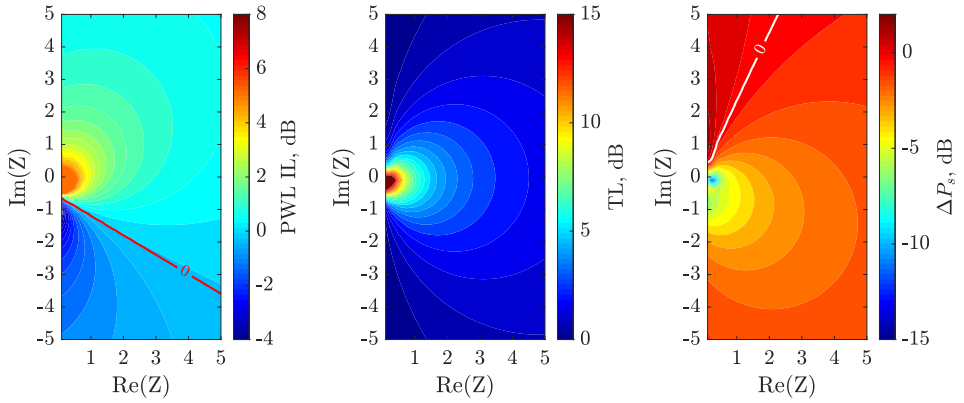

(a) Total PWL IL (b) Liner attenuation (c) Source modification

Figure 6.27: Contour maps of (a) the total PWL IL and the contributions of (b) the liner attenuation and (c) the source modification for an axial dipole at f=400 Hz $(x_s, r_s, \theta_s) = (0.5l_L, 0.95a, 0)$ with M=0.0 and COR=5.

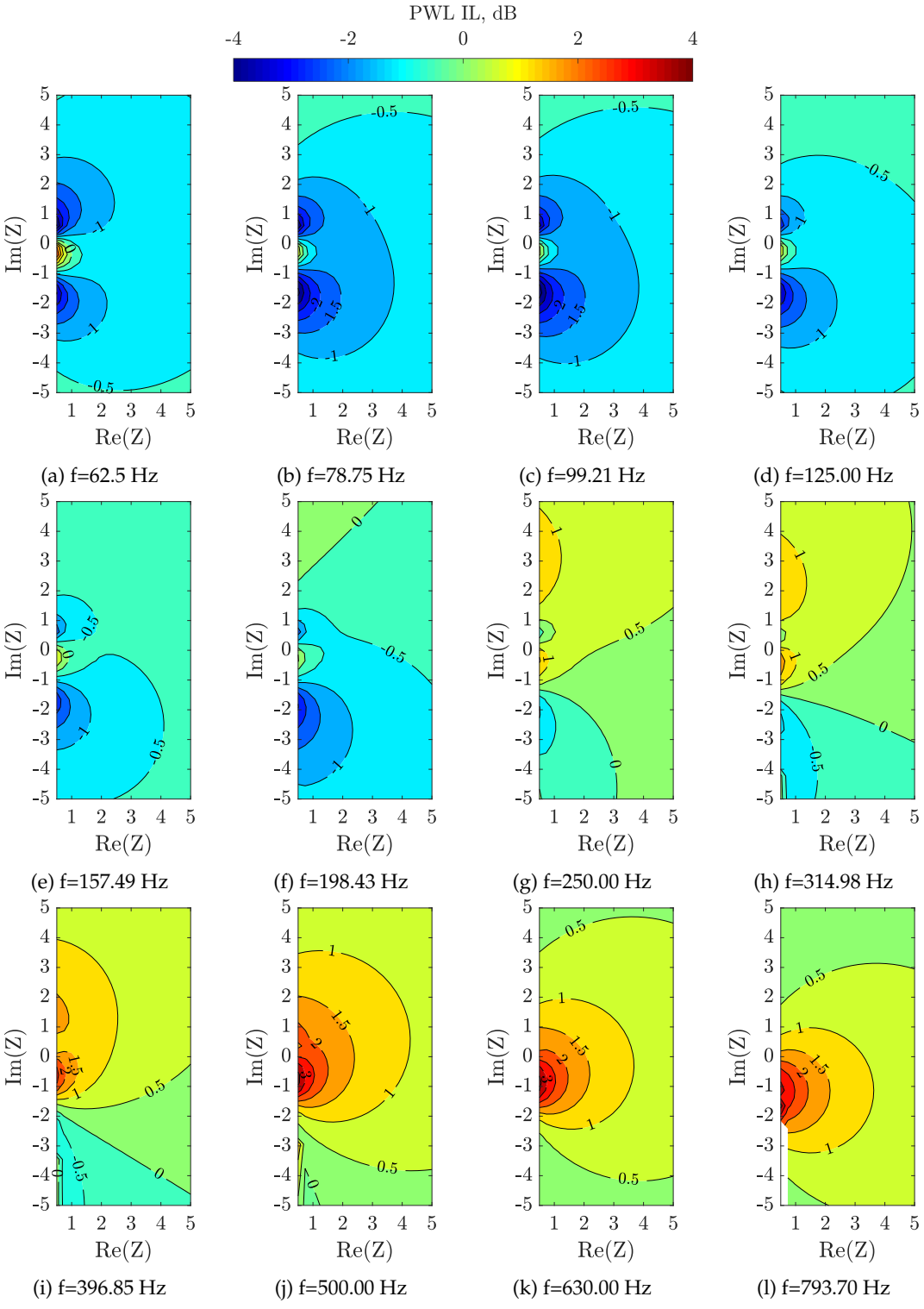

(a) f=62.5 Hz (b) f=78.75 Hz (c) f=99.21 Hz (d) f=125.00 Hz

(e) f=157.49 Hz (f) f=198.43 Hz (g) f=250.00 Hz (h) f=314.98 Hz

(i) f=396.85 Hz (j) f=500.00 Hz (k) f=630.00 Hz (l) f=793.70 Hz

Figure 6.28: Contour maps of the PWL IL for an axial dipole at $(x_s, r_s, \theta_s) = (0.1l_L, 0.95a, 0)$ with M=0.3 and COR=5.

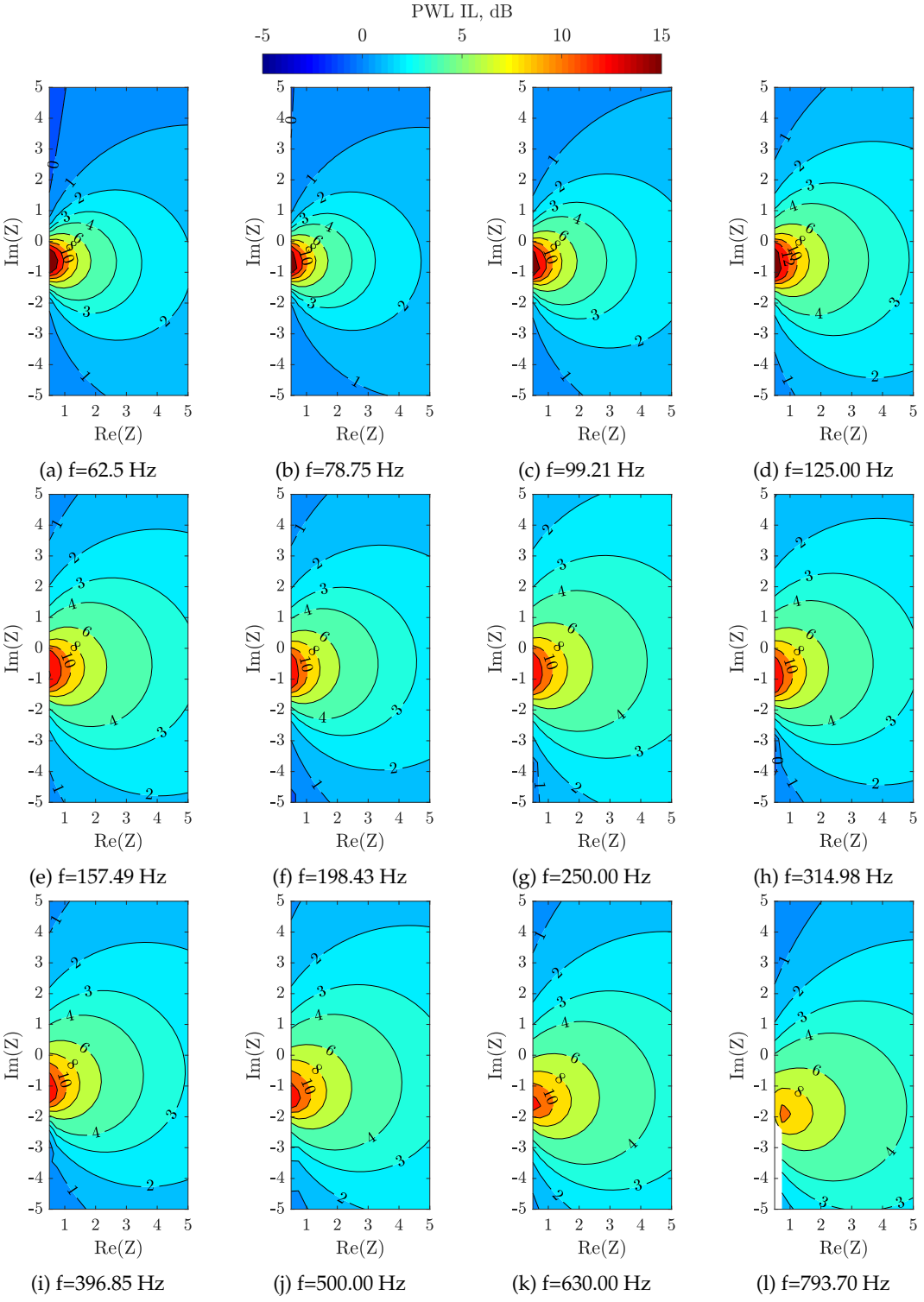

(a) f=62.5 Hz (b) f=78.75 Hz (c) f=99.21 Hz (d) f=125.00 Hz

(e) f=157.49 Hz (f) f=198.43 Hz (g) f=250.00 Hz (h) f=314.98 Hz

(i) f=396.85 Hz (j) f=500.00 Hz (k) f=630.00 Hz (l) f=793.70 Hz

Figure 6.29: Contour maps of the PWL IL for an axial dipole at $(x_s, r_s, \theta_s) = (0.9l_L, 0.95a, 0)$ with M=0.3 and COR=5.

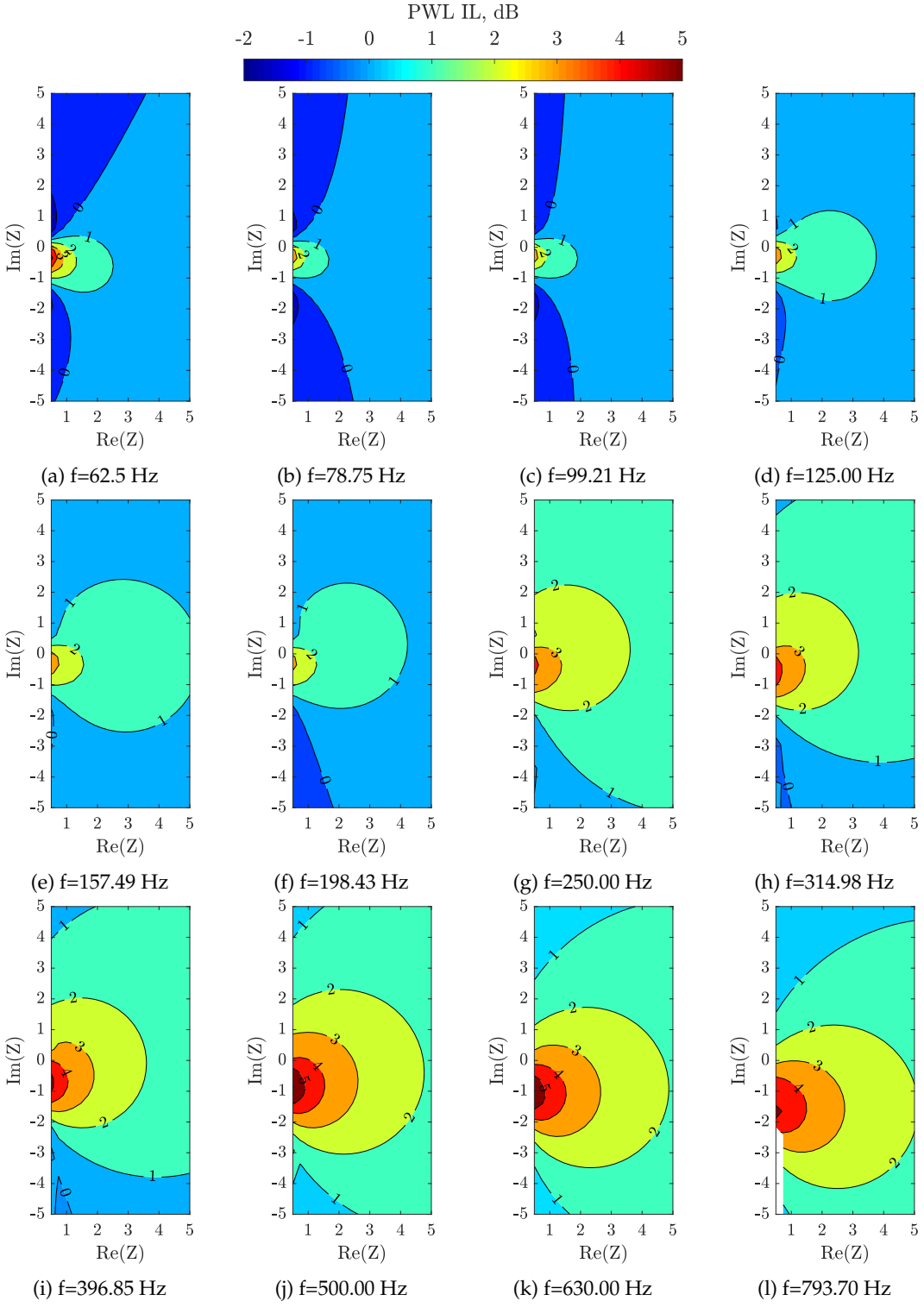

(a) f=62.5 Hz (b) f=78.75 Hz (c) f=99.21 Hz (d) f=125.00 Hz

(e) f=157.49 Hz (f) f=198.43 Hz (g) f=250.00 Hz (h) f=314.98 Hz

(i) f=396.85 Hz (j) f=500.00 Hz (k) f=630.00 Hz (l) f=793.70 Hz

Figure 6.30: Contour maps of the PWL IL for an axial dipoles at $(x_s, r_s, \theta_s) = (0.1l_L, 0.95a, 0)$ and $(x_s, r_s, \theta_s) = (0.9l_L, 0.95a, 0)$ with M=0.3 and COR=5.

6.3 Summary and conclusions

6.3.1 Summary

- The modelling work of previous chapters is combined here to provide a prediction model for the noise reduction of OTR liners. The impact of various features of the source model in the predicted SPL IL is studied, including the effect of rotating sources, radially variable stagger angle and chord and the axial position of the dominant noise mechanism/s.
- The OTR liner tests conducted in the W-8 rig [5] are reviewed and compared with the analytical OTR prediction model. The main points that need to be considered in the comparisons of the measured and predicted SPL IL are highlighted and the choice of parameters in the impedance and source models is described accordingly.
- A liner design study is performed by applying the OTR liner prediction model to a 'design' UHBR engine to show the potential benefits of OTR liners and guide the choice of liner parameters for their implementation in the next generation of turbofan engines.

6.3.2 Conclusions

- For a given OTR liner impedance, the main two features in the source model driving the predicted noise reductions are (1) the axial location of the dominant sources, related to the noise *attenuation* and (2) the radial distribution of the source strength, linked to the *source modification* effects.
- Comparisons of the measured SPL IL in the W-8 test rig with the analytical predictions show a reasonable agreement within the 1-2 dB uncertainty of the data, ignoring the cut-off theoretical singularities, that holds for the two liner configurations considered. This exercise shows that peak broadband noise estimates can be obtained with the analytical prediction model given the right assumptions in the source distribution.
- Comparison of the measured hard wall SPL in the SDT RAN test and the analytical predictions suggest evidence of cut-off spikes/humps present in the measured data, which could be masked in the W-8 tests by the boundary layer noise of the thicker boundary layer.
- A liner design study for a UHBR engine has shown the potential of OTR liners for improved noise suppression in the next generation of turbofan engines. Predictions suggest that OTR grooved liners covering the axial extent of the fan could yield up

to 4 dB inlet PWL IL for a fan with leading and trailing edge sources of similar strength and up to 9 dB for a trailing-edge noise dominated fan with a cavity depth of 3″ and specific acoustic resistance of 1. For typical values of resistance the contribution of the source modification effects can be up to 2 dB of additional noise reduction and 5 dB of noise amplification.

Chapter 7

Conclusions and future work

This thesis describes an investigation into Over-Tip-Rotor (OTR) liners with the dual objective of improving our understanding of the noise reduction mechanisms and assessing the potential for additional fan noise suppression in turbofan engines. This has been achieved through the development of an analytical prediction model, based on Green's functions, for the noise reduction performance of OTR liners, which includes the coupling of the fan sources, the sound propagation and the noise suppression. This work represents the first documented attempt at modelling the noise suppression of OTR liners analytically, in contrast to previously published research, which has concentrated solely on experimental modelling. Key characteristics of the analytical model are cross verified with reference FEM solutions. Noise reduction estimates obtained with the prediction model are compared with experimental data measured in the NASA W-8 test rig. In addition to the analytical work, a fundamental experiment has been conducted in a wind tunnel with the fan rotor represented by a static airfoil separated from an over-tip liner by a small tip gap. Finally, the OTR liner prediction model is applied to a rotor-inlet configuration of a typical future UHBR type engine to show the potential benefits of this liner technology and to indicate the choice of liner parameters for improved noise suppression. The main findings and suggested future work are summarised below.

7.1 Conclusions

Experimental evaluation in the wind tunnel of over-tip liners has shown that the acoustic treatment can suppress noise sources located in its vicinity, with measured peak broadband reductions of gap noise of 5-10 dB, corresponding to 2-3 dB of overall noise reduction when other sources are included. The noise suppression benefits of the over-tip liners are reduced as the gap size is increased, which confirms the benefit of proximity to the liner. This behaviour is also captured by evaluating an existing model for the acoustic field generated by a point source located over an infinite lined plane, which showed qualitative agreement with the measured data.

The power output of in-duct sound sources depends on the wall impedance, the source proximity to the wall, the frequency and the mean flow Mach number. To evaluate these effects, an existing Green's function is used for an infinite cylindrical duct containing uniform axial mean flow with a hard or lined wall. The source power output is computed by evaluating the axial acoustic power at the source plane. If the source power for a lined

configuration is lower than for its hard wall counterpart, there is an additional noise reduction benefit to that of the conventional noise attenuation as the waves propagate over the liner. Hence, it is proposed that the PWL Insertion Loss achieved by an OTR liner can be divided into two contributions: (1) the noise *attenuation*, measured with the Transmission Loss (TL), and, (2) the *source modification*, measured as the power difference between a hard and lined configuration at the source plane. A detailed study of contribution (2) shows that the effects of the source proximity to the wall are more pronounced when the source is very close to the wall ($e/\lambda < 0.5$), in agreement with the simplified over-tip liner experiments and classical half-space analytical models.

Acoustically treated circumferential grooves developed at NASA are a promising OTR liner configuration as these appear to minimise the aerodynamic performance losses and protect the acoustic liner septum, to some extent, from the severe aeroacoustic environment of the rotor blade tip. Two analytical impedance models have been formulated to represent the acoustic behaviour of physical grooves in the absence of grazing flow, one exact and the other a good approximation. Both models are 'semi-locally reacting' (locally reacting in the axial direction and non-locally reacting in the azimuthal direction) and result in an impedance that depends on the frequency and the azimuthal mode number. Predictions obtained with the OTR prediction model coupled with the groove impedance model agree with FEM predictions to within 0.2 dB for the same configuration but the latter includes the full multiple groove geometry.

Existing mode-matching techniques have been coupled with the Green's function representation to model the impedance discontinuities between the OTR liner section and the hard wall casing upstream and downstream of the fan section. The relatively short axial extent of the OTR liners can lead to fan noise sources located close to the impedance discontinuity, particularly when the dominant sources are located at the leading or trailing edge as it is often assumed. It is found that power continuity across the matching interface can be compromised by source proximity to the matching plane. A cut-off ratio of five is generally sufficient if the source is separated from the matching plane by at least 10% of the plane wave mode wavelength.

The noise reduction spectra obtained with the OTR prediction model exhibit the characteristic hard wall cut-on/cut-off singularities for in-duct monopole type sources in an infinite duct, with or without flow, and dipoles with flow but the singularities are not observed in the experimental data from the NASA W-8 rig. It has been then realised that reflections from a duct termination would in effect cancel out the singularity. A termination has been implemented by coupling the mode-matching scheme with the reflection coefficients from an unflanged duct termination, evaluated numerically with an existing Wiener-Hopf-based solution. This approach has been found to successfully cancel the hard wall point source singularity at the cut-on/cut-off transition. However, in the OTR hard-lined-hard configuration, the reflections can cause axial resonances in an otherwise

smooth spectrum. Comparison of the predictions with results of a FEM model of the W-8 bellmouth geometry has shown somewhat closer agreement with an anechoic termination except at the vicinity of the cut-off frequency, where the singularity is nullified as in the unflanged termination. This is not unexpected as the inlet bellmouth geometry of the W-8 rig is smoothly varying and should only produce weak reflections, except at cut-on. Comparison of the measured hard wall SPL in the SDT RAN test and the analytical predictions suggest evidence of cut-off spikes/humps present in the measured data, which could be masked in the W-8 tests by the noise of the thicker boundary layer.

The impact of various features of the source model in the predicted noise reduction spectra has been evaluated by comparison with the measured SPL Insertion Loss (IL). It is found that for a given OTR liner impedance, the main two features in the source model driving the predicted noise reductions are (1) the axial location of the dominant sources, which determines the noise *attenuation* and (2) the radial distribution of the source strength, linked to the *source modification* effects. The source rotation and stagger angle have a smaller effect in the predicted IL of only $\pm$ 0.5 dB.

The limitations of the prediction model and specific issues of the measured data restrict the range of frequencies over which the two can be compared. The analytical predictions fall within the 1-2 dB uncertainty of the data for both two liner configurations considered over the comparable frequency range. That is, ignoring the cut-off/cut-on theoretical singularities and focusing only on the broadband spectral shape. The comparisons have shown that given some information on the fan noise sources, particularity regarding the axial location of the dominant source mechanisms, reasonable peak broadband noise estimates can be obtained by using the analytical OTR liner prediction model developed here. This model is presented as a low-TRL tool to guide the design of OTR liners. The model has been applied to a liner design study for a UHBR engine, predicting a peak inlet PWL IL within 4 and 9 dB depending on the axial location of the dominant fan noise source mechanism, using a SDOF liner resistance of 1 and a cavity depth of 3 inches. For typical values of liner resistance close to 1 the contribution of the source modification effects can be up to 2 dB of additional noise reduction and 5 dB of noise amplification.

7.2 Future work

Several aspects of the current work would benefit from further improvements both in the modelling and to improve understanding of the OTR liner physical mechanisms. This section summarises recommendations for future work.

Physical mechanism of noise suppression

The source modification effects predicted in the OTR liner model are always purely acoustic and caused by the back-reaction effects on the source. However, it is not clear what the impact of the liner might be on the aerodynamically generated sources at the tip region. The experimental wind tunnel evaluation of over-tip liners with a static single airfoil described here included measurements with various liner configurations partially covered with a rigid hard wall surface, flush mounted to minimise noise attenuation over certain areas. These results suggested weak source modification effects but the results are inconclusive. Additional measurements of the unsteady pressure fluctuations on the airfoil surface with the over-tip liner or with a hard wall could give more insight into source modification effects caused by an over-tip liner.

Further work is suggested in the study of the back-reaction effects on the source power output in the presence of uniform mean flow by taking into account the power confined within the vortex sheet. The additional power term could be obtained with the expressions derived by Tester [137] using Möhring's [138] definition of intensity for shear flow or those of Eversman [133] obtained from energy conservation principles, as in [132].

Further developments of the prediction model

The current OTR liner prediction model could also be capable of predicting the noise reduction of fan case liners upstream of the rotor leading edge by placing the noise sources in the hard wall region downstream of the finite lined section. An obvious extension to this work would be to obtain estimates and perform a liner design study for a fan case liner.

One of the main assumptions in the current model is that of uniform mean flow in the lined fan and hard wall sections. However, numerical simulations indicate that a transition from a purely axial base flow upstream of the fan rotor to an axial and swirling base flow downstream of the fan occurs along the blade passage. Therefore, a natural extension of the work presented in this thesis could include the Green's function for swirling flow [36] in the fan section, which would also require a potentially challenging mode-matching between the duct sections with different swirling flow characteristics. The extended model could also be used as a design tool to guide the choice of interstage liners and include distributions of sources both for the fan and the OGVs.

The modelling of swirling flow in the duct would also permit study of the differing OTR liner noise reduction of co- and counter-rotating modes observed in the W-8 data with (1) the proposed modified groove impedance model with 'swirling' flow in the groove and, (2) the mean swirling flow in the duct. The groove impedance model with swirling

flow could then also be extended to the annular groove model rather than the simpler rectangular assumption adopted here, in order to include mean flow swirl in the grooves.

The cut-on/cut-off singularity problem has been solved by including reflections from an unflanged duct termination but clearly it is not the best physical representation of, for example, the W-8 test rig inlet. Therefore, it would be desirable to use a more realistic termination, but which still has the required behaviour at cut-on/cut-off singularities. In addition it should be recognised that in reality, non-linear effects would dampen the high amplitude singularities and viscous-thermal dissipation would reduce the strength of the singularity at the source. The latter might have a stronger effect on the modal wavenumber at and near cut-on and could be modelled through an additional acoustic admittance such as in [148], which would effectively generate an imaginary part to Lorentz axial wavenumber and prevent the singularity.

Application of the OTR liner technology

Over-tip-rotor liners have the potential to also be an effective noise suppression technology in applications other than turbofan engines. Some examples are urban ducted wind turbines, emerging air taxis or smaller transport and surveillance UAV vehicles. Testing and numerical investigation of tip noise and its noise suppression with OTR liners could benefit from the current and future modelling capabilities.

Appendix A

Flow-induced cavity noise tests

This test aimed at introducing an airfoil to represent the fan blade and the effect of grazing flow into the point source problem. The set-up used for this experiment is similar to the one described in Section 2.1 for the assessment of over-tip liners in reducing airfoil noise. However, it was modified by drilling two holes of different depth at the tip of the airfoil, which are expected to be acoustically excited by the grazing flow and to produce a near tonal noise that dominates the acoustic spectrum. The holes are circular with a diameter of W=3 mm, depths of $L_{1/2}$=[22,18] mm and located at x_1^h=0.25c and x_2^h=0.75c, where c is the airfoil chord. This test set-up is shown in Fig. A.1 and the liner inserts and measurement techniques utilised are the same described in Section 2.1. The far-field spectra was measured for gap sizes e=[2,5] mm, angles of attack AoA=[10,18] deg. and three flow speeds [S1,S2,S3]=[17,27,32] m/s for each insert configuration: hard wall, liner ID4 and liner ID5.

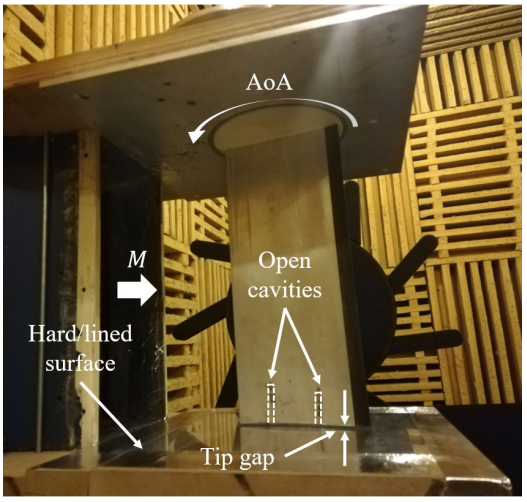

Figure A.1: Experimental set-up of the flow-induced cavity noise tests.

Rossiter [149] described two noise generation mechanisms for grazing flow over cavities that define the cavity resonance: (1) depthwise oscillations, related to the cavity modes and (2) lengthwise oscillations caused by the impingement of vortices shed in the upstream corner of the cavity impinging in the downstream corner. Block [103] provided semi-empirical expressions to predict the frequencies where these resonances occur and found that maximum excitation takes place around the frequencies where the two excitation mechanisms intersect.

- *Depthwise oscillations:*

$$f_D = \frac{c_0}{4D} \frac{1}{1 + 0.65(W/D)^{0.75}} \tag{A.1}$$

  where W/D is the with-to-depth ratio and c_0 the speed of sound.

- *Lengthwise oscillations:*

$$f_W = \frac{U}{W} \frac{n}{\frac{1}{0.57} + M\left(1 + \frac{0.514}{W/D}\right)} \tag{A.2}$$

  where n is the depthwise mode number and U the mean flow velocity.

Therefore, the predicted frequencies of the cavity noise depend on the geometry of the hole and the grazing flow over the cavities. Assuming the latter to be the mean flow from the nozzle, the estimated resonance frequencies of each hole are shown in Table A.1, which also includes the quarter wavelength frequency as reference. Note that these expressions are for a rectangular rather than a cylindrical cavity. In reality, the grazing flow over the cavities will be a combination of the incoming mean flow and the cross-flow through the gap, which will be influenced by the turbulent structures generated by the separation at the tip edges. Therefore, the flow topology of the grazing flow over the cavities is expected to be complex and bound to be affected when varying the gap size and the loading of the aerofoil.

Table A.1: Predicted cavity tone frequencies.

Depth	f_D	$f_{\lambda/4}$	f_W		
			S1	S2	S3
22 mm	3.37	3.86	2.84	4.21	4.83
18 mm	4.04	4.72	2.89	4.32	4.98

The measured far-field spectra for a selection of cases is shown in Fig. A.2 and Fig. A.3 to analyse the effect of airfoil loading and gap size respectively in the excitation of the cavities and the PSD spectra. Both sets of figures contain essentially the same data but presented differently to illustrate the findings more clearly. The spectra have been filtered with a Savitzky–Golay filter to smooth the data while maintaining the general trends. Note that quantitative comparisons of the tonal magnitude between two cases with different AoA can be misleading since the position of the far-field arc array remains constant for all the measurements of cavity noise.

Cavity tones can be clearly observed in the measured PSD spectra of Figs.A.2-A.3. However, the excitation of the cavities is highly sensitive to the problem variables, which would not necessarily be a problem for this study as long as it holds for a lined configuration. The loading of the airfoil can significantly change the flow topology at the tip region, as measured in the literature [46, 54] for a similar configuration without tip

cavities, and therefore the grazing flow over the cavities. Typical tip-gap aerodynamic structures, dominated by the gap jet, also suggests that the grazing flow over the first and the second cavity is likely to be different and to also change with the airfoil loading differently.

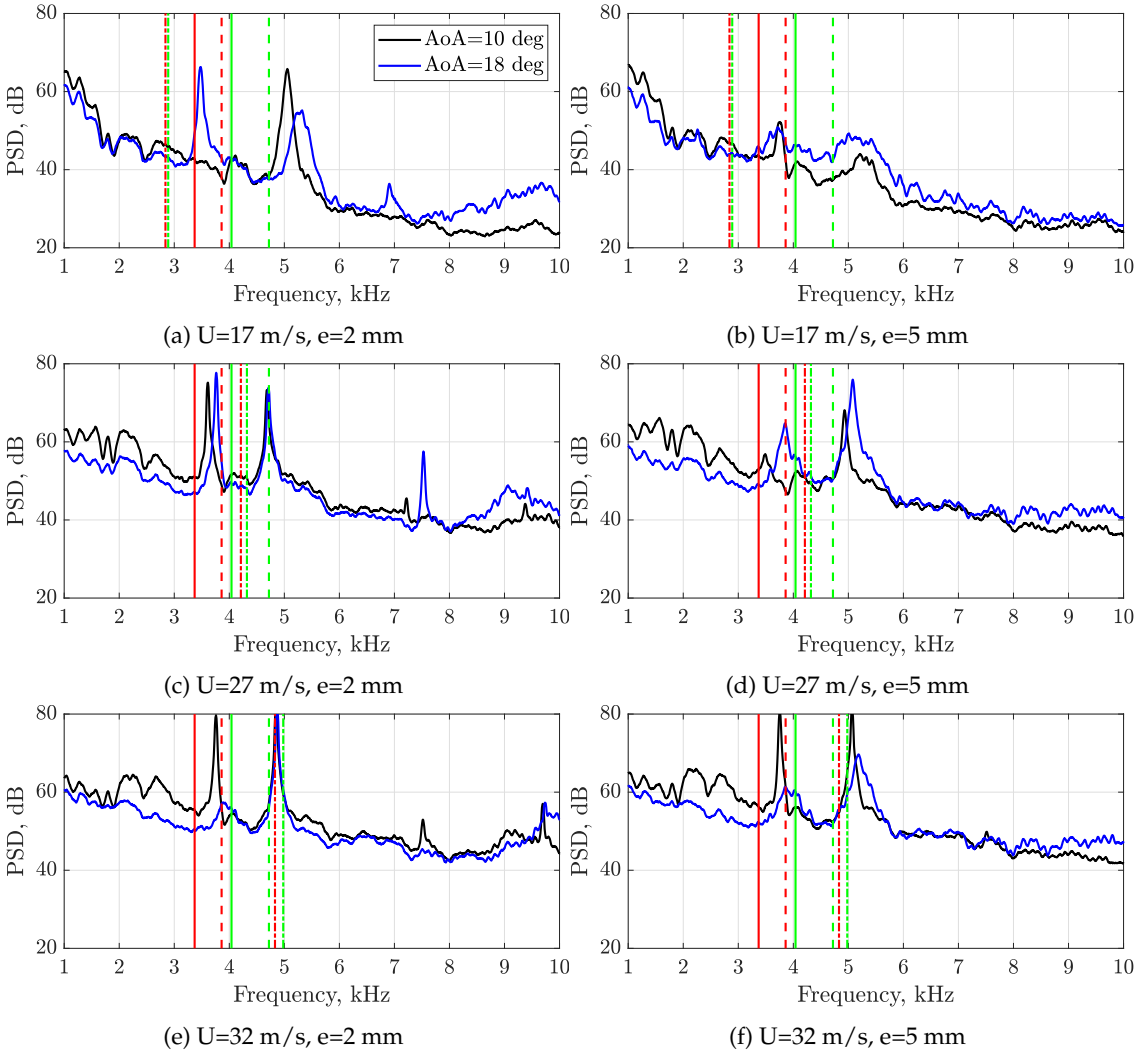

(a) U=17 m/s, e=2 mm (b) U=17 m/s, e=5 mm

(c) U=27 m/s, e=2 mm (d) U=27 m/s, e=5 mm

(e) U=32 m/s, e=2 mm (f) U=32 m/s, e=5 mm

Figure A.2: Measured PSD noise spectra: effect of the airfoil loading and predicted cavity noise frequencies. Key: red-hole 1, greed-hole 2 ; solid-f_D, dashed-$f_{\lambda/4}$, dot-dashed-f_W.

The comparison of the measured and predicted frequencies of the cavity tones are interpreted in two ways. The first and most likely follows the argument that the high variability in the magnitude of the grazing flow over the cavities makes the predicted frequencies based on Eq. A.1-A.2 not reliable. The presence of the support plate represents a significantly different configuration than those studied in [103, 149]. However, the standard quarter wavelength resonator consistently predicts reasonably well the two main tones. This would suggest that the first and second main tones correspond to the standard modal excitation of the first and second hole. Measurements in a different airfoil reported in [46, 54] showed that the gap jet can move from 75% of the chord at an

AoA=5 deg. to almost the leading edge for an AoA=18 deg. Although the topology can change here for a different airfoil and flow speed, this effect can be linked to the observed changes in the excitation of the first cavity when changing the AoA. The second interpretation of the cavity tones observed in Fig. A.2 links them to the excitation mechanisms rather than the hole location: the first one is attributed to the depthwise excitation and the second one to the lengthwise. This second approach could be acceptable at $U = 32$ m/s (Fig. A.2e-A.2f) but does not hold for the other cases at lower flow speeds.

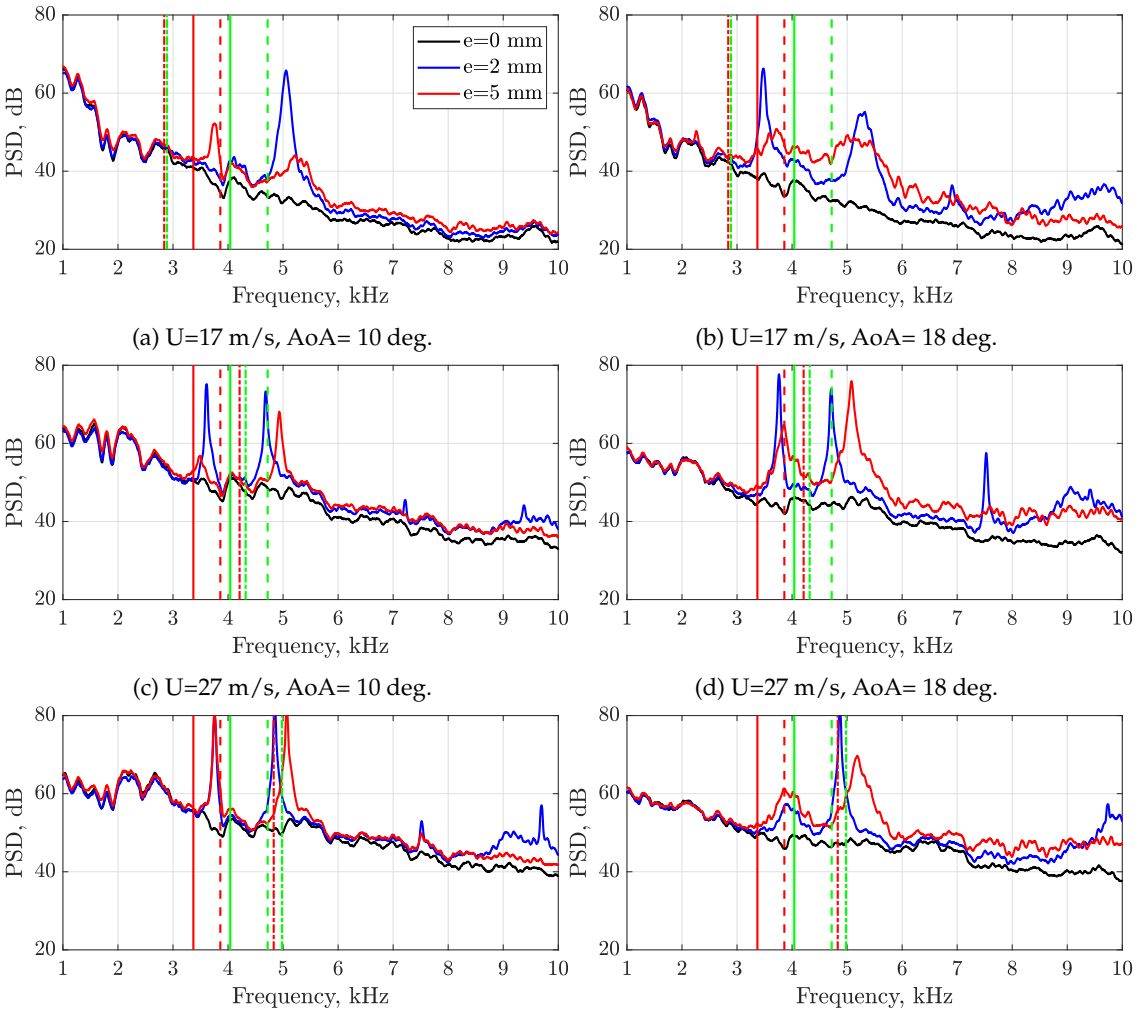

(a) U=17 m/s, AoA= 10 deg.

(b) U=17 m/s, AoA= 18 deg.

(c) U=27 m/s, AoA= 10 deg.

(d) U=27 m/s, AoA= 18 deg.

(e) U=32 m/s, AoA= 10 deg.

(f) U=32 m/s, AoA= 18 deg.

Figure A.3: Measured PSD noise spectra: effect of gap size and predicted cavity noise frequencies. Key: red-hole 1, greed-hole 2 ; solid-f_D, dashed-$f_{\lambda/4}$, dot-dashed-f_W.

The effect of gap size on the cavity excitation is illustrated in Fig. A.3. The inclusion of a tip gap generates additional broadband noise at higher frequencies, analysed in Chapter 2, and can also permit the excitation of the cavity tones. It can be observed that the first tone excited for a gap of 2 mm can be weakened for a larger gap of 5 mm. Following the hypothesis that each tone corresponds to one hole, this change can also be linked to a change in flow topology related to the gap size. An increase of gap size can move the

location of the mean gap flow towards the trailing edge [54] and significantly modify the grazing flow over each cavity. A general trend for the second tone is a shift towards higher frequencies that could also be attributed to the movement of the gap jet towards and over the second hole.

A detailed characterisation of the flow topology for this set-up would be necessary to confirm the hypothesis outlined in the analysis of the cavity excitation. Although this is an interesting aeroacoustic problem, this experiment does not serve its original purpose for this research and was not investigated further. The main reason for not perusing this line of work was that the cavity excitation can also depend on the liner impedance. Ideally, the acoustic excitation, i.e. the effective noise source, should be consistent for a hard or lined configuration for a given flow speed, gap size and AoA. This would allow a parametric study of the noise reduction of the over the tip liners tested in this experiment. However, the tones are not present or highly diminished when a liner insert is placed over the airfoil tip, as shown in Fig. A.5 for U=32 m/s and consistent with the results at lower flow speeds. The reduction in noise could either be that the liner suppresses very effectively the tonal noise or, more likely, the cavity is not excited due to the presence of a porous boundary near the gap entrance. The aeroacoustic interactions of the cavity excitation mechanisms with the hard/lined insert could be significant, especially considering that the gap is of the order of the hole width, as illustrated in Figure A.4.

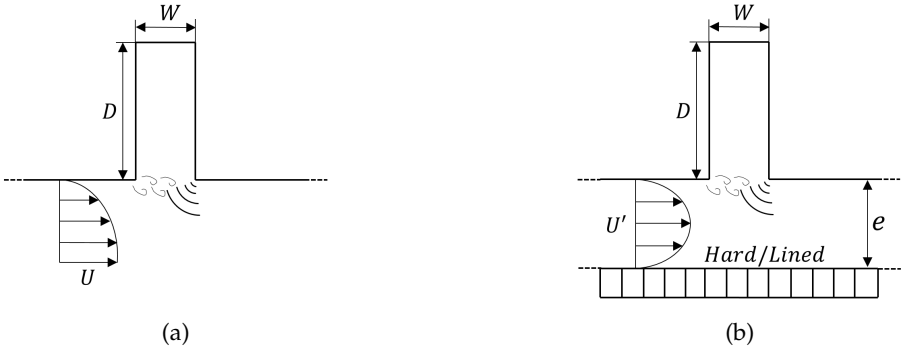

Figure A.4: (a) Typical cavity problem and (b) inclusion of a hard/lined surface close to the cavity entrance.

An alternative test to include the modifications on the Green's function due to the presence of the airfoil and account for convective effects would be the introduction of an artificial source as in Fig. 2.2 with the probe termination flush-mounted in the airfoil tip. This configuration would provide more control on the source amplitude and frequency and provide a benchmark for point source analytical models that include the effect of complex reflective surfaces.

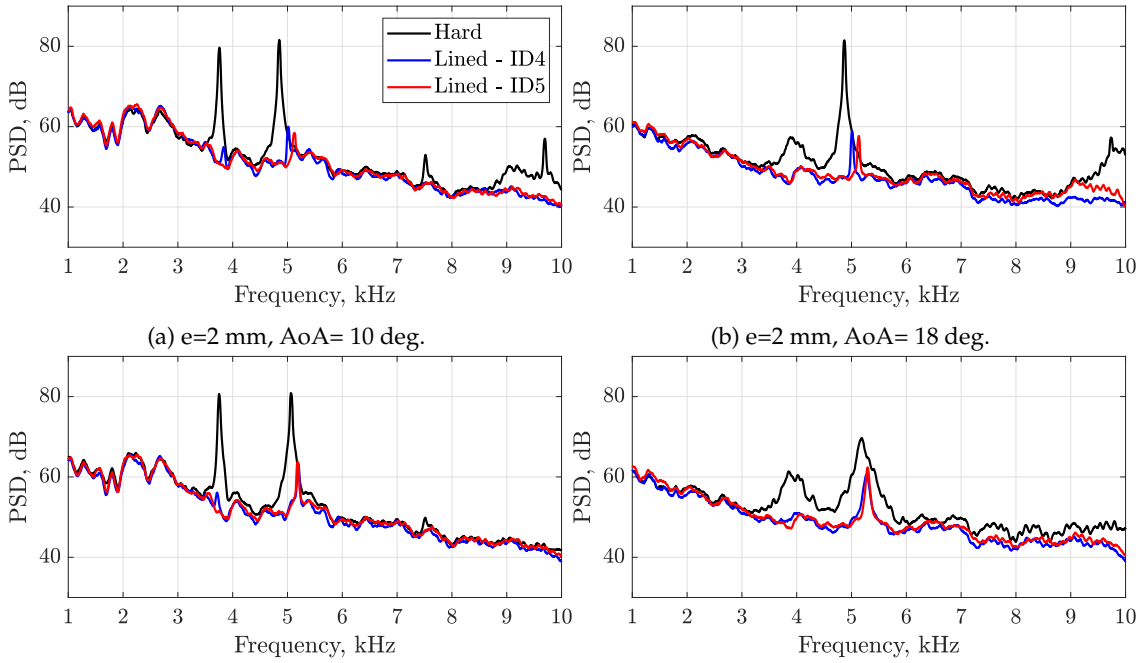

(a) e=2 mm, AoA= 10 deg.

(b) e=2 mm, AoA= 18 deg.

(c) e=5 mm, AoA= 10 deg.

(d) e=5 mm, AoA= 18 deg.

Figure A.5: Measured PSD spectra for U=32 m/s and hard/lined configurations.

Appendix B

Analytical modelling of a point source over an infinite lined plane

The analytical model adopted in this Appendix is based on the Thomasson [70] formulation of the pressure field of a monopole source over a lined surface in the form presented in [150]. The $e^{j\omega t}$-convention is used here. A diagram of the problem illustrating the method of images and the coordinate system is shown in Fig. B.1.

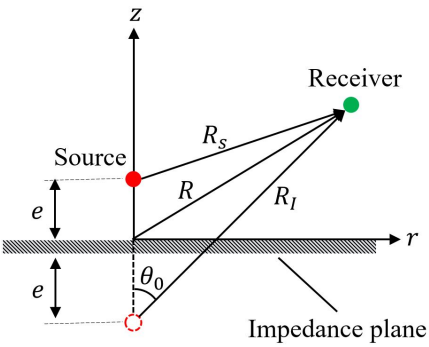

Figure B.1: Half-space problem indicating the positions of the source and the receiver, the coordinate system and the nomenclature.

The total pressure field is a superposition of the direct field radiated by the source p_S, by the image source p_I and a contribution to account for the lined boundary condition of the surface p_C. Expressed in cylindrical coordinates (r, z), where r is the radius in the (x, y) plane, that is

$$p(r,z) = p_S(r,z) + p_I(r,z) + p_C(r,z) \quad , \tag{B.1}$$

with

$$p_S(r,z) = -\frac{1}{4\pi R_S} e^{-jkR_S} \quad , \tag{B.2}$$

$$p_I(r,z) = -\frac{1}{4\pi R_I} e^{-jkR_I} \quad , \tag{B.3}$$

where $R_S = |\boldsymbol{x_R} - \boldsymbol{x_S}|$ and $R_I = |\boldsymbol{x_R} - \boldsymbol{x_I}|$ with $\boldsymbol{x_R}$, $\boldsymbol{x_S}$ and $\boldsymbol{x_I}$ being the position in space of the receiver, the source and the image source respectively and k the wavenumber. The reflected contribution from the lined surface p_C is given by Eq. B.4, the details of the derivation can be found in [70, 150].

$$p_C = \begin{cases} p_{SD} + p_B & \text{if } \mathrm{Re}(\gamma_1) < -1 \quad \text{and } \mathrm{Im}(A) > 0 \\ p_{SD} & \text{otherwise} \end{cases} \quad , \tag{B.4}$$

with

$$p_{SD} = -\frac{kA}{2\pi} e^{-jkR_I} \int_{t=0}^{+\infty} \frac{e^{-kR_I t}}{\sqrt{(-1+jt-\gamma_0)(-1+jt-\gamma_1)}} dt \quad , \tag{B.5}$$

$$p_B = \frac{kA}{2} H_0^{(2)} \left(kr\sqrt{1-A^2} \right) e^{jk(z+e)A} \quad , \tag{B.6}$$

where

$$\gamma_0 = A\cos\theta_0 + \sqrt{1-A^2}\sin\theta_0 \quad , \tag{B.7}$$

$$\gamma_1 = A\cos\theta_0 - \sqrt{1-A^2}\sin\theta_0 \quad , \tag{B.8}$$

$$t_1 = \frac{\mathrm{Im}\left[(\gamma_0+1)\,(\gamma_1+1)\right]}{\mathrm{Re}\left[(\gamma_0+1)+(\gamma_1+1)\right]} \quad , \tag{B.9}$$

e is the vertical distance from the source to the plane, $A = 1/Z$ the admittance of the lined plane and θ_0 the angle between the the z-axis and $\boldsymbol{R_I} = \boldsymbol{x_R} - \boldsymbol{x_I}$. As indicated in the literature [70], the square root in Eq. B.5 is taken with a negative real part unless the conditions (1) $\mathrm{Re}(\gamma_1) < -1$, (2) $\mathrm{Im}(A) > 0$ and (3) $t > t_1$ are simultaneously fulfilled.

A prediction of the PSD IL can be obtained by assuming that the sources are concentrated at the tube end/aerofoil tip, hence separated vertically from the surface by the gap size e, and making use of Eq. B.1 with the coordinates of the receiver as the relative locations of the far-field microphones. The model can be numerically extended to dipoles and quadrupoles by considering monopole sources of opposite phase separated by a distance ϵ such that $\epsilon << \lambda$ and $\epsilon << e$, as indicated in the third column of Table B.1.

The computation of the power radiated by a point source over a hard/lined plane across an arbitrary surface S in space is required to obtain an analytical prediction comparable with the measured PWL from the spiral microphone array. In particular, it should be possible to integrate the intensity field through the surface of the spiral array used in the experimental set-up, as indicated in Fig. B.2b. The computational domain has been discretised to allow for a numerical approximation of the acoustic particle velocity component normal to the surface of the spiral array (u_x) and the associated acoustic intensity (I_x):

$$u_x(x,y,z) = \frac{j}{\rho c k} \frac{p(x+\Delta x,y,z) - p(x,y,z)}{\Delta x} \quad , \tag{B.10}$$

$$I_x(x,y,z) = \frac{1}{2}\mathrm{Re}\left(p(x,y,z)u_x^*(x,y,z)\right) \quad , \tag{B.11}$$

and for numerical integration of the acoustic intensity over the spiral array surface to obtain the acoustic power. Note that the spiral array extent goes beyond the end of the support plate and therefore the numerical integration is only performed for the red area indicated in Fig. B.2b.

$$P = \int_S I_x dS = \sum_i \sum_j I_x(x,y_i,z_j)\Delta y \Delta z \quad . \tag{B.12}$$

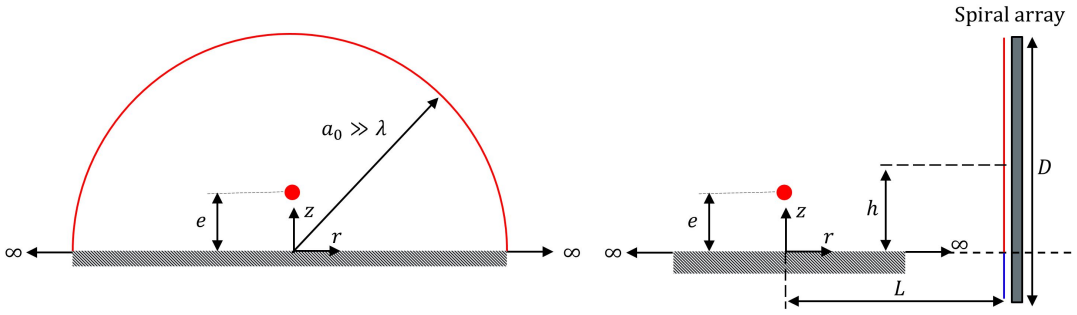

(a) Half-space problem (b) Integration over the spiral array

Figure B.2: Geometries used for (a) the verification of the source power computation and (b) the comparison with the post-processed spiral array data.

The numerical procedure described above is verified with the analytical solutions of Ingard and Lamb [10] and Levine [6]. The problem of a static point source (monopole, dipole and quadrupole) over an infinite rigid plane was considered by Ingard and Lamb [10]. Their analysis was based on the use of the method of images and the power output obtained by integrating the energy flux away from the source. They gave explicit analytical power amplification factors, defined as the ratio of power radiated in the presence of the plane (P) to the power radiated in free-field (P_f). A summary of the analytical expressions is shown in Table B.1, where $z = 2ke$, k is the wave number and e the distance from the source to the plane.

Table B.1: Summary of Ingard and Lamb [10] power amplification factors for a point source in the presence of a rigid plane and diagrams of the discrete models used for each type of point source.

Source	**Power amplification factor**	**Discrete Model**
Monopole	$\frac{P}{P_f} = 1 + \frac{\sin z}{z}$	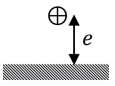
Dipole (horizontal)	$\frac{P}{P_f} = 1 + \frac{3}{z}\left[\frac{\sin z}{z^2} - \frac{\cos z}{z}\right]$	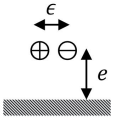
Quadrupole (longitudinal, vertical)	$\frac{P}{P_f} = 1 + \frac{5}{z}\left[\left(1 - \frac{12}{z^2} + \frac{24}{z^4}\right)\sin z + \left(\frac{4}{z} - \frac{24}{z^3}\right)\cos z\right]$	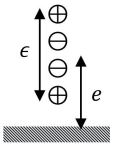

An alternative approach was introduced by Levine [6], consisting of a direct evaluation of a secondary source at the source position to account for the presence of the surface. The method was applied for a monopole point source with several plane and half-plane configurations, including an infinite lined plane. The power amplification factor corresponding to the power radiated *away* from the surface is expressed as

$$\frac{P}{P_f} = 1 + \frac{\sin z}{z} + 2\mathrm{Re}\left(Ae^{jAz}\left[E_1\left(j\left[1+A\right]z\right) - E_1\left(jAz\right)\right]\right) - 2\mathrm{Re}(A)\int_0^1 \frac{\mu d\mu}{\left|A+\sqrt{1-\mu^2}\right|^2} \quad , \tag{B.13}$$

where $z = 2ke$ as before and $E_1(\zeta)$ is defined as the integral

$$E_1(\zeta) = \int_\zeta^\infty \frac{e^{-\xi}d\xi}{\xi}, \quad |\arg(\zeta)| < \pi \quad . \tag{B.14}$$

The power obtained by integration of the intensity field through the hemisphere above the half-space is requited to compare the proposed procedure with the exact analytical expressions: Eq. B.13 for a monopole over a lined plane and the equations in Table B.1 for multipoles over a rigid surface. It is convenient to express the acoustic field in spherical coordinates for this verification exercise outlined in Fig. B.2a.

The comparison of the computed numerical amplification factors with the exact solution (Eq. B.13) is shown in Fig. B.3 for three values of liner impedance. The results are plotted as a function of e/λ: the gap size (e) normalised with the wavelength (λ). Note that the power output of the point source can be drastically reduced when located very close to the lined surface (relative to the wavelength): from $0.6P_f$ at e/λ=2 to $0.2P_f$ at e/λ=0.01 for $Z = 1$ (Fig. B.3b). An analogous comparison to verify the discrete model used for multipole sources is shown in Fig. B.4 for a hard wall plane. The results also present an excellent agreement and show the well-known result that the point source radiates twice the power when $e = 0$ (due to the image source) and tends to the free-field values as it moves away from the surface.

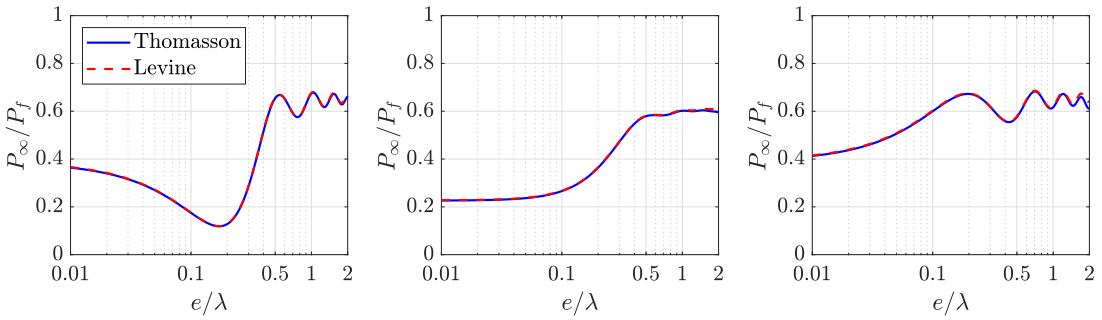

(a) $Z = 1 - j$ (b) $Z = 1$ (c) $Z = 1 + j$

Figure B.3: Verification of the discrete numerical integration for the power output of a monopole source over a lined infinite plane.

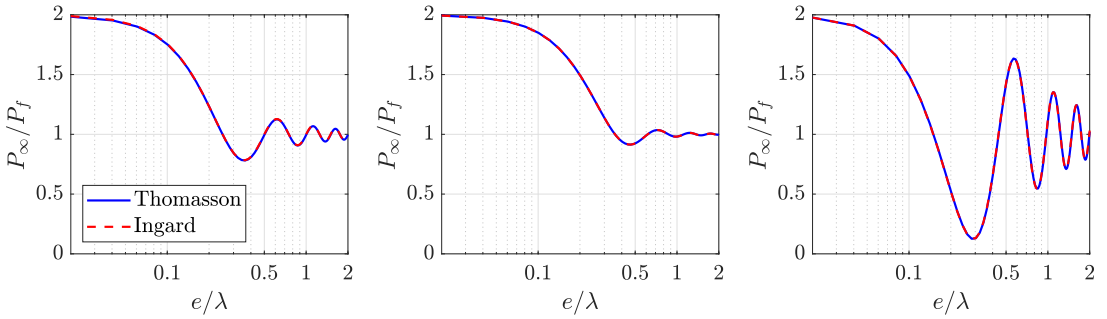

(a) Monopole (b) Horizontal dipole (c) Longitudinal vertical quadrupole

Figure B.4: Verification of the discrete model for the power output of multipole sources over a hard infinite plane.

References

[1] A. Kempton, "Acoustic liners for modern aero-engines," *15th CEAS-ASC Workshop*, 2011.

[2] S. Moreau, "Turbomachinery Noise Predictions: Present and Future," *Acoustics*, vol. 1, no. 1, pp. 92–116, 2019.

[3] J. F. Groeneweg, T. G. Sofrin, E. J. Rice, and P. R. Gliebe, "Turbomachinery Noise," in *Aeroacoustics of Flight Vehicles: Theory and Practice. Vol. 1: Noise Sources* (H. H. Hubbard, ed.), pp. 151–205, 1995.

[4] R. J. Astley, "Predicting and treating fan and turbomachinery noise current technology, research & facilities," in *UK-Japan Bilateral Workshop, Aircraft Emissions and Noise*, 2006.

[5] R. Bozak and R. P. Dougherty, "Measurement of Noise Reduction from Acoustic Casing Treatments Installed Over a Subscale High Bypass Ratio Turbofan Rotor," in *AIAA/CEAS Aeroacoustics Conference*, no. 4099, 2018.

[6] H. Levine, "Output of acoustical sources," *J. Acoust. Soc. Am.*, vol. 67, no. 6, pp. 1935–1946, 1980.

[7] P. Joseph, C. L. Morfey, and C. R. Lowis, "Multi-mode sound transmission in ducts with flow," *Journal of Sound and Vibration*, vol. 264, no. 3, pp. 523–544, 2003.

[8] G. Gabard and R. J. Astley, "Theoretical model for sound radiation from annular jet pipes: Far- and near-field solutions," *Journal of Fluid Mechanics*, vol. 549, pp. 315–341, 2006.

[9] C. E. Hughes, R. J. Jeracki, R. P. Woodward, and C. J. Miller, "Fan Noise Source Diagnostic Test — Rotor Alone Aerodynamic Performance Results," in *8th AIAA/CEAS Aeroacoustics Conference & Exhibit*, no. 2426, 2002.

[10] U. Ingard and G. L. Lamb, "Effect of a Reflecting Plane on the Power Output of Sound Sources," *The Journal of the Acoustical Society of America*, vol. 29, no. 6, pp. 743–744, 1957.

[11] C. Clark, "Noise: aircraft noise effects on health," tech. rep., London, 2015.

[12] Civil Aviation Authority, "Aircraft noise and health effects : Recent findings," tech. rep., CAP 1278, 2016.

[13] L. Leylekian, M. Lebrun, and P. L. An, "An Overview of Aircraft Noise Reduction Technologies," *AerospaceLab*, no. 7, pp. 1–15, 2014.

[14] International Civil Aviation Organization (ICAO), "Effects of Novel Coronavirus (COVID-19) on Civil Aviation: Economic Impact Analysis Air Transport Bureau Contents," 2020.

[15] P. Suau-sanchez, A. Voltes-dorta, and N. Cugueró-escofet, "An early assessment of the impact of COVID-19 on air transport: Just another crisis or the end of aviation as we know it?," *Journal of Transport Geography*, vol. 86, 2020.

[16] D. Casalino, F. Diozzi, R. Sannino, and A. Paonessa, "Aircraft noise reduction technologies: A bibliographic review," *Aerospace Science and Technology*, vol. 12, no. 1, pp. 1–17, 2008.

[17] D. L. Huff, "Technologies for Turbofan Noise Reduction," in *35th International Congress and Exposition on Noise Control Engineering*, 2006.

[18] D. P. Lockard and G. M. Lilley, "The Airframe Noise Reduction Challenge," tech. rep., NASA/TM–2004–213013, 2004.

[19] D. L. Sutliff, M. G. Jones, and T. C. Hartley, "High-Speed Turbofan Noise Reduction Using Foam-Metal Liner Over-the-Rotor," *Journal of Aircraft*, vol. 50, no. 5, pp. 1491–1503, 2013.

[20] M. G. Jones, D. Nark, B. Howerton, and M. C. Brown, "A Review of Acoustic Liner Experimental Characterization at NASA Langley," Tech. Rep. NASA/TP–2020–220583, 2020.

[21] E. Brambley, "Review of acoustic liner models with flow," in *Acoustics*, 2012.

[22] R. J. Astley, R. Sugimoto, I. M. Achunche, M. F. Kewin, P. Mustafi, and E. P. Deane, "A review of CAA for fan duct propagation and radiation, with application to liner optimisation," *Procedia Engineering*, vol. 6, pp. 143–152, 2010.

[23] J. R. Mathews and N. Peake, "The acoustic Green's function for swirling flow with variable entropy in a lined duct," *Journal of Sound and Vibration*, vol. 419, pp. 630–653, 2018.

[24] E. Nesbitt, "Current engine noise and reduction technology," *CEAS Aeronautical Journal*, vol. 10, no. 1, pp. 93–100, 2019.

[25] D. M. Nark and M. G. Jones, "Design of an Advanced Inlet Liner for the Quiet Technology Demonstrator 3," in *25th AIAA/CEAS Aeroacoustics Conference*, no. 2764, 2019.

[26] D. L. Sutliff and M. G. Jones, "Low-Speed Fan Noise Attenuation from a Foam-Metal Liner," *Journal of Aircraft*, vol. 46, no. 4, pp. 1381–1394, 2009.

[27] D. Elliott, R. Woodward, and G. Podboy, "Acoustic Performance of Novel Fan Noise Reduction Technologies for a High Bypass Model Turbofan at Simulated Flight Conditions," in *15th AIAA/CEAS Aeroacoustics Conference*, no. 3140, 2009.

[28] D. L. Sutliff, D. M. Elliott, M. G. Jones, and T. C. Hartley, "Attenuation of FJ44 turbofan engine noise with a foam-metal liner installed over-the-rotor," in *15th AIAA/CEAS Aeroacoustics Conference*, no. 3141, 2009.

[29] C. E. Hughes and J. A. Gazzaniga, "Effect of Two Advanced Noise Reduction Technologies on the Aerodynamic Performance of an Ultra High Bypass Ratio Fan," in *15th AIAA/CEAS Aeroacoustics Conference*, no. 3139, pp. 11–13, 2009.

[30] R. Bozak, C. Hughes, and J. Buckley, "The Aerodynamic Performance of an Over-The-Rotor Liner with Circumferential Grooves on a High Bypass Ratio Turbofan Rotor," in *Proceedings of ASME Turbo Expo 2013: Turbine Technical Conference and Exposition*, no. GT2013-95114, pp. 1–8, 2013.

[31] M. R. Gazella, T. Takakura, D. L. Sutliff, R. Bozak, and B. J. Tester, "Evaluating the Acoustic Benefits of Over-the-Rotor Acoustic Treatments Installed on the Advanced Noise Control Fan," in *23rd AIAA/CEAS Aeroacoustics Conference*, no. 3872, 2017.

[32] R. F. Bozak and G. G. Podboy, "Evaluating the Aerodynamic Impact of Circumferentially Grooved Fan Casing Treatments With Integrated Acoustic Liners on a Turbofan Rotor," in *Proceedings of ASME Turbo Expo 2019*, no. GT2019-91369, pp. 1–11, 2019.

[33] M. Jones, T. Parrott, D. Sutliff, and C. Hughes, "Assessment of Soft Vane and Metal Foam Engine Noise Reduction Concepts," in *15th AIAA/CEAS Aeroacoustics Conference*, no. 3142, 2009.

[34] M. G. Jones and B. M. Howerton, "Evaluation of Novel Liner Concepts for Fan and Airframe Noise Reduction," in *22nd AIAA/CEAS Aeroacoustics Conference*, no. 2789, 2016.

[35] N. Peake and A. B. Parry, "Modern Challenges Facing Turbomachinery Aeroacoustics," *Annual Review of Fluid Mechanics*, pp. 227–250, 2012.

[36] J. R. Mathews and N. Peake, "The acoustic Green's function for swirling flow in a lined duct," *Journal of Sound and Vibration*, vol. 395, pp. 294–316, 2017.

[37] R. Bozak, M. G. Jones, B. M. Howerton, and M. C. Brown, "Effect of Grazing Flow on Grooved Over-the-Rotor Acoustic Casing Treatments," in *25th AIAA/CEAS Aeroacoustics Conference*, no. 2564, 2019.

[38] M. J. T. Smith, *Aircraft Noise*. Cambridge: Cambridge University Press, 1989.

[39] A. McAlpine and M. J. Fisher, "On the prediction of "Buzz-saw" noise in aero-engine inlet ducts," *Journal of Sound and Vibration*, vol. 248, no. 1, pp. 123–149, 2001.

[40] J. M. Tyler and T. G. Sofrin, "Axial flow compressor noise studies," in *SAE Technical Paper*, SAE International, 1962.

[41] R. J. Astley, R. Sugimoto, and G. Gabard, "The Effect of Steady Flow Distortion on Mode Propagation in a Turbofan Intake," in *20th AIAA/CEAS Aeroacoustics Conference AIAA 2014-3113 Downloaded*, no. 3113, pp. 1–22, 2014.

[42] A. Mcalpine, M. C. Wrigth, H. Batard, and S. Thezelais, "Finite/boundary element assessment of a turbofan spliced intake liner at supersonic fan operating conditions," in *9th AIAA/CEAS Aeroacoustics Conference and Exhibit*, no. 3305, 2003.

[43] B. J. Tester, C. J. Powles, N. J. Baker, and A. J. Kempton, "Scattering of sound by liner splices: A kirchhoff model with numerical verification," *AIAA Journal*, vol. 44, no. 9, pp. 2009–2017, 2006.

[44] C. K. Tam, H. Ju, and E. W. Chien, "Scattering of acoustic duct modes by axial liner splices," *Journal of Sound and Vibration*, vol. 310, no. 4-5, pp. 1014–1035, 2008.

[45] J. E. Williams and L. H. Hall, "Aerodynamic sound generation by turbulent flow in the vicinity of a scattering half plane," *Journal of Fluid Mechanics*, vol. 40, no. 4, pp. 657–670, 1970.

[46] M. C. Jacob, J. Grilliat, R. Camussi, and G. C. Gennaro, "Aeroacoustic investigation of a single airfoil tip leakage flow," *International Journal of Aeroacoustics*, vol. 9, no. 3, pp. 253–272, 2010.

[47] P. Kholodov, M. Sanjose, and S. Moreau, "Tip flow evolution in a turbofan rotor for broadband noise diagnostic," in *AIAA AVIATION 2020 FORUM*, no. 2521, pp. 1–12, 2020.

[48] M. J. Lighthill, "On sound generated aerodynamically," *Proc. R. Soc. Lond. A*, vol. 221, no. 1107, pp. 564–587, 1951.

[49] J. E. Ffowcs Williams and D. L. Hawkings, "Theory relating to the noise of rotating machinery," *Journal of Sound and Vibration*, vol. 10, no. 1, pp. 10–21, 1969.

[50] M. E. Goldstein, *Aeroacoustics*. New York, [etc.]: McGraw-Hill, 1976.

[51] S. W. Rienstra and B. J. Tester, "An analytic Green's function for a lined circular duct containing uniform mean flow," *Journal of Sound and Vibration*, vol. 317, no. 3-5, pp. 994–1016, 2008.

[52] H. Posson and N. Peake, "The acoustic analogy in an annular duct with swirling mean flow," *Journal of Fluid Mechanics*, vol. 726, pp. 439–475, 2013.

[53] S. Rienstra and A. Hirschberg, *An Introduction to Acoustics*. 2015.

[54] J. Grilliat, M. Jacob, R. Camussi, and G. Caputi-Gennaro, "Tip Leakage Experiment - Part One: Aerodynamic And Acoustic Measurements," in *13th AIAA/CEAS Aeroacoustics Conference*, no. 3684, 2007.

[55] J. Boudet, M. C. Jacob, J. Caro, E. Jondeau, and B. Li, "Wavelet analysis of a blade tip-leakage flow," *AIAA Journal*, vol. 56, no. 8, pp. 3332–3336, 2018.

[56] R. Koch, M. Sanjose, and S. Moreau, "Large-Eddy Simulation of a Single Airfoil Tip-Leakage Flow," in *AIAA AVIATION Forum*, no. 2514, 2020.

[57] G. R. Yakhina, M. Roger, A. Finez, S. Bouley, V. Baron, S. Moreau, and J. Giez, "Localization of Swept Free-Tip Airfoil Noise Sources by Microphone Array Processing," *AIAA Journal*, vol. 58, no. 8, pp. 1–12, 2020.

[58] G. Bampanis and M. Roger, "Three-dimensional effects in the reduction of turbulence-impingement noise of aerofoils by wavy leading edges," in *Euronoise*, pp. 97–104, 2018.

[59] G. Bampanis, M. Roger, D. Ragni, F. Avallone, and C. Teruna, "Airfoil-Turbulence Interaction Noise Source Identification and its Reduction by Means of Leading Edge Serrations," in *25th AIAA/CEAS Aeroacoustics Conference*, no. 2741, pp. 1–18, 2019.

[60] R. E. Motsigner and R. K. Kraft, "Design and Performance of Duct Acoustic Treatment," in *Aeroacoustics of Flight Vehicles: Theory and Practice. Vol. 2: Noise Control*, 1991.

[61] J.-F. Piet and G.Elias, "Modelisation du champ acoustique incident sur la coiffe d'ariane 5 par des sources simples," *Office NationalD'Études et de Recherches Aerospatiales Rept. TAP–94-062*, 1994.

[62] E. J. Arcondoulis, C. J. Doolan, A. C. Zander, and L. A. Brooks, "A review of trailing edge noise generated by airfoils at low to moderate Reynolds number," *Acoustics Bulletin*, vol. 36, no. 2, pp. 33–40, 2011.

[63] C. K. Tam, "Discrete tones of isolated airfoils," *Journal of the Acoustical Society of America*, vol. 55, no. 6, pp. 1173–1177, 1974.

[64] A. Mcalpine, E. C. Nash, and M. V. Lowson, "Generation of Discrete Frequency Tones by the Flow around an Airfoil," *Journal of Sound and Vibration*, vol. 5, no. 222, pp. 753–779, 1999.

[65] H. Arbey and J. Bataille, "Noise generated by airfoil profiles placed in a uniform laminar flow," *Journal of Fluid Mechanics*, vol. 134, p. 33, sep 1983.

[66] M. Sanjose, A. Towne, P. Jaiswal, S. Moreau, S. Lele, and A. Mann, "Modal analysis of the laminar boundary layer instability and tonal noise of an airfoil at Reynolds number 150,000," *International Journal of Aeroacoustics*, vol. 18, no. 2-3, pp. 317–350, 2019.

[67] J. Grilliat, E. Jondeau, M. C. Jacob, M. Roger, and R. Camussi, "Broadband noise prediction models and measurements of tip leakage flows," in *14th AIAA/CEAS Aeroacoustics Conference*, no. 2845, 2008.

[68] R. K. Amiet, "Noise due to turbulent flow past a trailing edge," *Journal of Sound and Vibration*, vol. 47, no. 3, pp. 387–393, 1976.

[69] R. C. Dunne and M. S. Howe, "Wall-bounded blade-tip vortex interaction noise," *Journal of Sound and Vibration*, vol. 202, no. 5, pp. 605–618, 1997.

[70] S. Thomasson, "Reflection of waves from a point source by an impedance boundary," *The Journal of the Acoustical Society of America*, vol. 59, p. 780, 1976.

[71] U. Ingard, "On the Reflection of a Spherical Sound Wave from an Infinite Plane," *The Journal of the Acoustical Society of America*, vol. 23, no. 3, pp. 329–335, 1951.

[72] U. Ingard, "Influence of Fluid Motion Past a Plane Boundary on Sound Reflection, Absorption, and Transmission," *The Journal of the Acoustical Society of America*, vol. 31, no. 7, pp. 1035–1036, 1959.

[73] M. K. Myers, "On the acoustic boundary condition in," *Journal of Sound and Vibration*, vol. 71, pp. 429–434, 1980.

[74] B. J. Tester, "The propagation and attenuation of sound in lined ducts containing uniform or "plug" flow," *Journal of Sound and Vibration*, vol. 28, no. 2, pp. 151–203, 1973.

[75] S. W. Rienstra, "A classification of duct modes based on surface waves," *Wave Motion*, vol. 37, no. 2, pp. 119–135, 2003.

[76] E. J. Brambley and N. Peake, "Classification of aeroacoustically relevant surface modes in cylindrical lined ducts," *Wave Motion*, vol. 43, no. 4, pp. 301–310, 2006.

[77] Y. Aurégan and M. Leroux, "Experimental evidence of an instability over an impedance wall in a duct with flow," *Journal of Sound and Vibration*, vol. 317, no. 3-5, pp. 432–439, 2008.

[78] D. Marx, Y. Aurégan, H. Bailliet, and J. C. Valiere, "PIV and LDV evidence of hydrodynamic instability over a liner in a duct with flow," *Journal of Sound and Vibration*, vol. 329, no. 18, pp. 3798–3812, 2010.

[79] E. J. Brambley, "Fundamental problems with the model of uniform flow over acoustic linings," *Journal of Sound and Vibration*, vol. 322, no. 4-5, pp. 1026–1037, 2009.

[80] Y. Renou and Y. Aurégan, "Failure of the Ingard–Myers boundary condition for a lined duct: An experimental investigation," *The Journal of the Acoustical Society of America*, vol. 130, no. 1, pp. 52–60, 2011.

[81] S. W. Rienstra and M. Darau, "Boundary-layer thickness effects of the hydrodynamic instability along an impedance wall," *Journal of Fluid Mechanics*, vol. 671, pp. 559–573, 2011.

[82] E. J. Brambley, "Well-Posed boundary condition for acoustic liners in straight ducts with flow," *AIAA Journal*, vol. 49, no. 6, pp. 1272–1282, 2011.

[83] D. Khamis and E. J. Brambley, "Acoustic boundary conditions at an impedance lining in inviscid shear flow," *Journal of Fluid Mechanics*, vol. 796, pp. 386–416, 2016.

[84] G. Gabard, "A comparison of impedance boundary conditions for flow acoustics," *Journal of Sound and Vibration*, vol. 332, no. 4, pp. 714–724, 2013.

[85] D. C. Pridmore-Brown, "Sound propagation in a fluid flowing through an attenuating duct," *Journal of Fluid Mechanics*, vol. 4, no. 4, pp. 393–406, 1958.

[86] D. Khamis and E. J. Brambley, "Viscous effects on the acoustics and stability of a shear layer over an impedance wall," *Journal of Fluid Mechanics*, vol. 810, pp. 489–534, 2017.

[87] V. Masson, J. R. Mathews, S. Moreau, H. Posson, and E. J. Brambley, "The impedance boundary condition for acoustics in swirling ducted flow," *Journal of Fluid Mechanics*, vol. 849, pp. 645–675, 2018.

[88] E. J. Rice, "Model for the Acoustic Impedance of a Perforated Plate Liner with Multiple Frequency Excitation," *The Journal of the Acoustical Society of America*, vol. 51, no. 1A, pp. 94–95, 1972.

[89] E. J. Rice, "A model for the pressure excitation spectrum and acoustic impedance of sound absorbers in the presence of grazing flow," in *Aeroacoustics Conference*, 1973.

[90] J. Kooi and S. Sarin, "An experimental study of the acoustic impedance of Helmholtz resonator arrays under a turbulent boundary layer," in *7th Aeroacoustics Conference*, 1981.

[91] A. Cummings, "The Effects of Grazing Turbulent Pipe-Flow on the Impedance of an Orifice," *Acta Acustica United with Acustica*, vol. 61, no. 4, 1986.

[92] C. K. Tam, K. Kurbatskii, K. Ahuja, and R. J. Gaeta, "A numerical and experimental investigation of the dissipation mechanisms of resonant acoustic liners," in *7th AIAA/CEAS Aeroacoustics Conference and Exhibit*, no. 2262, 2001.

[93] H. Bóden, "The effect of high level multi-tone excitation on the acoustic properties of perforates and liner samples," in *18th AIAA/CEAS Aeroacoustics Conference*, no. 2151, 2012.

[94] P. B. Murray and R. Jeremy Astley, "Development of a single degree of freedom perforate impedance model under grazing flow and high SPL," in *18th AIAA/CEAS Aeroacoustics Conference (33rd AIAA Aeroacoustics Conference)*, no. 2294, pp. 4–6, 2012.

[95] H. Bóden, "Acoustic properties of perforates under high level multi-tone excitation," in *19th AIAA/CEAS Aeroacoustics Conference*, no. 2175, 2013.

[96] P. Murray, C. Donnan, C. Richter, and J. Astley, "Development of a single degree of freedom micro-perforate impedance model under grazing flow and high SPL," in *22nd AIAA/CEAS Aeroacoustics Conference, 2016*, no. 2982, pp. 1–10, 2016.

[97] S. Rschevkin, *Theory of Sound*. Pergamon Press, 1963.

[98] S. Rienstra, "Contributions to the theory of sound propagation in ducts with bulk-reacting lining," *Journal of Acoustical Society of America*, vol. 77, no. 5, 1985.

[99] P. Sijtsma and H. M. M. V. D. Wal, "Modelling a Spiralling Type of Non-locally Reacting Liner," in *9th AIAA/CEAS Aeroacoustics Conference and Exhibit*, no. 3308, 2003.

[100] "Simcenter 3D 2019.2 Documentation," 2019.

[101] H. Bériot, A. Prinn, and G. Gabard, "Efficient implementation of high-order finite elements for Helmholtz problems," *International Journal for Numerical Methods in Engineering*, no. 106, pp. 213–240, 2016.

[102] S. Palleja-Cabre, B. J. Tester, R. J. Astley, and R. Bozak, "Modelling of Over-The-Rotor Acoustic Treatments for Improved Noise Suppression in Turbofan Engines," in *25th AIAA/CEAS Aeroacoustics Conference*, no. 2580, 2019.

[103] P. J. W. Block, "Noise response of cavities of varying dimensions at subsonic speeds," Tech. Rep. NASA TN D-8351, 1976.

[104] S. Ko, "Sound Attenuation in Lined Rectangular Ducts with Flow and Its Application to the Reduction of Aircraft Engine Noise," *The Journal of the Acoustical Society of America*, vol. 50, no. 6A, pp. 1418–1432, 1971.

[105] W. Eversman, "Computation of axial and transverse wave numbers for uniform two-dimensional ducts with flow using a numerical integration scheme," *Journal of Sound and Vibration*, vol. 41, no. 2, pp. 252–255, 1975.

[106] L. Shampine and M. Reichelt, "The MATLAB ODE SUITE," *SIAM Journal on Scientific Computing*, vol. 18, pp. 1–22, 1997.

[107] B. J. Tester, N. J. Baker, A. J. Kempton, and M. C. Wrigth, "Validation of an Analytical Model for Scattering by Intake Liner Splices," *10th AIAA/CEAS Aeroacoustics Conference*, no. 2906, 2004.

[108] W. E. Zorumski, "Acoustic theory of axisymmetric multisectioned ducts," Tech. Rep. NASA-TR-R-419, L-9222, 1974.

[109] J. S. Alonso and R. A. Burdisso, "Sound Radiation from the Boundary in a Circular Lined Duct with Flow," in *9th AIAA/CEAS Aeroacoustics Conference and Exhibit*, no. 3144, 2003.

[110] J. . Alonso, L. Molisani, and R. A. Burdisso, "Spectral and Wavenumber Approaches to Obtain Green's Functions for Convected Wave Equation," in *10th AIAA/CEAS Aeroacoustics Conference*, no. 2943, 2004.

[111] J. S. Alonso and R. A. Burdisso, "Green's functions for the acoustic field in lined ducts with uniform flow," *AIAA Journal*, vol. 45, no. 11, pp. 2677–2687, 2007.

[112] C. Ventres, M. Theobald, and W. Mark, "Turbofan noise generation. Volume 1: Analysis," tech. rep., 1982.

[113] H. D. Meyer and E. Envia, "Aeroacoustic analysis of turbofan noise generation," tech. rep., 1996.

[114] S. A. L. Glegg, "Broadband Generated by Small Fan Noise Turbulence Scale," tech. rep., 1998.

[115] S. A. Glegg and C. Jochault, "Broadband self-noise from a ducted fan," *AIAA Journal*, vol. 36, no. 8, pp. 1387–1395, 1998.

[116] C. R. Lowis and P. F. Joseph, "Determining the strength of rotating broadband sources in ducts by inverse methods," *Journal of Sound and Vibration*, vol. 295, no. 3-5, pp. 614–632, 2006.

[117] A. McAlpine and M. J. Kingan, "Far-field sound radiation due to an installed open rotor," *International Journal of Aeroacoustics*, vol. 11, no. 2, pp. 213–245, 2012.

[118] Z.-H. Wang, I. V. Belyaev, X.-Z. Zhang, C.-X. Bi, G. A. Faranosov, and E. H. Dowell, "The sound field of a rotating dipole in a plug flow," *The Journal of the Acoustical Society of America*, vol. 143, no. 4, pp. 2099–2109, 2018.

[119] Q. Zhou and P. F. Joseph, "Frequency-Domain Method for Rotor Self-Noise Prediction," vol. 44, no. 6, 2006.

[120] W. K. Blake, *Mechanics of Flow-Induced Sound and Vibration*. Elsevier Inc, 2 ed., 2017.

[121] C. L. Morfey, "Sound transmission and generation in ducts with flow," *Journal of Sound and Vibration*, vol. 14, no. 1, pp. 37–55, 1971.

[122] C. L. Morfey, "Acoustic energy in non-uniform flows," *Journal of Sound and Vibration*, vol. 14, no. 2, pp. 159–170, 1971.

[123] W. Eversman, "Energy flow criteria for acoustic propagation in ducts with flow," *The Journal of the Acoustical Society of America*, vol. 49, p. 1717, 1971.

[124] Free Field Technologies, *Actran 17.0*, vol. 1.

[125] S. Guerin, A. Moreau, and U. Tapken, "Relation between source models and acoustic duct modes," in *15th AIAA/CEAS Aeroacoustics Conference*, no. 3364, 2009.

[126] D. L. Lansing and W. E. Zorumski, "Effects of wall admittance changes on duct transmission and radiation of sound," *Journal of Sound and Vibration*, vol. 27, no. 1, pp. 85–100, 1973.

[127] J. F. Unruh, "Finite length tuning for low frequency lining design," *Journal of Sound and Vibration*, vol. 45, no. 1, pp. 5–14, 1976.

[128] A. McAlpine, R. J. Astley, V. J. Hii, N. J. Baker, and A. J. Kempton, "Acoustic scattering by an axially-segmented turbofan inlet duct liner at supersonic fan speeds," *Journal of Sound and Vibration*, vol. 294, no. 4, pp. 780–806, 2006.

[129] G. Gabard and R. J. Astley, "A computational mode-matching approach for sound propagation in three-dimensional ducts with flow," *Journal of Sound and Vibration*, vol. 315, no. 4-5, pp. 1103–1124, 2008.

[130] M. Oppeneer, S. W. Rienstra, and P. Sijtsma, "Efficient mode matching based on closed-form integrals of pridmore-brown modes," *AIAA Journal*, vol. 54, no. 1, pp. 266–279, 2016.

[131] R. Kirby and F. D. Denia, "Analytic mode matching for a circular dissipative silencer containing mean flow and a perforated pipe," *The Journal of the Acoustical Society of America*, vol. 122, no. 6, pp. 3471–3482, 2007.

[132] G. Gabard, "Mode-matching techniques for sound propagation in lined ducts with flow," in *16th AIAA/CEAS Aeroacoustics Conference*, no. 3940, 2010.

[133] W. Eversman, "Acoustic energy in ducts: Further observations," *Journal of Sound and Vibration*, vol. 62, no. 4, pp. 517–532, 1979.

[134] W. Eversman, "The boundary condition at an impedance wall in a non-uniform duct with potential mean flow," *Journal of Sound and Vibration*, vol. 246, no. 1, pp. 63–69, 2001.

[135] M. Abramowitz and I. Stegun, *Handbook of Mathematical Functions*. New York: Dover Publications, INC., 1965.

[136] A. Cummings, "High frequency ray acoustics models for duct silencers," *Journal of Sound and Vibration*, vol. 221, no. 4, pp. 681–708, 1999.

[137] B. J. Tester, "Acoustic energy flow in lined ducts containing uniform or "plug" flow," *Journal of Sound and Vibration*, vol. 28, no. 2, pp. 205–215, 1973.

[138] W. Möhring, "Energy flux in duct flow," *Journal of Sound and Vibration*, vol. 18, no. 1, pp. 101–109, 1971.

[139] D. L. Lansing, "Exact solution for radiation of sound from a semi-infinite circular duct with application to fan an compressor noise," in *Analytic Methods in Aircraft Aerodynamics: NASA SP-228*, 1969.

[140] R. M. Munt, "The interaction of sound with a subsonic jet issuing from a semi-infinite cylindrical pipe," *Journal of Fluid Mechanics*, vol. 83, no. 4, pp. 609–640, 1977.

[141] R. M. Munt, "Acoustic transmission properties of a jet pipe with subsonic jet flow: I. The cold jet reflection coefficient," *Journal of Sound and Vibration*, vol. 142, no. 3, pp. 413–436, 1990.

[142] S. W. Rienstra, "Acoustic radiation from a semi-infinite annular duct in a uniform subsonic mean flow," *Journal of Sound and Vibration*, vol. 94, no. 2, pp. 267–288, 1984.

[143] C. Yang, Y. Fang, C. Zhao, and X. Zhang, "On modeling the sound propagation through a lined duct with a modified Ingard-Myers boundary condition," *Journal of Sound and Vibration*, vol. 424, pp. 173–191, 2018.

[144] R. Bozak, G. Podboy, B. Dougherty, M. Jones, D. Sutliff, and D. Nark, "W-8 Acoustic Casing Treatment Test Overview," in *Acoustics Technical Working Group (ATWG) Meeting*, 2017.

[145] J. Premo, P. Joppa, and T. B. Company, "Fan Noise Source Diagnostic Test - Wall Measured Circumferential Array Mode Results," in *8th AIAA/CEAS Aeroacoustics Conference & Exhibit*, no. 2429, pp. 1–13, 2002.

[146] R. Bozak, "W-8 Inlet In-duct Array Evaluation," in *Acoustics Technical Working Group Meeting*, 2018.

[147] R. P. Dougherty and R. F. Bozak, "Two-dimensional modal beamforming in wavenumber space for duct acoustics," in *2018 AIAA/CEAS Aeroacoustics Conference*, no. 2805, pp. 1–11, 2018.

[148] C. Weng and F. Bake, "An analytical model for boundary layer attenuation of acoustic modes in rigid circular ducts with uniform flow," *Acta Acustica united with Acustica*, vol. 102, no. 6, pp. 1138–1141, 2016.

[149] J. E. Rossiter, "Wind-Tunnel Experiments on the Flow ocer Rectangular Cavities at Subsonic and Transonic Speeds," *Ministry of Aviation, Reports and Memoranda*, vol. 3438, 1964.

[150] J.-P. Coyette and B. Van den Nieuwenhof, "A conjugated infinite element method for half-space acoustic problems," *The Journal of the Acoustical Society of America*, vol. 108, no. 4, pp. 1464–1473, 2000.